Strain-engineering of the Topological Insulator HgTe

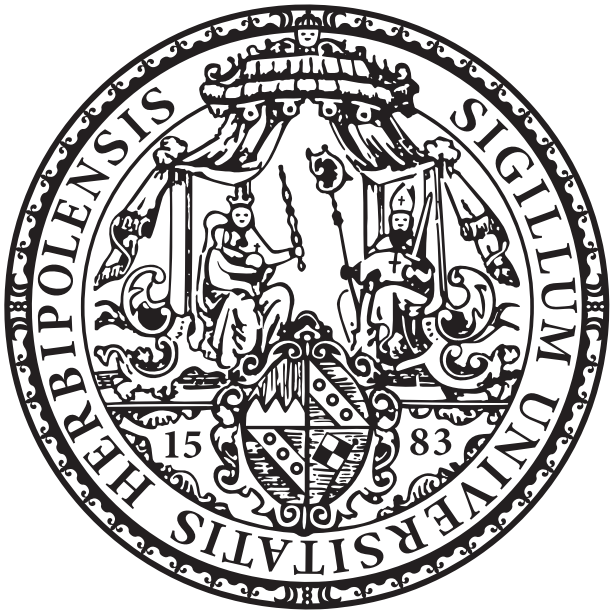

Dissertation zur Erlangung des naturwissenschaftlichen
Doktorgrades der Julius-Maximilians-Universität Würzburg

vorgelegt von

Philipp Leubner

aus Hersbruck

Würzburg, 2016

Eingereicht am: .....
bei der Fakultät für Physik und Astronomie

1. Gutachter: Prof. Dr. Hartmut Buhmann
2. Gutachter: Prof. Dr. Sven Höfling
3. Gutachter: .....
der Dissertation

Vorsitzende(r): Prof. Dr. Vladimir Dyakonov

1. Prüfer: Prof. Dr. Hartmut Buhmann
2. Prüfer: Prof. Dr. Sven Höfling
3. Prüfer: Prof. Dr. Giorgio Sangiovanni
im Promotionskolloquium

Tag des Promotionskolloquiums: 24. Juli 2017

Doktorurkunde ausgehändigt am: .....

Contents

Introduction **1**

1 Strain in layered crystals **5**

1.1 Strain and stress in (001) cubic crystals 5

1.2 Coherent epitaxy and critical thickness 8

1.3 Strain in Hg-based crystals 11

2 Heterostructure Growth **13**

2.1 Hg-based MBE 13

2.1.1 Introduction to MBE 13

2.1.2 Special aspects of Hg-based MBE 15

2.2 Sample Analysis 18

2.2.1 High-resolution X-ray diffraction 18

2.2.2 Reflection high-energy electron diffraction 19

2.2.3 Nomarski microscopy and atomic force microscopy 21

2.3 Epitaxy of CdTe on GaAs 23

2.3.1 Substrate preparation before CdTe epitaxy 23

2.3.2 CdTe buffer growth procedure 24

2.3.3 Residual strain in CdTe buffer layers 27

2.4 CdTe-$Cd_{0.5}Zn_{0.5}Te$ superlattices on GaAs 27

2.4.1 Effective lattice constant model 28

2.4.2 Growth procedure of MBE-ALE CdTe-$Cd_{0.5}Zn_{0.5}Te$ SLS 29

2.4.3 Study of SLS layer structure by HRXRD 31

2.4.4 Comparison of SLS crystal quality with CdZnTe solid solutions . 38

2.5 Hg-based heterostructures on different substrate types 39

2.5.1 Epitaxy on II-VI substrates 40

2.5.2 Determining the thickness of quantum wells 41

2.5.3 Critical thickness of strain-engineered heterostructures on superlattices . . . 44
2.5.4 Zn in barrier layers . . . 48
2.6 Strain-engineering of HgTe bulk layers . . . 50

3 The band structure of HgTe **53**
3.1 Band structure of bulk solid solutions . . . 53
3.2 Strain in HgTe bulk layers . . . 54
3.3 Band structure calculation of HgTe quantum wells . . . 57
3.3.1 Influence of quantum well thickness . . . 57
3.3.2 Strained quantum wells . . . 60
3.3.3 Temperature dependence of energy gap . . . 64

4 The quantum spin Hall effect **67**
4.1 Band inversion and the quantum spin Hall effect . . . 67
4.2 Measurements on microstructures . . . 70
4.3 Non-quantized conductance . . . 71
4.3.1 Experimental studies on sample size and temperature dependence 72
4.3.2 Backscattering mechanisms in helical Luttinger liquids . . . 74
4.3.3 Backscattering in neighboring electron reservoirs . . . 77

5 Magnetotransport measurements **81**
5.1 Sample fabrication, device geometry and measurement setup . . . 81
5.2 Strain-induced transition from semimetal to topological insulator in wide quantum wells . . . 82
5.2.1 Two-carrier conductance and band overlap . . . 85
5.2.2 Band gap measurement from thermally activated conductance . . 91
5.3 The influence of the magnitude of the band gap on transport in the quantum spin Hall regime . . . 93
5.3.1 Sample parameters . . . 94
5.3.2 Standard characterization . . . 96
5.3.3 Temperature and band gap dependence of edge state conductance 97
5.3.4 Persistence of edge state dominated transport . . . 99
5.3.5 Model of the temperature dependence of conductance . . . 102
5.3.6 Puddle density and electrostatic gating . . . 105
5.4 Hysteresis effects and edge state conductance . . . 110
5.4.1 Hysteretic training of edge state conductance . . . 110

5.4.2 Studies of the charging mechanism 114
5.4.3 Studies of the time dependence 116
5.4.4 Hysteresis in the positive gate voltage regime 117
5.5 The chiral anomaly in compressively strained bulk layers 119

Summary **125**

Zusammenfassung **129**

A Material parameters **133**

B Fits of temperature dependent minimum conductance **135**

C Additional data of hysteresis measurements of sample J **139**
C.0.1 Raw data of Hall resistance measurements 139
C.0.2 Carrier density of the large Hall bar 141

Abbreviations **143**

Bibliography **145**

List of publications **157**

Acknowledgements **161**

Introduction

Scientific progress in experimental physics is often driven by two different types of important contributions. On the one hand, there is the discovery of a new phenomenon which, so far, has been either predicted only by theory, or comes along entirely by surprise. An example of the former is the recent proof of the existence of gravitional waves [1], which has been predicted by Albert Einstein in 1916. The latter is exemplified by the discovery the Quantum Hall effect by Klaus von Klitzing [2], for which he was awarded the Nobel prize in 1985. On the other hand, there are discoveries which significantly alter the understanding of a phenomenon which was already known before, and by doing so, often widen the range of experimental parameters in which the phenomenon can be observed. This is often followed by an effort of industry to turn the discovery into a consumer product. An example is the semiconductor laser [3], which had the lasing technology move from laboratories to living rooms.

As it is the case for many attempts of categorization, the discrimination made above is not always strict. A good "intermediate" example is the prediction [4, 5] and experimental proof [6] of the quantum spin Hall (QSH) effect. The effect is observed in HgTe quantum wells (QWs), where the nontrivial topology of bands gives rise to a pair of one-dimensional, counterpropagating, spin-polarized, gapless channels on the edge of the sample. The system has therefore become known as the first two-dimensional topological insulator. On the one hand, many researchers see the discovery of these states as the pioneering work that lead to the birth of the huge research area of topological insulators. On the other hand, one can argue that the QSH insulating state extends the quantum Hall state, discovered by von Klitzing, to zero magnetic field. In that sense, the QSH state is an important step forward towards the fabrication of electronic devices based on the concept of topology-driven conductance.

Besides the need to apply a large magnetic field, there are other obstacles to overcome in order to achieve this goal. By now, studies of the QSH effect require low temperatures and small devices, due to the low energy gap and short inelastic mean-free path of the system [6]. One of the main motivations of this work was to address these limitations.

It should be noted that several theoretical works predict a connection between the two limitations, in the sense that an enlarged energy gap would suppress the backscattering that occurs in the QSH edge state [7, 8].

The approach we used to modify the band structure was to apply strain to the HgTe crystal, i.e. deform the cubic unit cell. This approach reflects the connection between the real-space crystal lattice and the Brillouin zone in reciprocal space. In particular, symmetries in real space often imply a degeneracy of electronic bands in reciprocal space, and lowering the symmetry lifts the degeneracy [9]. A recent example is the strain-driven lifting of the degeneracy of the two Γ_8-bands of bulk HgTe layers, which induces a small energy gap in the system, and turns it into a three-dimensional topological insulator [10].

	bulk crystals	quantum wells
tensile strain ($\varepsilon_{\|\|} < 0$)	■ *coherent growth on CdTe substrates.* Strain opens band gap. Three-dimensional topological insulators.	■ *Coherent growth on CdTe and $Cd_{0.96}Zn_{0.04}Te$ substrates.* Two-dimensional topological insulators. Wide QWs on CdTe are semimetals.
strain free ($\varepsilon_{\|\|} \approx 0$)	■ *Free standing bulk crystals, Fully relaxed on highly lattice mismatched substrates, growth on lattice matched substrates.* Zero gap semimetal.	■ *Growth on lattice matched substrates.* Two-dimensional topological insulators. Enlarged band gaps.
compressive strain ($\varepsilon_{\|\|} > 0$)	■ *Coherent epitaxy on substrates with smaller lattice constant.* Separate gapless points in **k**-space. Weyl semimetal predicted due to inversion asymmetry in zincblende lattice.	■ *Coherent epitaxy on substrates with smaller lattice constant.* two-dimensional topological insulators with large bandgaps.

Table 1: Influence of biaxial strain $\varepsilon_{||}$ (induced, e.g. by coherent growth on a lattice mismatched substrate) on bulk crystals and quantum wells. Possible fabrication methods are in italics, physical properties in roman letters. Systems with blue squares are synthesized for the first time in the course of this work.

Apart from using strain as a tool to maximize the energy gap in QWs, the more global aim of this work was to gain a deeper experimental insight into the influence of strain on the electronic properties of different HgTe epilayers, which were also in the focus of recent theoretical works [11, 12]. Table 1 provides an attempt to categorize the impact

of the different types of strain on the HgTe material system. In general, it is important to discriminate between bulk layers and QWs. The variety of different phenomena is evident. To the best of the author's knowledge, the systems labelled with blue squares have been fabricated for the first time in the course of this work. The epitaxial application of compressive strain ($\varepsilon_{||} > 0$, bottom row of table 1) is worth highlighting, as it opens up several interesting routes for future research. This new parameter space was realized by adding a new growth technique to the established molecular-beam epitaxy (MBE) of HgTe crystals. The technique is based on the use of CdTe $-$ $Cd_{0.5}Zn_{0.5}Te$ strained-layer superlattices (SLS) as artificial substrates. The lattice constant of these superlattices can be controlled within a wide range, and with that, we adjust the strain in the HgTe-based epilayers grown on top.

This thesis emphasizes the role of strain in a variety of experiments in HgTe-based research, and is organized as follows: In chapter 1, the general concept of strain in epitaxy is summarized, and the state of knowledge on the HgTe material system is presented. As the main part of this thesis, chapter 2 covers all aspects of HgTe MBE in large detail. Among the numerous techniques to analyze the as-grown crystals, we discuss high-resolution X-ray diffraction (HRXRD) in special detail, as it gives insight into crystal quality and layer thicknesses, as well as on the state of strain of the HgTe. The work builds on the comprehensive knowledge on the MBE of HgTe, and an outline of the state of the art is given. We then turn to the CdTe $-$ $Cd_{0.5}Zn_{0.5}Te$ SLS, which were grown in an all-new combination of MBE and atomic-layer epitaxy (ALE), and allow for high-accuracy lattice constant control. All these aspects are connected at the end of the section, which concludes with the growth of HgTe and $Cd_{0.7}Hg_{0.3}Te$ on SLS, and a modified way to grow barriers for heavily compressed quantum wells. With the choice of the SLS lattice constant, a new degree of freedom is added to the HgTe material system, and the impact of this parameter on the band structure is discussed theoretically in chapter 3. The predicted emergence of a Weyl semi-metal phase in compressively strained bulk layers is outlined. Furthermore, it is demonstrated that, for QWs, the combination of the two parameters strain and QW thickness yields a rich variety of band dispersions, including a regime with significantly enlarged energy gaps. As already noted in the beginning of this section, the QSH and its robustness against backscattering have been a possible application of strain-optimized QWs. The state of research of the QSH is covered in chapter 4, with special emphasis on the signatures and possible causes of deviations from the idealized model. Both experimental and theoretical works are discussed. In doing so, a connection is established between the previous chapters and the final chapter 5. We demonstrate how the new variety of energy dispersions (chapter 3), made available by the new SLS growth technique

(chapter 2) is reflected in characteristic magnetotransport signatures on Hall bar devices. We focus on the transport characteristics in the charge-neutral regime, where the QSH state is the dominant cause of conductance. We provide experimental data on the relationship between edge state conductance and QW energy gap, discuss a possible explanation for the observations, and present a new approach to enhance the edge state conductance. The section concludes with some first results on the predicted Weyl semi-metal phase in compressively strained bulk layers.

Finally, a comprehensive summary of the main findings of this thesis is given.

Chapter 1

Strain in layered crystals

The following chapter provides an introduction to the general concept of strain in crystals, with special emphasis on systems realized in the course of this work. We first clarify notation and justify some simplifications. Afterwards, the principle of coherent epitaxy on lattice mismatched substrates is presented, and limitations of this approach are discussed. Lastly, findings on the CdHgTe-CdZnTe material system are summarized. We will limit the discussion to crystals with cubic unit cells and stresses perpendicular or parallel to the basis vectors, since this covers all samples that were fabricated. For lower symmetry scenarios and a more comprehensive treatment of the topic, the reader is referred to Ref. [13]. As a first remark on terminology, note that in the field, terms like "stress" and "strain" are not always assigned to similar quantities. In older works, these terms often have the meaning of a pressure, whereas the response of the crystal is called "strain-induced deformation". In more recent works, pressures are often called "stress", and crystal deformations simply "strain" [14]. For the sake of brevity, this convention is followed here.

1.1 Strain and stress in (001) cubic crystals

Strain describes the distortion of the unit cell of a crystal from its "natural" shape. For simplicity, the concept is presented on a two-dimensional unit cell with basis vectors $\mathbf{b}_x$ and $\mathbf{b}_y$ [figure 1.1 (a)]. The location $\mathbf{r}$ of any object is given by a linear combination of these. Strain deforms the unit cell, modifies the basis vectors and consequently moves $\mathbf{r}$ to $\mathbf{r}'$. The nature of the deformation is described by strain components ε_{ij}, as illustrated in figure 1.1 (b). From the picture, one finds

$$\mathbf{b}'_x = (1-\varepsilon_{xx})\,\mathbf{b}_x - \varepsilon_{xy}\,\mathbf{b}_y \tag{1.1}$$

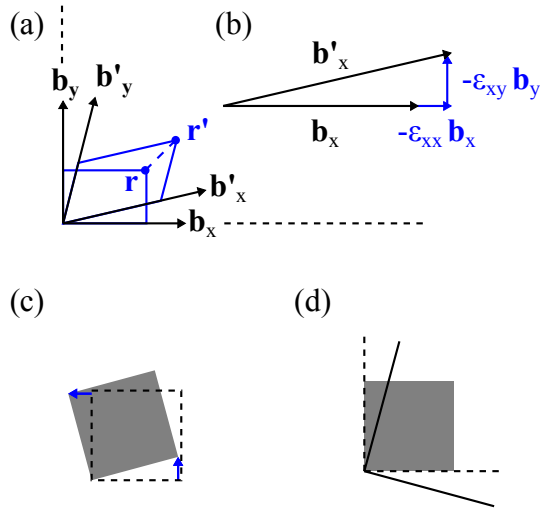

Figure 1.1: (a) Strain deforms the unit cell and displaces every position **r** in the crystal. (b) Definition of the strain components ε_{xx} and ε_{xy} in two dimensions. (c) Fully antisymmetric strain is equivalent to (d) - a rotation of the coordinate system.

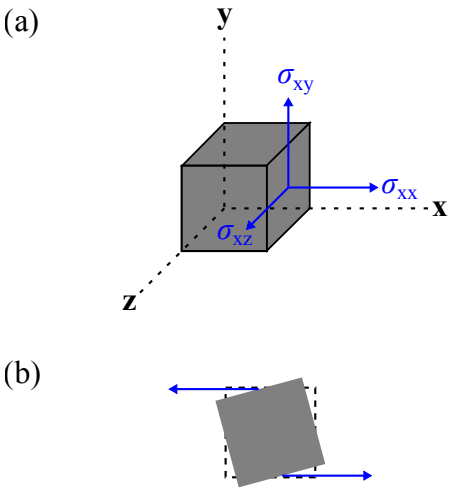

Figure 1.2: (a) Stresses σ_{ij} acting on one surface of a crystal. (b) shear stresses on only one pair of surfaces cause a torque on the object. In equilibrium, complementary stresses (not shown) have to cancel these out.

and similarly $\mathbf{b}'_y$. Note that, in general, all deformations are related to the length of the original basis vector [i.e. $\mathbf{b}_x$ in equation (1.1)]. Therefore, to be more accurate, $\mathbf{b}_y$ has to be replaced by $\mathbf{b}_y\ |\mathbf{b}_x|/|\mathbf{b}_y|$ in equation (1.1). For cubic unit cells, both are identical. The minus signs in equation (1.1) are a matter of convention. Here the sign is chosen such that the deformation caused by pushing forces (e.g. in a high pressure chamber) is positive - see the stress strain relation below [equation (1.4)]. The definition given by figure 1.1 (b) and equation (1.1) is the most instructive one and conserves the volume of the unit cell, if ε_{xx} and ε_{yy} are zero. However, the length of $\mathbf{b}'_x$ increases with ε_{xy}. The alternative definition of the ε_{ij} conserves the length of the basis vectors if the strain component parallel to the respective vector is zero. The ε_{ij} are then given by definition as:

- ε_{ii} is the change of the basis vector's length: $|\mathbf{b}'_i|/|\mathbf{b}_i| = -\varepsilon_{ii} + 1$.
- ε_{ij} is the tilt of the new basis vector $\mathbf{b}'_i$ towards $\mathbf{b}_j$. $\varepsilon_{ij} = \mathbf{b}'_i \cdot \mathbf{b}_j (|\mathbf{b}'_i||\mathbf{b}_j|)^{-1}$.

Both definitions are equivalent in the limit of small strains ε_{ij}. In this limit, the change in volume of the strained object is given by

$$\Delta V = -V\left(\varepsilon_{xx} + \varepsilon_{yy} + \varepsilon_{zz}\right). \tag{1.2}$$

In three dimensions, nine index combinations of ε_{ij} can be named. However, not all of them are independent quantities. In fact, all ε_{ij} with permutations of identical indices (i.e. ε_{xy} and ε_{yx}) have to be identical. This is illustrated as follows: for the extreme case of $\varepsilon_{xy} = -\varepsilon_{yx}$ [figure 1.1 (c)], the shape of the unit cell remains unchanged. The whole unit cell is rotated, which is equivalent to the choice of a rotated coordinate system [figure 1.1 (d)]. Obviously, for any arbitrary values ε'_{ij} given, e.g. ε'_{xy} and ε'_{yx}, the "true" deformation of the system is given by $\varepsilon_{xy} = \varepsilon_{yx} = 0.5\ (\varepsilon'_{xy} + \varepsilon'_{yx})$. The six independent ε_{ij} completely define the strain of the system and are written in vector notation as $\boldsymbol{\varepsilon} = (\varepsilon_{xx}, \varepsilon_{yy}, \varepsilon_{zz}, 2\varepsilon_{yz}, 2\varepsilon_{zx}, 2\varepsilon_{xy})$. This is called the "Voight notation". The factor two is introduced since off-diagonal elements appear twice in the original nine-component matrix.

Stress is the term used to describe forces that cause deformation of a solid. In this context, all forces are supposed to scale with the area of the surface they act on. Stresses are therefore forces normalized by this area, and given in units of pressure ($\mathrm{N\,m^{-2}}$). As for a cuboid object, stresses can act on three orthogonal surfaces and can be composed of three ortogonal directions of forces σ_{ij}. This is exemplified in figure 1.2 (a) for the surface with its normal in the x-direction. Since the objects investigated are free from any net force (i.e. are not accelerated), the opposite of any surface is always exposed to the opposite stress. This can be generalized to arbitrary shapes by cutting them into infinitesimal cubes. Furthermore, just as shown for the strain components, only six of the nine stress components σ_{ij} are independent quantities. For the shear components, i.e. the σ_{ij} with $i \neq j$, components with permutations of identical indices again have to be equal, since otherwise, a torque would act on the object. This is illustrated in figure 1.2 (b): shear stresses on one surface are finite (blue arrows), and no shear stresses on the orthogonal surface compensate the torque. The object would gain angular momentum. Again, the six independent stress components can be written jointly as a vector: $\boldsymbol{\sigma} = (\sigma_{xx}, \sigma_{yy}, \sigma_{zz}, \sigma_{yz}, \sigma_{zx}, \sigma_{xy})$.

For small strains ε_{ij}, Hookes law is valid, stating a linear relationship between stress and strain:

$$\boldsymbol{\sigma} = \boldsymbol{C} \cdot \boldsymbol{\varepsilon}. \tag{1.3}$$

And inversely $\boldsymbol{\varepsilon} = \boldsymbol{S} \cdot \boldsymbol{\sigma}$. Using the six-component vector notation of stress and strain, $\mathbf{C}$ and $\mathbf{S}$ can be expressed as 6×6 matrices, denoting the stiffness and compliance of the crystal (note the counterintuitive but common use of abbreviations: "$\mathbf{C}$" for stiffness and "$\mathbf{S}$" for compliance). Since the ε_{ij} are dimensionless, the matrix elements c_{ij} have the unit of pressures. Depending on the symmetries of the considered system, equation (1.3) can be simplified, i.e. the number of independent coefficients c_{ij} can be lowered. All materials discussed in this thesis crystallize in the zincblende scheme, which has cubic

crystal symmetry. For this symmetry, equation (1.3) simplifies to

$$\begin{pmatrix} \sigma_{xx} \\ \sigma_{yy} \\ \sigma_{zz} \\ \sigma_{yz} \\ \sigma_{zx} \\ \sigma_{xy} \end{pmatrix} = \begin{pmatrix} c_{11} & c_{12} & c_{12} & 0 & 0 & 0 \\ c_{12} & c_{11} & c_{12} & 0 & 0 & 0 \\ c_{12} & c_{12} & c_{11} & 0 & 0 & 0 \\ 0 & 0 & 0 & c_{44} & 0 & 0 \\ 0 & 0 & 0 & 0 & c_{44} & 0 \\ 0 & 0 & 0 & 0 & 0 & c_{44} \end{pmatrix} \cdot \begin{pmatrix} \varepsilon_{xx} \\ \varepsilon_{yy} \\ \varepsilon_{zz} \\ 2\varepsilon_{yz} \\ 2\varepsilon_{zx} \\ 2\varepsilon_{xy} \end{pmatrix}, \tag{1.4}$$

with three independent stiffness coefficients. As mentioned earlier, the factors 2 in equation (1.4) are a consequence of the symmetry-motivated Voight notation. Having them in the strain-vector and not in the stress-vector or the stress-strain matrix is a matter of convention. Values for the semiconductor materials used in this thesis are listed in table A.1 of the appendix.

1.2 Coherent epitaxy and critical thickness

The relationship between stress and strain is now studied with respect to the structures realized in this thesis. Since no external pressures are applied, all deformations and stresses are due to the layer sequence of the samples. We consider a crystal with thickness d, and strain-free lattice constant a_l, grown on a substrate with slightly different lattice constant a_s. The mismatch between the two is defined as $f = (a_\mathrm{l} - a_\mathrm{s})a_\mathrm{s}^{-1}$. The growth process is called "coherent" or "pseudomorphic" if the epilayer fully adopts the lattice constant of the substrate in the plane of the substrate-epilayer interface. In the case of epitaxy on (001) interfaces, this means a biaxial distortion of the unit cell of the form

$$\varepsilon_{xx} = \varepsilon_{yy} = \varepsilon_{||} = f\frac{a_\mathrm{s}}{a_\mathrm{l}} \approx f, \tag{1.5}$$

if coordinates are chosen such that growth is taking place along the z-axis [see equation (1.1)]. $\varepsilon_{||}$ is called in-plane strain. The out-of-plane strain $\varepsilon_\perp = \varepsilon_{zz}$ can be calculated from the third row of equation (1.4). Since there are no pressures acting perpendicular to the growth-plane, i.e. $\sigma_{zz} = 0$, one finds

$$\varepsilon_\perp = -2\,\frac{c_{12}}{c_{11}}\,\varepsilon_{||}. \tag{1.6}$$

Equation (1.6) is the two-dimensional equivalent of Poisson's effect, which is usually defined as a system's response to a deformation caused by uniaxial pressure. The quantity

which defines the ratio $-\varepsilon_{\perp}/\varepsilon_{||}$ is called Poisson's ratio ν. Care has to be taken not to confuse the two scenarios of biaxial (ν_{2D}) and uniaxial (ν_{1D}) pressure. All lattice mismatched layers discussed in this thesis are exposed to mismatch-induced biaxial pressure, where ν_{2D} is defined as $\nu_{2D} = 2\,c_{12}/c_{11}$ [see equation (1.6)]. Literature values of Poisson's ratio are usually given for uniaxial pressure, where $\nu_{1D} = c_{12}/(c_{11}+c_{12})$. Combining equation (1.6) and equation (1.2) shows that a crystal's tendency to conserve its volume when exposed to biaxial pressure is determined by ν_{2D}. The volume remains unchanged for $\nu_{2D} = 2$.

Using Hooke's law, it is straightforward to show that the force acting on a strained epilayer's surface normal to the substrate-epilayer interface is [14]

$$\sigma_{xx}\, d = d\, M\, \varepsilon_{||}. \tag{1.7}$$

Here, the force is normalized by the length of the edge of the sample parallel to the substrate-epilayer interface, and $M = c_{11}+c_{12}-2\,c_{12}^2/c_{11}$. By integrating equation (1.7), the energy stored in a strained epilayer normalized to the substrate-epilayer interface area is found as

$$E = d\, M\, \varepsilon_{||}^2. \tag{1.8}$$

The fact that the total force is proportional to the epilayer thickness d directly means that an upper limit for pseudomorphic growth has to exist. For small mismatches $f \lesssim 2\%$, pseudomorphic growth takes place up to a critical epilayer thickness d_c. For $d > d_c$ relaxation sets in, and the strain in the epilayer starts to decrease ($\varepsilon_{||} < f$). A lot of experimental and theoretical effort has been put in understanding the relaxation mechanisms and in quantifying d_c for various material systems. Reviews on the topic can be found in [14, 15]. However, even though there is consensus on the general mechanisms for strain relief in zincblende crystals, the critical thicknesses d_c that are predicted for a single substrate-epilayer system vary some orders of magnitude, depending on the model employed [16]. We therefore omit a more detailed discussion, but briefly summarize qualitative aspects of relaxation:

- Relaxation sets in above a critical thickness d_c. Many works predict a power-law dependency of the form

  $$d_c = A\, f^{-\alpha}. \tag{1.9}$$

  Here, A is a fitting parameter and values for α are e.g. $\alpha = 1$ [17], $\alpha = 1.5$ [18], $\alpha = 2$ [19]. The value of A is expected to decrease if the symmetry of the direction of growth is lowered [e.g. (111) or (112) instead of (001)]. However, the change is

low compared to the overall variation of d_c found in the literature. Ref. [20] predicts a change of 6 % for CdTe grown in (001) and (111) direction.

- For epilayer thicknesses $d > d_c$, the level of relaxation r increases with increasing d. All strains ε_i in the layer go down, and equation (1.5) becomes

$$\varepsilon_{||} \approx f\,(1-r), \tag{1.10}$$

with $0 < r < 1$. Ref. [17] predicts proportionality to the inverse of d,

$$\varepsilon_{||} = (f-\varepsilon_r)\,\frac{d_c}{d} + \varepsilon_r. \tag{1.11}$$

Even for very high layer thicknesses, $\varepsilon_{||}$ does not vanish entirely, but approaches a finite $\varepsilon_r \ll f$. Other groups find a weaker dependency, $\varepsilon_{||} \propto d^{-1/2}$ [21]. Experimental data for CdTe on GaAs (001) is presented in section 2.5.3.

- For sufficiently low mismatches f, relaxation is taking place along with the formation of misfit dislocation lines. Consequently, the crystal quality degrades during relaxation. This is evidenced by an increase of the ω full-width-at-half-maximum (FWHM) of the HRXRD reflections of the epilayer. For HgCdTe grown on CdZnTe, this is demonstrated in Ref. [22], and for HgTe on CdTe in section 2.5.3.

The two latter aspects clarify that it is highly undesirable to design layer stacks with partially relaxed individual layers, because of both the uncertainty in the actual level of strain in the final device and the poor crystal quality. This means, on the one hand, that quantum well structures have to be grown coherently, which restricts the layout of the layer stack, and sets the in-plane lattice constant of all layers equal to the one of the substrate. On the other hand, growth of layers with a different in-plane lattice constant than the substrate is commonly achieved by the growth of thick buffer layers on highly lattice mismatched ($f > 5\%$) substrates. Relaxation then takes place within only the first few nm of the buffer layer, and this highly defective region of the crystal is spatially separated from the functional heterostructure by a thick epilayer, in which the crystal quality increases gradually (see section 2.3). It must be noted that the relaxation characteristics listed above do not hold for such highly mismatched systems. Instead, it is energetically favorable that after a strained film of a few angstrom is grown (also called "wetting layer"), strain is relaxed by formation of pits and islands. This is called "Stranski-Krastanov growth". The transition mismatch f_{crit}, separating the two mechanisms of relaxation depends on both the material system and growth conditions. For SiGe on Si, $f_{crit} \approx 1.2\%$

is found [23]. A transition value for the $Cd_{1-x}Hg_xTe$ material system or another related II-VI compound is not known to the author.

1.3 Strain in Hg-based crystals

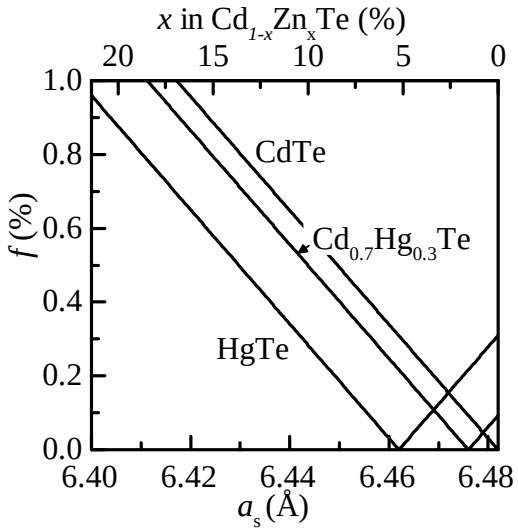

Figure 1.3: Lattice mismatch f of different $Cd_{1-x}Hg_xTe$ solid solutions as function of substrate lattice constant, which corresponds to a $Cd_{1-x}Zn_xTe$ solid solution with the Zn-fraction depicted by upper x-axis.

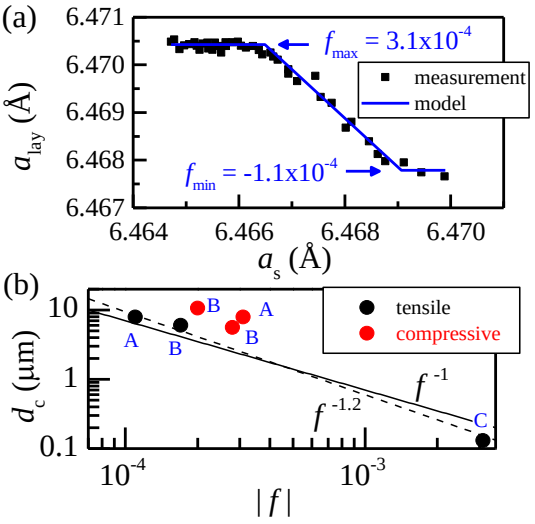

Figure 1.4: (a) Out-of-plane lattice parameter of $Cd_{0.35}Hg_{0.65}Te$ as function of substrate lattice parameter. Layer thickness is $d = 7.9\,\mu m$. From [24] (modified). (b) Critical thickness as function of lattice mismatch. Data from [24](A), [25](B) and [26](C).

In this paragraph, an overview of works considering strain and relaxation in $Cd_{1-x}Hg_xTe$ epilayers is provided. Mismatches in consideration are illustrated in figure 1.3 for the binaries HgTe and CdTe, as well as different $Cd_{1-x}Hg_xTe$ solid solutions. Theoretical values for the critical thickness of HgTe on CdTe ($f = -0.3\,\%$) vary from $d_{crit} \approx 50\,nm$ [27] to 200 nm [28]. This again shows the qualitative nature of models of strain and relaxation. Experimentally, most works focus on several micron thick, low-mismatch layers of $Cd_{1-x}Hg_xTe$ with $0.6 < x < 0.8$, which is used as long-wavelength infrared detector material. In Refs. [24, 25], such layers are grown on $Cd_{1-x}Zn_xTe$ (211)B substrates. Due to the inherent variation of Zn-content x in the substrate, the lattice mismatch f varies with position on the wafer. It is found that, if the absolute mismatch exceeds a threshold value, the strain in the epilayer saturates, and the layers seem to tolerate more compressive than

tensile strain before relaxation sets in [see values of $|f_{\max}|$ and $|f_{\min}|$ in figure 1.4 (a)]. However, the latter feature may also be a measurement artifact caused by the different thermal expansion coefficients of layer and substrate [29]. A larger lattice mismatch is investigated in Ref. [26], where $d_c = 130\,\mathrm{nm}$ is found for HgTe grown on CdTe. The experimental data on d_c of $Cd_{1-x}Hg_xTe$ is collected in figure 1.4 (b). The scatter in the data does not allow for a comparison with equation (1.9) (note, in particular, the non-monotonous characteristics of the compressively strained data). A power law dependency with $\alpha = 1$ to 1.5 seems plausible. In Ref. [30], experimental data for different mercury free II-VI material systems are compiled, and equation (1.9) is best fit with $d_{\mathrm{crit}} \propto f^{-1.5}$. We show further results in section 2.5.3.

Knowledge on the strain and relaxation mechanisms in crystals is essential in order to design heterostructures with low defect densities and a well-defined state of strain. In the next section, these aspects are implemented during the process of crystal growth.

Chapter 2

Heterostructure Growth

As the main part of this thesis, the following section reports on the MBE of a variety of II-IV crystal systems. In order to access growth-induced strain as a degree of freedom, the fabrication of CdTe-$Cd_{0.5}Zn_{0.5}Te$ strained-layer superlattices as artificial substrates has been developed (section 2.4). This work is based on the research on binary CdTe buffer layers grown on GaAs (section 2.3), developed in collaboration with C. Ames [31]. The subsequent deposition of strain-engineered, Hg-based heterostructures on these new substrates benefits from the expertise on epitaxy on commercial II-VI substrates (section 2.5.1), and concludes this chapter (section 2.5.3, section 2.5.4).

2.1 Hg-based MBE

In this section, the reader is familiarized with the concept of MBE. To this end, an overview of history, principles and technological aspects is given, with a short description of the two chambers used in this work. Focus will be on the epitaxy of high-quality Hg-based films. For a comprehensive general overview, the reader is referred to [32, 33].

2.1.1 Introduction to MBE

The first MBE machines were assembled in the late 1960s by Cho and coworkers at Bell labs in New Jersey, pursuing the fabrication of single crystal GaAs layers [34]. Shortly afterwards, Chang and coworkers at IBM used MBE to fabricate heterostructures with individual layer thicknesses on the scale of angstroms [35]. After having demonstrated its capabilities as versatile tool to fabricate semiconductor heterostructures on the sub-nm scale, the MBE research community became larger and larger, and companies started to offer "turnkey" MBE machines (the RIBER "MBE500" system, available in 1978). By

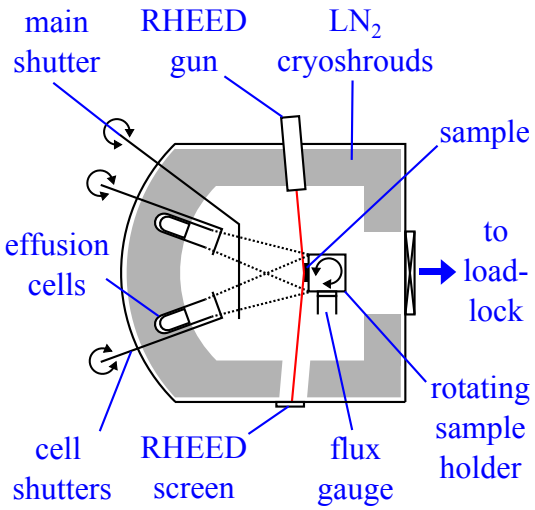

Figure 2.1: Sketch of most important components of a MBE system as used in this work. Red line indicates electron beam producing RHEED diffraction pattern. Dotted lines illustrate directions of molecular beams.

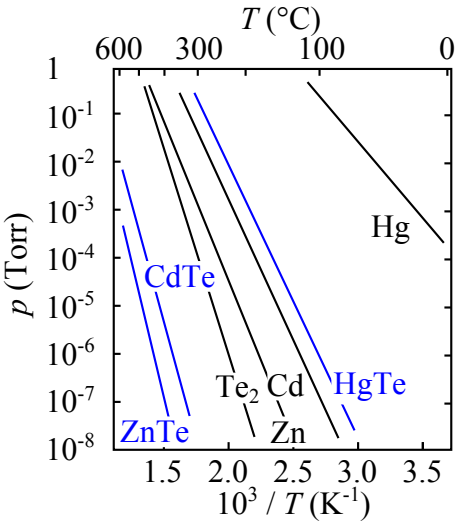

Figure 2.2: Equilibrium vapor pressures p as function of temperature of II-VI binary compound materials (blue) and constituent elements (black) discussed in this work. From [32] (modified).

now, MBE has been used to synthesize a vast number of semiconductor materials and heterostructures, and has found its way into large scale production of devices used in everyday consumer electronics [36].

Figure 2.1 illustrates the basic components of the MBE systems used in this work, and helps to outline the procedure of crystal growth. The base pressure of a chamber is about 1×10^{-10} Torr in standby mode, achieved by a combination of ion-getter pumps, ^{4}He-cryopumps and Ti-sublimation pumps [[Torr] is the most common unit for ultra-high vacuum (UHV) pressure measurements; 1 Torr = 1.33 mbar]. Molecular beams are produced by thermal evaporation of high-purity elemental or compound materials in the effusion cells. For all materials except Hg, standard effusion cells are used, featuring pyrolytic boron nitride crucibles, resistive heating filaments, and thermocouple temperature sensors. The beams can be blocked almost instantaneously by means of simple mechanical shutters. The sample holder allows for positioning of the substrate in the molecular beam, as well as for rotating the sample with respect to its azimuth to ensure spatially homogeneous epitaxy. It is also equipped with a heater to adjust the temperature of the sample, and a Bayard-Alpert pressure gauge to quantify the incoming molecular beams. Whereas, in principle, it is possible to calculate the number of incoming molecules per area (the "flux", J_x of a species x), it is more practical to simply keep track of the pressure ϕ_x of

the individual molecular beams at the growth position, also called "beam-equivalent pressure", since J_x is proportional to ϕ_x. Typical ϕ_x are at around 1×10^{-6} Torr for all sources except Hg. The background pressure in the chamber does not exceed 1×10^{-9} Torr significantly if the Hg-cell is closed. This pressure gradient of almost three orders of magnitude is achieved by an effective trapping of particles which are not part of the directed molecular beams to liquid-N_2-cooled cryopanels surrounding the whole interior of the chamber. All chambers are equipped with a reflection high-energy electron diffraction (RHEED) setup, which is used to monitor the crystal growth in real time. It consists of an electron gun and a phosphorous screen, and is discussed in more detail in section 2.2.2. Typically, all effusion cells needed during growth are ramped up to the working temperature and kept constant for approximately one hour to stabilize temperature of the source materials. Beam-equivalent pressures are measured before the substrate is loaded into the chamber. Computer-controlled heating of the sample to the desired substrate temperature and sequential opening and closing of shutters to initiate and terminate growth maximize accuracy and reproducibility.

2.1.2 Special aspects of Hg-based MBE

Originally, the request for epitaxy of Hg-based II-VI crystals was stimulated by the applicability of CdHgTe layers als focal plane arrays for infrared detectors, since the band gap (and therefore the cutoff frequency) can be tuned freely from $E_G = 0\,\text{eV}$ to $\approx 1.5\,\text{eV}$ by adjusting x in $Cd_{1-x}Hg_xTe$ (to be more specific, E_G is also slightly temperature dependent - see chapter 3). The main challenge regarding epitaxy of such crystals is given by the peculiar relation of equilibrium vapor pressures p_x of the constituents and crystals (figure 2.2). As a consequence of the high p_{Hg}, the sticking coefficient of Hg on the crystal surface is extremely low [37], and in order to circumvent crystal degradation due to Hg-re-evaporation, either growth has to be performed at very low substrate temperatures, or the surface has to be exposed to a tremendous excess of Hg during growth and cooldown. Both approaches were first realized by Faurie et al. in the early 1980s [37, 38]. It turned out that even though the latter approach is technically more challenging, it yields far superior crystals, and the key parameters for $Cd_{1-x}Hg_xTe$ MBE found back then still hold today:

- Hg excess in beam-equivalent pressure: $\phi_{Hg}/\phi_x = 200/1$ to $300/1$ [valid for $x =$ Te (HgTe growth) and $x =$ CdTe ($Cd_{1-x}Hg_xTe$ growth)].

- Substrate temperature during growth: $T_{sub} = 170$ to $200\,^\circ\text{C}$.

- As soon as the growth of the first Hg-containing layer is initiated, ϕ_{Hg} is kept constant to avoid Hg-re-evaporation. After growth, Hg exposure is not terminated until the sample has cooled down to $T_{\mathrm{sub}} \approx 100\,^{\circ}\mathrm{C}$.

Meeting the first of these requirements gives rise to the biggest technological challenge compared to "conventional" II-VI MBE systems, that is, to supply and pump the large ϕ_{Hg} (typically at around 3×10^{-4} Torr) and to handle the increased background pressure ($p \propto 1 \times 10^{-6}$ Torr) that comes along with it. Modern effusion cells, specially designed to supply Hg, feature a valve which allows for complete separation of the Hg reservoir and the growth chamber, as well as precise control of the orifice diameter and thereby ϕ_{Hg}. Moreover, p_{Hg} is controlled by setting the temperature of the reservoir appropriately, and since Hg is liquid at room temperature, the reservior can be refilled without breaking the UHV via a tube connector system. During normal operation, pumping is handled by cryopumps. These pumps are protected by liquid-N_2 cryotraps, which efficiently getter the high Hg background.

With the technology established, the field rapidly gathered knowledge on the finer aspects of the material system. In particular, all challenges regarding fabrication of focal plane arrays are studied extensively, to a good extend by military-related research facilities. (for review articles see [39–41]).

At the chair of EPIII Würzburg, the focus of research on Hg-based structures has in general been more on the physical properties of the layers, and not on aspects of fabrication. Some exceptions worth noting are a quantitative analysis of influence of $\phi_{\mathrm{Hg}}/\phi_{\mathrm{Te}}$ beam equivalent pressure ratio on crystal quality and carrier density [42], the transition from island growth mode to step flow growth mode at $T_{\mathrm{sub}} = 180\,^{\circ}\mathrm{C}$ [43], the n-type modulation doping of QWs using iodine [44] and p-type modulation doping using nitrogen [45].

All samples presented in this thesis were grown in two MBE chamber s, which are both part of the six-chamber MBE cluster at EPIII. The cluster allows for transfer between all chambers within an UHV environment, as well as access to multiple additional equipments, such as pregrowth plasma etching, X-ray photo-electron spectroscopy surface analysis, post-growth electron-beam metallization and sputter deposition. CdTe buffer layers (section 2.3) and CdTe-$Cd_{0.5}Zn_{0.5}$Te-SLS (section 2.4) were grown in a RIBER COMPACT 21 MBE machine, dedicated to all kinds of wide gap II-VI materials (e.g. ZnSe, BeSe, MgTe, ZdTe, CdTe and solid solutions thereof). All structures containing Hg (section 2.5) were grown in a RIBER 2300 machine, modified to meet the requirements that come along with Hg-epitaxy, as discussed previously. Even though it is possible, in principle, to produce both types of buffer layers (pure CdTe, and CdTe-

$Cd_{0.5}Zn_{0.5}Te$-SLS) in the Hg-chamber, the long growth time of these layers implies frequent refillings of the Cd, Zn and Te cells, and practically excludes doing so. Refilling an evaporation cell of the Hg-chamber requires extensive bakeout of the whole system, since warming up the cryoshrouds means Hg-contamination of the entire chamber, and thus causes machine downtime and recalibration time of roughly four weeks in total. In contrast, on the wide gap II-VI machine, refilling can be done within two to three days in Nitrogen atmosphere with the "glove bag" method, and no bakeout is required.

2.2 Sample Analysis

A variety of experimental techniques has been used to monitor the crystal growth and to analyze the properties of the layers. The most important ones are introduced briefly in the following. The methods are discussed in more detail whenever required. Magnetotransport measurements, which also provide information on crystal quality (mainly via density and mobility of carriers in the system), are discussed separately in section 5.1.

2.2.1 High-resolution X-ray diffraction

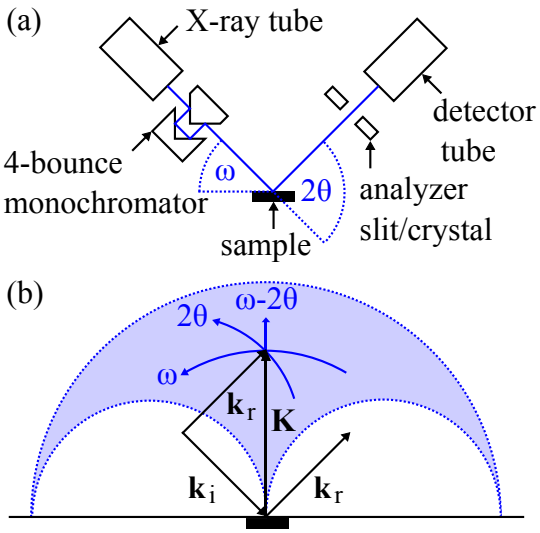

Figure 2.3: (a) Sketch of the HRXRD experimental setup. (b) Illustration of accessible **K**-space and direction of different scan types.

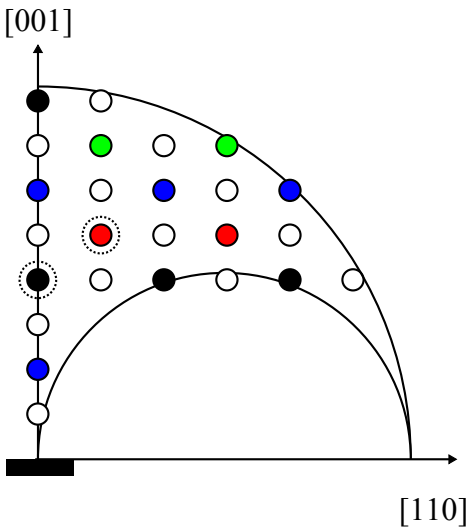

Figure 2.4: Reciprocal lattice of CdTe. Empty circles depict forbidden reflections, different structure factors are color-coded. Dashed circles highlight (004) and (115) reflection.

All samples are routinely analyzed by HRXRD, which is a non-destructive, straightforward method to quantify crystal quality and precise layer stack dimensions [46, 47]. The measurements are performed on a Philips X'Pert pro MRD and a Bruker D8 DISCOVER diffractometer. The experimental setup is sketched in figure 2.3 (a). A 4-bounce Ge (220) monochromator suppresses all radiation coming from the X-ray tube except the Cu-$K_{\alpha 1}$ line (wavelength $\lambda = 1.5406\,\text{Å}$). ω is the angle between incoming X-ray beam and sample surface, 2θ between incoming and reflected beam. Depending on the desired angular resolution $\Delta 2\theta$, the diffracted beam is passed through an analyzer slit or a 3-bounce Ge (220) crystal.

Incoming and reflected X-rays are described by wave vectors $\mathbf{k}_\mathrm{i}$ and $\mathbf{k}_\mathrm{r}$. Since energy transfer to the crystal can be neglected, the magnitude of both vectors is similar ($|\mathbf{k}_\mathrm{i}| = |\mathbf{k}_\mathrm{r}| = 2\pi/\lambda$). The scattering vector $\mathbf{K} = \mathbf{k}_\mathrm{r} - \mathbf{k}_\mathrm{i}$ is able to cover all values inside the "Ewald sphere", colored blue in figure 2.3 (b). The most common scan types are depicted by blue arrows. Rotating the sample with fixed detector position results in concentric scans in reciprocal space ("ω-scan"), whereas sweeping the detector twice as fast as the sample yields radial scans ("$\omega - 2\theta$-scan"). The trace of detector-only scans ("2θ-scan") depends on ω and is rarely used.

One can show that all three Laue equations

$$\mathbf{a_1} \cdot \mathbf{K} = 2\pi\ h,\ \mathbf{a_2} \cdot \mathbf{K} = 2\pi\ k,\ \mathbf{a_3} \cdot \mathbf{K} = 2\pi\ l \tag{2.1}$$

have to be fullfilled for an incident beam to be diffracted on a crystal. The $\mathbf{a_i}$ are the basis vectors of the crystal's unit cell and h,k,l are integers. With the reciprocal lattice vectors $\mathbf{G} = h\ \mathbf{g_1} + k\ \mathbf{g_2} + l\ \mathbf{g_3}$ linearly combined from $\mathbf{g_i} = 2\pi\ \mathbf{a_j} \times \mathbf{a_k} |\mathbf{a_i} \cdot (\mathbf{a_j} \times \mathbf{a_k})|^{-1}$, the sum of the Laue equations (2.1) is equivalent to the condition

$$\mathbf{K} = \mathbf{G}, \tag{2.2}$$

i.e. the scattering vector has to be identical to a reciprocal lattice vector. If the unit cell analyzed is not primitive - like in the case of the cubic unit cell of the zincblende lattice - (2.1) is still valid, however an additional structure factor F_hkl has to be taken into account when calculating the reflected intensity. All reciprocal lattice vectors of CdTe with $h = k \geq 0$, which are experimentally accessible, are shown in figure 2.4. Reflections with the same color have similar F_hkl, empty circles depict reflections with $F_\mathrm{hkl} = 0$. The reflections analyzed usually are the symmetric (004) and the asymmetric (115), highlighted by a dashed circle.

2.2.2 Reflection high-energy electron diffraction

RHEED is the most common technique to monitor crystal growth in-situ and in real time in MBE [48, 49]. The basic principle is outlined in figure 2.5 (a). An electron beam is accelerated at a small angle $\omega_i \approx 1 - 3^\circ$ onto the crystal surface, and reflected to a phosphorous screen. On this screen, the incoming electrons cause a fluorescence, which is visible to the bare eye. Since it is a diffraction experiment as well, several concepts of the previous HRXRD section can be adapted to understand the RHEED experiment. Typical electron energies are in the range of 10-20 keV, leading to an Ewald sphere much larger

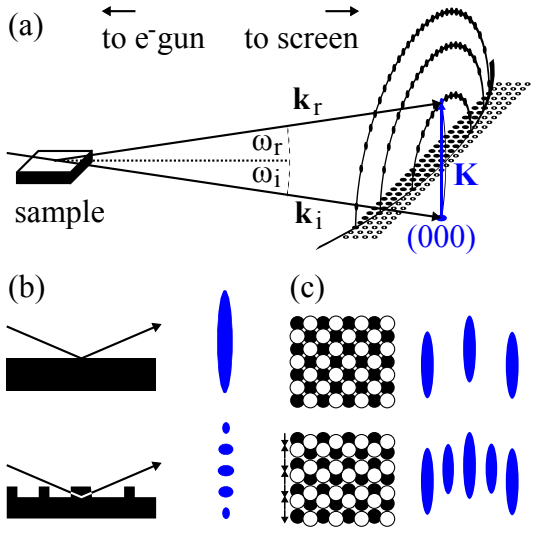

Figure 2.5: (a) sketch of the experimental setup and formation of the diffraction pattern in RHEED. Blue arrow shows scattering vector of the specular spot. (b) the effect of surface roughness (black) on the appearance of a single RHEED streak (blue). (c) surface reconstruction causes additional half-order streaks to appear in certain azimuths.

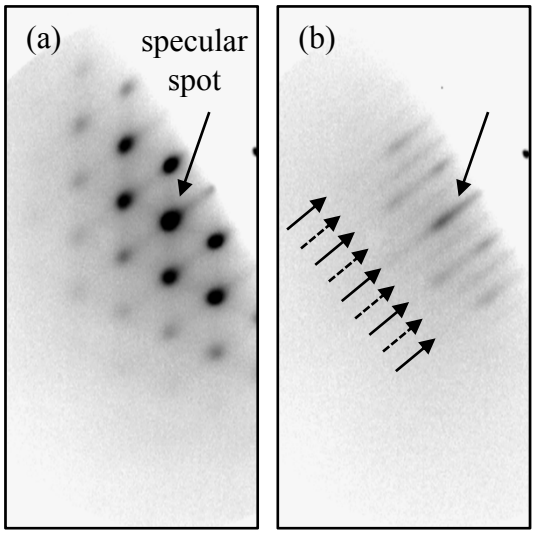

Figure 2.6: (a) RHEED image of 15 nm CdTe on 15 nm ZnTe on GaAs grown at very low temperatures ($T_{\mathrm{sub}} = 180\,^{\circ}\mathrm{C}$). (b) After annealing the sample at $T_{\mathrm{sub}} = 340\,^{\circ}\mathrm{C}$ for 2 hours.

than the reciprocal lattice spacing ($|\mathbf{k}| \approx 78\,|\mathbf{g_i}|$ for CdTe and 20 keV). Due to the small ω_i, the diffraction process is highly surface sensitive, and the out-of-plane component of the diffraction condition (2.1) is not defined. Descriptively speaking, this leads to constructive interference whenever a "reciprocal lattice rod" intersects with the Ewald sphere. The reflection reached by $\mathbf{K}$ with zero in-plane component is the specular spot [blue arrow in figure 2.5 (a)]. It is exclusively independent of sample rotation, and symmetrically reflected on the sample surface ($\omega_i = \omega_r$).

RHEED is used to qualitatively monitor the crystal quality during growth [figure 2.5 (b)]. Reflection on a sufficiently flat surface results in elongated fluorescence streaks due to the finite diameter of the reciprocal lattice rods. If a rough surface consists of islands with a sufficiently small diameter, a fraction of the beam will penetrate through these islands and the out-of-plane component of (2.1) becomes relevant again. The resulting fluorescence image is a sequence of spots with different intensity.

Since the symmetry of a crystal is broken on its surface, surface atoms often reorganize in an energetically favorable pattern which has a lower periodicity than its bulk coun-

terpart. As a consequence, the real-space unit cell is altered and additional non-integer reciprocal lattice rods are formed. These are seen as additional streaks in the RHEED signal [figure 2.5 (c)]. The symmetry of the reconstruction usually depends on the species of the surface atoms and can thus be utilized to distinguish between cation- and anion-rich growth conditions.

Typical features of a RHEED pattern are illustrated in figure 2.6. 15 nm CdTe is grown on 15 nm ZnTe on GaAs:Si. Since the substrate temperature ($T_{\mathrm{sub}} = 180\,^{\circ}\mathrm{C}$) is below the regime of good epitaxy for these material systems, a rough epilayer with small islands is formed, and the characteristic spots of three dimensional growth are seen [figure 2.6 (a)]. When the sample is kept at elevated temperatures ($T_{\mathrm{sub}} = 340\,^{\circ}\mathrm{C}$) for two hours, the small islands merge to larger ones, and the RHEED image becomes mostly two-dimensional [figure 2.6 (b)]. Dashed arrows indicate half-order reconstructed streaks, characteristic for surfaces with Te as topmost atoms.

Even though patterns from RHEED can be recorded and analyzed quantitatively to gain insight into e.g. surface coverage of a certain species of atoms or the level of relaxation in the crystal, its major application is to qualitatively monitor the growth process in real time. However, this monitoring is difficult to reproduce objectively in single pictures, since it relies to a good extend on seeing the diffraction pattern evolve as the sample rotates. The signal diffracted from a flat surface reproduces the rotation of the sample on the screen, whereas the location of spots coming from a rough surface is static. Therefore, in most cases, results from RHEED experiments are not shown as pictures, but described instead.

2.2.3 Nomarski microscopy and atomic force microscopy

The surface topography of all samples is analyzed by optical microscopy. While the lateral resolution is limited by the wavelength of the light source ($\approx 0.2\,\mu\mathrm{m}$), the height sensitivity is greatly enhanced by the differential interference contrast technology, also known as Nomarski microscopy (see [50] for a detailed introduction). A beam of linearly polarized light is split up into two branches, polarized perpendicular to each other. These are reflected at two slightly different positions at the sample, and thus may experience a phase shift relative to each other if the optical path length is different. After reflection, the two beams are recombined. The phase shift causes a rotation of the polarization with respect to the original beam. An analyzer, aligned perpendicular to the first polarizer, converts this rotation into an intensity signal, i.e. differential imaging of the interferred beams. If set up properly, the optics is sensitive to phase differences of a few percent of the wavelength, i.e. $5-10$ nm.

Even though the Nomarski microscope resolves height differences at the nm scale, sample features with lateral dimensions on a comparable scale remain invisible. To resolve these, atomic force microscopy (AFM) is used. A micron-size needle is scanned across the sample, in close proximity to the surface. The tip is attached to an elastic cantilever, which is forced to oscillate with its eigenfrequency. The eigenfrequency is altered by the distance-dependent interacting forces between tip and sample surface. A feedback loop algorithm monitors the eigenfrequency, calculates the height of the sample at the needle position, and keeps the distance between needle and surface constant. The resolution of an AFM image depends on the scanning time, the vibrational noise level, the sharpness of the resonance frequency of the cantilever and, above all, on the needle tip size. New needles feature tip diameters of less than 10 nm, and allow for lateral resolutions in the same range. In terms of height changes, steps of single atoms can be resolved. A common method to quantify the roughness of epilayers from AFM measurements is the root-mean-square deviation of the height profile, i.e.

$$\sigma_{\mathrm{h}}^2 = \frac{1}{N^2} \sum_{i=1}^{N} \left(h_i - \bar{h}\right)^2 . \tag{2.3}$$

Here, h_i is the measured height of an individual sample point, and the sum runs over all datapoints N of the image. This method of analysis, however, does not capture information on the actual "shape" of the features on the surface, for example if roughness is due to disordered small clusters, or an ensemble of flat surfaces, with some tilt to each other. Therefore, the respective images have to be checked before comparing σ_{h}^2 of different samples with each other.

2.3 Epitaxy of CdTe on GaAs

After the introduction to epitaxy and sample analysis has been given in the previous sections, we now turn to the detailed discussion of the variety of sample types fabricated during this work. Given the drawbacks of commercial CdTe and $Cd_{0.96}Zn_{0.04}Te$ substrates (small size, limited flexibility and high cost), a method to produce high-quality artificial substrates on n-type GaAs:Si (001) has been established. The idea is to grow thick, fully relaxed layers of CdTe (thickness approximately 4 µm), and is discussed in great detail in [31]. The method also serves as a technological starting point for the fabrication of CdTe-$Cd_{0.5}Zn_{0.5}Te$ SLS, presented in section 2.4. The main obstacle to overcome is the large lattice mismatch of $f = 12.8\,\%$ between GaAs and CdTe, which leads to immediate relaxation and a poor crystal quality at the interface. Given this challenge, it is not surprising that until this date, the crystal quality is inferior to commercial II-VI substrates. Nonetheless, the method offers several striking advantages to be noted. Layers are routinely grown on quarters of substrates with $2''$ diameter, outnumbering the wafer area of II-VI substrates (typically 10×10 cm^2) five times. This is not only beneficial with respect to cost, time and effort, but also allows for comparative experiments which require a large number of identical samples. Also, since n-type GaAs:Si wafers are used, electrical contacting of the substrates and thus backgating of the QWs has been realized. Due to practical reasons mentioned earlier (section 2.1.2), CdTe growth is performed in the wide gap II-VI MBE.

2.3.1 Substrate preparation before CdTe epitaxy

Before the growth of the CdTe buffer layer, the substrates are prepared as follows: Epi-ready GaAs:Si substrates are degassed in the load lock and then loaded into the MBE. In contrast to II-VI substrates, no ex-situ wet-chemistry sample preparation is required, a fact which also contributes to the reproducibility of the method. The native oxide is removed thermally by ramping up the substrate temperature until a characteristic change in the RHEED pattern from blurry to sharp and spotty is observed (typically at around $T_{\mathrm{sub}} = 620\,^{\circ}$C). The de-oxidized GaAs surface is rough and hosts pit-like defects. This is explained by the conversion of the most stable oxide Ga_2O_3 into the volatile Ga_2O, which consumes additional Ga from the bulk, and thereby causes inhomogeneous damage to the crystal [51]. Several methods succeeded in recovering a flat crystal surface, such as offering a precise amount of Ga during desorption [51, 52], or burying the holes underneath a thick GaAs layer [53]. We have performed the latter approach in the III-V chamber of the MBE cluster. However, it was found that even though the initial growth conditions are

greatly improved, no improvement followed in subsequent II-VI epitaxy [31]. Therefore, the recovery of the III-V surface has been abandoned.

After deoxidizing, the sample is cooled down to $T_{\mathrm{sub}} = 320\,^{\circ}\mathrm{C}$ and a thin layer of ZnTe is deposited. Having an intermediate lattice constant between CdTe and GaAs, this layer ensures that subsequent CdTe epitaxy takes place in the (001) direction [54]. The growth conditions of the ZnTe layer have been varied with respect to layer thickness, T_{sub} and Zn/Te beam equivalent pressure ratio. It turned out that the crystal quality of the following CdTe epilayer is best for a thin ($\approx 3\,\mathrm{nm}$) ZnTe layer that still is in the island growth regime, which can be checked by RHEED [31].

2.3.2 CdTe buffer growth procedure

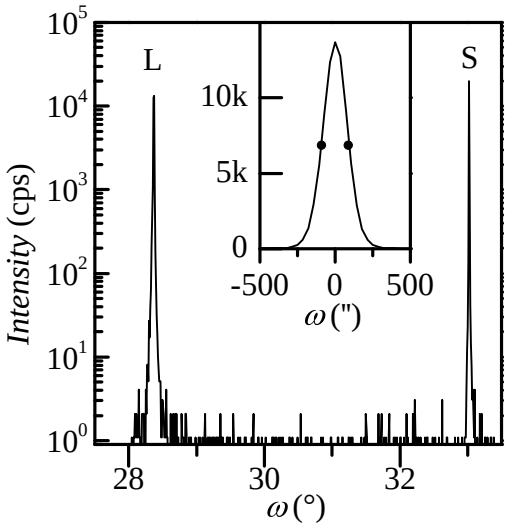

Figure 2.7: HRXRD $\omega - 2\theta$-scan of (004)-reflection of 4 µm CdTe on GaAs. Angular separation of the two reflections yields out-of-plane lattice parameter of CdTe. Inset shows scan in ω-direction of the CdTe layer. Dots indicate FWHM ($\Delta\omega \approx 180''$).

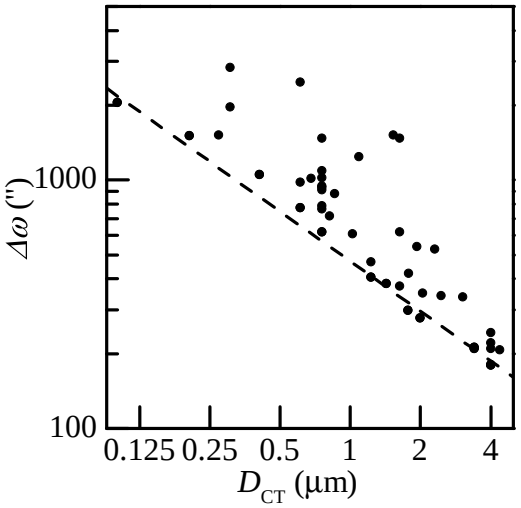

Figure 2.8: HRXRD FWHM $\Delta\omega$ of (004) CdTe peak vs. CdTe layer thickness, measured on many samples with different growth parameters. Dashed line is fit to (2.4) with $K = 470''\mu\mathrm{m}^{2/3}$

After the ZnTe deposition, the actual CdTe buffer layers are grown using elemental Cd and Te source materials. The detailed procedure is presented in this section. CdTe buffer layers were produced with a great variety of growth parameters. The crystal quality was analyzed using RHEED, optical Nomarski microscopy, atomic force microscopy and HRXRD. After the CdTe growth has started, the RHEED signal starts to improve gradually, and exhibits a 2D-like pattern after the growth of only around $20 - 40\,\mathrm{nm}$.

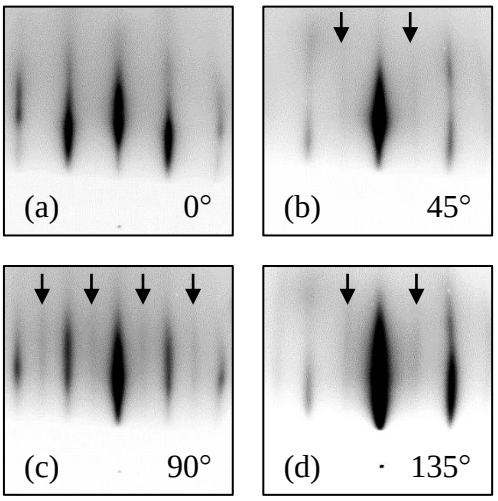

Figure 2.9: RHEED pictures of CdTe on GaAs during growth. CdTe layer thickness $\approx 500\,\mathrm{nm}$. Flux ratio $\phi_{\mathrm{Cd}}/\phi_{\mathrm{Te}} \approx 2/1$. Angles denote different azimuths. Arrows highlight reconstructions.

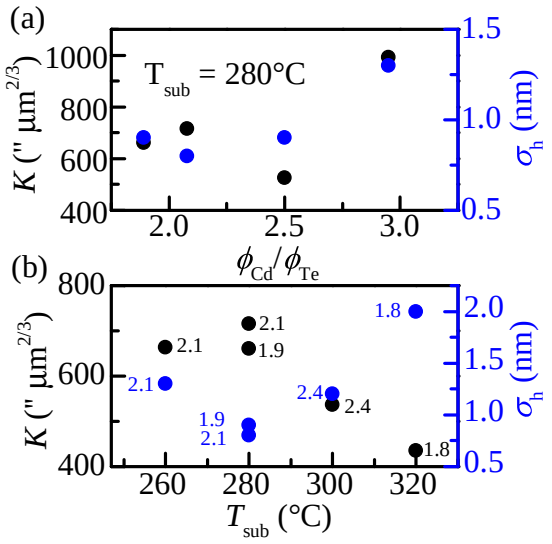

Figure 2.10: HRXRD crystal quality quantifier K and σ_{h} of AFM height profile, as a function of (a) beam-equivalent pressure ratio $\phi_{\mathrm{Cd}}/\phi_{\mathrm{Te}}$ at constant substrate temperature T_{sub} and (b) as function of T_{sub}. Labels in (b) denote beam equivalent pressure ratios.

Whereas microscopic surface roughness is quantified as root-mean-square deviation σ_{h} of the height profile measured by AFM [equation (2.3)], the FWHM of the (004) reflection in ω direction, $\Delta\omega$, is used to quantify average defect density of the bulk crystals [55]. An example is shown in the inset of figure 2.7. Figure 2.8 shows $\Delta\omega$ as a function of CdTe epilayer thickness for a large number of samples with different growth parameters. Despite considerable scatter in the data, $\Delta\omega$ of the best crystals approximately follows a power law dependency,

$$\Delta\omega = K\, D_{\mathrm{CT}}^{-2/3}, \tag{2.4}$$

with the fitting parameter K. This relationship reflects the fact that the crystal recovers from the abrupt change in lattice constant at the GaAs/ZnTe and ZnTe/CdTe interfaces and from the initial 3D island growth, which is also observed in RHEED. Since $\Delta\omega$ greatly depends on epilayer thickness, we chose to compare growth mechanisms of layers with different thicknesses using the parameter K rather than $\Delta\omega$ (note that throughout this thesis, K is calculated from $\Delta\omega$ in arcsec and D_{CT} in microns, i.e. its unit is [" $\mu\mathrm{m}^{2/3}$]).

Figure 2.10 (a) shows K and σ_{h} for a series of samples grown with varying Cd/Te flux ratio $\phi_{\mathrm{Cd}}/\phi_{\mathrm{Te}}$. In agreement with [56], the best crystals are obtained under Cd-rich

conditions. It is worth noting that the RHEED signal of a sample with $\phi_{Cd}/\phi_{Te} \approx 2/1$ (figure 2.9) shows (2×1) and $c(2 \times 2)$ reconstructed surface areas, which indicates a mixture of Te- and Cd-terminated surfaces. Determining the optimum growth temperature T_{sub} is not straightforward, since tendencies in σ_h and K are only weak, and show opposite trends [figure 2.10 (b)]. Whereas σ_h increases with increasing T_{sub}, $\Delta\omega$ goes down. The degradation regarding the surface morphology is illustrated in figure 2.11. By comparing the height profiles of buffer layers grown at $T_{sub} = 280\,°C$ (a) and 320 °C (b), one can see that the apparent increase in σ_h is caused by an increase in size and steepness of the island features.

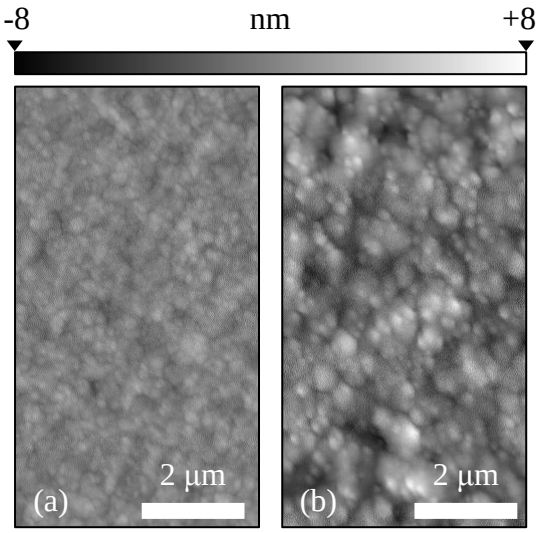

Figure 2.11: AFM image of CdTe grown on GaAs at (a) $T_{sub} = 280\,°C$ and (b) $T_{sub} = 320\,°C$

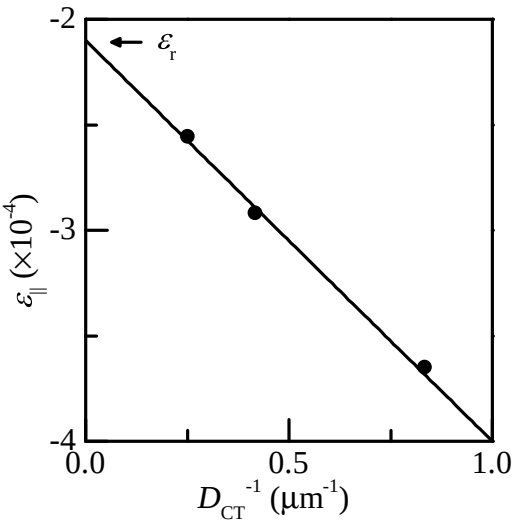

Figure 2.12: In-plane strain $\varepsilon_{||}$ of CdTe on GaAs (001) as function of inverse layer thickness D_{CT}^{-1}.

Based on the knowledge presented in the previous paragraphs, CdTe buffer layers for subsequent CdHgTe epitaxy are routinely fabricated as follows: Fluxes are adjusted such that $\phi_{Cd}/\phi_{Te} \approx 2.0/1$ to $2.2/1$. In order to obtain decent bulk crystal properties and finish growth with conditions providing a flat surface, T_{sub} is gradually lowered from 315 °C to 290 °C during growth. Growth is interrupted every 60 s and the sample is annealed in Cd-flux for 10 s to further smoothen the surface [56]. With total growth times of approximately 12 hours, typical layer thicknesses are $D_{CT} = 4\,\mu m$, with σ_h at around 1 to 1.5 nm and K at around 420 to $480''\,\mu m^{-2/3}$.

2.3.3 Residual strain in CdTe buffer layers

In order to compare the physical properties of CdTe buffer layers on GaAs to "real" bulk CdTe substrates, the level of relaxation is of considerable interest, especially for the accurate simulation of HRXRD profiles of heterostructures grown on top, and ultimately to correctly determine the level of strain in those. Due to the large lattice mismatches of GaAs/ZnTe and ZnTe/CdTe, relaxation sets in after just a few monolayers [57] (MLs - note that, throughout this work, one ML is defined as one atomic layer of the cation and the anion of the crystal). The residual in-plane strain $\varepsilon_{||}$ which persists in the system, is of the order of a few 10^{-4}. Since there is some variation in the literature on the value of $\varepsilon_{||}$, [58–60] (probably indicating an influence of the method of sample fabrication), we have determined $\varepsilon_{||}$ experimentally. For three layers with different CdTe thicknesses (1.2, 2.4 and 4.0 µm), the out-of-plane strain $\varepsilon_{\perp}$ was determined by calculating the out-of-plane lattice constant of the CdTe from HRXRD $\omega - 2\theta$ measurements (figure 2.7), and comparing it to the bulk value. The corresponding $\varepsilon_{||}$ was calculated using equation (1.6). By fitting the measured values to equation (1.11) the residual $\varepsilon_{||}$ can be extrapolated to infinitely thick layers. We find $\varepsilon_{||}(\infty) = \varepsilon_{\mathrm{r}} = 2.1 \times 10^{-4}$ (see figure 2.12). We suggest that the non-zero $\varepsilon_{||}$ at infinite D_{CT} is due to the thermal expansion mismatch $\varepsilon_{\mathrm{th}}$ between layer and substrate. This mismatch is given by

$$\varepsilon_{\mathrm{th}} = \int_{T_1}^{T_2} \alpha_{\mathrm{GaAs}}(T) - \alpha_{\mathrm{CT}}(T) dT, \tag{2.5}$$

with the thermal expansion coefficients α of CdTe and GaAs. Integrating (2.5) from $T_1 = 300\,^{\circ}\mathrm{C}$ to $T_2 = 20\,^{\circ}\mathrm{C}$ with values from Ref. [61] for α_{GaAs} and Ref. [62] for α_{CT} yields $\varepsilon_{\mathrm{th}} = 2.2 \times 10^{-4}$. This value is in good agreement with the measured ε_{r}, and thus supports our assumption.

2.4 CdTe-$Cd_{0.5}Zn_{0.5}$Te superlattices on GaAs

The major technical achievement of this thesis is the control of the strain of HgTe layers in a parameter range which was not accessible before. This control is realized by coherent growth of CdHgTe barriers and HgTe layers on substrates with varying lattice constant. In related literature, one finds that the infrared detector community is facing a very similar challenge [62, 63], which is to provide substrates for lattice matched epitaxy of thick layers $Cd_{1-x}Hg_xTe$. The composition x varies from 0.6 to 0.8, depending on its application as mid-wavelength or long-wavelength infrared detector device [63]. The substrate material system of choice is almost exclusively the solid solution $Cd_{1-x}Zn_xTe$, with the lattice

constant ranging from $a_{x=1} = 6.104\,\text{Å}$ to $a_{x=0} = 6.482\,\text{Å}$ [64, 65]. Technically, two different approaches can be found. One is to grow "real" bulk crystals using, in most cases, the Bridgman growth technique [66]. This yields substrates of the highest quality (see also section 2.5.1). Unfortunately, the obvious way to perform strain-engineering, that is to buy $Cd_{1-x}Zn_xTe$ substrates, is impractical for several reasons. If one is interested in a wide range of different strains, this would require a broad stock of substrates with different x compositions. The fact that suppliers require to purchase the entire rod if the composition is different from the common $x = 0$ and 4 % means a impractical financial effort [67]. Furthermore, the standard procedure to improve the substrate surface quality after ex-situ wet-etching, which is to grow a CdTe buffer (see section 2.5.1), becomes inapplicable for large x values, due to the large lattice mismatch between substrate and buffer layer. As a trade-off between crystal quality and wafer prize, the second approach is to grow thick layers of CdZnTe (in the range of several µm) on more common substrates like Si and GaAs, using techniques such as metalorganic vapor phase epitaxy (MOVPE) [68–70] and MBE [71–73]. The biggest challenge in both methods mentioned above is the inhomogenious distribution of Zn in the crystals, causing both a variation of the resulting lattice constant across the surface [74–76], and a significant degradation of crystal quality, as seen in HRXRD $\Delta\omega$ measurements [71, 74].

To avoid these problems, the fabrication of CdTe-ZnTe SLS instead of solid solutions was suggested [77]. Advantages and drawbacks of this approach are discussed in the following, with emphasis on why, despite notable experimental experience on these structures [56, 78–82], replacing solid solutions with SLS is not entirely straightforward. A new growth procedure to address this challenge is presented.

2.4.1 Effective lattice constant model

For a SLS composed of alternating layers of material 1 and 2 with strain-free lattice constants a_1 and a_2, and individual layer thicknesses d_1 and d_2, each being identical for every period of the SLS, one finds for the effective lattice constant of the free-standing SLS

$$a_{\text{SLS}} = a_1 \left(1 + \frac{f}{1 + m\,r}\right), \tag{2.6}$$

with the lattice mismatch $f = (a_2 - a_1)/a_1$, the layer thickness ratio $r = d_1/d_2$ and the stiffness parameter ratio $m = M_1/M_2$ [see equation (1.8) for the definition of M]. Equation (2.6) is obtained straightforward by balancing the forces of the two layers of one SLS period [i.e. $h_1\sigma_{xx1} = h_2\sigma_{xx2}$ in equation (1.4)], and simplifies to Vegard's law for $m = 1$. Note that in some works, m is incorrectly replaced by the shear modulus ratio

$g = G_1/G_2 = c_{44,1}/c_{44,2}$ [83]. This is only valid for isotropic materials, where c_{44} can be expressed in terms of c_{11} and c_{12}, and is in any case misleading, since the strain energy stored in the crystal does not directly depend on c_{44} [equation (1.8)]. One conceptual advantage of SLS compared to solid solutions is the fact that r is the only degree of freedom in equation (2.6) for one pair of epilayer materials. Consequently, if the growth rate of both constituents is known, a_{SLS} can be controlled precisely by adjusting the growth time ratio, without having to care about incorporation efficiency of elements and its dependence on beam equivalent pressure and substrate temperature.

An important condition to be fulfilled in SLS growth is the fact that each individual layer of the two material types has to be grown coherently on the underlying crystal. This sets a limit to the layer thicknesses $d_{1,2}$, which is given by

$$\frac{d_1\, d_2}{d_1 + d_2} \leq d_{\mathrm{c}}. \tag{2.7}$$

Here, d_{c} is the critical thickness at which relaxation sets in if one of the materials is grown on an infinitely thick layer of the other one [84] (see section 1.2). For the CdTe-ZnTe material system, d_{c} is in the range of 4 to 6 ML [85–87]. With respect to CdHgTe lattice matching, the difficulty that results from having to meet equation (2.7) is best illustrated by calculating actual layer thicknesses of a SLS lattice matched to, for instance, $Cd_{0.3}Hg_{0.7}Te$ (mid-wavelength detector). Such a SLS has to have a lattice constant of $a_{\mathrm{SLS}} = 6.468\,\text{Å}$, which requires a very high layer thickness ratio of $r = d_{\mathrm{CT}}/d_{\mathrm{ZT}} = 31$. Using equation (2.7), this limits d_{CT} and d_{ZT} to $d_{\mathrm{CT}} \leq d_{\mathrm{c}}(1+r) \approx 176$ ML, and $d_{\mathrm{ZT}} \lesssim d_{\mathrm{c}}$. Naturally, since the SLS has to handle additional stress from subsequent CdHgTe epitaxy as well as from lithographic chemical and thermal stress and thermal mismatch stress during cooldown in magnetotransport experiments, one would choose d_{ZT} well below d_{c}. This, however, results in very short MBE growth times ($\approx 10\,\mathrm{s}$ ZnTe growth time for moderate beam equivalent pressures), and consequently to shutter sequences too short to result in stable fluxes on the sample surface. Even though, all-MBE SLS which meet the requirements with respect to critical thicknesses can be grown in principle (in contrast to the assumption of Ref.[79]), we have established an alternative growth procedure which handles the issue of highly uneven layer thicknesses d_{CT} and d_{ZT} more elegantly. This procedure is presented in the next section.

2.4.2 Growth procedure of MBE-ALE CdTe-$Cd_{0.5}Zn_{0.5}$Te SLS

Whereas CdTe layers are grown in MBE mode, ZnTe layers are grown in atomic-layer epitaxy (ALE) mode. In ALE, the surface of a binary compound is exposed to an alter-

nating flux of its two constituents, each at a time. Since the II-VI bond is significantly more stable than the II-II and VI-VI bond in both CdTe and ZnTe, the growth process is self-limiting within appropriate growth conditions. For ZnTe, the growth stabilizes to 0.5 ML per ALE cycle [80, 88]. This is counterintuitive at first, but can be explained by the fact that a Zn-saturated ZnTe surface exhibits a $c(2\times 2)$-reconstructed RHEED signal, indicating a surface coverage of one Zn atom on every 2nd lattice site [89].

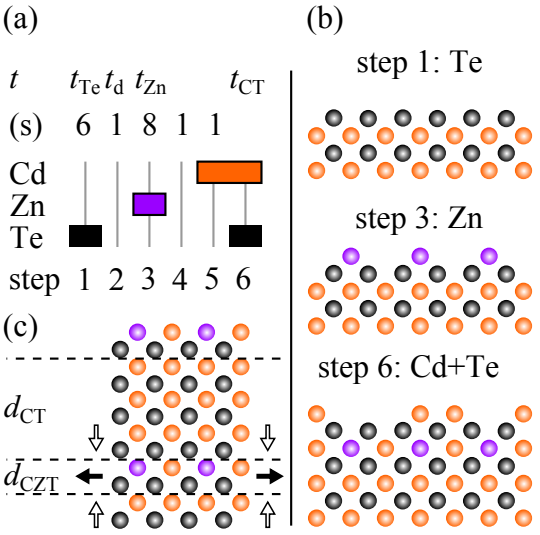

Figure 2.13: (a) Shutter sequence of one SLS cycle. Boxes indicate open shutters. Constant shutter times of standard SLS are given. (b) Growth front during one SLS cycle. Black dots: Te, magenta dots: Zn, orange dots: Cd. (c) The resulting layer stack. Filled arrows indicate strain in $Cd_{0.5}Zn_{0.5}Te$ layer due to mismatch, empty arrows from Poisson's ratio.

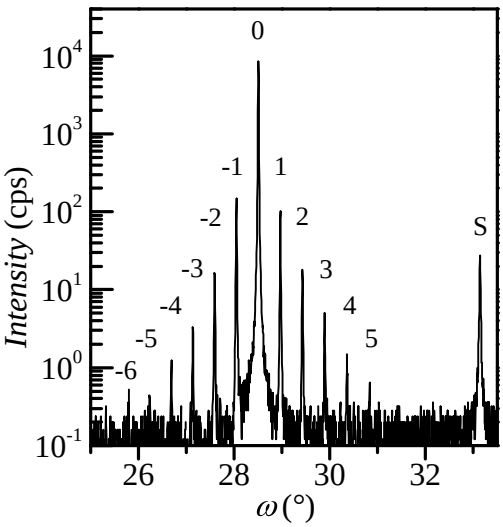

Figure 2.14: HRXRD $\omega - 2\theta$ scan of the (004) reflection of a typical SLS. Reflection of the GaAs substrate is labelled "S", zero-order Bragg-peak and higher order satellites of the SLS are labelled "0" and "$\pm 1, \pm 2, \pm 3 \ldots$".

Similar to standard CdTe buffer layers, SLS are grown on GaAs:Si (001). Thermal deoxidizing and deposition of a 3 nm ZnTe intermediate layer to maintain the (001) crystal direction are also identical (see section 2.3). The SLS growth procedure is illustrated by the standard shutter sequence of one SLS cycle [figure 2.13 (a)] and a sketch of the epilayer surface at the three distinct stages of growth [figure 2.13 (b)]. In step 1 the sample is exposed to Te, resulting in a Te-coverage of one atomic layer. Exposure to Zn in step 3 yields the aforementioned half-filled atomic layer of Zn on the surface. The CdTe epilayer is grown in step 6 in MBE growth mode and the Cd shutter is opened slightly before the Te shutter (step 5) to initiate growth in group-II rich conditions. Dead times (steps 2 and

4) minimize beam intermixing. Assuming perfect ZnTe ALE, the expected layer stack of one SLS period consists of one ML $Cd_{0.5}Zn_{0.5}Te$ with fixed thickness d_{CZT} and a binary CdTe layer with controllable thickness d_{CT} [figure 2.13 (c)]. For further modelling, the material properties of the $Cd_{0.5}Zn_{0.5}Te$ ML are estimated as mean values of the ones of CdTe and ZnTe (section A of the appendix), and thus $f_{CT\text{-}CZT} = (a_{CZT} - a_{CT})/a_{CT}$, and $m = M_{CT}/M_{CZT}$ in equation (2.6) (in the following sections, the index "CZT" represents the composition $Cd_{0.5}Zn_{0.5}Te$).

For standard SLS, which were grown to tune the effective lattice constant a_{SLS}, the constant shutter times are also depicted in figure 2.13 (a). Beam equivalent pressures are set to $\phi_{Zn} \approx 6 \times 10^{-7}$ Torr, $\phi_{Cd} \approx 1.3 \times 10^{-6}$ Torr and $\phi_{Te} \approx 6 \times 10^{-7}$ Torr. As it will be shown later, due to the self-limiting ALE process, the precise ϕ_{Zn} is not relevant for the effective a_{SLS}, and the same holds for ϕ_{Cd}, as long as $\phi_{Cd}/\phi_{Te} \geq 2/1$. The latter ensures both an optimized surface smoothness, as seen in section 2.3, and a linear relationship between ϕ_{Te} and CdTe growth speed. In contrast to the standard procedure for binary CdTe epitaxy (section 2.3.2), the substrate temperature is kept constant during growth ($T_{sub} = 320$ K). This is done since the CdTe growth speed slightly depends on T_{sub}, and a gradient in CdTe layer thickness throughout the SLS periods would result in a gradient in a_{SLS}. Even though this could, in principle, be compensated by an appropriate gradient in CdTe growth time t_{CT}, it was preferred to keep the method simple, and both T_{sub} and t_{CT} constant. Just as CdTe buffer layers, standard SLS were routinely grown over night, and the number of SLS cycles was adjusted according to the duration of a single cycle to obtain total growth times of roughly 12 hours.

2.4.3 Study of SLS layer structure by HRXRD

Apart from the easy composition control, another advantage of SLS compared to $Cd_{1-x}Zn_xTe$ solid solutions is the additional information that can be obtained from HRXRD analysis of the layers. The $\omega - 2\theta$ scan of the (004) reflection of a SLS grown with the standard shutter sequence is shown in figure 2.14. The number of cycles was 350 and the CdTe growth time was $t_{CT} = 107$ s. The reflection of the GaAs substrate "S" is used as reference. Superlattice satellite peaks "$\pm 1, \pm 2, \pm 3 \ldots$" are resolved up to 6th order, indicating aprupt interfaces and uniform SLS period thicknesses p. From the angular spacing $\delta\omega$ of two neighboring satellites, p can be calculated using

$$p = \frac{\lambda}{\delta\omega} \frac{\sin(\overline{\varepsilon})}{\sin(\overline{2\theta})}, \tag{2.8}$$

with the average of the two angles between incoming and diffracted beam (2θ), and the average of the two angles between diffracted beam and sample surface ($\varepsilon = 2\theta - \omega$) [46]. For the SLS shown in figure 2.14, one finds $p = 109\,\text{Å}$. From the angular spacing between S and the zero-order SLS peak "0", the out-of-plane lattice constant of the SLS is found straightforward using the Bragg equation $a_{\text{SLS}\perp} = 2\lambda / \sin(\theta)$, and the lattice constant of GaAs (appendix section A) as reference. For the SLS shown in figure 2.14, one finds $a_{\text{SLS}\perp} = 6.478\,\text{Å}$. For the same reasons already discussed in section 2.3, the residual in-plane ($\varepsilon_{||}$) and out-of-plane strain ($\varepsilon_{\perp}$) are not exactly equal to zero. Since the effective Zn-fraction in all SLS discussed in this work is small, and the total SLS thickness can be deduced from p and the number of SLS periods, $\varepsilon_{||}$ can be approximated from figure 2.12. With Poisson's ratio [equation (1.6)], the in-plane $a_{\text{SLS}\,||}$, and the lattice constant of the (hypothetical) fully free-standing SLS, a_{SLS}, can be calculated.

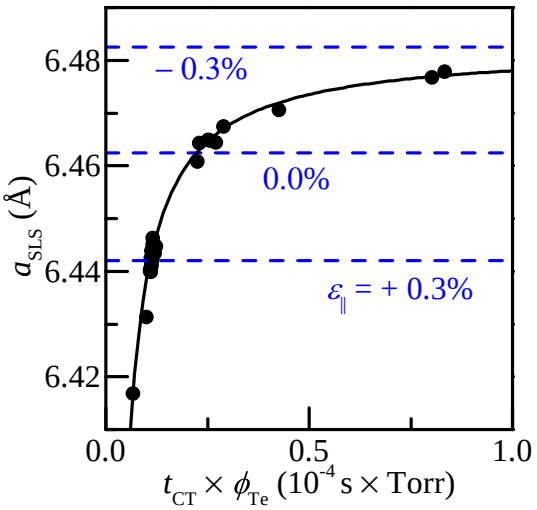

Figure 2.15: Strain-free lattice constant a_{SLS} of a series of SLS with different CdTe growth time t_{CT} and beam-equivalent pressure ϕ_{Te}. Lines guide the eye to standard HgTe on CdTe (-0.3%), lattice matched to HgTe (0.0%) and SLS applying compressive strain of +0.3 % to HgTe. Solid line is a fit of equation (2.6) with fit parameter α [equation (2.9)].

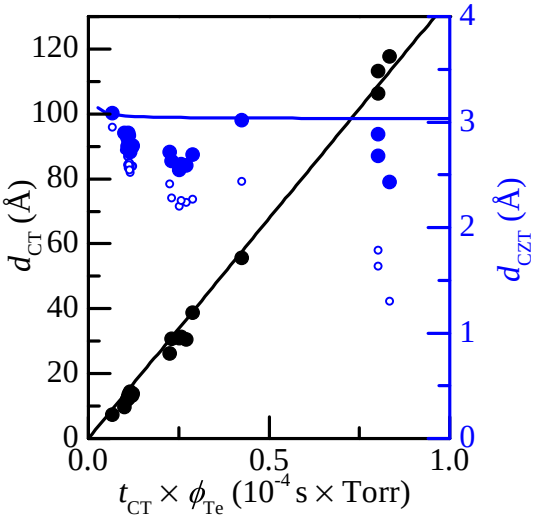

Figure 2.16: Individual layer thicknesses d_{CT} (black dots) and d_{CZT} (filled blue dots) of a series of SLS with different CdTe growth time t_{CT} and ϕ_{Te}. Black straight line is a guide to the eye. Blue line depicts dc_{CZT}. Empty blue dots are calculated d_{CZT}, assuming oversimplified $\varepsilon = 0$.

Figure 2.15 shows a_{SLS} of a series of 29 SLS, grown with the standard parameters discussed in the previous section and the shutter sequence shown in figure 2.13 (a), as function of the product of CdTe growth time and Te beam-equivalent pressure ($t_{\text{CT}} \times \phi_{\text{Te}}$). The

product $t_{CT} \times \phi_{Te}$ was varied by more than one order of magnitude (0.07 to 0.83×10^{-4} s Torr), resulting in structures with a_{SLS} from 6.417 Å to 6.478 Å. Since several layers were grown to serve as substrates for strain-free ($\varepsilon = 0.0\%$) or compressively strained ($\varepsilon = +0.3\%$) HgTe epilayers, a_{SLS} is not distributed uniformly. The solid line in figure 2.15 is a fit of equation (2.6) to the data after substituting r by

$$r = \alpha \left(t_{CT} \times \phi_{Te} \right), \tag{2.9}$$

and using α as a fit parameter. The substitution in equation (2.9) combines the CdTe growth speed and the thickness of the $Cd_{0.5}Zn_{0.5}Te$ layer in the fitting parameter α. Good agreement is found for $\alpha = (4.1 \pm 0.3) \times 10^5$ $s^{-1}\,Torr^{-1}$. The fact that the fit matches for the entire $t_{CT} \times \phi_{Te}$ range indicates that the growth speed of CdTe is stable for different CdTe thicknesses, and, as expected, that the $Cd_{0.5}Zn_{0.5}Te$ layer thickness d_{CZT} is constant. Both these aspects greatly simplify the fabrication of SLS with a specific lattice constant. Since $t_{CT} \times \phi_{Te}$ is the only degree of freedom in equation (2.6) combined with equation (2.9), a_{SLS} can be controlled straightforward by adjusting t_{CT} after a reference sample has been grown, in contrast to CdZnTe solid solutions, where a precise adjustment of beam equivalent pressures (i.e. effusion cell temperatures) is required. In this context, it is also worth mentioning that the SLS presented in figure 2.15 were not produced directly one after another, but with several interruptions and chamber openings in between. The good agreement between fit curve and the measured a_{SLS} of the whole ensemble of samples shows the reliability of the method.

The fact that the measured a_{SLS} can be fit by equation (2.6) combined with equation (2.9) does not require a particular d_{CZT} as long as it is constant. However, with

$$r = \frac{d_{CT}}{d_{CZT}} \qquad \text{and} \qquad p = d_{CT} + d_{CZT}, \tag{2.10}$$

the thicknesses d_{CT} and d_{CZT} can be calculated from equation (2.6) and (2.8). Results for the SLS grown by the standard procedure are shown in figure 2.16. Again, a linear increase in d_{CT} and constant d_{CZT} reflect the validity of the growth model. To illustrate the influence of residual strain ε on the fitting procedure, d_{CZT} is also shown assuming $\varepsilon = 0$ (small blue empty dots). This oversimplified calculation results in overall lower d_{CZT} and an approximately linear decrease with increasing $t_{CT} \times \phi_{Te}$. This can be explained as follows: The assumption of an entirely strain-free SLS ($\varepsilon = 0$) causes an offset in the calculation of a_{SLS} from the HRXRD measurement, which is approximately constant for comparable total epilayer thicknesses. The impact of this offset on d_{CZT} can be analyzed straightforward using equation (2.6). One finds an linear decrease of d_{CZT} with

increasing d_{CT}. This is in agreement with the trace of the empty blue data points, since $d_{\mathrm{CT}} \propto (t_{\mathrm{CT}} \times \phi_{\mathrm{Te}})$.

To gain further insight into the validity of our growth model, it is insightful to analyze whether exactly 1 ML of $Cd_{0.5}Zn_{0.5}Te$ is grown in one SLS cycle, as ideally expected. To do so, we compare the measured thickness d_{CZT} to the theoretical thickness dc_{CZT} of one complete ML. The thickness of one ML of unstrained $Cd_{0.5}Zn_{0.5}Te$ is 1/2 $a_{\mathrm{CZT}} = 3.15\,\text{Å}$. However, since the $Cd_{0.5}Zn_{0.5}Te$ layer is heavily strained tensile in-plane in all SLS discussed in this work, the out-of plane lattice constant measured by HRXRD is considerably lower [Note that this strain of the $Cd_{0.5}Zn_{0.5}Te$ epilayers only must not be confused with the (much lower) residual strain of the complete SLS, mentioned earlier]. Since $d_{\mathrm{CT}} \gg d_{\mathrm{CZT}}$ in all SLS discussed here, the strain in the $Cd_{0.5}Zn_{0.5}Te$ epilayer is always approximately $f_{\text{CT-CZT}}$. With Poisson's ratio [equation (1.6)], the expected dc_{CZT} can be calculated from a_{SLS}, and is approximately constant: $dc_{\mathrm{CZT}} \approx 3.04\,\text{Å}$. In figure 2.16, dc_{CZT} is shown in figure 2.16 as blue line. Notable deviations from this approximation are not expected until $d_{\mathrm{CT}} \approx d_{\mathrm{CZT}}$, i.e. $\phi_{\mathrm{Te}} \times t_{\mathrm{CT}}$ becomes very small. This can be seen by the small kink of the theoretical dc_{CZT} in figure 2.16 for $(\phi_{\mathrm{Te}} \times t_{\mathrm{CT}}) \to 0$. From all the samples shown in figure 2.16, we calculate an average $d_{\mathrm{CZT}} = (2.77 \pm 0.13)$ Å. This value is considerably lower than dc_{CZT}, which leads to the assumption that less than 0.5 ML ZnTe is grown during each ALE sequence.

The suspicion of an incomplete ALE step was studied in greater detail. By examining the growth procedure [figure 2.13 (a)], four most plausible reasons are found as the cause of this incompleteness:

- The incomplete Te-saturation of the surface in step 1,
- the re-evaporation of Te in step 2,
- the deposition of less than one Zn atom on every two Te atoms in step 3,
- or the re-evaporation of Zn in step 4.

To address these mechanisms, multiple sets of samples have been grown, with a large variety of growth parameters. The results are presented in the following.

To study if the amount of Te provided in step 1 saturates all Cd bonds on the surface, we have varied the Te-only time by a factor of two ($t_{\mathrm{Te}} = 4\,\text{s}$ and $8\,\text{s}$). No significant change in d_{CZT} occured. However, a complete coverage of Te is not stable on a CdTe surface at the typical growth temperatures [90]. To quantify the temperature dependence of the Te desorption, we have performed a series of RHEED experiments. A standard CdTe layer grown on GaAs is exposed to a Te flux. The RHEED intensity of the (2×1) reconstruction

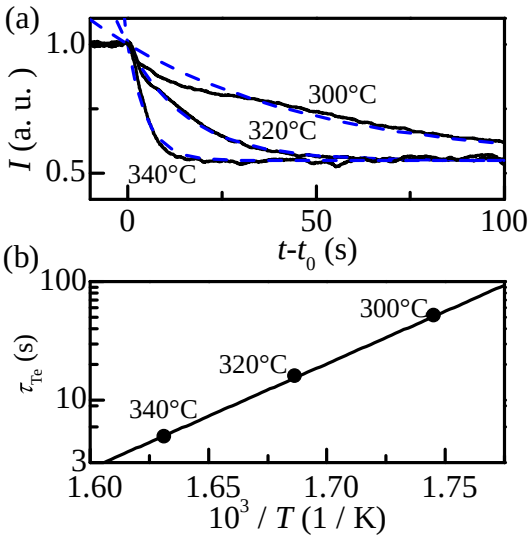

Figure 2.17: (a) RHEED intensity of the (2×1) reconstruction line of a CdTe surface. At $t = t_0$, Te exposure is terminated. y-axis scale is arbitrary. Blue lines are fits to equation (2.11). (b) Te desorption time versus inverse of sample temperature. Line is fit to equation (2.12).

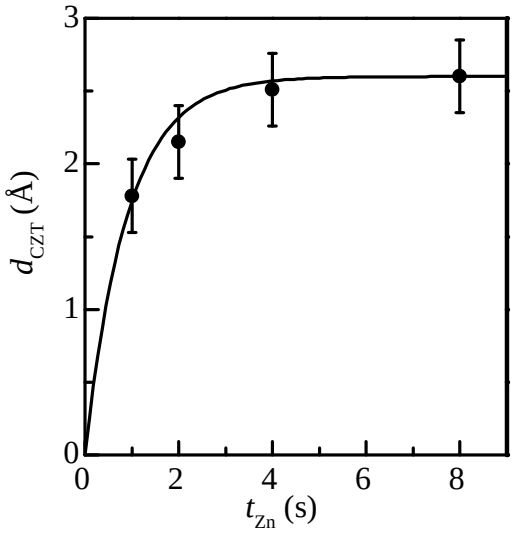

Figure 2.18: $Zn_{0.5}Cd_{0.5}Te$ layer thickness of a set of SLS with varying Zn-only time [step 3 in figure 2.13 (a)]. Line is fit to equation (2.13).

line, which is caused by pairing of the Te dangling bonds, serves as a measure of the Te coverage c_{Te} of the surface. This intensity was recorded using a dedicated RHEED CCD camera system and software analysis tool [figure 2.17 (a)]. At $t = t_0$, the Te exposure is terminated, and the intensity of the reconstruction goes down. This procedure was done at three different substrate temperatures $T = 300$, 320 and 340 °C. By fitting the intensity of the reconstruction to

$$I(t) = A + B\,\exp\left(-\frac{t}{\tau_{\mathrm{Te}}}\right), \tag{2.11}$$

we determine the temperature-dependent surface lifetime τ_{Te} of the Te atoms. The Te desorption is activated thermally, and by fitting $\tau_{\mathrm{Te}}(T)$ to

$$\tau_{\mathrm{Te}}(T) = C\,\exp\left(\frac{E_{\mathrm{a}}}{k_{\mathrm{B}}T}\right), \tag{2.12}$$

[figure 2.17 (b)] the Te activation energy can be obtained as $E_{\mathrm{a}} = 1.8\,\mathrm{eV}$, which is in reasonable agreement with Ref. [90] ($E_{\mathrm{a}} = 1.95\,\mathrm{eV}$). As an intermediate result, we have confirmed that the Te-only exposure time in step 1 (typically 6 s) is sufficient to achieve a steady Te coverage, and found the timescale at which it returns to its equilibrium state in

UHV. To investigate the value of c_{Te} during Te exposure, we have grown three SLS with identical shutter times, but different growth temperatures $T = 300\,^{\circ}\mathrm{C}$, $310\,^{\circ}\mathrm{C}$ and $320\,^{\circ}\mathrm{C}$. If the Te layer was incomplete ($c_{\mathrm{Te}} < 1$ at $t = t_0$), then the value of c_{Te} would depend on the surface lifetime τ_{Te}, which changes by a factor of 3.3 for these temperatures [see figure 2.17 (b)]. This would result in a change in d_{CZT} of the samples by a factor of a comparable magnitude. This is not observed, and we therefore conclude that $c_{\mathrm{Te}} = 1$ at $t = t_0$. Regarding the value of c_{Te} in the absence of any fluxes, Ref. [91] reports a saturation towards $c_{\mathrm{Te}\infty} = 0.55$ at typical growth temperatures.

Next, we address the completeness of the half-filled atomic layer of Zn. To do so, we have grown a set of SLS with varying Zn exposure time t_{Zn} [step 3 in figure 2.13 (a)], and analyzed the $Cd_{0.5}Zn_{0.5}Te$ layer thickness d_{CZT}. The result is shown in figure 2.18. d_{CZT} saturates towards a $d_{\mathrm{CZT}\infty}$ and, given the statistical uncertainty, is safely in agreement with $d_{\mathrm{CZT}\infty}$ at $t_{\mathrm{Zn}} \geq 4\,\mathrm{s}$. A fit of the data to

$$d_{\mathrm{CZT}}(t_{\mathrm{Zn}}) = d_{\mathrm{CZT}\infty}\left[1 - \exp\left(-\frac{t_{\mathrm{Zn}}}{\tau_{\mathrm{Zn}}}\right)\right] \tag{2.13}$$

yields an estimate of the time constant of the saturation process, $\tau_{\mathrm{Zn}} = (0.9 \pm 0.4)\mathrm{s}$, at the temperature and Zn flux of the experiment. A re-desorption of Zn after the Zn exposure, as observed for the case of the Te-rich surface, is not expected since the obtained 50 % Zn coverage is in the range of the equilibrium situation of II-VI crystals. Also, no change in the RHEED reconstruction of such surfaces was observed up to $T = 380\,^{\circ}\mathrm{C}$ [92].

So far, we have confirmed that the exposure to elemental Te and Zn in the corresponding steps is sufficient to saturate the sample surface in both cases. We now quantify the amount of Te desorption in the time period between the closing of the Te-shutter and the full Zn-stabilization of the surface. To accomplish this, another set of samples was grown, with varying dead time $t_{\mathrm{d}} = 0$, 1, 5, 25 and 60 s between Te and Zn exposure [step 2 in figure 2.13 (a)]. The completeness of the $Cd_{0.5}Zn_{0.5}Te$ ML, defined as $d_{\mathrm{CZT}}/dc_{\mathrm{CZT}}$, is shown in figure 2.19 (black dots). Due to the sufficient Zn-exposure and the absence of Zn-desorption, this quantity is expected to be similar to the completeness of the Te atomic layer c_{Te}. With the two time constants τ_{Te} (desorption) and τ_{Zn} (coverage), we model the Te desorption as

$$\frac{d}{dt}\left(c_{\mathrm{Te}}(t)\right) = -\left(1 - \frac{d_{\mathrm{CZT}}(t - t_{\mathrm{d}})}{d_{\mathrm{CZT}\infty}}\right)\frac{c_{\mathrm{Te}}(t) - c_{\mathrm{Te}\infty}}{\tau_{\mathrm{Te}}}, \tag{2.14}$$

with $d_{\mathrm{CZT}}(t - t_{\mathrm{d}})$ given by equation (2.13) for $t - t_{\mathrm{d}} > 0$, and $d_{\mathrm{CZT}}(t - t_{\mathrm{d}}) = 0$ for $t - t_{\mathrm{d}} < 0$. The term in brackets in equation (2.14) is the ratio between (volatile) surface exposed and

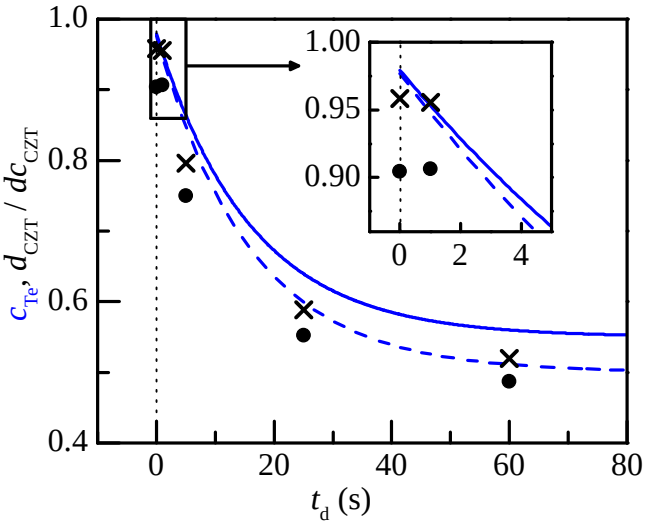

Figure 2.19: Black dots: measured thickness of $Cd_{0.5}Zn_{0.5}Te$, normalized to theoretical dc_{CZT} for different dead times t_d between Te and Zn exposure. Black crosses: d_{CZT} calculated assuming M_{CZT} lowered by 5 %. Blue continuous (dashed) line: Te coverage from integrating equation (2.14), assuming $c_{Te\infty} = 0.55(0.50)$ %. Inset shows closeup of short t_d.

(stable) Zn-bound Te atoms. As an initial condition, we have previously found $c_{Te}(0) = 1$. For $t_d \to \infty$, a solution to equation (2.14) is $c_{Te}(t) = (1 - c_{Te\infty})\exp(-t/\tau_{Te}) + c_{Te\infty}$, in agreement with equation (2.11). For finite t_d, we integrate equation (2.14) numerically, and compare it to the completeness of the $Cd_{0.5}Zn_{0.5}Te$ ML in figure 2.19 (blue continuous line). A closeup of the result for very short t_d is shown in the inset. Due to the finite time needed to saturate the Te surface with Zn, the layer is incomplete even for $t_d = 0$. While the overall trend of d_{CZT}/dc_{CZT} is reproduced, the model still overestimates the layer completeness for both short and long t_d. Additional adjustments are needed to resolve the remaining discrepancy. One possibility is to lower the elastic constant M_{CZT}, used to calculate m in equation (2.6), by approximately 5 %. Such a deviation may be due to the extrapolation from bulk values to ultra thin layers, or the heavy strain (see for example [93–95]). Calculated d_{CZT}/dc_{CZT} with these modified elastic constants are shown as black crosses in figure 2.19. Agreement between model and data can be further improved by assuming a perfectly stochiometric equilibrium CdTe surface ($c_{Te\infty} = 0.5$) instead of a slightly Te-rich one ($c_{Te\infty} = 0.55$). This deviation is well in the range of the typical uncertainty of the method used in Ref. [91] (X-ray photo-electron spectroscopy). The modified solution of equation (2.14) is shown as blue dashed line in figure 2.19.

Even though a good agreement between theory and experiment is found, we have to emphasize that this is only possible with a small adjustment of the fitting parameter

M_{CZT}, and the magnitude of this adjustment is in principle a result of the fit, based on the assumption that the half-ML ALE model is exact, i.e. $d_{CZT} = dc_{CZT}$ [88]. However, as mentioned previously, the absolute value of d_{CZT} does not affect the accuracy of the SLS lattice constant control, as long it is constant. As shown in figure 2.16 (blue filled dots), no systematic dependency of d_{CZT} on $t_{CT} \times \phi_{Te}$ is found.

2.4.4 Comparison of SLS crystal quality with CdZnTe solid solutions

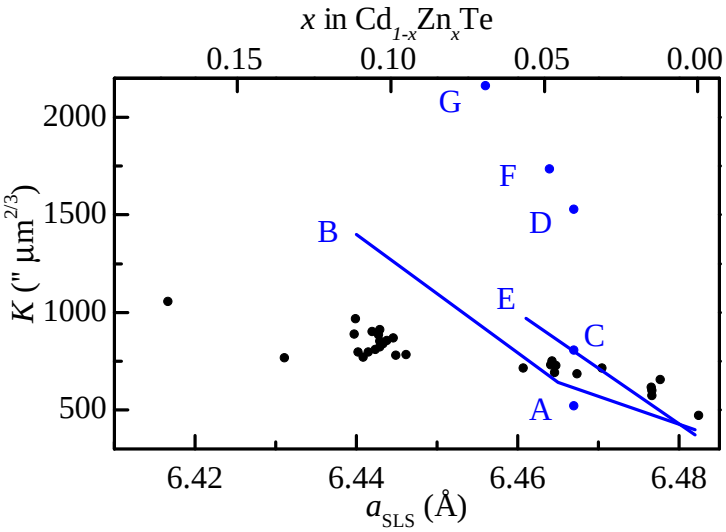

Figure 2.20: Black dots: crystal quality quantifier K measured by HRXRD as function of SLS lattice constant. Upper x-axis represents Zn content of $Cd_{1-x}Zn_xTe$ solid solution with identical lattice constant. Blue dots and lines: K-values of various solid solutions listed in table 2.1. Lines indicate best (i.e. lowest) values in works with a lot of scatter in the data.

The discussion of the epitaxy of SLS is concluded with some remarks on the crystal quality of SLS, which is influental to the properties of the heterostructures grown on top. In comparison with binary CdTe on GaAs, we do not observe a significant difference regarding surface roughness analyzed in Nomarski microscopy and AFM. The RHEED signal, however, begins to degrade slightly for SLS with very short periods. The problem of uneven Zn-distribution, found in early CdZnTe solid solutions [71, 74], is unlikely to exist in the SLS presented here, since this would prevent us from measuring sharp SLS satellites, as they are seen in figure 2.14. The crystal quality quantifier K, measured by HRXRD, is found to increase approximately linear with decreasing a_{SLS}, with the highest value $K \approx 1100'' \mu m^{-2/3}$ for $a_{SLS} = 6.417$ Å (figure 2.20), i.e. the crystal quality goes down. This trend qualitatively resembles observations that are made in solid solutions.

	year	growth mode	substrate	D [μm]	comment	Ref.
A	1993	MOVPE	GaAs (001)	3	same results for miscut and non-miscut substrates.	[68]
B	1993	MOVPE	GaAs on Si (001)	8	a lot of scatter in data, line shows best values.	[69]
C	1993	MBE	Si (001)	11.5	miscut 8° towards (011).	[72]
D	1993	MBE	Si (001)	11.5	non-miscut substrate.	[72]
E	1995	MBE	Si (001)	10	a lot of scatter in data, line shows best values, miscut 4 or 8° towards (111).	[73]
F	2002	MOVPE	GaAs (001)	3	miscut 2° towards (110).	[70]
G	2002	MOVPE	GaAs (001)	3	miscut 4° towards (110).	[70]

Table 2.1: Key sample specifications of solid solutions depicted in figure 2.20.

However, the rate of crystal quality decay with respect to increasing Zn-content seems to be less severe in SLS. This is illustrated by plotting K-values for CdZnTe solid solutions produced by a large variety of epitactical methods (see table 2.1) in figure 2.20 (blue dots and lines). Refs. [69, 73] (lines B and E) present data on a large number of samples with a lot of scatter in $\Delta\omega$, the lines show best values. Whereas MOVPE appears to yield decent crystals for moderate Zn contents ($x < 7\%$), the K-value of SLS is significantly lower than the one of solid solutions, if $x > 10\%$. This observation encouraged us to use SLS with high effective Zn content as artificial substrates for HgCdTe epitaxy, see section 2.5.3 and 2.5.4.

2.5 Hg-based heterostructures on different substrate types

As discussed in the previous sections, one result of the work presented in this thesis is the extendend variety of substrates available for Hg-based MBE. Whereas previously, the choice was limited to commercial CdTe or $Cd_{0.96}Zn_{0.04}Te$, it is now extended to large-area substrates of CdTe on GaAs:Si, and, in partcular, to SLS artificial substrates with freely adjustable lattice constants. The epitaxy on these new substrates is based on the existing expertise on II-VI substrates, which is discussed in section 2.5.1. Closer attention to coherent (i.e. relaxation-free) growth of the heterostructure is required due to the large mismatches between individual layers and the substrate (section 2.5.3), in particular regarding highly compressed QWs (section 2.5.4).

2.5.1 Epitaxy on II-VI substrates

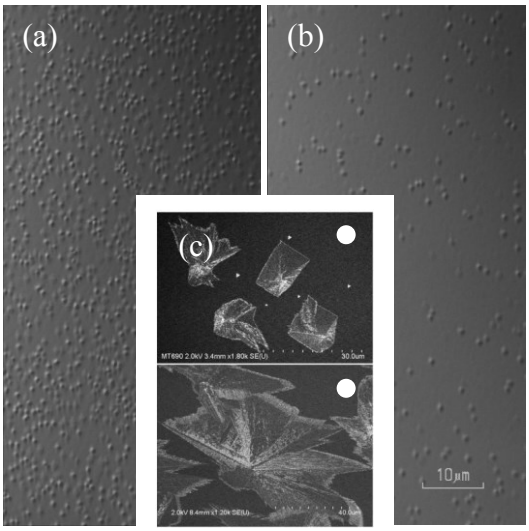

Figure 2.21: Nomarski images of QW-structure grown at (a) $\Delta T_{\mathrm{sub}} \approx +4\,^{\circ}\mathrm{C}$ and (b) close to optimum T_{sub}. (c) SEM picture of void defects on HgTe grown on (211)B $Cd_{0.96}Zn_{0.04}Te$ at $\Delta T_{\mathrm{sub}} + 6\,^{\circ}\mathrm{C}$ (upper picture) and $+8\,^{\circ}\mathrm{C}$ (lower picture). Slightly altered from [96].

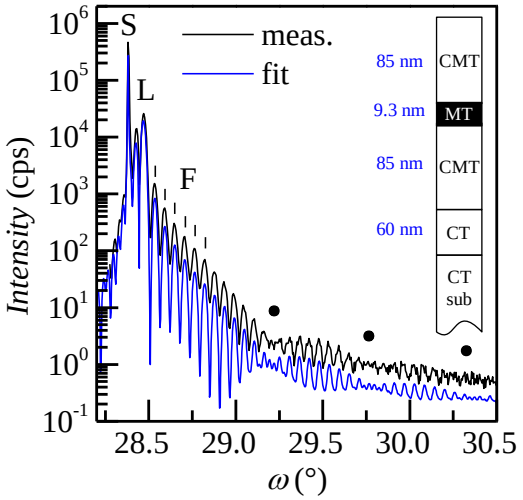

Figure 2.22: HRXRD $\omega - 2\theta$ scan of the (004) reflection of a symmetric QW. Beating pattern of the barrier's thickness fringes caused by the QW is indicated by dots. Inset shows layer stack. Simulation is offset for clarity.

Due to the outstanding quality of bulk crystals, CdTe or $Cd_{0.96}Zn_{0.04}Te$ substrates still are the starting point of choice to grow state-of-the-art HgTe-CdHgTe heterostructures, if the state of strain in the HgTe layer, induced by these substrate types, is appropriate or irrelevant for the intended experiment. The wafers are de-oxidized in HCl before being introduced into the UHV system. Since this preparation step frequently produces isolated macroscopic defects on the surface caused by residuals of the etching solution, and wet-chemistry is in general undesirable in MBE, some effort has been put into wafer-preparation by dry-etching. It was found that the surface oxide can be removed effectively by exposing the sample to (thermally cracked) atomic hydrogen, but epilayers grown in-situ on dry-etched samples were of poor quality. X-ray photo-electron spectroscopy analysis showed that this is most likely due to residual carbon on the surface, which is stable against hydrogen and probably originates from the supplier's polishing procedure. Therefore, up to now, etching in HCl is still the method of choice for the preparation of II-VI substrates before epitaxy.

Initially the RHEED signal is spotty, indicating microscopic damaging of the surface

in the polishing process. With the deposition of a buffer layer of approximately 60 nm CdTe at $T_{sub} = 320\,^{\circ}\mathrm{C}$, a flat surface with a streaky RHEED signal is recovered, and persists throughout the following Hg-based growth. The weak Hg-Te bond [97] and high vapor pressure of elemental Hg have several implications on the growth of HgTe and CdHgTe: With $T_{sub} = 180\,^{\circ}\mathrm{C}$ the optimum growth temperature is low compared to other material systems and the temperature window for low-defect crystals is only $\Delta T_{sub} \approx \pm 2\,^{\circ}\mathrm{C}$ [96]. Thus, special emphasis is on accurate and reproducible control of the substrate temperature. Therefore, substrates are glued to molybdenium blocks using Ga or In to ensure good thermal contact, and the thermocouple temperature sensor is in direct contact to the block as well. Furthermore, all molybdenium blocks in use have been calibrated individually with the In- and Sn-melting point method. Since the mechanical contact between thermocouple and molybenium block may change at a chamber opening, the procedure is redone after every opening. After epitaxy, the surface morphology of the layers also gives insights on the optimum growth temperature. Higher temperatures ($\Delta T_{sub} \approx +4\,^{\circ}\mathrm{C}$) imply characteristic high-temperature void defects, which, with increasing ΔT_{sub}, become more and more frequent, change their shape from rhombic to star-shaped [96] and are visible in the optical Nomarski microscope and in the scanning-electron microscope (SEM) (figure 2.21). In order to avoid damaging of the surface due to re-evaporation of Hg, an excess flux of Hg is maintained during growth and subsequent cooldown with a typical beam equivalent pressure ratio of $\phi_{Hg}/\phi_{x} \approx 300/1$ for both x = Te and x = CdTe [98]. Consequently, the main shutter is always open, and growth of HgTe and CdHgTe is controlled by opening the shutter of the Te elemental or CdTe compound cell, respectively. Close to optimum growth conditions, the latter results in the growth of the high quality solid solution $Cd_{0.70\pm0.02}Hg_{0.30\pm0.02}Te$, which is used as standard barrier material for HgTe QWs. The substrate temperature and total fluxes are adjusted to achieve typical growth rates of approximately $1\,\text{Å}\,\mathrm{s}^{-1}$. CdI_2 is routinely used as a dopant for n-type doping. Typically, the doped layer is 10 nm thick, and located in the bottom CdHgTe barrier, 70 nm away from the QW to suppress carrier scattering on electrostatic potential fluctuations induced by charged donors [44]. After the growth has been completed, the sample is cooled down to 100 °C. The Hg-flux is maintained constant to avoid surface degradation due to re-evaporation of Hg.

2.5.2 Determining the thickness of quantum wells

Since the QW thickness is a critical parameter for the resulting band structure (section 3.3.1), special attention is paid on precise calibration of the growth rate. The method of counting intensity oscillations in the RHEED pattern, routinely performed on various

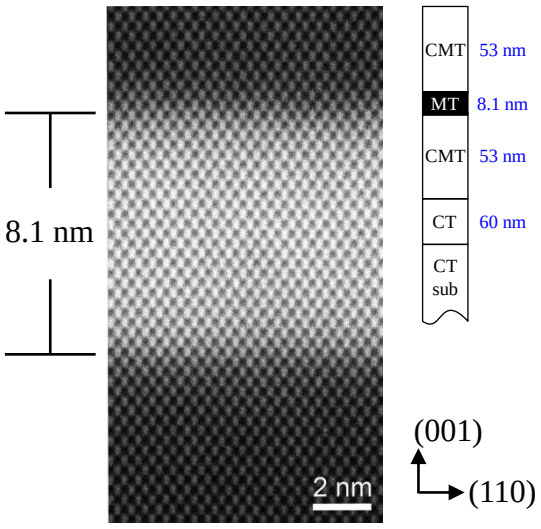

Figure 2.23: Scanning tunneling electron microscopy picture of a symmetric QW. Small sketch shows layer stack. Picture taken by N. Tarakina.

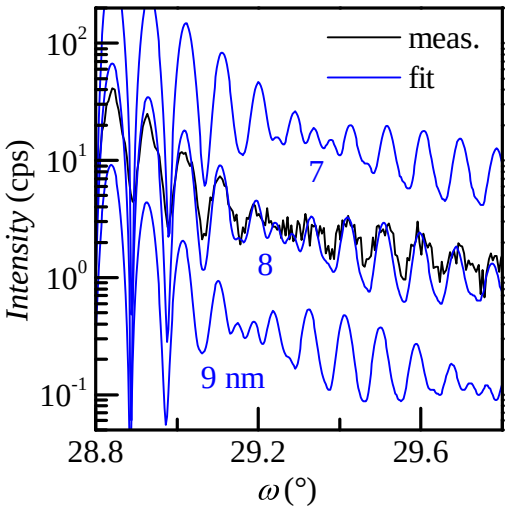

Figure 2.24: Closeup of the first beating node of HRXRD-scan of the sample shown in figure 2.23. Fits of three different QW thicknesses are shown (offset for clarity).

II-VI systems, is not applicable in HgTe epitaxy, since good crystals grow in step-flow mode rather than in island growth mode, and no oscillations are seen [43]. Therefore, growth rate calibration is carried out by analysis of HRXRD $\omega - 2\theta$ scans of various types of reference samples. These are grown after every chamber opening as well as on a regular basis. An example is given in figure 2.22. For thick layers CdHgTe and HgTe ($d \gtrsim 30\,\mathrm{nm}$), d can be deduced directly from the so-called "Pendellösung-fringes", originating from multiple reflections of the X-ray beam on the epilayer's interface, some highlighted with small ticks labelled "F" in figure 2.22. In most cases, the scattering volume of a typical QW is too low to produce an X-ray signal which yields direct information on its thickness. However, if a QW is sandwiched between two sufficiently thick CdHgTe epilayers, a phase shift will occur between the diffracted waves of the two layers. The period of the resulting beating pattern on the intensity of the Pendellösung-fringes allows to measure the QW thickness [99]. The effect can also be seen in figure 2.22, where nodes of the beating are marked by black dots. The precision achieved in beating-node measurements depends on crystal quality and measurement time, as well as on reference sample design. On $Cd_{0.96}Zn_{0.04}Te$ substrates, the CdTe buffer creates additional features in the diffraction pattern, which, along with a statistical variation in the actual Zn fraction of the substrates, complicate the fitting procedure. Therefore, in order to maximize the precision of the QW thickness measurement, CdTe should be used as substrate. To retrieve a simple

and distinct beating pattern, CdHgTe barriers should be of identical thickness of at least $d \geq 50\,\text{nm}$. The thickness of a QW embedded in such a heterostructure can be measured with an uncertainty of $\Delta d \approx \pm 5\,\text{Å}$. The accurateness of the method and the commercial fitting software is confirmed by comparing scanning tunneling electron microscopy (figure 2.23) and HRXRD data (figure 2.24) of a QW structure. The limit in resolution is illustrated by fits with the QW thickness off by $\pm 1\,\text{nm}$. Based on the analysis of many reference QWs, it was found that the growth rate of thin wells cannot be extrapolated from bulk HgTe values, but is approximately 10 % larger.

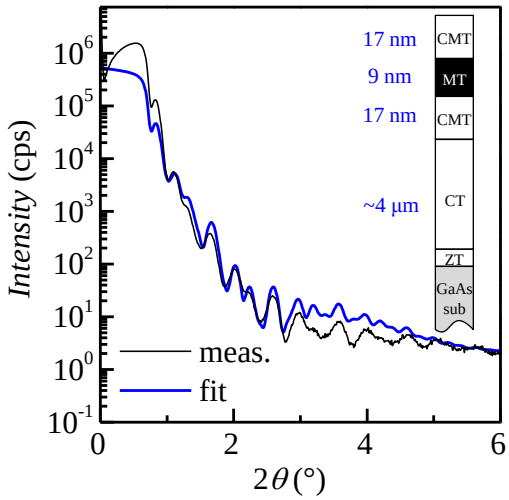

Figure 2.25: XRR scan of a QW with narrow barriers. Inset shows layer stack. Only thicknesses of CdHgTe barriers and HgTe QW are relevant for the fit.

The determination of the position of the beating node in an $\omega - 2\theta$-scan is only possible if the signal of the barriers is distinct, i.e. if the barriers are sufficiently thick and highly crystalline. If this is not the case, layer thicknesses can be determined from an X-ray reflectometry (XRR) measurement. With this method, the reflectivity of the sample is probed by performing a symmetric $\omega - 2\theta$ at a very low angle. Regarding the reciprocal space (figure 2.4), this is a scan in the vicinity of the (000) "reflection". An example is shown in figure 2.25. The intensity oscillates due to interference of beams coming from different interfaces, and the rate of decay with increasing angle 2θ depends on the roughness of the interfaces. Information on individual layer thicknesses and roughnesses can be obtained from a fit to the data. Sample informations which are related to the lattice structure of the crystal, such as precise composition, strain and relaxation are not captured in XRR measurements. Conveniently, these are still accessible from HRXRD scans, and, in particular regarding highly strained layers on SLS, a combination of XRR

and HRXRD measurements allows for complete characterization of the layer stack and its state of strain.

2.5.3 Critical thickness of strain-engineered heterostructures on superlattices

HgTe QWs and other CdHgTe-based heterostructures are grown in a similar approach on the two different types of artificial substrates CdTe-GaAs and CdTe-$Cd_{0.5}Zn_{0.5}Te$-SLS-GaAs. Artificial substrates are transferred directly from the wide gap II-VI chamber into the Hg-chamber, without breaking UHV. In contrast to layers on commercial II-VI substrates, no CdTe buffer is grown, and only a mild anneal at 250 °C is performed before deposition of mercury-containing layers at the usual beam-equivalent pressures and substrate temperature. With this straightforward approach, QWs with decent magneto-transport properties are obtained on binary CdTe on GaAs substrates, with low carrier densities and mobilities close to the best values found in layers grown on commercial II-VI substrates [31]. In contrast, the mobility of QWs on SLS decreases steadily with increasing Zn-content (see section 5.3.2). This is in agreement with the increase of the HRXRD parameter K, discussed previously in section 2.4.4, and should be a subject of investigation following up on this work.

Whereas the procedure for the growth on SLS substrates is straightforward, care has to be taken when designing the actual layer stacks. The requirement to grow both the barriers and the QW coherently is met easily for ordinary substrates like CdTe and $Cd_{0.94}Zn_{0.04}Te$, since the lattice mismatch between substrate and $Cd_{0.7}Hg_{0.3}Te$ barriers is very low ($\varepsilon_{||} = -9 \times 10^{-5}$ on CdTe and $+1.4 \times 10^{-4}$ on $Cd_{0.96}Zn_{0.04}Te$, see figure 1.3). This changes considerably if SLS are employed which are designed to yield strain-free or even compressively strained QWs. For example, fabricating a QW with $\varepsilon_{||,\mathrm{QW}} = +0.3\,\%$ (i.e. same magnitude but inverse sign compared to that of a QW grown on CdTe), requires coherent epitaxy of compressively strained $Cd_{0.7}Hg_{0.3}Te$ barrier material with $\varepsilon_{||,\mathrm{barrier}} = +0.52\,\%$. Thus, the critical thickness of the barrier material will drop significantly, and is the limiting factor in the sample layout.

To specify the generic properties of strain and relaxation of $Cd_{0.7}Hg_{0.3}Te$ (see section 1.2), and in particular to find the critical thickness for coherent epitaxy (see section 1.3), two sets of samples have been grown and analyzed in HRXRD, with the method outlined as follows: The deformation of the unit cell of an epilayer grown on a substrate with slightly larger lattice constant (e.g. HgTe on CdTe) is sketched in figure 2.26 (a) for the case of a fully strained and fully relaxed layer. Since $|\mathbf{a}_i| = |\mathbf{g}_i|^{-1}$ for cubic crys-

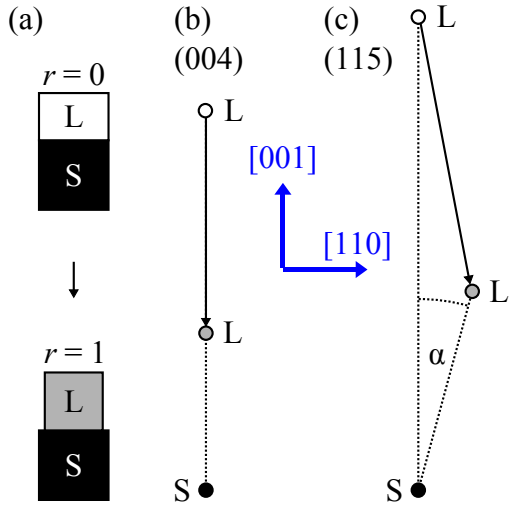

Figure 2.26: (a) Deformation of unit cell of fully strained and fully relaxed epilayer "L" with smaller lattice constant than substrate "S". (b) and (c) Sketch of (004) and (115) reciprocal lattice points. Arrow depicts relaxation line, α is the relaxation angle. Directions in reciprocal space are shown in blue.

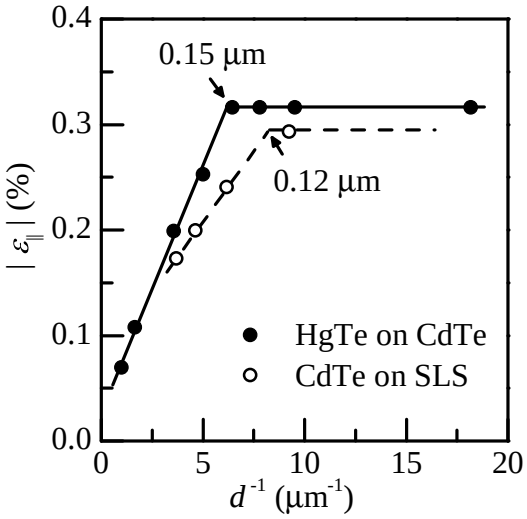

Figure 2.27: Residual strains as function of inverse layer thickness. Strain is tensile ($\varepsilon_{||} < 0$) for HgTe on CdTe and compressive for CdTe on the $CdTe - Cd_{0.5}Zn_{0.5}Te$ SLS ($\varepsilon_{||} > 0$).

tals, reciprocal lattice vectors can be calculated using equations (1.10) and (1.6). Figures 2.26 (b) and (c) show the corresponding relative positions of the (004) and (115) reflections. Since $\nu_{2D} > 1$ for all materials which were analyzed in this work, the strain-induced shift of the epilayer reflection (arrow) is larger than the separation between substrate and unstrained epilayer (dashed line). With increasing relaxation, the epilayer peak moves along the arrow. If the strain-free lattice constant a_l and elastic constants c_{ij} of the epilayer are known, r can be calculated from the relative positions of the (004) reflection of substrate and epilayer. Otherwise, the degree of relaxation r can be deduced from the relaxation angle α, linearly increasing from $\alpha = 0°$ ($r = 0$) to $\alpha = \arctan(\sqrt{2}/5) \approx 15.8°$ ($r = 1$).

The first set is a series of HgTe bulk layers with $55\,\text{nm} \leq d \leq 1000\,\text{nm}$, grown on commercial CdTe substrates. The in-plane strain $\varepsilon_{||}$ is shown in figure 2.27 as function of inverse layer thickness d^{-1}. As expected, $\varepsilon_{||}$ is constant ($\varepsilon_{||} = f$) until relaxation sets in at a critical thickness d_c. We find $d_c \approx 155\,\text{nm}$, slightly higher than the value reported in Ref. [26] (130 nm). This again shows that, whereas the approximate characteristics of strain and relaxation behavior seem to be universal, the detailed results still depend on

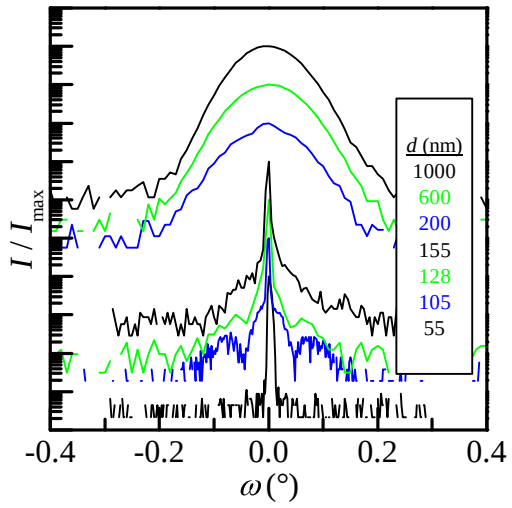

Figure 2.28: HRXRD scans in ω direction of the (004) reflection of HgTe layers with different thicknesses grown on CdTe. Data is normalized and offset for clarity.

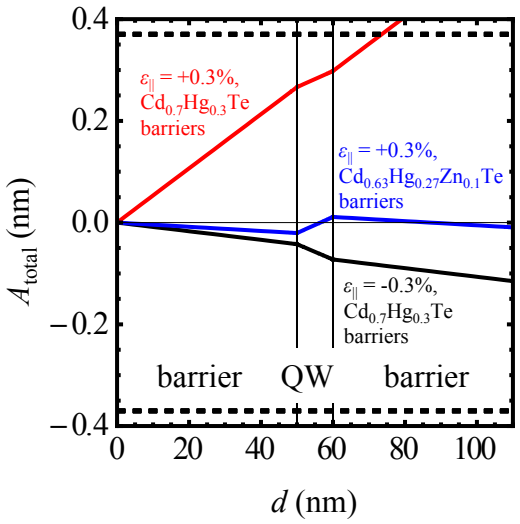

Figure 2.29: Strain-thickness product of a symmetric QW with $d_{\mathrm{QW}} = 10\,\mathrm{nm}$ and $d_{\mathrm{barrier}} = 50\,\mathrm{nm}$. Notes in figure depict strain in QW and composition of barrier solid solution. Dashed lines indicate estimated threshold value A_{CdTe} at which relaxation sets in.

the experiment (here most likely the growth conditions). Since the strain is relieved by the formation of crystal defects, the width of the HRXRD layer peak increases abruptly in ω-direction as soon as $d > d_{\mathrm{c}}$ (see figure 2.28). This demonstrates that relaxation in the heterostructure is highly undesirable. As one can see from the plot of $\varepsilon_{||}$ versus d^{-1} (figure 2.27), a linear dependency $\varepsilon_{||} \propto d^{-1}$ fits the data for $d > d_{\mathrm{c}}$, and the overall trace supports a relaxation behavior following equation (1.11). With equation (1.11) confirmed, further conclusions can be drawn regarding the scaling of the critical thickness as function of the lattice mismatch (figure 1.4). With equation (1.9), one can substitute d_{c} by f in equation (1.11), and by assuming $\varepsilon_{\mathrm{res}} \ll f$, one finds

$$\varepsilon_{||} = \frac{A}{d}\, f^{1-\alpha} \tag{2.15}$$

for $d > d_{\mathrm{c}}$. From the data presented in Refs. [24, 25] [figure 1.4 (a)] one can infer that $\varepsilon_{||}$ is independent from f in this regime, which means that $\alpha = 1$. With this result, the scaling of the critical thickness of the $Cd_{1-x}Hg_xTe$ material system (equation (1.9)) becomes simply

$$d_{\mathrm{c}} = \frac{A}{f}. \tag{2.16}$$

The parameter A is often referred to as "strain-thickness product", and depicts the "amount of strain" a crystal can stand, before relaxation sets in. For HgTe on CdTe, we have $A_{\mathrm{HgTe}} \approx 0.48\,\mathrm{nm}$.

As already mentioned in section 1.3, it is not entirely clear if the $Cd_{1-x}Hg_xTe$ is more robust against compressive strain than against tensile strain. This issue is adressed in the second set of samples. CdTe epilayers with different thicknesses $108\,\mathrm{nm} < d < 270\,\mathrm{nm}$ have been grown on a SLS with $a_{\mathrm{SLS}||} = 6.463\,\text{Å}$. Hence, strain is compressive, with $f = +0.29\,\%$. Even though strained CdTe epilayers are not present in all-in-situ QWs, we have decided to study compressive strain in these layers instead of in $Cd_{1-x}Hg_xTe$ barrier material. This is done for two reasons. Firstly, just as for HgTe layers, the analysis of binary crystals is more straightforward, since the strain-free lattice constant is known, and the level of relaxation can be calculated directly from the (004) layer-substrate peak separation [figure 2.26 (b)]. Secondly, to compare layers with different thicknesses, the sample has to be exposed to air, either to cleave the SLS substrate in several pieces, or to load- and unload it between growth- and HRXRD analysis cycle. Any of these two approaches has to be followed by the usual HCl wet-etching step to deoxidize the surface again. This would require the growth of a CdTe buffer layer before the actual $Cd_{1-x}Hg_xTe$ layer, since the latter does grow very poorly directly on substrates which have been prepared by wet-chemistry etching (section 2.5.1). The onset of relaxation would then depend on the total strain energy such a bilayer system, and would not yield direct information on the critical thickness of the $Cd_{1-x}Hg_xTe$ layer itself.

The in-plane strain of the CdTe layers grown on the SLS is shown in figure 2.27 as empty dots. The result is qualitatively similar to the data of HgTe on CdTe. From a best fit to equation (1.11), $d_c \approx 120\,\mathrm{nm}$ is found. As the strain-thickness product is even lowered compared to HgTe on CdTe ($A_{\mathrm{CdTe}} = 0.37\,\mathrm{nm}$) there is no evidence that more compressive strain than tensile strain can be applied to the crystal before relaxation sets in. It has to be emphasized, though, that the crystal quality of SLS is inferior compared to commercial CdTe substrates, with respect to surface roughness and defect density (see section 2.4.4). Since most relaxation mechanisms require a sufficient amount of preexisting crystal defects, the value of A will also, to some extend, depend on the substrate quality.

With the knowledge presented in the previous sections, we now address the problem of the coherent growth of QW heterostructures. To obtain a qualitative picture of the critical thickness of standard sample layouts, we assume that equation (2.16) holds for stacks of k layers with individual mismatches f_i and thicknesses d_i, i.e. relaxation does

not occur as long as

$$A_{\text{total}} = \sum_{i=1}^{k} d_i \, f_i \; < \; A_{\text{CdTe}}. \tag{2.17}$$

The lower strain-thickness product A_{CdTe} was chosen as upper limit. Figure 2.29 illustrates the strain-thickness product as function of increasing sample height for three different sample designs. The layer stack is similar: $d_{\text{barrier}} = 50\,\text{nm}$ (symmetric) and $d_{\text{QW}} = 10\,\text{nm}$. The black trace shows A_{total} for a QW grown on a CdTe substrate ($\varepsilon_{||,\text{Hg}} = -0.3\,\%$). Due to the small lattice mismatch between barriers and substrate, the stack layout is far from critical. If, however, the same structure is grown on a SLS with inverted mismatch ($\varepsilon_{||,\text{Hg}} = +0.3\,\%$, red trace), the critical thickness is exceeded, and relaxation will occur. Since we cannot rule out that chemical processing or additional thermal stress during cooldown in a cryostat initiates relaxation at even lower strain-thickness products, the maximum A_{total} was further limited to approximately $0.5\,A_{\text{CdTe}}$ in QWs intended for magnetotransport experiments. Therefore, compressively strained QWs with standard $Cd_{0.7}Hg_{0.3}Te$ barriers are always fabricated with very low barrier thicknesses (see sections 5.2 and 5.3).

2.5.4 Zn in barrier layers

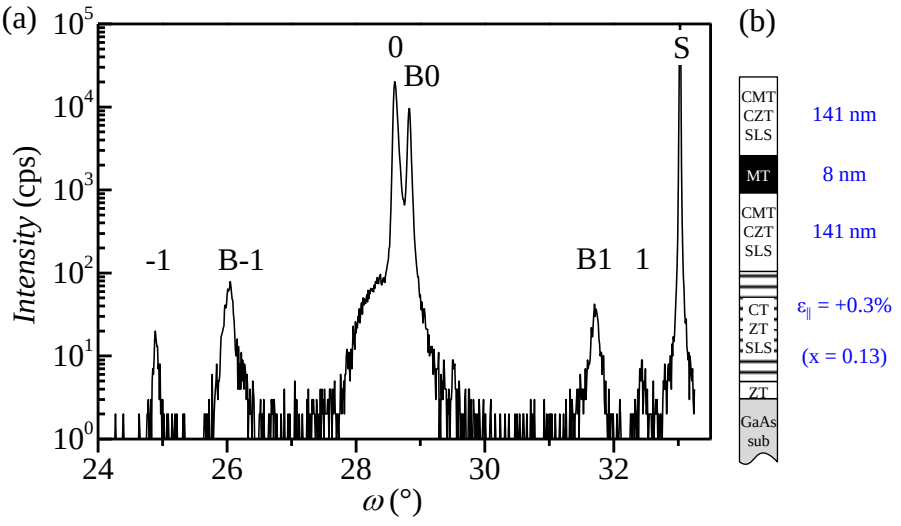

Figure 2.30: (a) $\omega - 2\theta$-scan of the (004) reflection of a symmetric heterostructure with SLS barriers on a SLS substrate. substrate reflection is labelled "S", substrate bragg- and satellite reflections "0" and "±1", barrier bragg- and satellite reflections "B0" and "B±1". (b) layer stack of the sample.

The easiest approach to avoid relaxation of barriers is to lower their thickness. However, it is known that the magnetotransport properties of QWs benefit from a large spacing to impurities, which may be introduced by e.g. a doping layer in the bottom barrier or by defects on the sample surface. Also, considering highly compressed QWs, it is questionable if coherent epitaxy of standard $Cd_{0.7}Hg_{0.3}Te$ barriers is possible at all, keeping in mind the previously discussed transition to Stranski-Krastanov growth at high mismatches (section 1.2). An optimized sample design would therefore feature barriers with the lattice constant adapted to the SLS substrate, which then can be grown in any thickness without increasing A_{total}. This adaptation can be realized by adding Zn to the barriers. As an example, a compressively strained $50-10-50$ nm QW with barriers consisting of $Cd_{0.63}Hg_{0.27}Zn_{0.1}Te$ is shown as blue trace in figure 2.29. Due to the almost perfect lattice match of barriers and SLS, the strain-thickness product is the lowest of the three structures shown. To achieve such a lattice match, the incorporation of Zn in the barriers of the QW has been attempted in various ways:

- At first, it was tried to grow the quaternary alloy by simply adding a low Zn flux from a evaporation cell filled with elemental Zn during standard barrier growth. This resulted in a poor RHEED signal already for very low Zn fractions incorporated.

- Some improvement was achieved by adding Zn in a pseudo-ALE fashion. While Hg flux was maintained, the compound CdTe and elemental Zn cells were opened alternatingly. Due to the low growth temperature, the Zn deposition was not self limiting, and therefore Zn exposure was kept short. This resulted in SLS with periods consisting of $Cd_{0.70}Hg_{0.30}Te$ and $Zn_yHg_{1-y}Te$. By choosing proper shutter sequences, this method did yield barriers with total Zn fractions of up to 10 % before the RHEED signal began to degrade.

- Because of the fact that standard $Cd_{0.70}Hg_{0.30}Te$ barriers are grown most reliably by evaporating CdTe from a single CdTe compound effusion cell, the Zn cell was replaced by a compound ZnTe cell. Just as before, the best layers were produced by growing SLS instead of quaternary solid solutions, i.e. opening CdTe and ZnTe alternatingly.

Using the last approach, layers with a promising RHEED signal have been produced. Figure 2.30 (a) shows the HRXRD diffraction pattern of a heterostructure with both the substrate and the QW barriers realized as SLS. The corresponding layer stack is illustrated in figure 2.30 (b) (note that in sketches of layer stacks with SLS substrates, the composition x of a $Cd_{1-x}Zn_xTe$ with the same lattice constant is given as orientation). Satellites

of both the artificial substrate SLS (labelled "±1") as well as the two barrier SLS (labelled "B±1") are clearly seen, and allow for calculation of the periods p. The number of SLS cycles of bottom- and top barrier was 80 each, and with its period $p_{\mathrm{barr}} = 17.6\,\text{Å}$, a total barrier thickness of 141 nm is deduced. The shoulder at the left of the SLS "0" reflection is caused by the QW. Remarkably, due to the large mismatch to substrate and barriers, it is directly visible in the measurement, despite its low thickness compared to the barriers. The relative positions of the two Bragg reflections of artificial substrate and barriers ("0" and "B0") indicate that the Zn-fraction of the barriers even exceeds the amount needed for lattice-matching. If one assumes that the growth using the ZnTe cell results in a solid solution with a composition similar to the one using the CdTe cell, i.e. $Zn_{0.7}Hg_{0.3}Te$, the total composition of the barriers can be approximated from their reflection as $Cd_{0.54}Zn_{0.16}Hg_{0.3}Te$. Magnetotransport data of this layer is shown in section 5.4. The successful incorporation of Zn into the barriers encouraged us to produce a set of heavily compressed QWs with narrow SLS barriers based on the same approach. The largest compressive strain we achieved was $\varepsilon_{||} = +1.4\,\%$. Transport measurements of this sample are shown in section 5.3.

2.6 Strain-engineering of HgTe bulk layers

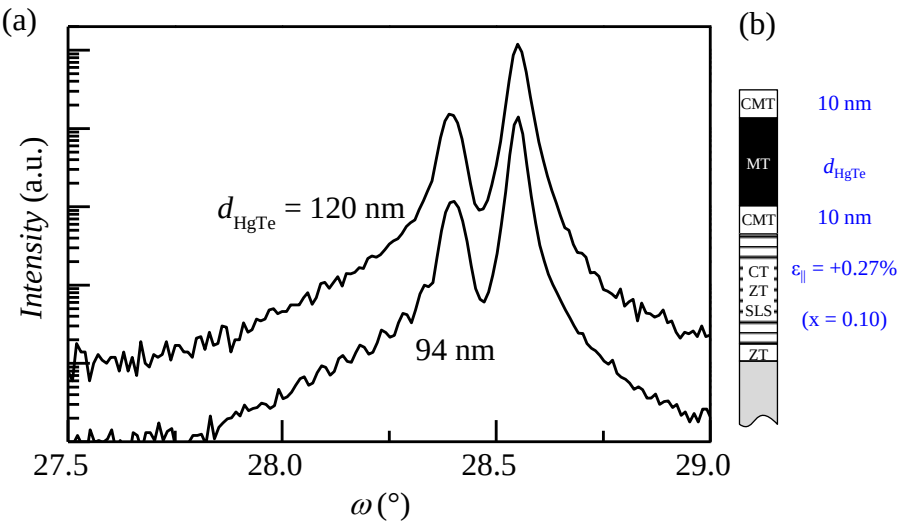

Figure 2.31: (a) $\omega - 2\theta$-scan of the (004) reflection of two compressively strained bulk layers. Measurements are offset for clarity. Labels denote different thicknesses of the HgTe layer as illustrated in (b), the layer stack of the sample.

To cover the whole spectrum of strain-engineered samples which were produced in

the course of this work, we briefly summarize the growth of strain-engineered bulk layers of HgTe. In these samples, the sequence of layers is similar to QWs, and so is the growth procedure. However, since the thickness of the active HgTe layer is much larger compared to QWs (typically, $d_{\mathrm{HgTe}} \propto 70 - 100$ nm), and the barrier thickness is usually lowered ($d_{\mathrm{barr}} \propto 0 - 20$ nm), the strain-thickness product A_{total} [equation (2.17)] is dominated by the HgTe layer. The HRXRD diffraction pattern of two such layers is shown in figure 2.31 (a). The SLS are designed such that they compressively strain the HgTe layer ($\varepsilon_{||} = +0.27\,\%$). The layer stacks are similar, except for the different thickness d_{HgTe} of the HgTe layer [figure 2.31 (b)]. The strain-thickness products of the whole heterostructures are $A_{\mathrm{total}} = 0.34\,\mathrm{nm}$ and $0.42\,\mathrm{nm}$ for the structures with $d_{\mathrm{HgTe}} = 94\,\mathrm{nm}$ and $120\,\mathrm{nm}$, respectively. The onset of relaxation is seen in the thick sample by the absence of thickness fringes, which are still observed in the narrow sample. Given the fact that the two A_{total} enclose the critical value for compressed CdTe ($A_{\mathrm{CdTe}} = 0.37\,\mathrm{nm}$, see section 2.5.3), this observation is plausible. Due to the strain-induced modification of the band structure of compressively strained bulk HgTe material (section 3.2), the system is predicted to exhibit Weyl-fermionic states [11]. First magnetotransport signatures of these states are presented in section 5.5.

Chapter 3

The band structure of HgTe

The coherent growth HgTe epilayers on SLS provides a method to control the strain in the HgTe in a very flexible manner. We now discuss the influence of this new degree of freedom on the band structure strained epilayers. Therefore, the most important aspects of the band structure of $Cd_{1-x}Hg_xTe$ are outlined, and the strain-induced shift of bulk bands is shown. In QWs, the two-dimensional band dispersion is determined by the thickness of the QW and its state of strain. The interplay of these aspects is analyzed in larger detail.

3.1 Band structure of bulk solid solutions

The composition dependence of the band dispersion of $Cd_{1-x}Hg_xTe$ bulk material was first adressed theoretically by Harman et al. [102]. The main qualitative results are shown in figure 3.1. The band structure of pure CdTe [figure 3.1 (a)] is typical for semiconductors of the zincblende-type, such as CdTe, GaAs or Si. The states in the conduction band are of Γ_6-type, i.e. have s-type symmetry, and $j = 1/2$ total angular momentum. The states in the valence band are Γ_8, p-type and have $j = 3/2$ angular momentum. The light- and heavy hole bands are degenerate at $\mathbf{k} = 0$ due to the cubic symmetry of strain-free crystals. Because of spin-orbit interaction, the Γ_7 band ($j = 1/2$) is energetically lowered by the spin-orbit splitting energy $\Delta_{so} \approx 1\,\mathrm{eV}$ [103]. In contrast, the energetic ordering of the Γ_6 and Γ_8 bands is inverted in HgTe [figure 3.1 (c)]. Therefore, if defined as energetic separation between the Γ_6 and Γ_8 bands, the band gap of HgTe is negative, with $E(\Gamma_6) - E(\Gamma_8) = -0.3\,\mathrm{eV}$ at $T = 0\,\mathrm{K}$. The reason for the inversion are relativistic corrections to the Hamiltonian, which are particularly pronounced in HgTe, due to the heavy Hg atoms [100]. In intrinsic crystals, the light-hole Γ_8 band is fully occupied, i.e. is the valence band, and the heavy-hole Γ_8 band is the conduction band. Since the two bands are degenerate at $\mathbf{k} = 0$, HgTe is described more accurately as "zero-gap" material. Band

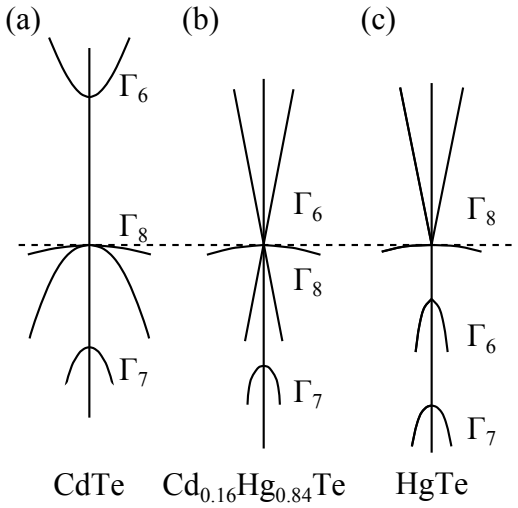

Figure 3.1: Sketch of the band dispersion around $\mathbf{k} = 0$ and $T = 0\,\mathrm{K}$ for different compositions x in $Cd_{1-x}Hg_xTe$. Dashed line indicates Fermi level of intrinsic material. From [100] (modified).

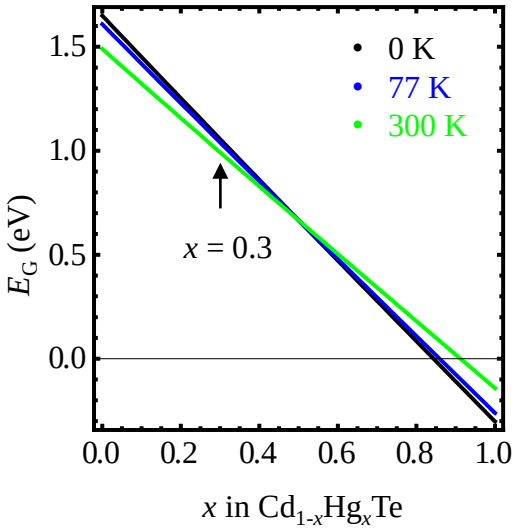

Figure 3.2: Band gap E_G as function of composition in $Cd_{1-x}Hg_xTe$ for different temperatures. Arrow indicates value for QW barriers ($x = 0.3$). Data from [101].

structure properties of $Cd_{1-x}Hg_xTe$ solid solutions can be obtained to a good accuracy by linear interpolation of HgTe and CdTe values [104]. In particular, the band gap can be adjusted with the composition x (figure 3.2). The energetic inversion of the Γ_6 and Γ_8 bands is the key property which turns HgTe into a topological insulator material. The adiabatic lifting of the band inversion at an interface to a material with non-inverted band ordering, such as HgTe-CdTe or HgTe-vacuum necessarily comes along with the closing of the band gap, both at the surface of a strained bulk crystal, or at the edge of a QW.

3.2 Strain in HgTe bulk layers

The influence of strain on the band dispersion of bulk HgTe layers has been studied theoretically by Liu et al. [105]. Applying uniaxial strain to the HgTe crystal lowers its symmetry and lifts the degeneracy of valence- and conduction band at $\mathbf{k} = 0$. An analytical expression for the energies of valence- and conduction band is given as

$$E_{\mathrm{CB,VB}}(k) = A\,k^2 \pm \left[B^2k^4 - C^2\left(k_{||}^2k_{\perp}^2 + \frac{1}{8}k_{\perp}^4(1-\cos 4\phi)\right) + \Delta^2 - B\,\Delta\left(2\,k_{||}^2 - k_{\perp}^2\right)\right]^{1/2}. \tag{3.1}$$

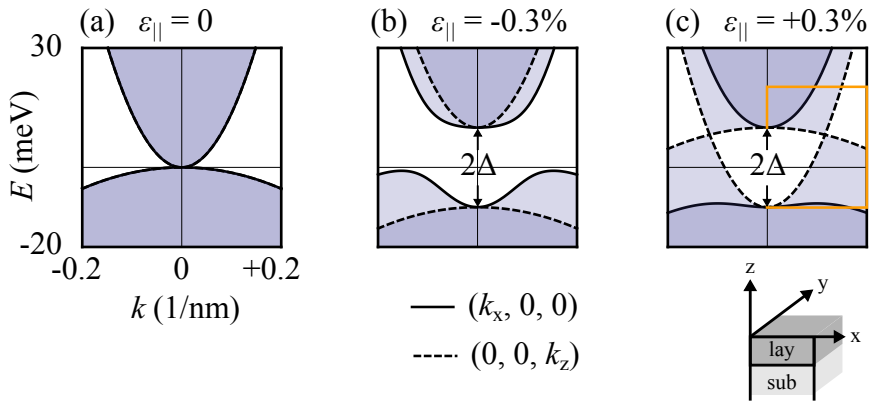

Figure 3.3: Energy dispersion of bulk HgTe material. (a) strain-free, (b) biaxial tensile strained and (c) biaxial compressively strained. In-plane dispersion along $\mathbf{k}_y$ is similar to dispersion along $\mathbf{k}_x$ (see sketch of sample) and is therefore not shown. The regime in the orange frame is shown again in figure 3.4 (a)

A, B, and C are material parameters (see appendix section A). The plus and minus sign in $\pm$ correspond to conduction- and valence band, respectively. The value of Δ depends on the magnitude of the strain, and is half of the energy separation between the conduction- and valence band at $\mathbf{k} = 0$. Equation (3.1) is discussed in Ref. [105] for externally applied uniaxial stress. To adopt it to epitaxially grown crystals, we make use of the equivalence of uniaxial and biaxial stress if their sign is changed [106], and align $k_{||}$ in the x-y-plane (see sketch in figure 3.3). Then, ϕ is the angle between $k_{||}$ and one high symmetry direction in the plane, and Δ is approximately $-11\,\text{meV}$ for $\varepsilon_{||} = -0.3\,\%$ [10]. Energy dispersions calculated using equation (3.1) are shown in figure 3.3 for different amounts of in-plane strain $\varepsilon_{||}$. As mentioned earlier, HgTe is a semimetal for $\varepsilon_{||} = 0$. Conduction- and valence band touch at $\mathbf{k} = 0$ [figure 3.3 (a)]. For tensile strain $\varepsilon_{||} < 0$, a finite energy gap E_G opens, and a pronounced anisotropy for in-plane versus out of plane direction of $\mathbf{k}$ emerges [figure 3.3 (b)]. With the strain-induced energy gap of $E_G \approx 11\,\text{meV}$, and the persisting inversion of the Γ_8 and Γ_6 bands, it was found that bulk HgTe grown on CdTe is a three-dimensional topological insulator, with an insulating bulk and gapless two-dimensional surface states [10, 107–109].

Due to the circumstance that Ref. [105] was published roughly 20 years before the discovery of topological insulators, the observation of a simple opening of a bulk gap was not in the focus of attention. Instead, the effect of uniaxial tensile strain (corresponding to biaxial compressive strain $\varepsilon_{||} > 0$) was discussed in greater detail. As illustrated in figure 3.3 (c), this situation causes a crossing of the two bands at two separate points in the bulk Brillouin zone. The induced change of sign of the effective mass of hole-like carriers

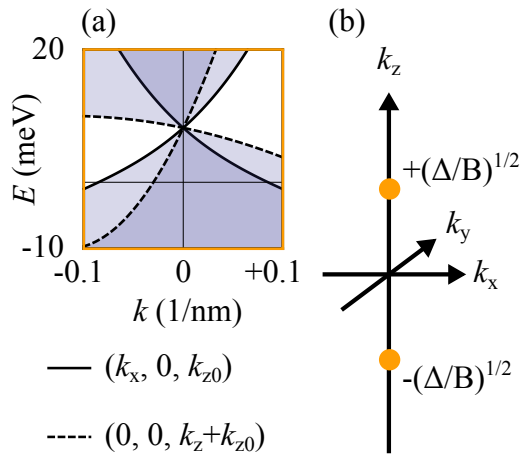

Figure 3.4: (a) Energy dispersion of biaxial compressively strained HgTe around $(0,0,k_{z0})$. Dispersion along $\mathbf{k}_y$-direction is similar to $\mathbf{k}_x$ direction. (b) The zero-gap points in k-space.

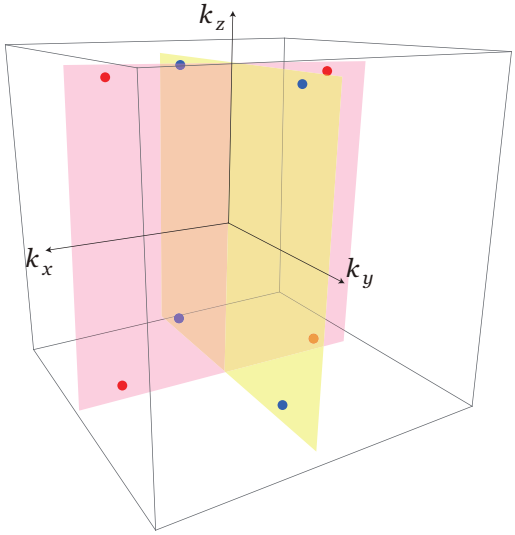

Figure 3.5: Due to the bulk-inversion-asymmetry, each zero-gap point in k-space splits into four Weyl points. From [11].

is speculated to give rise to a negative differential resistance in the I-V curve [105]. To the best of the author's knowledge, this characteristic has not been confirmed experimentally, and the peculiar band dispersion of compressed bulk HgTe was not studied further until the topics of topology and, in particular, Weyl fermions emerged in condensed matter research [110]. Originally proposed by H. Weyl as elementary particles [111], Weyl fermions can be realized as quasiparticles in crystals with appropriate band dispersion. The Brillouin zone of such crystals features distinct non-degenerate nodes at $\mathbf{k}_i$ where the energy gap vanishes, and the dispersion is linear, i.e. $E(\mathbf{k}) \propto |\mathbf{k} - \mathbf{k}_i|$. Based on the work of Liu et al. [105], Ruan et al. proposed that compressively strained bulk HgTe is a possible host of Weyl fermions [11]. Their reasoning is summarized as follows: The crossing of conduction- and valence band of HgTe with $\varepsilon_{||} = +0.3\,\%$ is shown in figure 3.4 (a). One can see that the energy dispersion is linear in all $\mathbf{k}$-directions around the nodal points $(0,0,\pm k_{z0})$, with $k_{z0} = (\Delta/B)^{1/2}$ [figure 3.4 (b)]. Since the states are still degenerate at these points, the system resembles a Dirac metal. This, however, does not describe the situation accurately, since Ref. [105] explicitly neglects the inversion asymmetry of the HgTe zincblende crystal. As demonstrated in Ref. [11], this asymmetry causes the two node points to split into four points each, located at $(\pm k_x^*, 0, \pm k_z^*)$ and $(0, \pm k_y^*, \pm k_z^*)$ (figure 3.5), which are identified as Weyl nodes. With the growth techniques established in

this thesis, it is possible to fabricate structures which feature the correct strain configuration to host these nodal points, just as suggested in Ref. [11]. First samples are shown in section 2.6, measurements are presented in section 5.5.

3.3 Band structure calculation of HgTe quantum wells

We now turn to the discussion of the band structure of two-dimensional HgTe based systems. In Ref. [112], an algorithm for the calculation of QW band structures has been developed, showing results in good agreement with experimental data [113]. The code is able to take into account various experimental parameters, such as $Cd_{1-x}Hg_xTe$ composition x of both QW and barriers, potential gradients due to doping or gating, device temperature, QW thickness and QW strain. In the following, we present a detailed overview of the most striking dependencies. We will particularly focus on the influence of strain, which has hardly been covered in Ref. [112]. Barrier composition is kept fixed to $Cd_{0.7}Hg_{0.3}Te$. The potential gradient in growth direction, lifting the degeneracy of spin up and down due to Rashba-type spin-orbit interaction [114], is assumed to be zero. This is justified, as long as the samples in consideration do not feature heavy asymmetric doping close to the QW or an electric field induced by a top gate very close to the QW. Except for section 3.3.3, where the temperature dependence is studied explicitly, the temperature is set to $T = 0\,\mathrm{K}$ in the calculations.

3.3.1 Influence of quantum well thickness

HgTe QWs are realized as thin slabs of HgTe sandwiched in between $Cd_{1-x}Hg_xTe$ barriers (usually $x = 0.3$). Phenomenologically, the thickness of the QW (d_{QW}) influences the band structure of the system in two different ways:

- For sufficiently low layer thickness, any crystalline epilayer undergoes a transition from bulk material to a QW. When the electron is confined in z-direction, k_z is no longer a good quantum number, and a two-dimensional electron gas (2DEG) is formed. Each bulk band splits into multiple subbands. The energetic separation between the subbands increases with decreasing QW thickness.

- The wavefunction of electrons in the QW penetrates into the barriers. Therefore, the subband energetic order resembles the scheme of the barrier material for very narrow QWs, and the one of HgTe for wide QWs. Since the Γ_6 - Γ_8 ordering flips from QW to barrier material, the same happens with the lowest conduction- and highest valence band at a critical QW thickness d_{c}.

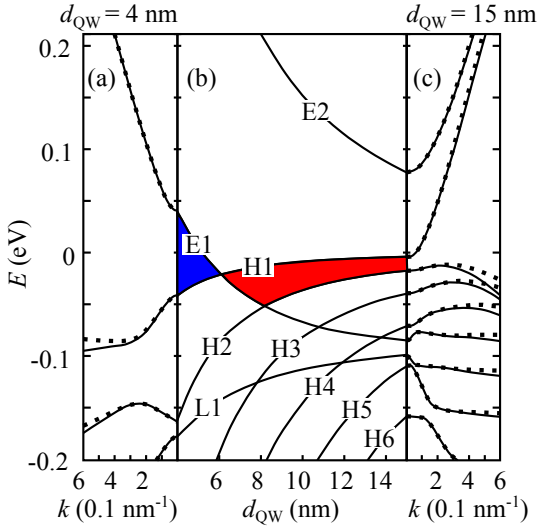

Figure 3.6: (a) Band structure of a strain-free QW with $d_{QW} = 4\,nm$. (b) Subband energies at the Γ-point as function of d_{QW}. Blue and red areas indicate normal and inverted regime. (c) Band structure of a strain-free QW with $d_{QW} = 15\,nm$. Solid and dashed lines in (a) and (c) denote **k**-vectors parallel to (100) and (110) respectively. From [112] (modified).

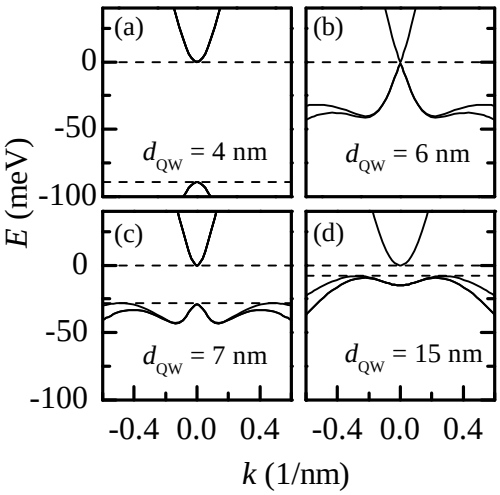

Figure 3.7: (a)-(d) Energy dispersions of strain-free HgTe QWs for different d_{QW}, indicated in the figure. Dashed lines indicate thermal band gap. Two lines of valence band dispersion denote (100) and (110) crystal directions - the (110) dispersions bend more upwards.

These two aspects are illustrated in figure 3.6. The energies of the subbands of a strain-free QW at $\mathbf{k} = 0$ are displayed in figure 3.6 (b) as function of d_{QW}. Energy dispersions of QWs with $d_{QW} = 4\,nm$ and $15\,nm$ are shown in figure 3.6 (a) and (c). The energy separation between the subbands is notably larger for the narrow QW. Let us add some remarks regarding nomenclature: The subbands are named according to convention in the literature [112]. For low d_{QW}, the names reflect the characteristics of the subbands, i.e. the largest bloch component of the "E1" band is Γ_6-type. Whereas for the "E" and "L"-type bands a mixing of bloch components occurs and, at large d_{QW}, the largest component of the E1 band is in fact light-hole Γ_8-type, the "H" bands are always fully heavy-hole Γ_8-type at $\mathbf{k} = 0$ (at finite **k**, a mixing of states occurs as well). Examples of subband characteristics are depicted in figure 3.9, and will be discussed in section 3.3.2. The aforementioned inversion of the energetic order of bands is highlighted by different colors in figure 3.6 (b). In the blue regime, the lowest conduction band is the Γ_6-type E1 band, and the highest valence band is the H1 band, similar to the band ordering of "normal" zincblende heterostructures, such as GaAs-AlGaAs QWs. In the red regime, the lowest

conduction band, H1, is heavy-hole Γ_8-type. This is the inverted regime. The transition to a non-inverted band ordering at the edge of the sample leads to the formation of gapless edge states.

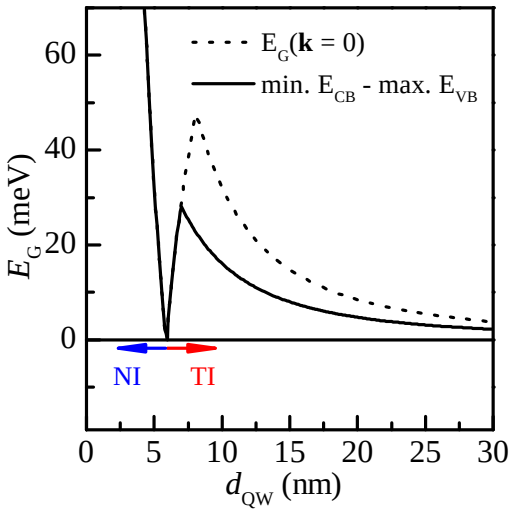

Figure 3.8: Band gap of strain-free QW as function of d_{QW}. Dotted line is energy gap at Γ-point. Solid line shows distance between minimum of conduction band and maximum of valence band. Arrows indicate normal-insulator and topological-insulator regime.

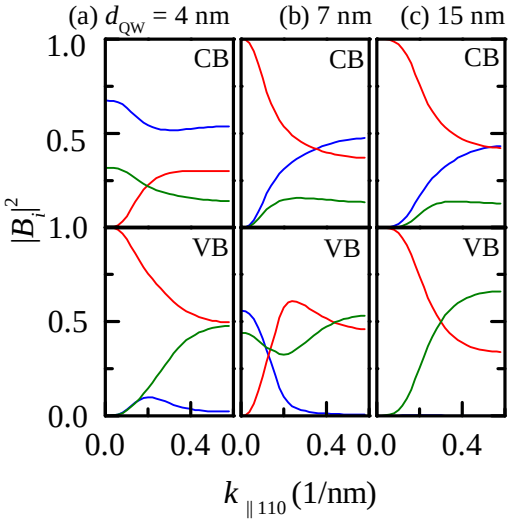

Figure 3.9: Bloch components of the conduction- and valence band (CB and VB) of 4 nm QW (a), 7 nm QW (b) and 15 nm QW (c). Color-coding: blue: $\Gamma_{6\pm1/2}$, red: $\Gamma_{8\pm3/2}$ and green: $\Gamma_{8\pm1/2}$. Wave vectors along (110)-direction.

Energy dispersions at characteristic QW thicknesses are given in figure 3.7. In the normal regime, the system is a direct band gap semiconductor [figure 3.7 (a)]. Large band gaps can be achieved in very narrow QWs, where no surface states exist. At the critical thickness $d_{\mathrm{QW}} = d_{\mathrm{c}}$, the band gap vanishes, and the energy dispersion is linear around the charge-neutrality point [figure 3.7 (b)]. In the inverted regime, the valence band dispersion exhibits anisotropic camel-back features, which limit the maximum bandgap and cause the gap to be indirect. Figure 3.7 (c) shows the dispersion at $d_{\mathrm{QW}} = 7\,\mathrm{nm}$, where the direct and indirect band gaps are identical and the latter is largest in the inverted regime. For even larger d_{QW}, the highest valence band is the H2 band [figure 3.6 (b)], and both the gap at $\mathbf{k} = 0$ and the indirect gap go down [figure 3.7 (d)]. The thickness dependencies of the indirect and direct band gap are shown in figure 3.8. For the strain-free system, the maximum band gap in the inverted regime is $E_{\mathrm{G}} = 28\,\mathrm{meV}$ at $d_{\mathrm{QW}} = 7.0\,\mathrm{nm}$, and the critical thickness is $d_{\mathrm{c}} = 6.0\,\mathrm{nm}$. Note that the conduction- and valence bands never overlap, i.e. $E_{\mathrm{G}} > 0$ for large d_{QW}. As it will be shown in the following, all these characteristics

are affected by the strain of the QW.

3.3.2 Strained quantum wells

As discussed in section 1.2, the cubic symmetry of HgTe crystals is lifted by coherent epitaxy on lattice mismatched substrates, since $\varepsilon_{||} \neq \varepsilon_{\perp}$. For bulk crystals, this lifts the heavy-hole-light-hole degeneracy (see section 3.2). In QWs, the real-space symmetry is already lifted by quantum confinement in growth direction, and the influence of strain is found in the change of position and shape of the individual subbands. Since the subband characteristics (i.e. their constituting bloch components) depend on the thickness of the QW, the strain-induced energy shift also depends on d_{QW}.

A comprehensive insight into this topic is given in Ref. [115]. Strain gives rise to an additive term H_{s} to the Hamiltonian of the strain-free system H_0, and the system is then described by

$$H = H_0 + H_{\mathrm{s}}. \tag{3.2}$$

The algorithm developed in [112] takes the Γ_6, the two Γ_8 and the split-off Γ_7 into account to calculate the full subband dispersion. Since the spin-orbit splitting energy Δ_{so} is large compared to other energy scales in the system, H and E subbands around the Fermi level are mainly composed of Γ_6 and Γ_8 components. Thus, for simplicity, the strain-effects are discussed with Γ_7 components of all wavefunctions set to zero. The numeric error is marginal at low strains ε. Choosing the usual set of basis vectors, ($|\Gamma_6,+1/2\rangle$, $|\Gamma_6,-1/2\rangle$, $|\Gamma_8,+3/2\rangle$, $|\Gamma_8,+1/2\rangle$, $|\Gamma_8,-1/2\rangle$, $|\Gamma_8,-3/2\rangle$), H can be written as a 6×6 matrix, and for (001)-oriented QWs, H_{s} becomes:

$$H_{\mathrm{s}} = \varepsilon_{||} \cdot \begin{pmatrix} -2\,C(1-\frac{c_{12}}{c_{11}}) & 0 & 0 & 0 & 0 & 0 \\ 0 & -2\,C(1-\frac{c_{12}}{c_{11}}) & 0 & 0 & 0 & 0 \\ 0 & 0 & -b(1+2\frac{c_{12}}{c_{11}}) & 0 & 0 & 0 \\ 0 & 0 & 0 & b(1+2\frac{c_{12}}{c_{11}}) & 0 & 0 \\ 0 & 0 & 0 & 0 & b(1+2\frac{c_{12}}{c_{11}}) & 0 \\ 0 & 0 & 0 & 0 & 0 & -b(1+2\frac{c_{12}}{c_{11}}) \end{pmatrix}. \tag{3.3}$$

To obtain equation (3.3) from its more general counterpart given in Ref. [115], off-diagonal strain elements ε_{ij} are assumed zero, and equation (1.6) is used. Note that equation (3.3) has been adapted to the sign convention of ε of this thesis. Deformation potentials of HgTe, $C = -3.83\,\mathrm{eV}$ and $b = -1.5\,\mathrm{eV}$ have been measured by pressure-dependent IR-absorption [116] and magnetoresistance measurements [117]. The hydrostatic deformation potential of the Γ_8 band is found to be $a = 0$ in [112], and therefore omitted

in equation (3.3). Since equation (3.3) does not have any off-diagonal components, the strain-induced energy shift of an eigenstate $|\psi_0\rangle$ of H_0 in first order perturbation simply is

$$\Delta E_\mathrm{s} \approx \langle\psi_0|H_s|\psi_0\rangle = \sum_i h_{ii}\,|b_i|^2, \tag{3.4}$$

with the diagonal elements h_{ii} of H_s, given in equation (3.3), and the coefficients b_i of the bloch states. Even though spin up- and down states are degenerate, this simple perturbative approach is possible, because matrix elements for spin up- and down are identical. It should be noted that, even though H_s is discussed perturbatively for illustration, all energy dispersions displayed in this work are obtained by directly calculating $H\,|\psi\rangle = E\,|\psi\rangle$ using the code from [112]. Usually, the difference is marginal for $\varepsilon_{||} < 0.5\,\%$, and is more pronounced if the state is not "pure" with respect to its bloch components, like for example the valence band state of a 7 nm QW [figure 3.9 (b)]. Values of the matrix elements h_{ii} are

$$\begin{aligned} h_{11} = h_{22} \qquad\qquad &= 2.45\,\mathrm{eV}\cdot\varepsilon_{||}, \\ h_{33} = h_{66} = -h_{44} = -h_{55} &= 3.54\,\mathrm{eV}\cdot\varepsilon_{||}. \end{aligned} \tag{3.5}$$

At a given $\varepsilon_{||}$, the sign of the energy shift is similar for $\Gamma_{6\pm1/2}$ and $\Gamma_{8\pm3/2}$ states, and opposite to $\Gamma_{8\pm1/2}$ states. Using equation (3.3) and equation (3.5), the strain-induced energy gap between the pure Γ_8 heavy-hole valence band, and Γ_8 light-hole conduction band at the Γ-point of bulk HgTe grown on CdTe ($\varepsilon_{||} = -0.3\,\%$) can be calculated as $2\,h_{33} = 21\,\mathrm{meV}$.

The band structure of QWs is calculated in [112] using the envelope function approach. The envelope functions $f^{(i)}(z)$ capture the symmetry-breaking in z-direction, and to perform calculations of the form of equation (3.4), the bloch components are found as $|b_i|^2 = \int |f^{(i)}(z)|^2\,dz$. Bloch components of strain-free QWs with three different thicknesses and $\varepsilon_{||} = 0$ are shown in figure 3.9. Since the effect of strain is similar for components which only differ by the sign of the m_j quantum number, the sum of those components is plotted, for example: $|B_{\Gamma6\pm1/2}|^2 = |b_{\Gamma6+1/2}|^2 + |b_{\Gamma6-1/2}|^2$. As discussed already in section 3.3.1, the conduction band of a non-inverted QW [$d_\mathrm{QW} = 4\,\mathrm{nm}$, figure 3.9 (a)] is mostly $\Gamma_{6\pm1/2}$-type, and the valence band is purely $\Gamma_{8\pm3/2}$-type at $\mathbf{k} = 0$. Since conduction- and valence band dispersions are parabola with high curvature [figure 3.7 (a)], transport is caused by carriers which reside at the vicinity of the Γ points of the Brillouin zone. By evaluating equation (3.4) for the b_i of the conduction- and valence band of the 4 nm QW, one finds $dE_\mathrm{G}/d\varepsilon_{||} \approx -3.0\,\mathrm{eV}$, i.e. the band gap E_G is lowered if the QW is compressed biaxially. However, the effect is negligible compared to the very pronounced influence of d_QW on the band gap of non-inverted QWs (see figure 3.8). With

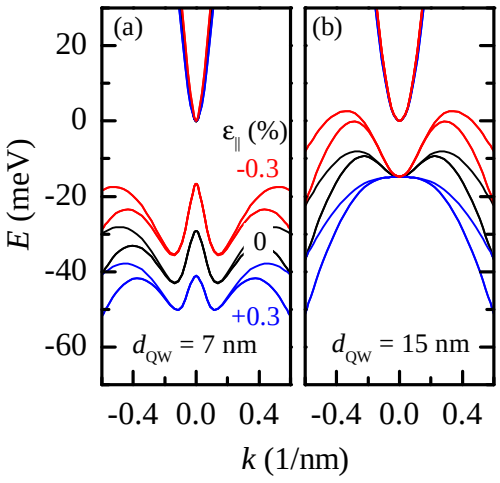

Figure 3.10: Energy dispersions of QWs with (a) $d_{\mathrm{QW}} = 7\,\mathrm{nm}$ and (b) 15 nm at different strains $\varepsilon_{||}$. Two lines of valence band dispersion denote (100) and (110) crystal directions - the (110) dispersions bend more upwards.

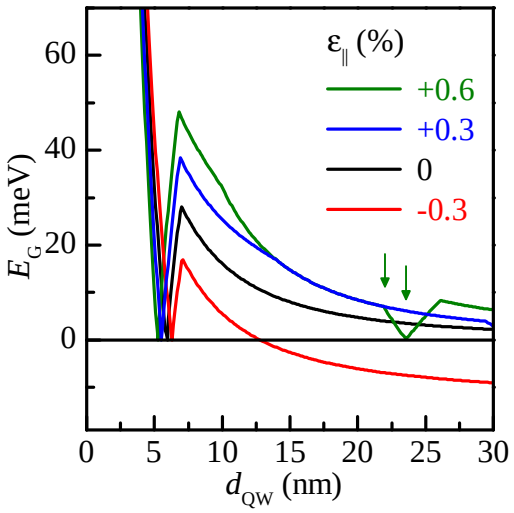

Figure 3.11: $E_G = \min(E_{\mathrm{CB}}) - \max(E_{\mathrm{VB}})$ for different in-plane strains $\varepsilon_{||}$. $\varepsilon_{||} = -0.3\,\%$ is obtained if HgTe is grown on CdTe as substrate.

increasing d_{QW}, the valence bands become highly non-parabolic, and the camel-back features become relevant for transport. The bloch components of a 7 nm QW are displayed in figure 3.9 (b), and the effect of varying $\varepsilon_{||}$ is illustrated in figure 3.10 (a). Since the fraction of the $\Gamma_{8\pm1/2}$ of the valence band states does not change significantly for varying $\mathbf{k}$ values, its shape is sustained for different $\varepsilon_{||}$. The energy gap, however, depends on $\varepsilon_{||}$, due to the different overall components of the valence- and conduction band. This characteristic changes significantly for wide QWs. Figure 3.9 (c) shows the bloch components of a 15 nm QW. Since both valence- and conduction bands are pure $\Gamma_{8\pm3/2}$-type at $\mathbf{k} = 0$, they are similarly shifted by strain. However, as the valence band becomes partly $\Gamma_{8\pm1/2}$-type with increasing $\mathbf{k}$ values, the camel-back feature is affected by $\varepsilon_{||}$, and disappears for large compressive strains [see figure 3.10 (b)].

As it was shown in the previous paragraphs, the combination of QW strain and thickness affects the band dispersion in a great number of aspects. An overview is given in figure 3.11, and figure 3.12 shows a contour-plot of the magnitude of E_{G} as function of strain and thickness. Obviously, the experimental realization of strained layers in MBE becomes more difficult as the magnitude of strain (i.e. the mismatch between substrate and QW) increases. As discussed in section 1.2, a critical mismatch f_{crit} is expected to exist, at which coherent epitaxy is no longer possible. Although no value is known to the

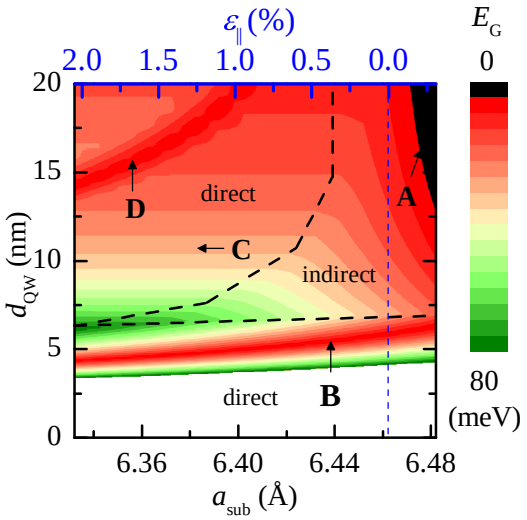

Figure 3.12: Energy gap as function of QW thickness and strain. Black dashed lines denote transition from direct band gap to camel-back-limited indirect band gap regime. Bold letters highlight characteristic features discussed in the main text. Blue dashed line shows transition from tensile to compressive strain.

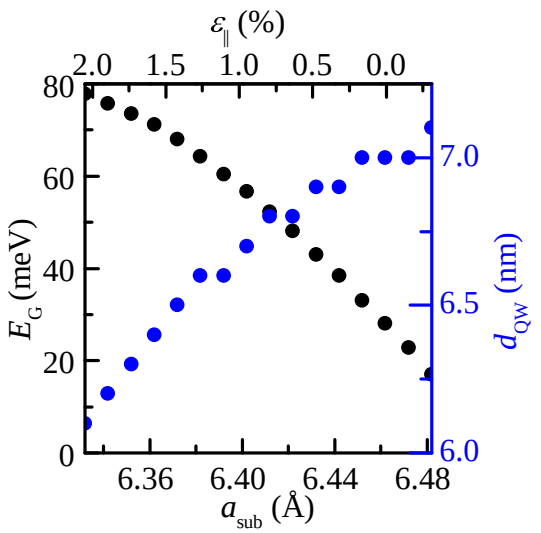

Figure 3.13: Maximum thermal energy gap in the inverted regime and corresponding QW thickness as function of strain. Datapoints were extracted from figure 3.12. Plateaus in d_{QW} reflect the resolution of the grid (1 Å).

author for the HgTe material system, it is likely to be comparable to other systems [23], and we therefore only consider $\varepsilon_{||} < f_{crit} \approx 2\,\%$. Different regimes regarding the band dispersion characteristics can be identified in the strain-thickness map shown in figure 3.12, and are labelled with capital letters. The most notable features and dependencies within this parameter range are:

- Since the camel-back feature of the valence band is suppressed by compressive strain, a transition from an indirect to a direct semiconductor occurs as $\varepsilon_{||}$ increases [black dashed lines in figure 3.12, dispersions shown in figure 3.10 (b)].

- The critical thickness which separates the normal insulator- and topological insulator regime gradually decreases as the system is compressed (red valley labelled **B** in figure 3.12).

- In the regime where valence- and conduction band are purely $\Gamma_{8\pm3/2}$-type at $\mathbf{k} = 0$, the energy gap is not affected by strain, as soon as it is direct (horizontal contours in figure 3.12, indicated by **C**).

- A second valley, resembling the normal insulator-topological insulator transition **B** is observed at wide, heavily compressed QWs (**D** in figure 3.12, kink at around 23.5 nm of green trace in figure 3.11). This is due to the E2 band, which is energetically lowered by compressive strain, and intersects the H1 band [figure 3.6 (b)]. As a consequence, one could expect a gradual transition to a very narrow regime, where the system is a normal insulator again (green arrows in figure 3.11), before the E2 band intersects the H2 band and thus the conduction band is again $\Gamma_{8\pm3/2}$-type. However, by analyzing the bloch components $|B_i|$ of this regime ($d_{\mathrm{QW}} = 22.6\,\mathrm{nm}$, $\varepsilon_{||} = +0.6\,\%$), one finds that the E2 band is mostly $\Gamma_{8\pm1/2}$-type, thus the argument is debatable.

- For wide, tensile strained layers, conduction- and valence band overlap, and the system becomes a two-dimensional semimetal (red trace in figure 3.11, black regime indicated by arrow **A** in figure 3.12). A characteristic dispersion of a 15 nm QW is shown in figure 3.10 (b) (red trace). Such systems have been investigated previously in magnetotransport experiments [118–122], and are studied in section 5.2.

- Most notably, the maximum E_{G} in the inverted regime increases considerably as the QW is compressed, and the thickness d_{QW} at which E_{G} is maximized goes down. Values of the maximum energy gap and the corresponding QW thickness are given in figure 3.13. This effect is studied in detail in section 5.3.

3.3.3 Temperature dependence of energy gap

The chapter concludes with some remarks on the temperature dependence of the band structure of HgTe QWs. Investigations on this subject have been done using infrared absorption and reflectivity measurements on HgTe-HgCdTe superlattices [123, 124]. Dependencies for transition energies between two bands have been found. Linear approximations with a constant $\kappa_{\text{band1-band2}} = dE_{\text{band1-band2}}/dT$ are given. For the H1-E1 transition, Ref. [123] reports a value of $\kappa_{\text{H1-E1}} \approx 0.3\,\mathrm{meV\,K^{-1}}$ for a layer thickness $d_{\mathrm{QW}} = 6\,\mathrm{nm}$. The influence of d_{QW} on $\kappa_{\text{H1-E1}}$ is small [123]. It should be noted that Ref. [123] only shows values of $\kappa_{\text{H1-E1}}$ for non-inverted structures, i.e. $d_{\mathrm{QW}} < d_{\mathrm{c}}$. Even though overall good agreement is found between theory and experiment, the value found for $\kappa_{\text{H1-E1}}$ at $d_{\mathrm{QW}} = 13.8\,\mathrm{nm}$ in Ref. [124] seems to be smaller than predicted theoretically. This is explained by free charge carriers, which affect the measurement of this particular transition.

Calculated band gaps of different strain-free QWs are shown in figure 3.14 for temperatures $0 < T < 100\,\mathrm{K}$. The qualitative characteristics are similar for strained structures,

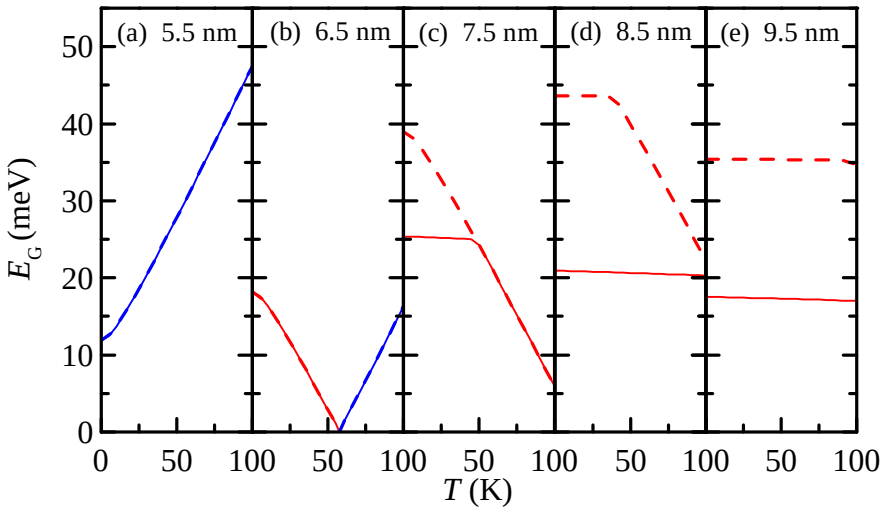

Figure 3.14: Temperature dependence of E_G for different d_{QW} with $\varepsilon_{||} = 0$. Blue and red traces indicate normal and inverted band ordering, respectively. Dashed lines show magnitude of direct energy gap at the Γ-point, solid lines $\min(E_{CB}) - \max(E_{VB})$.

however, the characteristic transition thicknesses are shifted to lower values with increasing compressive strain. E_G is temperature independent as long as the lowest conduction- and highest valence subbands are H-type [figure 3.14 (e), see figure 3.6 (b)]. The relative energy of the E1 subband rises with temperature. This first lowers the direct band gap, but does not affect the absolute value [figure 3.14 (d)]. At critically high temperatures and low d_{QW}, the absolute E_G is affected [figure 3.14 (c)] and finally, the inversion of the subbands is lifted [figure 3.14 (b)]. It should be noted that at room temperature, the band inversion in HgTe quantum wells is always lifted. Therefore, HgTe-based QSH devices working at room temperature cannot be realized, irrespective of the low-temperature energy gap. This effect is investigated experimentally in Ref. [125]. Furthermore, non-constant energy dispersions can complicate the analysis of temperature-dependent magnetotransport experiments. Therefore, care was taken in section 5.3 to design QWs for which E_G is constant over the full range of temperatures investigated.

Chapter 4

The quantum spin Hall effect

In this section, the QSH effect in HgTe QWs is introduced, and its origin in the inverted band ordering of the material system is shown (see section 3.3). After summarizing the pioneering works, which confirmed the predicted characteristics of helical QSH edge states, the focus will be on discrepancies between experimental findings and the idealized model. The most striking discrepancies are as follows: The predicted quantized edge state conductance is only observed in samples with very short edges ($\lesssim 10\,\mu m$), and the measured temperature dependence of the edge state conductance contradicts theoretical predictions on gapless helical edge states. The first of these two aspects gave one of the original motives of this thesis, as several works predict a relationship between the stability of the QSH edge states and the magnitude of the band gap. With the strain-induced control of the band gap demonstrated in the previous chapter 3, and the stability and temperature dependence of the QSH edge states discussed in chapter 5, this chapter serves as the connection between the sample engineering part and the sample performance part of this thesis.

4.1 Band inversion and the quantum spin Hall effect

After the discovery of the quantum Hall (QH) effect in two-dimensional electron gases at large magnetic fields [2], the concept of topology of bands has been introduced to explain the quantized Hall conductance σ_{xy} and, in particular, its accurate reproducibility in samples with considerably different overall characteristics. One observes

$$\sigma_{xy} = n \frac{e^2}{h}, \tag{4.1}$$

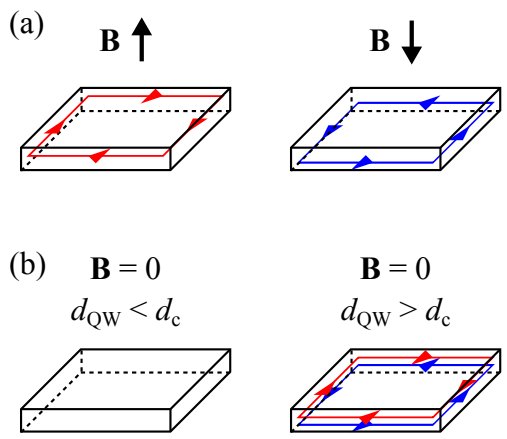

Figure 4.1: (a) Sketch of quantum Hall edge states in a 2DEG for $n = 1$. Edge states are "chiral", i.e. their direction of motion depends on orientation of magnetic field. (b) Sketch of topologically trivial and nontrivial HgTe QWs. QSH edge states are "helical", i.e. arise in counterpropagating, oppositely spin-polarized pairs.

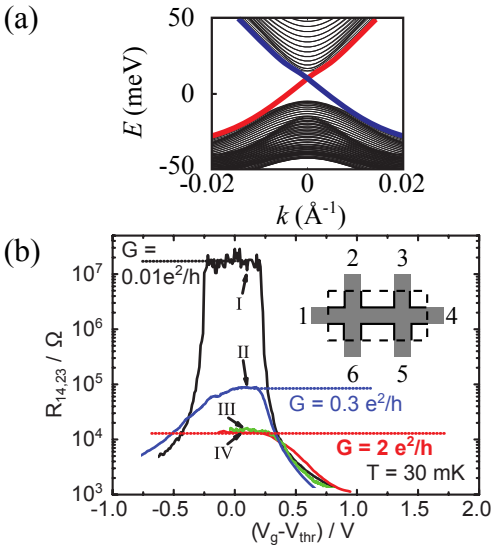

Figure 4.2: Sketch of energy dispersion of QSH edge states. Colors indicate opposite spin polarization. From [126] (modified). Longitudinal resistance of HgTe QWs of different d_{QW} and device dimensions. From [6] (modified). Inset shows measurement configuration. Dashed rectangle indicates gated area, solid lines are edge current paths.

with an integer $n \in \mathbb{N}$, and e^2/h being the inverse of the Klitzing constant $h/e^2 = R_K = 25812.8074555(59)\ \Omega$ (CODATA 2014). The quantity n is called Chern number. It counts the number of occupied Landau levels, and specifies the topology of the band dispersion. For the sake of accurateness, we note that in systems with very high carrier mobilities, additional conductance plateaus are also observed for values of n, which correspond to fractions of integers. This is called the fractional QHE [127].

In 2005 and 2006, two groups showed independently [4, 5] that one does not have to break time reversal symmetry (i.e. apply a magnetic field) to create topologically nontrivial states of matter. Instead, such states were predicted in systems with strong spin-orbit interaction, and therefore were named quantum spin Hall (QSH) edge states. Shortly afterwards, it was postulated that the gap closing in HgTe QWs (see section 3.3.1) is a topological phase transition, and that for $d_{QW} > d_c$, these systems are two-dimensional topological insulators (2DTIs) [128]. The fingerprint feature of 2DTIs are the aforementioned QSH states at the sample edge and can be pictured as superposition of two sets of $n = 1$ quantum Hall edge states with opposite direction of the magnetic field [figure 4.1 (a)

and (b), right]. In that sense, the theoretical conductance of any edge of the sample is expected to correspond to a single-mode one-dimensional channel without any scattering, i.e.

$$G_{1D} = \frac{e^2}{h}. \tag{4.2}$$

As illustrated in figure 4.2 (a), the energy dispersion of the edge states is linear at $k = 0$, i.e. $E(k) = \hbar\, v_F\, k$. The fermi velocity v_F of HgTe edge states is approximately $5 \times 10^5\,\mathrm{m\,s^{-1}}$ [129]. The width of the wavefunction of the edge states, perpendicular to its direction of propagation depends on the QW properties: In growth direction, the wavefunction is localized almost completely inside the QW [112]. Perpendicular to that, the decay length into the bulk of the QW depends on its band gap E_G. For simplicity, the wavefunction is often [7, 130] modelled as localized in a stripe at the edge with the width

$$w_{QSH} = \hbar\, \frac{v_F}{E_G}. \tag{4.3}$$

The signatures of edge states in transport experiments can be understood with the help of the Landauer-Büttiker formalism. The Landauer-Büttiker transmission matrix T [131] maps chemical potentials μ_i to currents I_i in a N-terminal device as

$$I_i = \frac{e}{h} \sum_{j=1}^{N} T_{ij}\, \mu_j. \tag{4.4}$$

Using the QH-QSH analogy, the QSH transmission matrix T_{QSH} can be calculated as the sum of two QH matrices with $n = 1$, and the magnetic field pointing in opposite directions:

$$T_{QSH} = T_{QH+} + T_{QH-} =$$

$$\begin{pmatrix} -1 & 0 & \cdots & 1 \\ 1 & -1 & & 0 \\ \vdots & & \ddots & \vdots \\ 0 & 0 & \cdots & -1 \end{pmatrix} + \begin{pmatrix} -1 & 1 & \cdots & 0 \\ 0 & -1 & & 0 \\ \vdots & & \ddots & \vdots \\ 1 & 0 & \cdots & -1 \end{pmatrix} = \begin{pmatrix} -2 & 1 & \cdots & 1 \\ 1 & -2 & & 0 \\ \vdots & & \ddots & \vdots \\ 1 & 0 & \cdots & -2 \end{pmatrix}. \tag{4.5}$$

With T_{QSH} and equation (4.4), the resulting chemical potentials can be calculated for any current that flows from terminal k to terminal l ($I_k = -I_l = I$ and $I_{i \neq k,l} = 0$), and an important difference between QH and QSH edge conductance is found: In the QH case, the measured voltage between a pair of contacts $U_{ij} = (\mu_i - \mu_j)\, e^{-1}$ only depends on whether it is possible to connect the two voltage probes by an arbitrary line inside the mesa of the sample and the two current contacts by another such line, without the two

lines intersecting each other. In contrast, in the ideal QSH case, the measured U_{ij} depends on the number of terminals N and their distribution along the edges of the device [132]. This is because an electron which enters a voltage-probe regime will scatter and loose its spin alignment with respect to the edge state from which it came from. Therefore, scattering into one of the two edge states on the interfaces between sample edge and voltage probe takes place with the same probability. For a device with the same number of terminals on opposite sides of the current path, one can define the conductance of two adjacent contacts

$$G_{\mathrm{QSH}} = \frac{I}{U_{i,i+1}} = 2\,\frac{e^2}{h} = 2\,G_{\mathrm{1D}}. \tag{4.6}$$

In particular, equation (4.6) is the conductance expected theoretically, if the longitudinal 4-terminal conductance of a standard Hall bar device is measured in the QSH regime. This configuration, often referred to as "local configuration", is the standard approach to analyze edge state conductance in the literature as well as in this thesis. Furthermore, the mechanism which protects the edge states from backscattering, i.e. justifies unity transmission coefficients in equation (4.5) is different for QH and QSH systems. In the QH case, backscattering is forbidden, since the direction of motion of carriers at a given edge is fixed by the orientation of the magnetic field ("chiral" edge states). In the QSH case, backscattering is in principle possible, since two counterpropagating channels exist on each edge. However, since the two channels are oppositely spin polarized ("helical" edge states), a backscattering event has to flip the electron spin, i.e. break time-reversal symmetry. In that sense, QSH edge channels are protected by time-reversal symmetry. It turned out that the QSH edge state protection is far less rigid than the QH one, and this will be the subject of the following sections.

4.2 Measurements on microstructures

The existence of QSH edge states was verified experimentally shortly after its theoretical prediction by König et al. [6], and since this thesis frequently refers to this work, the main findings are briefly summarized in the following. The measurements are shown in figure 4.2 (b). The longitudinal resistance R_{xx} (labelled $R_{14\,23}$ in the figure) is measured on four different Hall bar devices at $B = 0\,\mathrm{T}$ and $T = 30\,\mathrm{mK}$ as a function of gate voltage. With the Fermi level tuned into the band gap, conductance in the plane of the QW is suppressed, and QSH edge state conductance is observed. Samples III and IV are topologically nontrivial QWs ($d_{\mathrm{QW}} > d_{\mathrm{c}}$), and the measured resistance agrees well with equation (4.6): $R_{\mathrm{max}} = 0.5\,h\,e^{-2} = G_{\mathrm{QSH}}^{-1}$. Further evidence on the edge-localized nature

of the conductance is given by the fact that R_{max} does not scale with the width of the device [$w \times l = (1.0 \times 1.0)$ µm^2 for device III and $w \times l = (0.5 \times 1.0)$ µm^2 for device IV]. As expected, QSH edge states are absent in the topologically trivial device I ($d_{\mathrm{QW}} < d_{\mathrm{c}}$), where the measured R_{max} exceeds the values observed in devices III and IV by almost three orders of magnitude. This observation illustrates the convenient property of the 2D HgTe material system, that its characteristics can be changed from 2DTI to normal insulator by simply lowering d_{QW}. In many follow-up experiments, this feature has been used to prove the topological origin of a measurement feature, simply by demonstrating its absence in a topologically trivial QW. Lastly, some insight on the stability of QSH edge states is given by measurements on the larger device II [$w \times l = (20.0 \times 13.3)$ µm^2]. In this structure R_{max} significantly exceeds 0.5 R_{K}. Therefore, backscattering has to occur, despite the edge channel protection by time reversal symmetry. Numerous explanations for the backscattering mechanisms are proposed. An overview is given in section 4.3, and new findings are discussed in section 5.3.

After its existence was confirmed, the QSH state was investigated in greater detail in subsequent works. In Ref. [133], QSH edge state conductance was demonstrated in devices different from Hall bars. The validity of equation (4.4) was again confirmed. In particular, the aforementioned dependency of the measured QSH conductance on the number and arrangement of terminals N was shown, and a QSH signal in a fully nonlocal contact configuration was presented. However, the agreement between theory and experiment is limited by some statistical uncertainty, probably due to device imperfections. The spin polarization of edge states was shown in Ref. [134] in a combination of the QSH effect and the spin-Hall effect, which has been observed previously in the same material system [135].

4.3 Non-quantized conductance

As already mentioned in section 4.2, the quantization of QSH edge state conductance at $G_{\mathrm{QSH}} = 2e^2/h$ is only observed in very small devices, and the overall precision of the quantization is significantly inferior compared to QH edge states. The difference between the idealized model and actual measurements has been studied both theoretically and experimentally. However, up to now, no conclusive picture has been found. The main findings are summarized in the following. On the experimental side, parameters such as temperature, sample size and electrostatic environment have been adressed (section 4.3.1). On the theoretical side, the contributions can be divided into two groups: The first group discusses backscattering mechanisms in the channel itself, looking for

candidates that are, in contrast to single-particle elastic backscattering, not protected by time-reversal symmetry (section 4.3.2). The second group considers the possibility that the electrons couple to electron reservoirs in the vicinity of the sample edge, where the scattering protection no longer holds (section 4.3.3).

4.3.1 Experimental studies on sample size and temperature dependence

The breakdown of conductance quantization for larger samples has already been shown in Ref. [6]. Compatible observations were made in samples with higher edge channel lengths (l_{edge}). Resistances of several 100 kΩ were found for $l_{\mathrm{edge}} \approx 100\,\mu\mathrm{m}$ [136], and Ref. [137] finds $R_{\mathrm{max}} \approx 400\,\mathrm{k}\Omega$ in wide QWs ($d_{\mathrm{QW}} = 14\,\mathrm{nm}$) with $l_{\mathrm{edge}} \approx 400\,\mu\mathrm{m}$. However, the specific edge state resistivity $\rho_{\mathrm{edge}} = 2\ R_{\mathrm{max}}/l_{\mathrm{edge}}$ changes notably from one experiment to the other (the factor two results from taking into account that the current flows along both sides of the device, and it has to be assumed that the current distribution is symmetric). Ref. [138] reports on very long edge channels with $l_{\mathrm{edge}} \approx 1\,\mathrm{mm}$ and R_{max} from 0.3 to 2 MΩ, whereas Ref. [139] finds $R_{\mathrm{max}} = 230$, 500 and 1400 kΩ for short edges of only 6, 12 and 36 µm. The latter series of resistances was observed on a single device, and it is concluded, that R_{max} scales with the length of the edge channel for $R_{\mathrm{max}} \gg 2\ R_{\mathrm{K}}$, i.e. ρ_{edge} is constant. Unfortunately, the sample design used in Ref. [139] does not allow to distinguish between edge state conductance and diffusive residual bulk conductance, which, given the exceptionally high ρ_{edge}, may also be the current-carrying mechanism at hand. The observation of a constant ρ_{edge} is also made in section 5.2.2 and 5.3. However, due to a more appropriate device geometry, we are able to clearly classify the measured conductance as induced by edge states. Furthermore, we find values of ρ_{edge} that are one to two orders of magnitude lower than the ones reported in Ref. [139], further substantiating the suspicion that edge state conductance, if present at all, is strongly disturbed in Ref. [139].

The temperature dependence of the edge state conductance is a promising feature to give insight in the mechanisms causing non-quantized G_{edge} in the QSH regime, since scattering mechanisms are usually strongly temperature dependent. In Ref. [6], the close-to-quantized G_{edge} is found to increase only slightly as the temperature is raised by a factor of 60 (from 30 mK to 1.8 K), and universal conductance fluctuation (UCF) features on the plateau are washed out [figure 4.3 (a)]. This result has been qualitatively reproduced in a wide QW ($d_{\mathrm{QW}} = 14\,\mathrm{nm}$) with comparable edge channel lengths ($l_{\mathrm{edge}} \approx 5\,\mu\mathrm{m}$) [137]. Similar observations are made in the non-quantized regime [138], where G_{edge} is

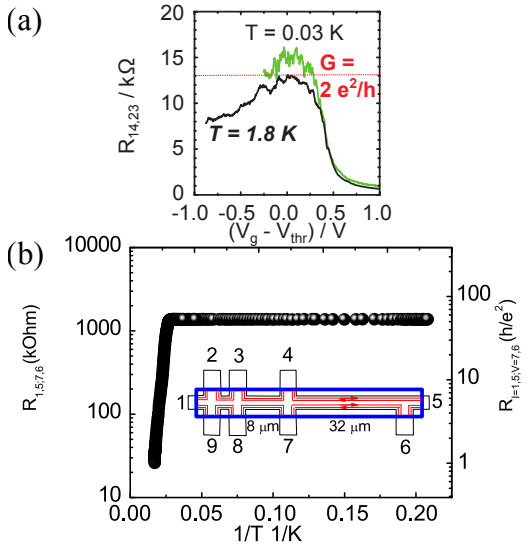

Figure 4.3: (a) QSH edge state resistance for $T = 30\,\mathrm{mK}$ and $1.8\,\mathrm{K}$. $l_{\mathrm{edge}} \approx 2\,\mu\mathrm{m}$. From [6] (modified). (b) QSH edge state resistance as function of inverse of temperature. $l_{\mathrm{edge}} \approx 36\,\mu\mathrm{m}$. Inset shows device geometry. From [139] (modified).

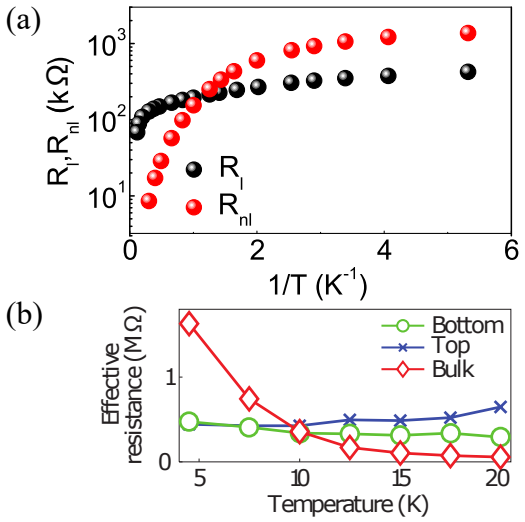

Figure 4.4: QSH edge state resistance as function of inverse of temperature, measured locally (black dots $R_{\mathrm{l}} = R_{\mathrm{max}}$) and non-locally (red dots) on a wide QW ($d_{\mathrm{QW}} = 14\,\mathrm{nm}$, $l_{\mathrm{edge}} \approx 400\,\mu\mathrm{m}$). From [137] (modified). (b) Temperature dependence of effective resistance of the bulk (red) and edge states (blue and green) of a HgTe QW in the QSH regime ($l_{\mathrm{edge}} \approx 50\,\mu\mathrm{m}$). Measured by scanning SQUID technology. From [140] (modified).

almost constant for $80\,\mathrm{mK} < T < 1\,\mathrm{K}$, and for $430\,\mathrm{mK} < T < 1.95\,\mathrm{K}$ [136], even though it is questionable if the Fermi level was adjusted fully into the band gap in the latter work. Furthermore, Ref. [139] claims to see the absence of any change in G_{edge} for $4\,\mathrm{K} < T < 20\,\mathrm{K}$, before, at higher temperatures, thermally activated bulk conductance sets in [figure 4.3 (b)]. As already noted, results of Ref. [139] are to be handled with some caution, due to the high ρ_{edge}. In contrast to this, a weak temperature dependence, $R_{\mathrm{max}} \propto T^{-0.5}$, is found for temperatures as low as $T < 0.5\,\mathrm{K}$ in a wide QW [137] [figure 4.4 (a)]. This is explained as weak localization of a one dimensional wire. However, given that the experimentally obtained energy gap is only $1.2\,\mathrm{meV}$, and that the measured G_{edge} on the $5\,\mu\mathrm{m}$ device fabricated from the same wafer is higher than $2\ e^2h^{-1}$, residual bulk conductance may be present. This interpretation is adressed in greater detail in section 5.3. In Ref. [140], the current distribution in a HgTe QW is spatially resolved using a scanning superconducting quantum interference device (SQUID) technology. Aside

from providing a very clear proof that the current is flowing along the edges as the Fermi level is tuned into the band gap, the current distribution is also investigated as function of temperature. It is found that, whereas bulk conductance freezes out at lower temperatures, ρ_{edge} remains almost constant for $4\,\text{K} < T < 20\,\text{K}$ [figure 4.4 (b)]. In Ref. [141], the backscattering mechanisms are faced from a different perspective. The QSH conductance of a QW is monitored as function of a local electrical perturbation, induced by a mobile charged tip in the proximity of the device. It is found that scattering occurs at distinct positions along the edge, which are separated by distances in the order of $1\,\mu\text{m}$. These scattering sites are identified as the aforementioned carrier reservoirs. These are local areas where the Fermi energy is in the valence- or conduction band, while the global Fermi level is in the energy gap.

In summary, despite the different sample details and experimental approaches, all works mentioned in this section indicate only a weak temperature dependence of G_{QSH}, and particularly, most of them find an increase in G_{QSH} with increasing temperature. As it will be shown in the following section, this behaviour turned out to be difficult to model theoretically.

4.3.2 Backscattering mechanisms in helical Luttinger liquids

Shortly after the discovery of quantized and non-quantized edge state conductance [6], several groups suggested theoretical explanations for these observations. The fact that single particle backscattering is forbidden due to time-reversal symmetry has already been pointed out in several pioneering works on QSH edge states [4, 142, 143], as well as the possibility of inelastic two-particle backscattering [4, 143]. Phenomenologically, backscattering modifies the conductance of a single helical edge state as

$$G_{\text{edge}} = \frac{e^2}{h} - \Delta G, \tag{4.7}$$

and an appropriate theoretical model should provide a physical mechanism which can cause a non-zero ΔG even at low temperatures, as well as reproduce the obervations discussed in section 4.3.1, at least qualitatively. Since the picture of almost free quasiparticles with an effective mass breaks down for systems with a dimensionality lower than two, one dimensional edge channels are frequently analyzed within the framework of Luttinger liquid theory [144], and QSH edge states are referred to as "helical Luttinger liquids" [143]. In this context, collective excitations are the eigenstates of the system. The strength of the interactions between single particles is quantified by the Luttinger parameter K_{L}. K_{L} is equal to one if interactions are absent, and $K_{\text{L}} < 1$ for repulsive interactions.

Depending on the microscopic mechanism proposed to cause backscattering, some works specify a K_{crit}, below which the mechanism is "relevant" in the sense that it induces a energy gap in the edge channel dispersion, and supresses edge state conductance entirely for $T \to 0\,\mathrm{K}$. If $K_{\mathrm{L}} > K_{\mathrm{crit}}$, ΔG is often found to follow a power law dependence

$$\Delta G \propto T^{\alpha}, \tag{4.8}$$

with α being a function of K_{L}. Dependencies of the form of equation (4.8) are derived in the linear response regime, assuming that the voltage drop across the edge channel is smaller than the thermal energy, $eU_{\mathrm{edge}} \ll k_{\mathrm{B}}T$. If this criterion is not fulfilled, a power law relationship between ΔG and U_{edge} is expected as well. This dependency should be seen as non-ohmic edge conductance, i.e. $dG_{\mathrm{edge}}/dU_{\mathrm{edge}} \neq 0$ for large excitation voltages [145, 146]. The magnitude of K_{L} for HgTe edge states is expected to depend on sample-specific properties such as carrier density and distance between QW layer and gate electrode. Most authors expect it to be close to unity, due to the large dielectric constant ε_{r} of HgTe, which gives rise to an effective screening of Coulomb interactions. Ref. [147] finds $K_{\mathrm{L}} \simeq 1$, Ref. [145] 0.98 , and Ref. [148] 0.8. An exceptionally low value $0.5 < K_{\mathrm{L}} < 0.55$ is deduced in Ref. [130], where the authors correct their previous estimation of $0.8 < K_{\mathrm{L}} < 0.9$ [149]. However, in the same contribution [130], an analytical expression is given to estimate K_{L} as

$$K_{\mathrm{L}} \approx \left[1 + \frac{2\,e^2}{\pi^2\,\varepsilon_{\mathrm{r}}\varepsilon_0\,\hbar\,v_{\mathrm{F}}} \ln\left(\frac{d}{w_{\mathrm{QSH}}}\right)\right]^{-1/2}, \tag{4.9}$$

which, for realistic sample properties, always yields values close to unity (d is the distance between edge state and gate electrode). Unfortunately, the input parameters which resulted $0.5 < K_{\mathrm{L}} < 0.55$, are not specified. The following listing summarizes theoretical works on backscattering mechanisms in helical luttinger liquids. Calculated results on K_{crit}, and the temperature dependence of ΔG can be found in table 4.1.

- *Phonons*. Single electron inelastic backscattering due to the presence of phonons is investigated in Ref. [150]. It is found that even though time-reversal symmetry does not protect the system against this backscattering mechanism, its correction on the current, and therefore on G_{edge}, vanishes.

- *Kondo impurities*. Ref. [147] suggests coupling to a local accumulation of electrons close to the edge states. If the number of trapped electrons is odd, a magnetic impurity is formed. A backscattering event then flips the spin both of the electron in

the edge state and of the impurity. Thus, in total, time reversal symmetry is preserved, even though the electron did switch the edge channel type. The authors also calculate the conductance of a helical edge in the limit of strong interactions (i.e. $K_{\mathrm{L}} < K_{\mathrm{crit}}$), and find $G \propto T^{1/2K_{\mathrm{L}}-2}$. The conductance correction due to backscattering on Kondo impurities, however, is doubted by Tanaka et al. in the case of DC excitation [151]. Due to the fact that each impurity alternately backscatters a left- and right moving electron as it flips its spin, the effective correction to the current carried by the edge states vanishes if the excitation frequency is much lower than the rate of spin-flip events at a single scattering site.

- *Rashba spin-orbit coupling*. Ref. [130] discusses two-particle backscattering due to a spatially inhomogeneous Rashba spin-orbit interaction (i.e. a varying electric field perpendicular to the plane of the QW). This mechanism is investigated as well in Refs. [152, 153], however, different K_{crit} and scalings of conductance are found. A slightly different approach is presented in [154]. Here, the mechanism is single particle backscattering, assuming that the spin is not a good quantum number. This is justified due to the dependence of the strength of the spin-orbit coupling on the k-vector of the particle. Since the magnitude of the Rashba spin-orbit coupling can be controlled to a large extend by the sample properties (in particular, asymmetric doping [155]), the existence of Rashba-induced backscattering should be testable by e.g. comparing the stability of QSH edge state conductance in symmetrically and asymmetrically doped QWs. Even though such studies have not yet been carried out systematically, the use of either asymmetrically doped or undoped QWs in QSH experiments showed no indications of such a dependency.

Ref.	K_{crit}	$\Delta G \propto$	regime	remarks
[147]	$1/4$	$T^{8K_{\mathrm{L}}-2}$	$K_{\mathrm{L}} > 1/4,\ T \to 0$	results questioned in
		$-\mu - \gamma \ln(E_{\mathrm{G}}/T)$	$K_{\mathrm{L}} > 1/4$, high T	the dc limit by [151]
[152]	$1/4$	$T^{4K_{\mathrm{L}}}$	$K_{\mathrm{L}} > 1/2$	
		$T^{8K_{\mathrm{L}}-2}$	$1/4 < K_{\mathrm{L}} < 1/2$	
[130]	$3/8$	not specified	not specified	
[153]	$1/2$	$T^{4K_{\mathrm{L}}-1}$	$1/4 < K_{\mathrm{L}} < 1$	
		$T^{8K_{\mathrm{L}}-2}$	$K_{\mathrm{L}} < 1/4$	
[154]		T^4	single particle	

Table 4.1: Characteristic quantities of different backscattering mechanisms in helical luttinger liquids.

If one compares the variety of backscattering mechanisms in helical Luttinger liquids,

and the related scaling of ΔG (table 4.1) with the experimental data (section 4.3.1), the result is not satisfying. Most strikingly, almost all contributions predict a decrease in edge state conductance with increasing temperature, and a power-law dependency $\Delta G \propto T^{\alpha}$. No such behavior has been observed. An exception is the work of Maciejko et al. [147], who finds a logarithmic increase of G_{edge} for high temperatures. However, at low temperatures, the model also predicts a recovery of the ideal $G_{\text{edge}} = e^2/h$, unless one assumes a strong interaction $K_{\text{L}} < 1/4$, which is probably not realistic for HgTe QWs. Furthermore, the low-temperature saturation of G_{edge} towards a non-quantized $G_{\text{edge}} \ll e^2/h$ in large samples is not explained by any of these works.

4.3.3 Backscattering in neighboring electron reservoirs

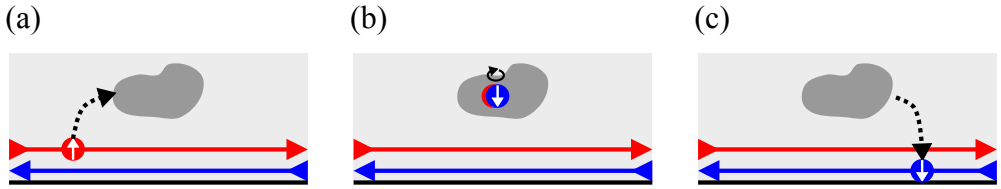

Figure 4.5: Charge puddle backscattering. (a) Electron tunnels into local n- or p regime (dark gray). (b) Electron may flip its spin. (c) Electron tunnels back into branch of helical edge state with opposite group velocity.

Motivated to some extend by the fact that experiments contradict most models of backscattering in helical Luttinger liquids, a different approach has been discussed by Väyrynen et al. [7, 8] and Essert et al. [156]. The approach has first been introduced by Roth et al. (supplementary online material of [133]), however, without discussing the temperature dependence. Figure 4.5 illustrates the mechanism. Instead of considering backscattering in the edge channel itself, the electrons are allowed to tunnel into a region close to the sample edge, where the Fermi level is locally either in the conduction- or the valence band. While dwelling in this "puddle" the electron then may flip its spin and tunnel back into the edge channel with opposite group velocity. As mentioned previously, signs of such charge puddles at the edge of the sample were found in scanning gate experiments [141]. Phenomenologically, the drop in conductance caused by a single puddle depends on the tunneling probability and the spin-flip efficiency (i.e. the inverse of the dephasing time). In the extreme case of very short dephasing times, every electron tunnels into the puddle, its spin is fully randomized, and the backscattering probability is 50 %. In that case, each puddle can be seen as an additional voltage probe, which increases the resistance of the edge by h/e^2 [equation (4.4)]. In Ref. [156] it is argued that this case

is realized for very short dephasing times. Since the dephasing time is very likely to decrease with increasing temperature, G_{edge} is expected to saturate if T exceeds a certain threshold.

In contrast to Essert et al. [156], Väyrynen et al. [8] attempt to specify the dephasing mechanism in the puddles. Refining their previous work [7], they model a charge puddle as a quantum dot, and consider the possibility of a spin-singlet charge configuration in such a dot. It is argued that for appropriate puddle sizes and low temperatures, the dominant backscattering occurs in dots occupied with an odd number of electrons. Just as in the case of the Kondo effect in a conventional quantum dot, this gives rise to a modified temperature dependence of conductance. For a long edge state and $k_{\mathrm{B}}T \ll \delta$, G_{edge} is proposed to follow

$$G_{\mathrm{edge}} \propto \frac{1}{n_{\mathrm{p}}\, w_{\mathrm{QSH}}}\, \ln^2\left(\frac{\delta}{k_{\mathrm{B}}T}\right). \tag{4.10}$$

Here, n_{p} is the density of puddles, w_{QSH} is the penetration depth of the edge state into the QW plane [equation (4.3)], and $\delta \approx 1\,\mathrm{meV}$ is the average energy level spacing in the dots. For high temperatures, the authors also predict a saturation of the backscattering efficiency of a single puddle directly at the edge, similar to a virtual voltage probe.

Similar to the mechanisms discussed in section 4.3.2, the agreement of predictions based on puddle-induced backscattering mechanisms with edge state conductances observed experimentally is far from conclusive. Nonetheless, the predicted temperature dependence of G_{edge} of Ref. [156] (close to constant in the full-dephasing regime) and Ref. [8] [logarithmic at low temperatures (equation (4.10)) and constant at high temperatures] is, by now, closest to measurements. If one assumes a very efficient spin randomizing process in the reserviors, both of them would yield the absence of any T-dependence of G_{edge}.

Regarding actual values of G_{edge}, Ref. [8] not only comments on the temperature dependence $G_{\mathrm{edge}}(T)$, but also on the influence of sample properties, particularly on the influence of the magnitude of the energy gap. E_{G} affects G_{edge} in two ways [equation (4.10)]: on the one hand, the edge channel width scales as $w_{\mathrm{QSH}} \propto v_{\mathrm{F}}/E_{\mathrm{G}}$. On the other hand, the puddle density n_{p} depends on E_{G}. As soon as the energy gap significantly exceeds the average potential fluctuations ΔV in the QW ($E_{\mathrm{G}} \gg \langle \Delta V^2 \rangle^{1/2}$), the puddle density decreases with increasing band gap:

$$n_{\mathrm{p}} \propto \exp\left(-\alpha\, E_{\mathrm{G}}^2\right). \tag{4.11}$$

Since the model only considers intentional doping as source of potential fluctuations, it does not entirely capture the situation of realistic samples (in particular, according to the

model, any undoped QW should always exhibit perfectly quantized edge state conductance). The transition at which this exponential decay dominates as well as the slope of the decay (i.e. the parameter α) depend on the specific sample layout. The dependency given by equation (4.11) leads to one of the major applications we envisioned for the strain-engineering technology, as it allows to maximize the band gap E_G (see figure 3.13), and thereby should stabilize the edge state conductance. Studies of this application are presented in section 5.3.

Chapter 5

Magnetotransport measurements

As demonstrated in chapter 3, a wide variety of different band dispersions can be realized by controlling the strain degree of freedom (see figure 3.12). This chapter presents experimental studies of the magnetotransport signatures of this variety. The main focus is on two-dimensional systems. We show that the calculated dispersions are in agreement with measurements, all the way from semi-metallic wide QWs to heavily compressed QWs with energy gaps of unreached magnitude. Based on theoretical considerations outlined in chapter 4, we investigate the temperature dependence of the QSH effect and the influence of a maximized band gap on its stability. A possible explanation for the discrepancies between experimental data and theoretical predictions is suggested, and a different approach to improve the edge state conductance in large samples is introduced. Finally, the focus is changed from two-dimensional to three-dimensional systems. We show signatures of the chiral anomaly in compressively strained HgTe bulk layers, a fingerprint feature of the Weyl semi-metal phase, which is predicted to be present in these types of samples.

5.1 Sample fabrication, device geometry and measurement setup

Hall bar devices were fabricated using standard optical lithgraphy procedures. The mesa was defined using dry Ar^+-etching. The gate electrode was insulated from the QW by a 110 nm $SiO_2 - Si_3N_4$ dielectric. Ohmic contacts and the gate electrode consist of 50 nm AuGe and 50 nm Au [157]. A micrograph of a fully processed sample is shown in figure 5.1. Each device consists of two Hall bars on one chip. The four voltage probes enclose an area with similar length-to-width ratio for both large [$l \times w = (600 \times 200)\ \mu m^2$]

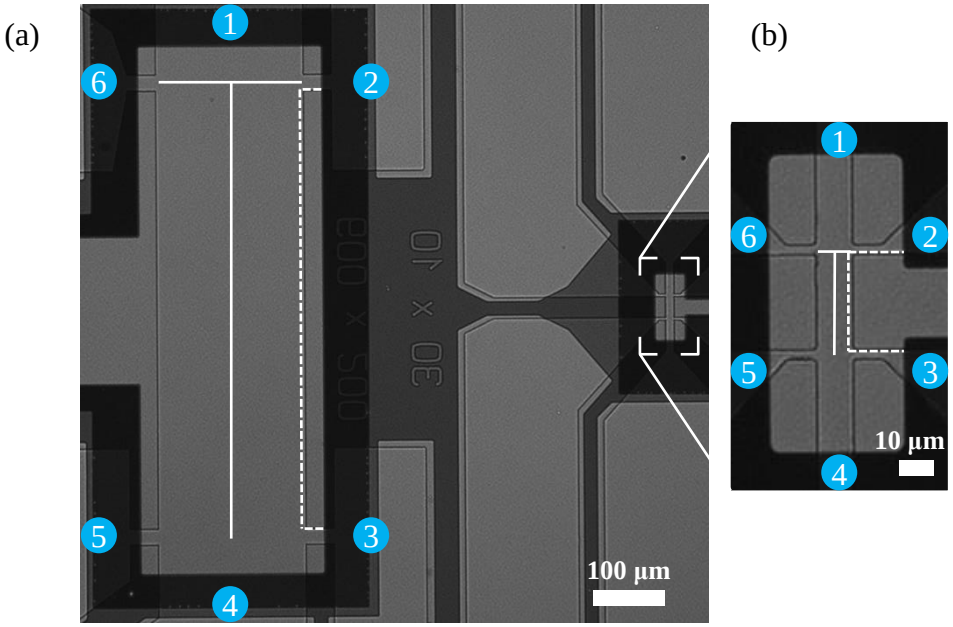

Figure 5.1: (a) Micrograph of the standard Hall bar device layout. Contacts are numbered. The solid T-shaped white lines indicate length-to-width ratio of area between the voltage probes. The dashed white lines exemplify one edge of the mesa area that is covered by the top gate. (b) shows closeup of small Hall bar.

and small Hall bar [$l \times w = (30 \times 10)\,\mu\text{m}^2$], as indicated by T-shaped lines. The length of the current path in the QSH regime between two voltage probes is defined by the length of the mesa edge which is covered by the top gate (dashed lines). Values for large and small Hall bar are $l_{\text{edge, lHB}} = 620\,\mu\text{m}$ and $l_{\text{edge, sHB}} = 58\,\mu\text{m}$, and significantly exceed typical path lengths where quantized conductance is observed (see section 4.2).

Magnetotransport measurements were performed on several ^{4}He cryostats at temperatures ranging from 1.8 K to ≈ 100 K. Typically, longitudinal and Hall resistances R_{xx} and R_{xy} were measured. With the Hall bar terminals labelled according to figure 5.1, current I is sent from 1 to 4 by via 10 mV DC excitation (if not specified differently). Longitudinal voltages U_{xx} are measured at pairs 2-3 and 6-5, Hall voltages U_{xy} at pairs 2-6 and 3-5. Resistances are then calculated as $R_{xx} = U_{xx}/I$ and $R_{xy} = U_{xy}/I$.

5.2 Strain-induced transition from semimetal to topological insulator in wide quantum wells

The measurements on the first pair of samples serve as a proof-of-concept of the strain-control of HgTe QWs. In order to confirm the state of strain inferred from HRXRD

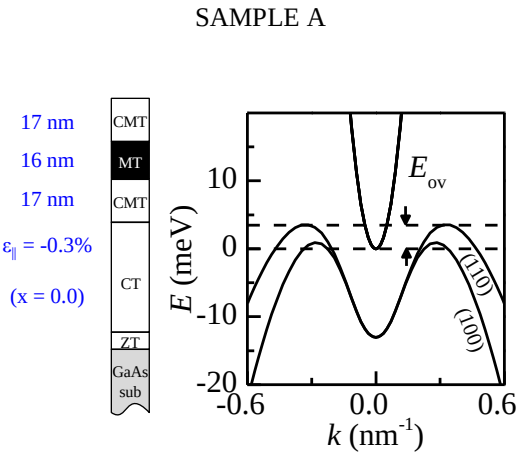

Figure 5.2: Layer stack and calculated band structure of sample A. Tensile strain ($\varepsilon_{||} < 0$) causes energy overlap E_{ov} between valence- and conduction band.

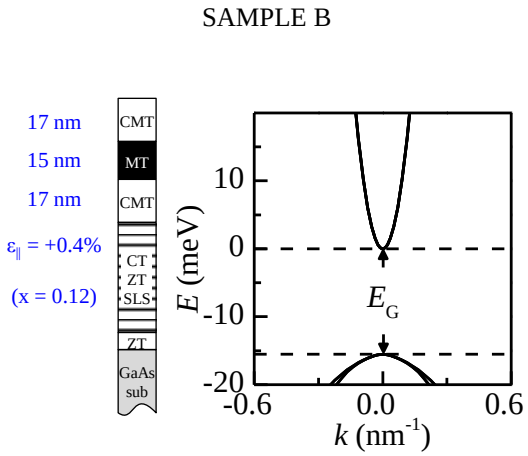

Figure 5.3: Layer stack and calculated band structure of sample B. Compressive strain ($\varepsilon_{||} > 0$) suppresses the camel-back feature in the valence band and induces finite band gap E_{G}.

measurements, and to validate the band structure calculations, a parameter set is chosen for which the strain is expected to alter the magnetotransport characteristics most significantly. As discussed in section 3.3.2, a transition from a two-dimensional semimetal with overlapping conduction- and valence band to a direct band gap semiconductor occurs in wide QWs if the strain is changed from tensile ($\varepsilon_{||} < 0$) to compressive ($\varepsilon_{||} > 0$). However, since the transition can only be achieved in inverted QWs ($d > d_{\mathrm{c}}$) it is described more accurately as semimetal-2DTI-transition. This transition is realized epitaxially with samples A and B. The layer stacks are illustrated in figure 5.2 and 5.3. The HgTe QW and CdHgTe barriers were fabricated using identical growth parameters. QW thicknesses (measured by XRR) are 16 nm for sample A and 15 nm for sample B. In order to ensure coherent growth of CdHgTe barriers, which are rather highly mismatched with respect to the SLS substrate of sample B, their thickness is kept comparatively low ($d_{\mathrm{CMT}} = 17$ nm, each). On the one hand, this is disadvantageous with respect to carrier mobility, as screening of charged defects located at the sample surface is less effective compared to samples with thick CdHgTe top barriers. On the other hand, the carrier density can be adjusted over a wide range without encountering hysteresis effects, which are frequently seen in samples with thick top barriers [155]. For sample A, a binary CdTe epilayer is used as artificial substrate, and gives rise to a tensile strain of $\varepsilon_{||} = -0.3\%$. In contrast, a CdTe-CdZnTe SLS artificial

substrate compressively strains the QW of sample B ($\varepsilon_{||} = +0.4\%$). The change in sign of $\varepsilon_{||}$ is confirmed by comparing HRXRD $\omega - 2\theta$ scans of the (004) reflection (figure 5.4). Arrows highlight the opposite strain-induced shift of the CdHgTe barriers of samples A and B. The measured diffraction profiles are in agreement with simulations of fully coherent layer stacks, indicating that no relaxation took place in the heterostructures. To simplify the fitting procecure, the artificial substrates are modelled as $Cd_{1-x}Zn_xTe$ solid solutions with identical lattice constant ($x = 0\%$ and 12% for samples A and B). Therefore the 1st SLS satellite of sample B at $\omega = 32.2°$ is not reproduced in the simulation.

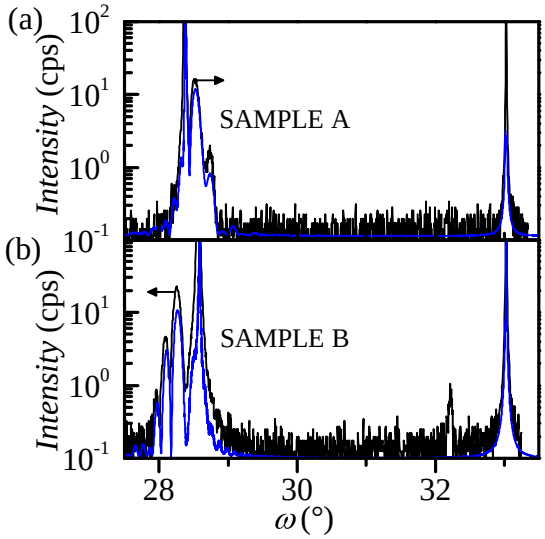

Figure 5.4: HRXRD $\omega - 2\theta$ measurement of the (004) reflection of (a) sample A and (b) sample B. Arrows indicate strain-induced shift of CdHgTe QW barriers. Simulated diffraction profiles (blue lines) are slightly offset for clarity.

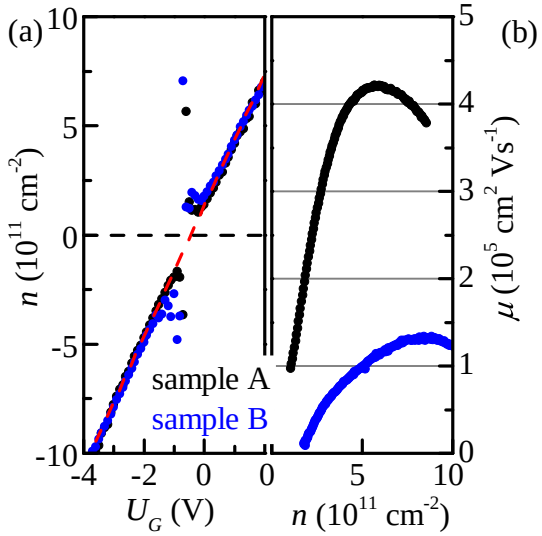

Figure 5.5: (a) carrier density $n = n_e - n_h$ as function of gate voltage. Red line is linear fit to the data. (b) Mobility as function of carrier density in the highly n-type regime, calculated using equation (5.4) and (5.6).

With the strain and thickness of the two QWs known, the energy dispersions can be calculated. Results are shown in figure 5.2 and 5.3. Given the circumstance that the thicknesses of the two QWs are almost identical, the difference is remarkable. The impact of this difference on magnetic field- and temperature dependent transport properties is discussed in the following.

5.2.1 Two-carrier conductance and band overlap

The first set of experiments addresses the presence and absence of the band overlap in samples A and B, and the magnitude of the overlap in sample A. To this end, a series

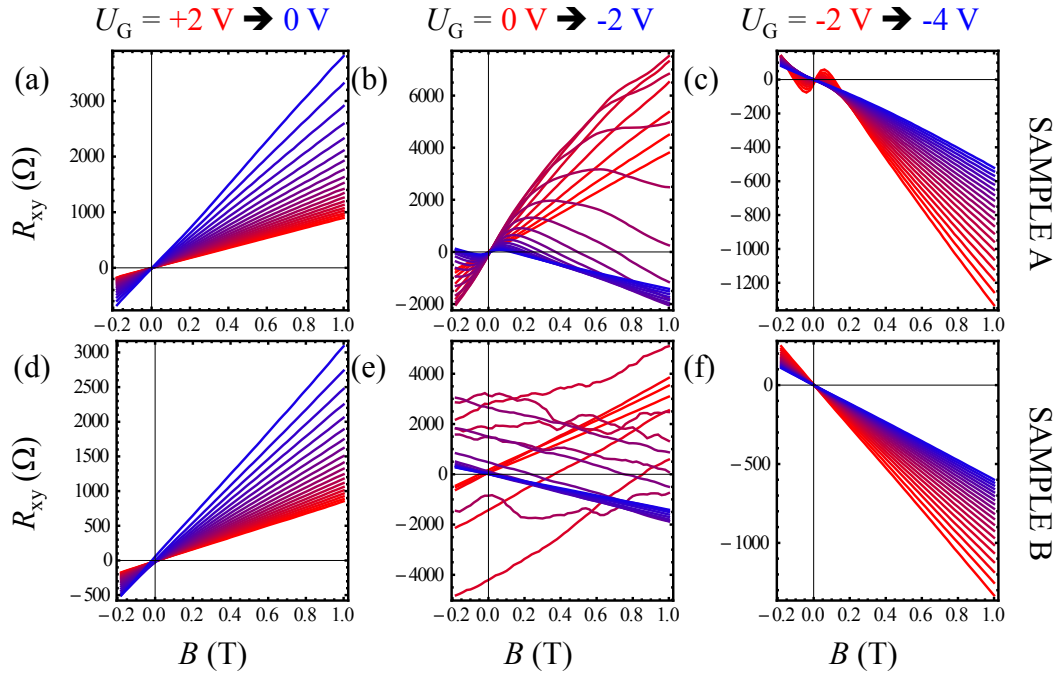

Figure 5.6: Hall resistances R_{xy} of sample A [(a)-(c)] and sample B [(d)-(f)]. Color-coding denotes different gate voltages U_G. Step size between two measurements is 0.1 V.

of magnetic field sweeps was performed from $B = -200\,\mathrm{mT}$ to $+1\,\mathrm{T}$ at a fixed temperature $T = 4.2\,\mathrm{K}$. Measurements were taken at gate voltages from $U_G = -4\,\mathrm{V}$ to $+2\,\mathrm{V}$, at 0.1 V step size. A first qualitative indication of the different characteristics of the two samples is the two-terminal resistance $R_{2\mathrm{terminal}}$, measured for various contact configurations. Whereas the semimetallic sample A exhibits very low $R_{2\mathrm{terminal}} = 1-6\,\mathrm{k\Omega}$ at room temperature, which increase only moderately at 4.2 K ($2-11\,\mathrm{k\Omega}$), the two-terminal resistances of sample B are comparable at room temperature ($2-8\,\mathrm{k\Omega}$), but, as characteristic for undoped semiconductors, are significantly larger after the sample has been cooled down ($70-170\,\mathrm{k\Omega}$).

Due to the overlapping conduction- and valence band of sample A, coexistence of electrons and holes is expected around the charge-neutrality point (CNP). In order to gain a better understanding of the signatures of this coexistence in the measurements, a brief summary of classical two-dimensional magnetotransport in the presence of multiple carrier types is given. In the absence of quantization effects, the conductivity matrix [158]

$$\boldsymbol{\sigma} = \frac{ne\mu}{1+(\mu B)^2}\begin{pmatrix} 1 & -\mu B \\ \mu B & 1 \end{pmatrix} \tag{5.1}$$

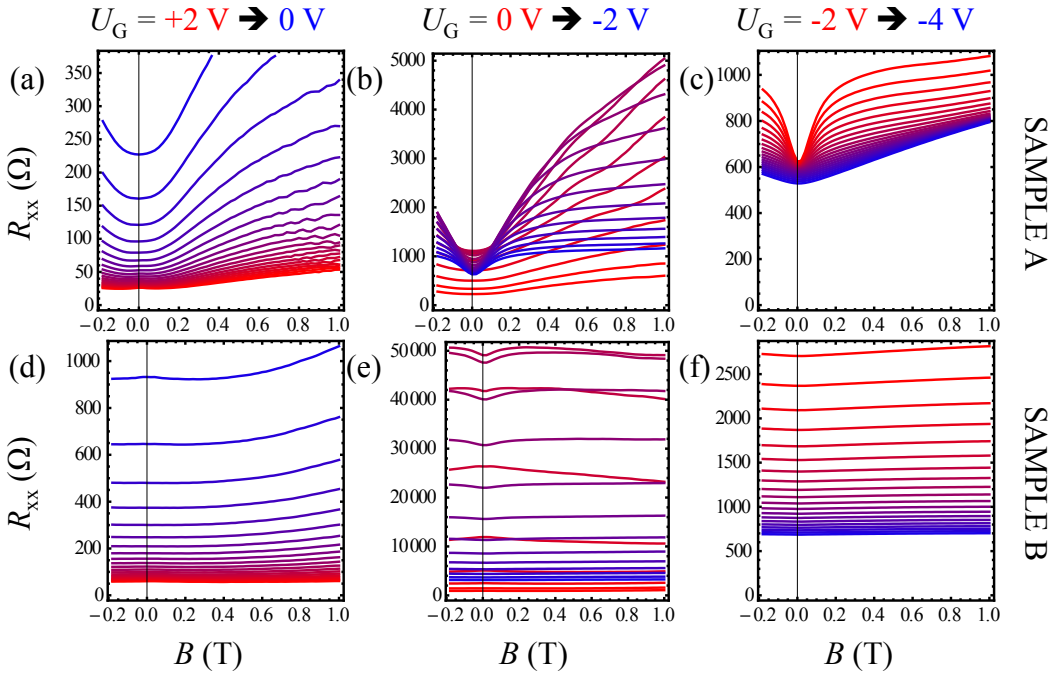

Figure 5.7: Longitudinal resistances R_{xx} of sample A [(a)-(c)] and sample B [(d)-(f)]. Color-coding denotes different gate voltages U_G. Step size between two measurements is 0.1 V.

relates current density to electric field in $\mathbf{j} = \boldsymbol{\sigma}\mathbf{E}$. Both $\mathbf{j}$ and $\mathbf{E}$ have components only in the plane of the QW, and the magnetic field B is perpendicular to that plane. In equation (5.1), n is the density and μ is the mobility of carriers. If electrons and holes coexist in the system, their conductivities add up as $\boldsymbol{\sigma} = \boldsymbol{\sigma}_e + \boldsymbol{\sigma}_h$ and the Hall- and longitudinal resistances of a rectangular shape with dimensions $l/w = 3/1$ are given by [158]:

$$R_{xy} = \frac{B}{e} \cdot \frac{\mu_e^2 n_e - \mu_h^2 n_h + \mu_e^2 \mu_h^2 (n_e - n_h) B^2}{(\mu_e n_e + \mu_h n_h)^2 + \mu_e^2 \mu_h^2 (n_e - n_h)^2 B^2} \tag{5.2}$$

and

$$R_{xx} = \frac{3}{e} \cdot \frac{\mu_e n_e + \mu_h n_h + \mu_e \mu_h (\mu_e n_h + \mu_h n_e) B^2}{(\mu_e n_e + \mu_h n_h)^2 + \mu_e^2 \mu_h^2 (n_e - n_h)^2 B^2}. \tag{5.3}$$

In equation (5.2) and (5.3), electrons and holes are charged with $-e$ and e, respectively, and both densities n_e and n_h are positive numbers. Some special scenarios lead to simplified versions of equation (5.2) and (5.3). For high fields $B \to \infty$, equation (5.2) becomes

$$R_{xy} = \frac{B}{e} \cdot \frac{1}{n_e - n_h}, \tag{5.4}$$

similar to the well known Hall resistance $R_{xy} = B\ (ne)^{-1}$ with $n = n_e - n_h$. A helpful

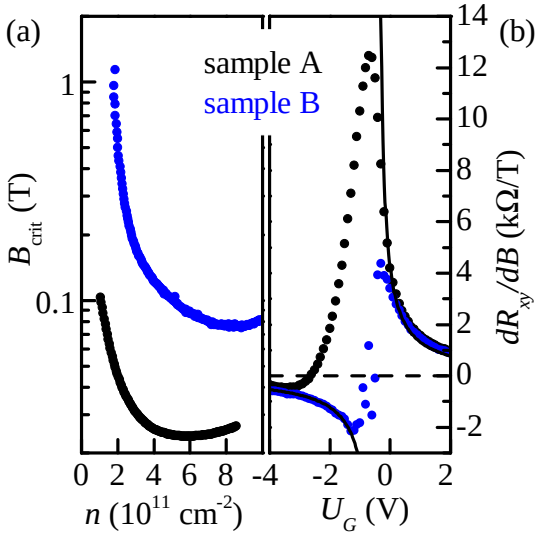

Figure 5.8: (a) Critical field B_{crit} for Drude fits of R_{xx} and R_{xy} in highly n-type regime as function of carrier density. (b) low-field slope of R_{xy} as function of gate voltage. Black line is hyperbolic fit to data of sample B.

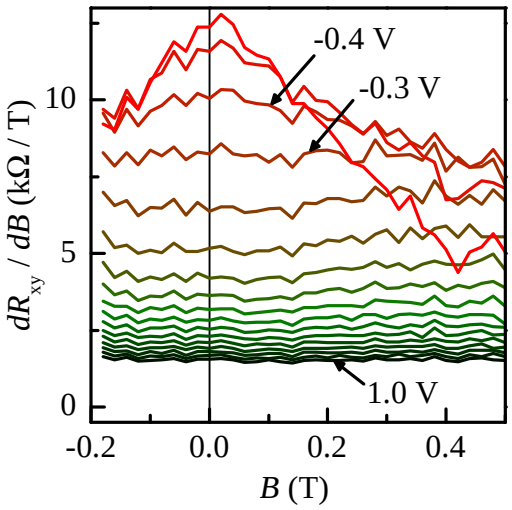

Figure 5.9: Derivative of magnetoresistance dR_{xy}/dB of sample A as function of magnetic field. Data is shown for gate voltages from $U_{\mathrm{G}} = 1\,\mathrm{V}$ to $-0.6\,\mathrm{V}$ Curvature sets in between $-0.3\,\mathrm{V}$ and $-0.4\,\mathrm{V}$.

property of equation (5.4) is that it is independent of the carrier mobilities. However, since equation (5.1) is only valid in the classical regime, equation (5.4) can only be applied at moderate magnetic fields to approximate n. In the opposite limit of very low fields $B \to 0$, equation (5.2) becomes

$$R_{\mathrm{xy}} = \frac{B}{e} \cdot \frac{\mu_{\mathrm{e}}^2 n_{\mathrm{e}} - \mu_{\mathrm{h}}^2 n_{\mathrm{h}}}{\left(\mu_{\mathrm{e}} n_{\mathrm{e}} + \mu_{\mathrm{h}} n_{\mathrm{h}}\right)^2}, \tag{5.5}$$

where the sign of the slope of R_{xy} is mainly determined by the carrier species with higher mobility. For single-carrier conductance ($n_{\mathrm{e}} = 0$ or $n_{\mathrm{h}} = 0$), R_{xx} is independent of the magnetic field:

$$R_{\mathrm{xx}} = \frac{3}{e\, n\, \mu}. \tag{5.6}$$

For finite and similar densities ($n_{\mathrm{e}} = n_{\mathrm{h}} = n$), R_{xx} increases parabolically with magnetic field as

$$R_{\mathrm{xx}} = \frac{3}{e} \cdot \frac{1 + \mu_{\mathrm{e}}\mu_{\mathrm{h}}\, B^2}{n\left(\mu_{\mathrm{e}} + \mu_{\mathrm{h}}\right)}. \tag{5.7}$$

The measured Hall- and longitudinal resistances of samples A and B are shown in figure 5.6 and 5.7, respectively. Traces are gradually color-coded according to the gate voltage (see legends), and divided into three regimes for clarity. Both samples change

from highly n-type [(a) and (d)] to p-type [(c) and (f)] as the gate voltage is lowered from $+2\,\mathrm{V}$ to $-4\,\mathrm{V}$. The total carrier density n is calculated from dR_{xy}/dB at $B = 1\,\mathrm{T}$ [equation (5.4)], and is shown in figure 5.5 (a). The CNP of both samples is at $U_G \approx -0.45\,\mathrm{V}$ (red dashed line: density interpolated around $n = 0$), and the gate efficiency is $dn/dU_G = 3.0 \times 10^{11}\,\mathrm{cm}^{-2}\,\mathrm{V}^{-1}$. The mobility of both samples is shown in figure 5.5 (b) in the n-type regime. The measured values are comparable to results on QWs fabricated on commercial II-VI substrates, and the slope is typical for the material system [159]. This is remarkable, considering the aforementioned tradeoff regarding CdHgTe barrier thicknesses. The lower maximum value of sample B is a first indication of the general trend that the mobility goes down with increasing Zn-content in SLS artificial substrates (a more systematic study is shown in section 5.3). The drop in mobility is correlated to the gradual degradation of SLS crystal quality with increasing Zn fraction (see section 2.4.4). Aside from global similarities, the different band lineups are reflected qualitatively in several aspects of the transport characteristics:

- As the Fermi level is swept across the CNP, the Hall traces of sample A exhibit a pronounced curvature [figure 5.6 (b)], which is typical for a system where electrons and holes of comparable amount exist. In contrast, as the Fermi level approaches the energy gap of sample B, traces of R_{xy} are neither point symmetric with respect to magnetic field, nor vanish at $B = 0\,\mathrm{T}$ [figure 5.6 (e)]. This is an indication that U_{xy} is not caused by the Hall effect, but by the inhomogeneous distribution of charges across the sample in the highly resistive regime.

- At large negative gate voltages, both samples show a negative slope of R_{xy} at high magnetic fields [figure 5.6 (c) and (f)], indicating that holes are the majority carrier type [equation (5.4)]. At $B = 0\,\mathrm{T}$, the slope of sample A remains positive, which reveals the existence of residual n-type carriers with much higher mobilities compared to hole-like majority carriers [see equation (5.5)]. The feature is absent in sample B, as expected from the energy dispersion. The feature is illustrated more clearly by plotting dR_{xy}/dB at $B = 0\,\mathrm{T}$ as function of gate voltage in figure 5.8 (b). Data of sample B can be fit with two hyperbola which are point symmetric around the CNP. Data of sample A does not diverge, and has its maximum in the p-regime ($n_h > n_e$). It intersects the y-axis at the gate voltage, where $n_e/n_h = (\mu_e/\mu_h)^2$ [see equation (5.5)].

- At a first glance, it seems as if the two carrier characteristics of sample A is also reflected in its magnetoresistance $R_{xx}(B)$. A parabolic increase is seen in a wide range of gate voltages [figure 5.7 (a)-(c)]. As illustrated by the extreme case $n_e = n_h$

[equation (5.7)], the feature is most pronounced around the CNP. Due to the finite E_G, electrons and holes are separated energetically in sample B, and the effect is suppressed strongly [figure 5.7 (d)-(f)]. However, the presence of a different mechanism is indicated by the fact that a finite magnetoresistance is also observed at gate voltages where the samples are supposed to be purely n-type [figure 5.7 (a) and (d)] and accordingly, no curvature in the Hall traces is observed. As we explain in the following, we can assign the magnetoresistance effects in the far n-type regime to the field dependence of the mobility $\mu(B)$. As a criterion for the absence of magnetoresistance effects in the single-carrier regime, where resistance is simply $R_{xx} = 3/(n\,e\,\mu)$, the cyclotron frequency ω_c needs to be smaller than the scattering rate, $\omega_c < \tau^{-1}$ [160]. With $\tau = \mu\, m_e\, e^{-1}$ one can deduce a critical field $B_{crit} = \mu^{-1}$, below which the longitudinal resistance is independent of B. Outside this regime (i.e. at fields larger than B_{crit}), carriers are able to complete a significant fraction of the cyclotron orbit before they scatter. This deflection can be taken into account in the Drude model by a decrease in $\mu(B)$ [160]. The critical field of both samples is shown in figure 5.8 (a) for the n-type regime. Due to the high mobility of sample A, B_{crit} is as low as $B_{crit} \approx 0.02\,\mathrm{T}$ at the highest mobility. This shows that magnetoresistance effects cannot be used as a direct indication of two-carrier conductance in the high-mobility n-type regime. Accordingly, the magnetoresistance effects observed in the n-type regime of sample B are less pronounced, due to its lower overall mobility and the higher critical field that follows [figure 5.8 (a)]. The ambiguity of two-carrier- and mobility-induced magnetoresistance has to be taken into account in the following section, where the two-carrier conductance of sample A is analyzed.

The qualitative behaviour of sample A [in particular the characteristic curvature of the Hall resistance around the CNP [figure 5.6 (b)]], points to pronounced two-carrier conductance, as expected from the band structure calculations [figure 5.2]. We now turn to the quantitative analysis of the energy dispersion. As discussed previously, magnetoresistance effects cannot be related unambiguously to two-carrier conductance, due to the high mobility of the QW in the n-type regime. We therefore identify the onset of two-carrier conductance by the emerging curvature in the Hall resistance, i.e. where $R_{xy} = B\,(ne)^{-1}$ no longer holds. In figure 5.9, we plot the derivative of the Hall resistance, dR_{xy}/dB for the relevant set of gate voltages, and identify the first trace which has a non-horizontal component as related to the threshold gate voltage where two-carrier conductance sets in. We find a threshold $U_G = -0.4\,\mathrm{V}$. In the two-carrier regime (i.e. at negative gate voltages larger than $-0.4\,\mathrm{V}$), densities of n-type and p-type carriers were obtained by simultane-

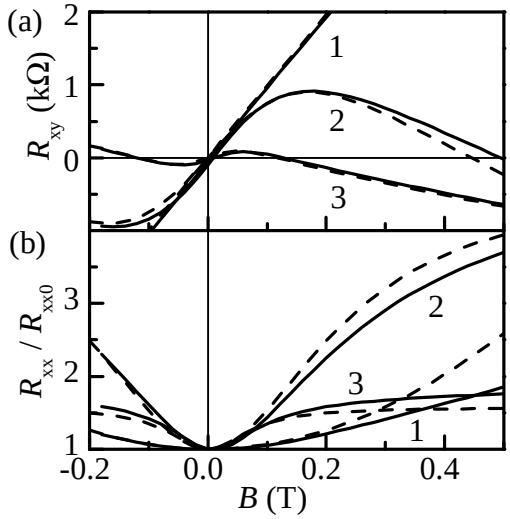

Figure 5.10: (a) R_{xy} and (b) R_{xx}/R_{xx0} of sample A at characteristic gate voltages: $U_G = -0.4\,V$ (1), $-1.0\,V$ (2) and $-1.8\,V$ (3). Dashed lines show best simultaneous fits to equation (5.2) and (5.3).

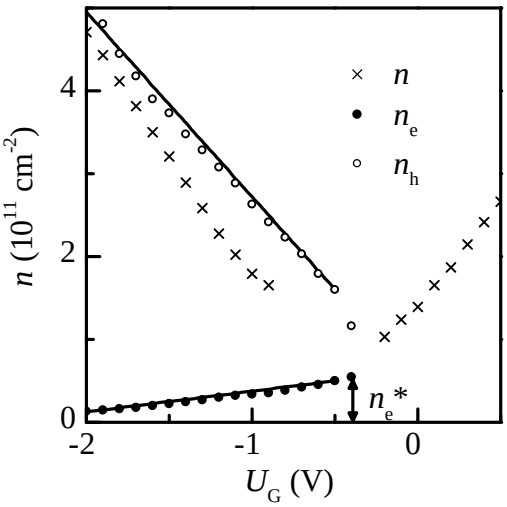

Figure 5.11: Carrier densities of sample A as function of gate voltage. Individual densities of electrons n_e (•) and holes n_h (○) obtained from two-carrier fit. Crosses × denote total carrier densities estimated from $e\ (dR_{xy}/dB)^{-1}$. Straight lines are guides to the eye. Black arrow indicates n-type carrier density n_e^* at the onset of two-carrier conductance.

ous fits of equation (5.2) and (5.3) to the data. Examples of fits are shown in figure 5.10. Deviations at low densities and high magnetic fields (traces 2 and 3) are observed, since the model does not consider the aforementioned magnetic field dependence of mobilities, as well as emerging quantization effects.

Fitting results of the carrier densities are shown in figure 5.11. As expected, n_e decreases and n_h increases with increasing negative gate voltage. As a consistency check, the approximate total carrier density obtained from dR_{xy}/dB at $B = 1\,T$ [equation (5.4)] is also plotted again (crosses), and it shows that $n = n_h - n_e$ holds. The different gating efficiencies of electrons and holes $dn_{e,h}/dU_G$ reflects the fact that the density of states of holes is much larger than the one of electrons in the overlapping regime. We find $dn_h/dU_G\ (dn_e/dU_G)^{-1} = 8.9$ (slopes of black lines). The intersection of the Fermi energy with the valence band is identified by the onset of two-carrier conductance, and can be used to determine the overlap of conduction- and valence band E_{ov} (figure 5.2, dashed

lines). At the transition (arrow in figure 5.11), we find an n-type carrier density of

$$n_e^* = 5.5 \times 10^{10}\,\mathrm{cm}^{-2}. \tag{5.8}$$

Since the energy dispersion of the conduction band is parabolic for low Fermi energies, E_{ov} is simply

$$E_{ov} = E_F = n_e^* \frac{\pi\hbar^2}{m_e} = 4.5\,\mathrm{meV}. \tag{5.9}$$

The experimental value is slightly larger than the one expected from the band structure calculation, $E_{ov} = 3.6\,\mathrm{meV}$ (figure 5.2), but confirms the overall characteristic of the energy dispersion. In equation (5.9), the effective mass $m_e = 0.028\ m_0$ is deduced from the conduction band dispersion (figure 5.2) using $m_e^{-1} = \hbar^{-2}\ d^2E/dk^2$ (m_0 is the mass of the free electron). The major uncertainties to consider are the band deformation potentials [116] and the limitation of the fitting procedure, discussed previously (figure 5.10).

5.2.2 Band gap measurement from thermally activated conductance

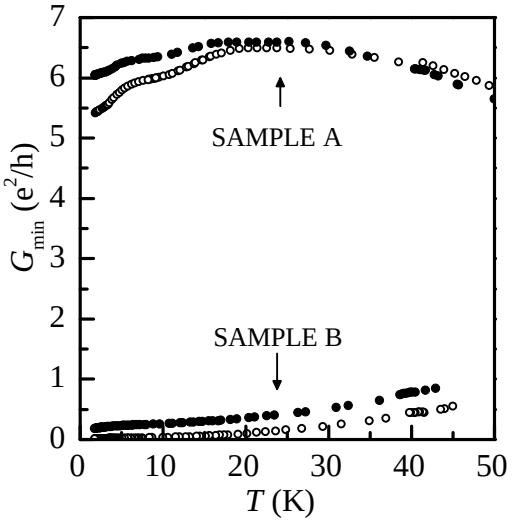

Figure 5.12: Minimum conductance of samples A and B as function of Temperature. ○ (●) data points are measured on large (small) Hall bar.

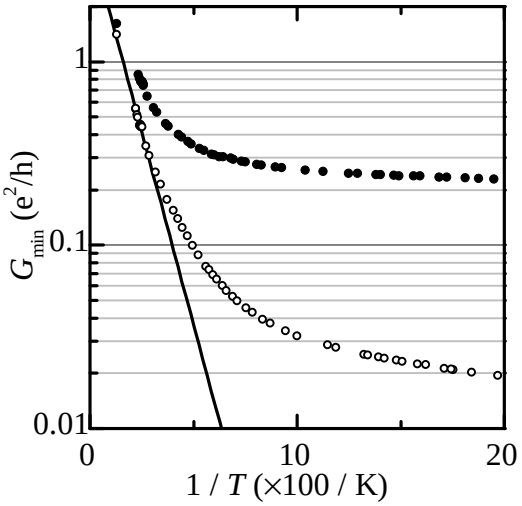

Figure 5.13: Arrhenius plot of G_{min} of sample B for $T > 5\,\mathrm{K}$. ○ (●) data points are measured on large (small) Hall bar. Line is fit of equation (5.10) to large Hall bar data.

After the experimental determination of the magnitude of the overlap of valence- and conduction band of sample A, we now turn to the analysis of the energy gap between the two bands in sample B. As stated earlier, the Hall traces of sample B are irregular in the

vicinity of the CNP [figure 5.6 (e)], and do not allow for further quantitative analysis of the band dispersion. Instead, the band gap was studied by the characteristic thermal excitation behaviour of a semiconductor. We have measured R_{xx} as function of gate voltage at $B = 0\,\mathrm{T}$ at temperatures from $T = 1.8\,\mathrm{K}$ to $77\,\mathrm{K}$. The minimum conductance G_{min}, corresponding to the Fermi level being situated at the CNP, was extracted for each temperature. Measurements were done on the large and small Hall bar of sample A and sample B.

Before we focus on sample B, we first demonstrate that the semi-metallic energy dispersion of sample A is also reflected in its temperature dependent conductance. G_{min} is shown in figure 5.12 as function of temperature. The minimum conductance of sample A is much larger compared to sample B, the relative change with temperature is weak, and the magnitude is comparable for large and small Hall bar within the whole range of temperatures. This supports the interpretation that the current flows in the two-dimensional plane of the QW, because in that case the conductance is determined by the conductivity and the ratio l/w of the device, which is identical for both Hall bars (figure 5.1). The overall weak temperature dependence is expected, since no thermal activation of carriers is necessary due to the overlapping conduction- and valence band. Regarding the shape of $G_{\mathrm{min}}(T)$, Ref. [161], attributes the weak increase at low temperatures to long-range smooth disorder in the energy landscape at the CNP. The decrease at higher temperatures may be due to phonon-induced scattering effects.

The behavior of sample B is significantly different. The conductance is much lower and increases monotonously with increasing temperature. G_{min} is shown again in figure 5.13 as function of T^{-1} on a logarithmic scale for $T > 5\,\mathrm{K}$. Strikingly, at low temperatures, the minimal conductances of the large and small Hall bar saturate at two distinct values. The ratio of the conductance values can be used to show that the 2DTI edge-channel conductance is the dominant conductance mechanism at low temperatures. Since both channels are considerably longer than channels where quantized conductance is found [6], the measured values are significantly lower than $2e^2/h$, and the number of scattering events is supposed to scale with the length of the channel. Accordingly, the ratio of the two low-temperature conductances qualitatively matches the inverse of the respective edge channel lengths: $G_{\mathrm{min,\,sHB}}/G_{\mathrm{min,\,lHB}} \approx 10/1 = l_{\mathrm{edge,\,lHB}}/l_{\mathrm{edge,\,sHB}}$ (section 5.1). As the temperature increases, the thermally activated conductance of the whole plane of the QW sets in, and the conductances of large and small Hall bar begin to converge. The thermally activated conductance of intrinsic semiconductors follows approximately [162]

$$G_{\mathrm{min}} = G_{\mathrm{th}} = A_{\mathrm{th}}\ \exp\left(-\frac{E_{\mathrm{G}}}{2\,k_{\mathrm{B}}T}\right), \tag{5.10}$$

with the sample-specific prefactor A_{th}. A fit of the high-temperature data of the large Hall bar to equation (5.10) (black line in figure 5.13) yields

$$E_{\mathrm{G}} = 17\,\mathrm{meV}, \tag{5.11}$$

in good agreement with the value expected from band structure calculations ($E_{\mathrm{G}} = 16\,\mathrm{meV}$, figure 5.3). The fit is only possible for the large Hall bar, since edge state conductance still notably contributes to the total conductance of the small Hall bar, even in the limit of high temperatures. We note that the accordance of experiment with theory requires a correct implementation of strain in the band structure calculations, accurate control of the growth parameters, and a clear identification of the thermally activated sheet conductance. Meeting all these requirements is not trivial, and discrepancies were reported by other groups [137, 139].

5.3 The influence of the magnitude of the band gap on transport in the quantum spin Hall regime

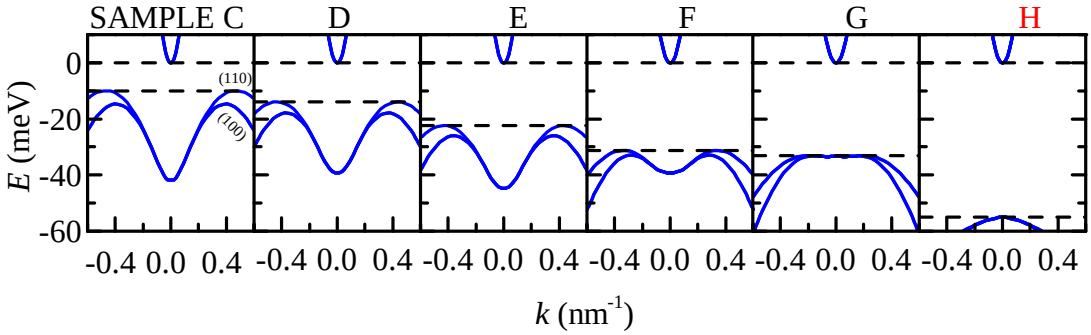

Figure 5.14: Energy dispersions of samples C to H. In contrast to samples C to G, a modified approach has been used to grow the barriers of sample H.

In the previous section, the calculated influence of strain on the band dispersion was confirmed experimentally. We now turn to the interplay between band dispersion and characteristics of edge state transport. From a pragmatic point of view on the principles of 2DTIs, increasing the magnitude of the bulk energy gap E_{G} is of interest, since this should, on the one hand, enhance the "insulating" characteristics of the bulk material, while on the other hand, conductance induced by the gapless edge states should persist. A dependency between edge state conductance and E_{G} can be found in different aspects of theoretical models (sections 4.3.2 and 4.3.3). With an increase of E_{G}, the

width of the edge state, w_{QSH}, goes down [equation (4.3)], i.e. the wavefunction of the state becomes more localized to the edge of the sample. This may, on the one hand, enhance any backscattering mechanisms that occur at the sample edge, where the crystal is more imperfect because of its exposure to processing chemistry, physical etching, or simply atmosphere. On the other hand, as w_{QSH} goes down, the Luttinger parameter K_{L} is expected to decrease slightly [equation (4.9)], enhancing possible interaction effects (section 4.3.2). Regarding backscattering in external reservoirs, the stability of the QSH edge state should increase, since the density of residual charge puddles is expected to go down with increasing E_{G} [see equation (4.11) [8]]. In the following section, experimental results on the thermal stability and robustness against backscattering in QWs with different energy gaps are shown.

5.3.1 Sample parameters

sample	$\varepsilon_{\|\|}$ (%)	d_{QW} (nm)	d_{barrier} (nm)	E_{G} (meV)
C	-0.31	8.6	17	10
D	-0.21	8.8	17	14
E	+0.01	8.4	17	21
F	+0.38	9.0	17	31
G	+0.62	9.8	16	33
H	+1.38	7.5	18	55

Table 5.1: Properties of samples C to H. E_{G} is obtained from band structure calculations.

We discuss measurements obtained from six different wafers, with parameters listed in table 5.1. The overall growth process was kept similar for samples C to G. The barriers were kept thin to avoid any crystal relaxation (section 2.5.3), and the QWs were designed just thick enough to exlude any temperature-driven change of the energy gap in the range of temperatures investigated (section 3.3.3). For sample H, the T-dependence of E_{G} sets in at a temperature regime close to the highest temperature we have studied (see remarks at the end of this section). Due to the heavy compressive strain in sample H, the growth procedure of the barrier material had to be modified to circumvent relaxation processes. The properties of sample H are described in more detail in a separate paragraph below. By changing the Zn-content in the SLS, the strain of the QWs was varied from $\varepsilon_{||} = -0.31\,\%$ to $+1.38\,\%$, and with this, E_{G} changed by a factor of approximately five (see the energy dispersions of the samples in figure 5.14). Similar to sample A, sample C is grown on a

pure CdTe-GaAs:Si bulk layer and not on a SLS. The samples are sorted alphabetically according to increasing E_G.

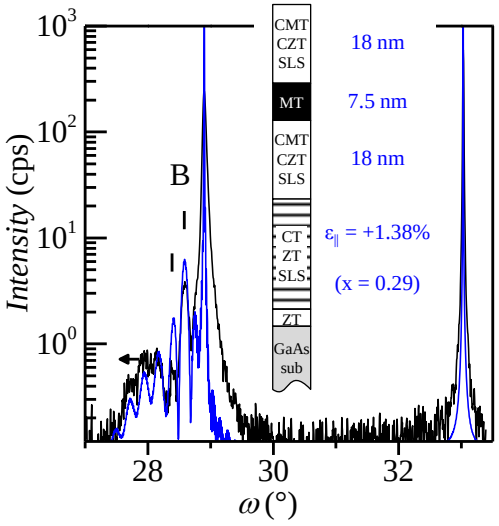

Figure 5.15: HRXRD scan of sample H. Reflections related to barriers are labelled "B". Arrow highlights highly displaced set of fringes originating from the QW. Simulated diffraction pattern (blue) is calculated assuming fully strained layers. Inset gives details of the layer stack.

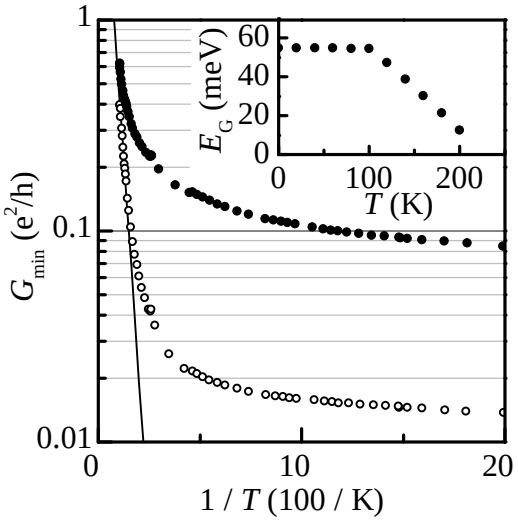

Figure 5.16: Arrhenius plot of G_{min} of sample H for $T > 5\,K$. ○ (●) data points are measured on large (small) Hall bar. Line is fit of equation (5.10) to large Hall bar data, with fit parameter $E_G = 55\,meV$. Inset shows calculated band gap as function of temperature.

As already mentioned, the growth procedure of sample H is different compared to samples C to G. The structure features modified barriers, where Zn is added to lower the mismatch between substrate and barriers (see section 2.5.4). The HRXRD scan is shown in figure 5.15 and the layer stack is sketched in the inset. The Zn content of a solid solution of $Cd_{1-x}Zn_xTe$ with similar lattice constant is found to be as high as $x = 29\,\%$. From the position of the barrier reflections (ticks labelled "B"), their composition can be estimated as $Zn_{0.20}Cd_{0.56}Hg_{0.24}Te$ (From the fit, we can tell the amount of Zn in the barriers, but not the exact ratio of the Cd and Hg atoms that are replaced by Zn. The aforementioned composition is found by assuming that the substitution takes place evenly. The exact compositon, however, is not relevant). Remarkably, the HgTe layer is visible as an isolated set of fringes (arrow), due to its large mismatch to substrate and barriers. Furthermore, by comparing the measured signal with the appropriate simulation (blue), the HgTe layer is proven to be fully strained. This shows that the HgTe layers hold strains up to $\varepsilon_{||} = 1.38\,\%$.

The magnitude of the band gap of heavily compressed QWs is very sensitive to the

thickness of the QW (see figure 3.12). Given the uncertainty of the XRR measurement, we find $E_G = (55 \pm 5)$ meV (figure 5.14, right). Using the analysis of temperature-activated conductance (similar approach as discussed in section 5.2.2), this value is confirmed experimentally by a fit of equation (5.10) to G_{min} of the large Hall bar. The fit is shown in figure 5.16. As a major finding of this thesis, this band gap value is by far the largest ever reported for inverted HgTe QWs. In particular, E_G is well larger than $k_B T$ at room temperature. This observation, however, does not imply room temperature edge state conductance, due to the temperature-driven lifting of the band inversion (see section 3.3.3). The calculated temperature dependence of the band gap is shown in the inset of figure 5.16. As the sample temperature exceeds 100 K, E_G begins to decrease, and the band inversion is lifted for temperatures higher than 220 K. So far, we did not study the sample in the high-temperature regime of T-dependent E_G. Despite the limitation set by the regime of constant E_G, we will demonstrate in the following paragraphs that the threshold temperature below which edge state conductance is the dominant transport mechanism significantly increases along with E_G.

5.3.2 Standard characterization

Before the samples have been investigated in the QSH regime, The gate-voltage dependent carrier density and carrier mobility of the 2DEGs were measured at $T = 4$ K. Results are shown in figure 5.17, where the mobility is plotted as a function of carrier density. Routinely, these standard characterization measurements are carried out in a fixed gate voltage range ($U_G = -2$ V to $+2$ V). Since sample G is p-type at 0 V, the trace in figure 5.17 ends at an early $n = 3.4 \times 10^{11}\,\mathrm{cm}^{-2}$. As already observed for samples A and B, the mobility in the n-type regime drops significantly with increasing Zn content in the substrate. This trend is accompanied by an increase in the critical density n at which the Hall resistance becomes distorted [lower limit of the traces figure 5.17, the features in R_{xy} are similar to the ones shown in figure 5.6 (e)], which will be discussed in greater detail in section 5.3.6. Even though, due to their topological protection, the drop in mobility can not be directly mapped to a change in the conductance of the edge states, it is still indicative of a pronounced overall decrease in heterostructure quality, which has to be kept in mind when comparing the samples.

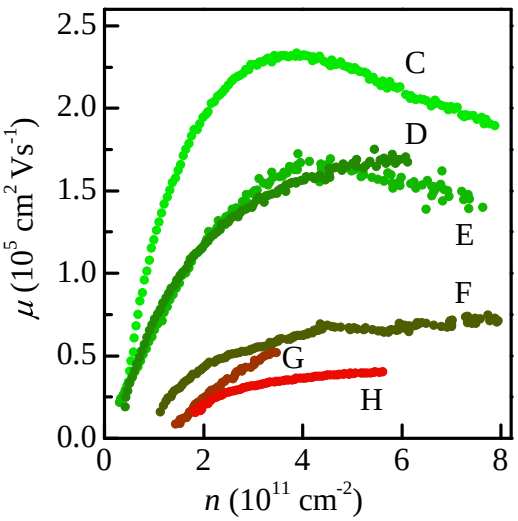

Figure 5.17: Mobility μ as function of carrier density n for the small Hall bar of samples C, D, ..., H. Upper limit in n is given by measurement range (maximum $U_G = +2\,V$), lower limit by onset of irregular Hall resistance (see text).

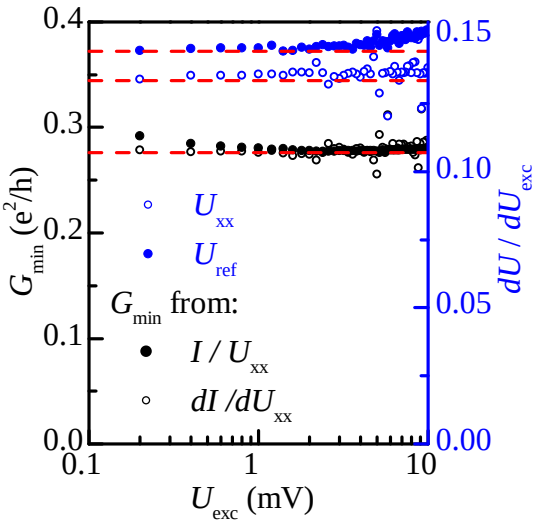

Figure 5.18: G_{min} of small Hall bar of sample D as function of excitation voltage. $T = 1.8\,K$. Blue dots denote derivatives of the voltage drop at the sample (○) and the reference resistor (●). Conductances are calculated from measured voltages (●) or their derivatives (○). Dashed horizontal lines are guides to the eye.

5.3.3 Temperature and band gap dependence of edge state conductance

The temperature dependence of the edge state conductance of samples C to H has been analyzed with an approach similar to section 5.2.2. Gate-dependent measurements of the longitudinal resistance R_{xx} have been performed at different temperatures. The maximum of R_{xx} was converted into G_{min}. Measurements have been carried out on various cryostatic setups, with different base temperatures $1.5\,K < T_{base} < 2.0\,K$ and maximum temperatures $77\,K < T_{max} < 100\,K$. To rule out significant sample heating due to the dissipated power in the mesa and nonlinearities due to Luttinger liquid effects (see section 4.3.2), we checked that the measured conductances are ohmic, i.e. do not depend on the excitation voltage U_{exc}. The result of such a check, carried out on the small Hall bar of sample D, is shown in figure 5.18. The voltage drops across the sample and the reference resistor increase almost linear with U_{exc}. This is illustrated by their derivatives with respect to U_{exc}, which are aligned almost perfectly horizontal (blue dots). Small nonlinearities are observed in both traces similarly, and may be due to a weak Schottky-like contribution to

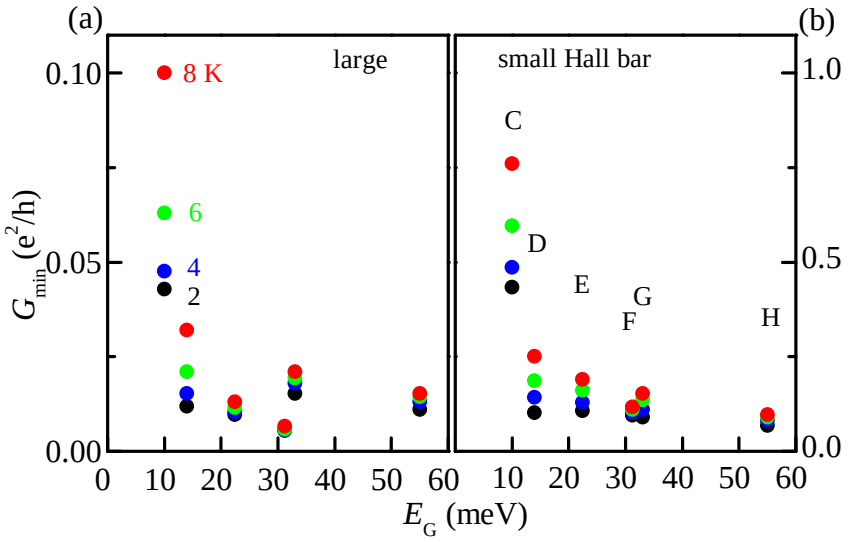

Figure 5.19: Minimum conductance G_{min} of samples C to H [labels in (b)] as function of band gap E_{G} for temperatures 2, 4, 6, and 8 K [labels in (a)]. (a): large Hall bar data. (b): small Hall bar data.

the contact resistances. A gentle increase of $G_{\mathrm{min}} = I/U_{\mathrm{xx}}$ is observed for low excitation voltages (filled black dots). This is a measurement artifact caused by a constant voltage offset of the amplifiers used, and vanishes if G_{min} is not calculated from the absolute voltages, but from their derivatives with respect to U_{exc} (empty black dots). Similar results were obtained for the large Hall bar and at higher temperatures. For sample G, we also checked AC-excitation as low as 50 µV without indications of non-ohmic behavior. Thus, no excitation-voltage driven sample heating and Luttinger liquid effects are observed, and all changes of G_{min} presented in the following are purely temperature-driven.

The overview plot, figure 5.19, shows G_{min} for the large and small Hall bar of all samples C to H for temperatures $2\,\mathrm{K} < T < 8\,\mathrm{K}$ as function of the energy gap. The upper temperature limit is chosen such that the edge state conductance is still the dominant conductance mechanism compared to thermally activated bulk conductance. Before going into greater detail, some qualitative trends and its exceptions are summarized:

- The scaling of the edge state conductance with the inverse of its path length is overall confirmed [$l_{\mathrm{edge,\,lHB}}/l_{\mathrm{edge,\,sHB}} \approx 10/1$, the scale of figure 5.19 (b) is ten times the scale of (a)]. The largest deviation is observed for sample F with $G_{\mathrm{min,\,sHB}}/G_{\mathrm{min,\,lHB}} \approx 16/1$ at $T = 2\,\mathrm{K}$. Since non-quantized G_{min} are due to sample imperfections, and therefore subjected to statistic variation, this is still reasonable.

- Just as in other experimental works found in the literature (section 4.3.1), the minimum conductance decreases with decreasing temperature, i.e. $dG_{\mathrm{min}}/dT > 0$, and

appears to saturate towards a finite G_0. This is in strong contrast to almost all theoretical models for pure helical edge state conductance, which predict $dG_{\mathrm{min}}/dT < 0$ (sections 4.3.2 and 4.3.3). A single exception of this behavior was observed in the large Hall bar of sample F in the low temperature regime (see section B of the appendix).

- Similar to the absolute value of G_{min} itself, the magnitude of the temperature dependent change $G_{\mathrm{min}}(T+\Delta T) - G_{\mathrm{min}}(T)$ scales with the length of the edge [Compare, for example the distance between the 2K and 8K data for similar E_{G} in figure 5.19 (a) and (b)]. This shows that, at sufficiently low temperatures, the temperature activated current also flows along the edge of the sample.

- Already at $T \leq 8\,\mathrm{K}$, the temperature dependence of G_{min} tends to become more pronouced with decreasing E_{G}, at least for small band gaps (samples C to F). This effect is discussed in greater detail in section 5.3.4.

- There is no clear dependency $G_0(E_{\mathrm{G}})$, in contrast to several theoretical models [see equation (4.10) [8]]. On the small Hall bar, where the edge state conductance is expected to be visible more clearly, most of the data saturates to $G_0 \approx 0.1\ \mathrm{e}^2/\mathrm{h}$ at low temperatures. The only exception is sample C, the only one with a Zn-free artificial substrate. However, in this context, the large change in mobility has to be kept in mind (figure 5.17). Although unlikely, a compensation of two opposing influences (increasing E_{G} and decreasing μ) it cannot be ruled out strictly.

5.3.4 Persistence of edge state dominated transport

As shown in the previous section, we do not find an increase of the edge state conductance when increasing E_{G} by a factor of five [see black dots in figure 5.19 (a) and (b)]. This contradicts theoretical predictions [7, 8], and requires further consideration. A possible cause of this contradiction will be discussed in section 5.3.6. Nonetheless, as it will be demonstrated in the following, maximized band gaps are efficient in suppressing parasitic bulk conductance, and therefore allow to study edge state dominated transport at elevated temperatures.

In order to discuss trends in bulk versus edge state conductance, we again make use of the different geometrical scaling of the two types current paths on the large (lHB) and small Hall bar (sHB). The raw ratio of minimum conductances,

$$\gamma = \frac{G_{\mathrm{min,\ sHB}}}{G_{\mathrm{min,\ lHB}}} \tag{5.12}$$

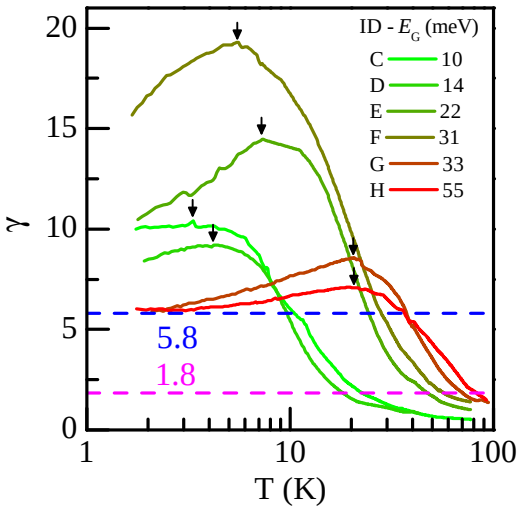

Figure 5.20: The ratio γ [equation (5.12)] for the samples C, D, ..., H. Arrows indicate maxima. Dashed blue (magenta) line indicates threshold where bulk conductance equals edge state conductance in large (small) Hall bar.

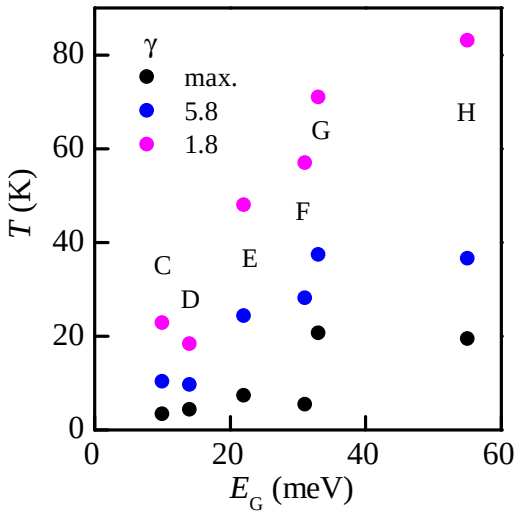

Figure 5.21: Temperatures of characteristic ratios of small and large Hall bar minimum conductance of samples C-H. See figure 5.20 and equation (5.13).

of samples C, D, ..., H is calculated, and shown in figure 5.20 as function of temperature. The most important observation is of qualitative nature: Whereas the overall profile of all traces is comparable, the characteristic temperature scale significantly increases with increasing band gap. This trend can be quantified by looking at distinct threshold temperatures of the system. Without any knowledge on the details of the individual temperature dependencies of the bulk (G_{bulk}) and edge (G_{edge}) conductance and by considering only the device dimensions ($l_{\text{edge,sHB}}/l_{\text{edge,lHB}} = 58/620$), one finds a theoretical expression for γ:

$$\gamma = \frac{G_{\text{bulk}} + G_{\text{edge,sHB}}}{G_{\text{bulk}} + \frac{58}{620} G_{\text{edge,sHB}}}. \tag{5.13}$$

In the limit of vanishing bulk conductance, equation (5.13) reproduces the ratio of the edge path lengths $\gamma \approx 10$. In section 5.2.2, it was already shown that the bulk conductance in samples with finite energy gaps is caused by thermal activation, and freezes out at low temperatures [equation (5.10)]. Since the scaling of edge state conductance with the inverse of the path length is caused by sample imperfection, the scaling of different samples scatters notably (figure 5.20). In particular, for sample F, γ is 16 at $T = 2\,\text{K}$, and rises to 19 (topmost black arrow). This reflects the exceptionally low G_{min} of the large Hall bar, as seen in figure 5.19. Given the scattering in the data, all following discussions

on threshold temperatures only have qualitative character. With increasing temperature, bulk conductance sets in, and $\gamma \to 1$, since the aspect ratios of both Hall bars are similar. In between the two extrema $\gamma = 1$ and $\gamma = 10$ one can identify characteristic values of $\gamma = 5.8$ and 1.8, which correspond to the situations when the bulk conductance G_0 equals the edge state conductance of the large ($G_0 = 58/620 \times G_{\mathrm{min,sHB}}$) and small Hall bar ($G_0 = G_{\mathrm{min,sHB}}$). The characteristic temperatures at which these criteria are met are shown as dashed lines in figure 5.20, and the extracted values are plotted in figure 5.21 as function of E_{G} (blue and magenta dots). The increase of the characteristic γ-values with increasing E_{G} is evident, and is a clear indication that maximized energy gaps significantly increase the temperature regime where edge state conductance is the dominant transport mechanism in the bulk gap. Moreover, this shows that care has to be taken when assigning a measured current to pure edge state conductance if the band gap is very small. For example, given that E_{G} is as low as 1.2 meV in Ref. [137], the observed power-law dependency $R_{\mathrm{edge}} \propto T^{-0.5}$ (see section 4.3.1) may be due to residual bulk conductance. Interestingly, γ does not drop monotonously from its ratio at the lowest temperature to $\gamma = 1$ at high temperature. Instead, an intermediate maximum is observed for all samples (the one of sample C being questionable). It is marked by arrows in figure 5.20, and moves to higher temperatures as the band gap increases, similar to the threshold temperatures discussed previously (black dots in figure 5.21). In the previous section 5.3.3, it was shown that the edge state conductance increases considerably already below temperatures where bulk conductance becomes dominant. The maximum of γ is located in the regime where the edge-state-type increase of conductance is most pronounced, and still dominates the exponential bulk conductance. This reflects the trend that, while the magnitude of the temperature-activated edge conductance approximately scales with the low-temperature limit of edge state conductance $G_{\mathrm{min}}(0\,\mathrm{K})$, it is slightly more pronounced in the small Hall bar data [as an example, see figure 5.22 in the following section 5.3.5]. We do not have a definitive explanation for this behaviour. One candidate may be found in the slightly different geometries of the large and small Hall bar devices. They are not perfectly rescaled versions of each other. Instead, the fraction of the edge state path which follows the voltage leads is considerably larger for the small Hall bar (figure 5.1). An emergent hopping conductance, too low to be seen as an increase of bulk conductance, but sufficient to allow for hopping between the two opposite edges of the leads, would effectively lower the length of the edge current path l_{edge} and by that increase G_{min} (which is proportional to l_{edge}^{-1}). Due to the sample geometry, such an effect would be more pronounced in the small Hall bar, in agreement with the observations. However, the absolute power-law increase of $G_{\mathrm{min}}(T)$ is much too large to be explained by a lowered effective

l_{edge} only.

5.3.5 Model of the temperature dependence of conductance

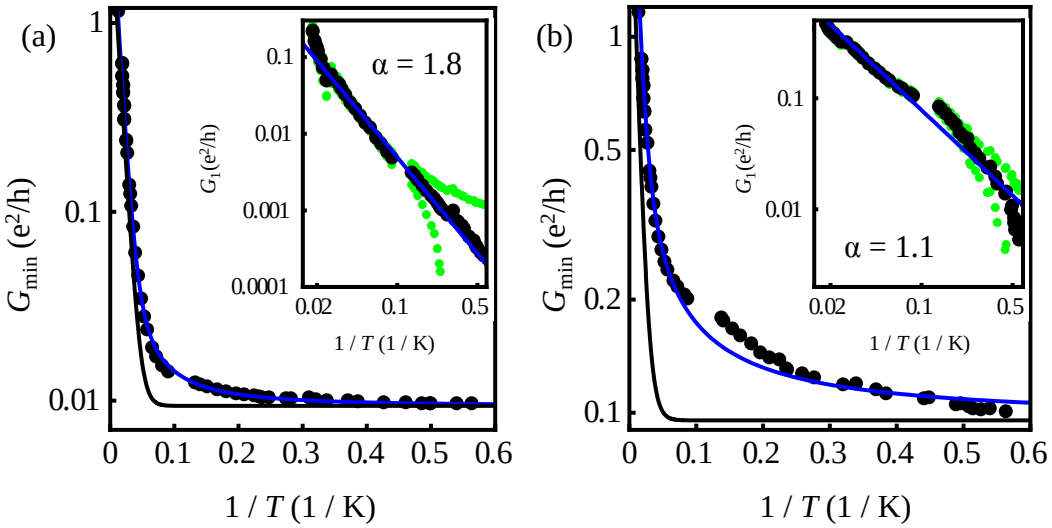

Figure 5.22: Arrhenius plot of temperature dependence of G_{min}. Data for sample E. (a): large Hall bar. (b): small Hall bar. Blue line is fit of equation (5.14), using equation (5.15). The black line has $G_1 = 0$, its deviation from the measured data is shown in the insets on a log-log scale. Straight blue line is fit to equation (5.15). Green dots show change in G_1 if subtracted data is rescaled by $\pm 10\,\%$.

Based on the qualitative observations discussed in the previous sections, we now turn to a more detailed analysis of $G_{\mathrm{min}}(T)$. In figure 5.22, G_{min} of sample E is shown over the whole range of measured temperatures (plots of all other samples are collected in section B of the appendix). Again, the data is plotted as function of T^{-1} on a logarithmic scale. The black lines are a model of a total conductance consisting of a constant edge state contribution G_0, and thermally activated conductance given by equation (5.10). Clearly, this fit does not capture the whole phenomenology of the system. The question arises whether the observed temperature dependence of G_{min} at temperatures below the regime of dominant bulk conductance ($T < 10\,\mathrm{K}$) is due to an additional trivial conducting channel, shows the temperature dependence of the edge channel itself, or is even caused by an interaction of bulk and edge states. To investigate this question, we split the low temperature edge state conductance G_{edge} in two parts [$G_{\mathrm{edge}}(T) = G_0 + G_1(T)$], and model the total G_{min} as

$$G_{\mathrm{min}}(T) = G_{\mathrm{th}}(T) + G_0 + G_1(T), \tag{5.14}$$

with the temperature activated bulk conductance G_{th}, discussed previously in section 5.2.2 [equation (5.10)]. If one does not limit the search for an explanation of $G_1(T)$ to works which focus on topological conductance, a wide variety of temperature dependencies can be found in the literature. For two-dimensional systems, an overview is found in Ref. [163], and many mechanisms exhibit an "exponential" type of temperature activation. Conductance in an impurity band is expected to result in a $G \propto \exp(-E_2/2k_{\mathrm{B}}T)$ dependency, variable-range hopping in $G \propto \exp[-(T_0/T)^{\nu}]$ with ν depending on the density of states at the Fermi level [164]. We have carried out various fits of this exponential type of $G_1(T)$. Whereas individual samples can be modelled satisfyingly, in many others, the fit only works in a limited temperature regime. Furthermore, the fitting parameter range of either activation energies E_2 or temperatures T_0 is very broad, and in particular, does not coincide for small and large Hall bar of the same sample. This observation led us to discard these types of fits, since both E_2 and T_0 are parameters which should be assessable from material parameters [163, 164], and should therefore be identical for small and large Hall bar. Instead, we have found that $G_1(T)$ can be modelled as a power law trace of the form

$$G_1(T) = A_1\, T^{\alpha}, \tag{5.15}$$

for most samples and a wide range of temperatures. By subtracting $G_0 + G_{\mathrm{th}}$ (black line) from the measured data, one can extract $G_1(T)$. Plotting $G_1(T)$ on a log-log scale (insets of figure 5.22) results in linear traces, and the exponent α in equation (5.15) can be determined by a linear fit on the log-log scale. The sensitivity of the power-law scaling to the fitting procedure is illustrated by the green dots in the insets of figure 5.22, which are obtained by changing the subtracted $G_0 + G_{\mathrm{th}}$ by $\pm 10\,\%$. Occasionally, the fit does not reproduce the measured G_{min} over the whole temperature range. Some exceptions are shown in section B of the appendix. Note that, even though equation (5.15) has a form similar to ΔG in equation (4.8), this does not point to Luttinger liquid physics, since G_1 is added to the conductance, whereas ΔG is subtracted, as it is a backscattering term.

The power α of samples C to H is shown in figure 5.23 as function of the band gap. Values of $0.9 < \alpha < 2.1$ are found. The set of data allows to suspect a trend of decreasing α with increasing E_{G}. For the large Hall bars, this trend sets in only at higher energy gaps, and is very abrupt [samples F and G in figure 5.23 (a)]. Clearly, a larger set of data is needed to make this observation definitive. When discussing the presence (or absence) of clear systematics in $\alpha(E_{\mathrm{G}})$ one also has to note the irregular shape of the measured traces $R_{\mathrm{xx}}(U_{\mathrm{G}})$, which were used to determine G_{min}. Traces of sample C and E are shown in figure 5.24 as examples. The width of the curves is not related to the magnitude of E_{G}, and the shape is usually different for large and small Hall bars. The gate-voltage position of

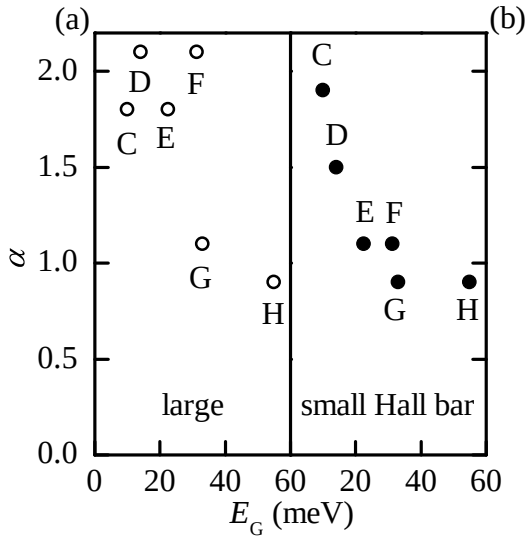

Figure 5.23: Power α obtained from fitting equation (5.15) to $G_{\min}$ of (a) large and (b) small Hall bar.

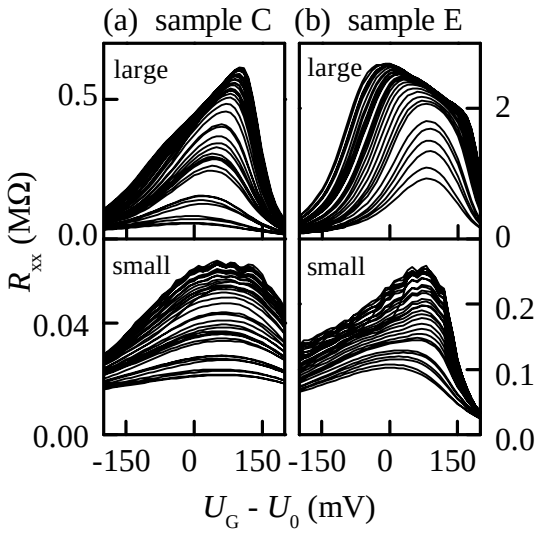

Figure 5.24: R_{xx} as function of gate voltage (relative to the voltage at maximum R_{xx}). Temperatures from 1.7 K (high R_{xx}) to 20 K (low R_{xx}). (a): sample C ($E_G = 10$ meV). (b): sample E ($E_G = 22$ meV).

the maximum $R_{xx}(U_G)$ moves with increasing temperature, indicating a thermal activation of trapped charges. The direction of the shift is varying (see for example large and small Hall bar data of sample E). All these features point to a spatially inhomogeneous influence of the gate electrode on the Fermi energy. Depending on the local density of trapped charges, the gate voltage that is needed to deplete the 2DEG changes slightly. Therefore, the onset of n-type or p-type conductance takes place at slightly different gate voltages for different areas of the mesa, resulting in the irregular shapes of $R_{xx}(U_G)$. Note the presence of reproducible spikes in the small Hall bar data, a signature of universal conductance fluctuations (UCFs). Similar features were found in [136], and were attributed to the gate-induced resonance and off-resonance of backscattering at a charge puddle [8, 133]. This requires the number of scatterers to be in the $\lesssim 100$ range, which is in agreement with the observed $G_{\min}$. In the large Hall bar data, no such features are observed, indicating that the number of scatterers is high enough to average out their individual resonances. All these observations suggest that the details of the gating mechanism of the Fermi energy are an important aspect regarding the sample characteristics in the QSH regime. This aspect will be discussed in the next section.

5.3.6 Puddle density and electrostatic gating

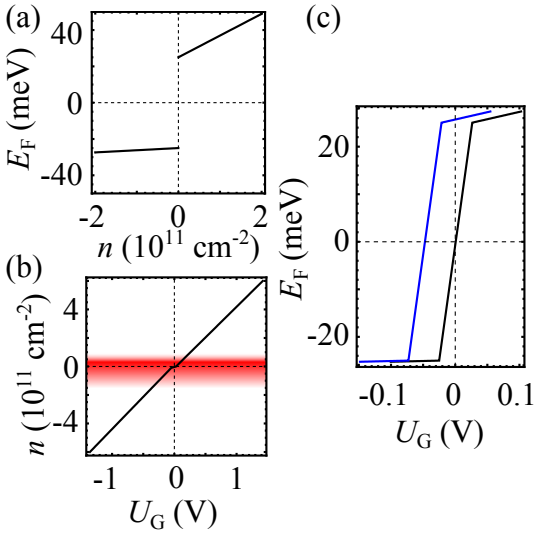

Figure 5.25: (a) Fermi energy vs. carrier density of a QW with $E_G = 50\,\text{meV}$. (b) Carrier density as function of gate voltage [equation (5.16)]. Red area indicates typical regime where Hall resistance measurements are not meaningful. (c) Fermi energy vs. gate voltage for interface carrier density $n_{int} = 0$ (black) and $1.3 \times 10^{10}\,\text{cm}^{-2}$ (blue).

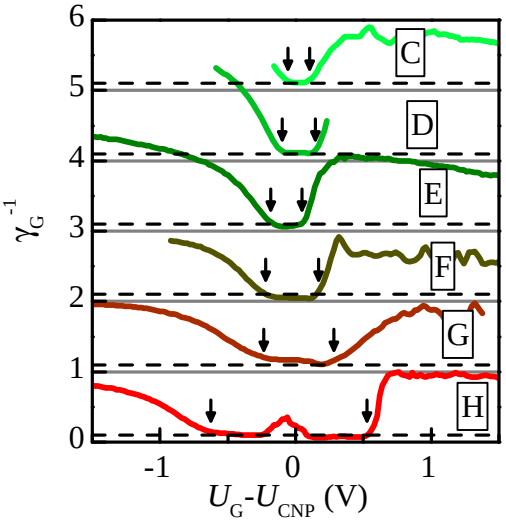

Figure 5.26: Ratio of conductance [equation (5.17)] as function of gate voltage for samples C to H. Measurements of samples C, D,...,G are offset by $+5, +4, \ldots, +1$ for clarity. Dashed lines at 0.1 indicate ideal value of pure edge conductance. Arrows guide the eye to the onset of sheet conductance.

Summarizing the experimental observations on the edge state conductance, we have to notice that, so far, a discrepancy between theory and measured $G_{min}(T, E_G)$ persists, just as discussed previously in section 4.3. The increase of G_{min} with increasing temperature is in strong contrast to all theories based on Luttinger liquid models (section 4.3.2). Considering the charge-puddle-scattering theory (section 4.3.3), the temperature dependence indicates puddles with large dwell times of electrons, and/or short dephasing times (i.e. large puddles with high density of states) [156]. The presence of such a scattering mechanism is supported by scanning-gate experiments [141], and the presence of UCFs on $R_{xx}(U_G)$ (figure 5.24). However, the fact that the puddle density n_p seems to be insensitive to E_G is not expected [7, 8]. We provide some remarks on the differences between the theoretical model of Refs. [7, 8] and the actual experimental situation to address this discrepancy.

In Refs. [7, 8], the calculation of $n_p(E_G)$ is based on the assumption that the Fermi level is located in the center of the energy gap, and n_p decreases with increasing E_G since

it becomes less likely that defect-charge-induced offsets of the conduction- or valence band intersect with E_F and form a puddle. By having a closer look on the actual control of E_F by means of electrostatic gating, we demonstrate that this situation is hard to realize in our devices. A large band gap QW with $E_G = 50\,\mathrm{meV}$ and parabolic bands with typical effective masses $m_e = 0.02\ m_0$, $m_h = 0.2\ m_0$ of electrons and holes is chosen as a model system for the discussion. Using the density of states of a two dimensional system with parabolic energy dispersion $D_{2D} = m_{e,h}\pi^{-1}\hbar^{-2}$ and the linear relationship between the carrier density and density of states $n = D_{2D}(E_F - E_{VB,CB})$ (where $E_{CB,VB}$ is the energy of the valence- or conduction band, depending on the type of carriers), one finds a dependency between carrier density and Fermi level as shown in figure 5.25 (a). Note, in particular, the different slopes for electrons and holes. To calculate the relationship between carrier density n and gate voltage U_G, we adopt a simple capacitor model [162], and find:

$$U_G(n) = n\,\frac{e}{\varepsilon_0\,\varepsilon_{CMT}}\,d_{barrier} + (n - n_{int})\,\frac{e}{\varepsilon_0\,\varepsilon_{ins}}\,d_{ins} + \frac{E_F(n)}{e}. \tag{5.16}$$

With the dielectric constants of the barrier material and the gate insulator $\varepsilon_{CMT} = 12.7$ and $\varepsilon_{ins} = 5.1$ [155], and a possible charge at the interface with the density n_{int}. The carrier density as function of the gate voltage is shown in figure 5.25 (b) for the typical insulator and top barrier thicknesses (d_{ins}, $d_{barrier}$) of samples C to H. The calculated gate efficiency $dn/dU_G = 4.0 \times 10^{11}\,\mathrm{cm^{-2}\,V^{-1}}$ is slightly higher than the one we find experimentally for samples A to H (in the range of $3 \times 10^{11}\,\mathrm{cm^{-2}\,V^{-1}}$, see figure 5.5), indicating that the actual dielectric constant of the insulator is lower, probably because of the low-temperature deposition method [165]. This, however, is not relevant for the following argumentation. The function $n(U_G)$ is almost a straight line, and the regime where the carrier density is identically zero is very narrow. In fact, the small flat step at $U_G = 0$ has not been resolved in $n(U_G)$ measurements on any sample presented in this thesis. In contrast, in samples with non-zero energy gaps (B to H) we observe that the Hall voltage becomes highly irregular already at finite densities [critical densities are typically $\approx \pm 1 \times 10^{11}\,\mathrm{cm^{-2}}$, red area in figure 5.25 (b)], and n can no longer be calculated from R_{xy} [see figure 5.5 and figure 5.6 (e)]. This shows that the metal-insulator transition (MIT) in our semiconducting 2DEGs is dominantly driven by localization effects [163, 166]. In the presence of an inhomogeneous potential landscape in the QW, carriers in an energetic regime close to the edge of the conduction- or valence band are localized, and do not contribute to conductance, unless they are activated thermally [163]. This means that in the largest fraction of the gate voltage regime where the sample is insulating, the Fermi energy is pinned to the conduction- or valence band, and the presence or absence of charge puddles does not necessarily depend on the band gap of the QW. In this context, one has

to consider the fact that charged traps at the interface of the CdHgTe top barrier and the $SiO_2 - Si_3N_4$ insulator material are likely to cause an irregular potential landscape in the QW [167, 168] (see also the discussion in the later section 5.4). Figure 5.25 (c) illustrates the shift of the Fermi energy with respect to U_G for a charged interface area with $n_{int} = 1.3 \times 10^{10}\,cm^{-2}$. Such a local charge is sufficient to render the electrostatic gating of the Fermi energy in the center of the energy gap impossible to achieve for different areas of the device simultaneously. As a possible cause of the observed absence of a clear $G_{min}(E_G)$ dependency, we thus suggest that the measurement of $G_{min}(U_G)$ in devices larger than a few μm^2 does not probe the pure edge state conductance when the Fermi energy is in the center of the energy gap, but instead at a regime where E_F is pinned to the top of the valence band, the puddle density is large, and the bulk is still insulating due to localization effects (because of the larger density of states in the valence band and the lower mobility of holes, the pinning to the valence band is probably favored over the conduction band).

sample	E_G (meV)	ΔU_G (V)	Δn ($10^{11}cm^{-2}$)	$\Delta U_G/E_G$
C	10	0.16	0.5	16
D	14	0.24	0.7	17
E	21	0.23	0.7	10
F	31	0.39	1.2	13
G	33	0.51	1.5	15
H	55	1.15	3.5	21

Table 5.2: Characteristics of the transition from sheet- to edge conductance of samples C to H. Band gap E_G, Regime of edge conductance ΔU_G (arrows in figure 5.26), density shift in the insulating regime Δn, and ratio of edge conductance regime and band gap.

This assumption is supported by the very irregular shape of $G_{min}(U_G)$ as shown previously (figure 5.24), and the fact that the regime where the resistance scales with the length of the edge channel persists for a range of gate voltages much larger than the range where the bulk of the sample is charge-neutral. The latter observation is illustrated in figure 5.26. The ratio of conductances

$$\gamma_G^{-1}(U_G) = \frac{G_{lHB}(U_G)}{G_{sHB}(U_G)} \tag{5.17}$$

is shown as function of gate voltage for samples C to H (the index "G" is given to indicate the gate-dependency of γ_G^{-1}, in contrast to equation (5.12), where γ is calculated from the ratio of the minimum conductances G_{min}). Incomplete traces are due to inappropriate ranges of gate voltage scans with respect to the CNP. In the simplest case, $\gamma_G^{-1} = 0.1$

indicates pure edge state conductance and $\gamma_G^{-1} = 1$ pure sheet conductance. For realistic samples, effects like different mobilities of large and small Hall bar and the aforementioned irregular shape of $R_{xx}(U_G)$ at the CNP complicate the signal (in particular, the latter is the cause of the spike-artifact in the trace of sample H at $U_G \approx 0\,V$). Nonetheless, one can clearly identify sheet- and edge-conducting regimes as function of U_G (indicated by arrows). Due to the transition to the insulating regime already at finite carrier densities, the U_G-width of the edge dominated regime, ΔU_G, is more than one order of magnitude larger than the U_G-range, where the sample is charge neutral [identical to the band gap of the sample, see figure 5.25 (c)]. The values of ΔU_G, E_G and their ratios are listed in table 5.2. It is worth noting that ΔU_G is also larger than the typical width of the maximum in resistance $R_{xx}(U_G)$ (see figure 5.24), which is routinely identified as the regime of pure edge conductance. This is another indication that by simply measuring the maximum of $R_{xx}(U_G)$, one does not probe the (supposedly constant) edge state resistance. Instead this approach probes the edge state conductance in the regime where the scattering interaction of the edge states with charge puddles is maximized, and the bulk conductance has not set in yet. With the gating efficiency $dn/dU_G \approx 3 \times 10^{11}\,cm^{-2}\,V^{-1}$, the amount of localized carriers Δn can also be calculated (table 5.2), and reasonable numbers are found [163]. Furthermore, at first sight, one is tempted to correlate E_G and ΔU_G (figure 5.26). However, according to the model discussed above [equation (5.16)], an increase in E_G should be added to ΔU_G with a scaling factor of one, which is not observed. Instead, we suggest that the trend in ΔU_G is caused by a decrease in quality from samples C to H (figure 5.17) which leads to an onset of localization already at higher carrier densities. The conclusion to draw from the previous discussion is that a distinct $G_{min}(E_G)$ dependency, as predicted by [7, 8], may be absent in our measurements, because we probe the edge state conductance in a regime where the density of puddles (i.e. scatterers) is maximized and independent of E_G. Based on this assumption, we have employed a different approach to alter the puddle density. First results on hysteretic gating in the QSH-regime are presented in section 5.4.

Whereas the previous discussion offers a mechanism to explain the absence of a dependency $G_{min}(E_G)$, the origin of the power-law increase in $G_{min}(T)$ remains unresolved, and a definitive answer cannot be given based on the data presented in this work. However, we want to collect some remarks and preliminary conclusions in the following. The edge state conductance was modelled as

$$G_{edge} = G_0 + A_1 T^{\alpha} \tag{5.18}$$

(section 5.3.5). Even though, an edge state conductance G_{edge} larger than $2e^2/h$ was never

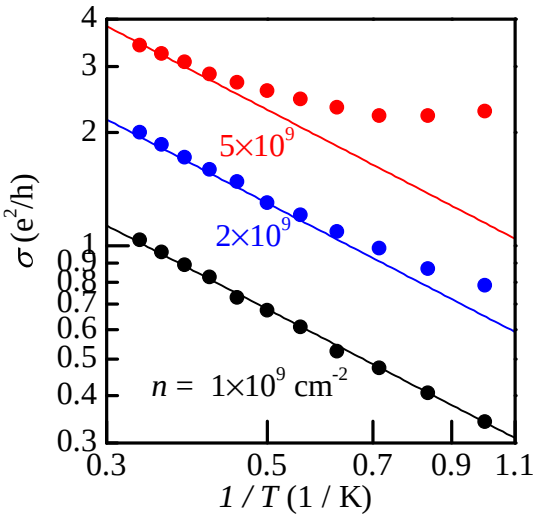

Figure 5.27: Temperature dependence of conductance of a n-type GaAs 2DEG, for three different carrier densities. Data from [169]. Lines are fits to equation (5.15), with $\alpha = 1$.

observed directly in this work because of the dominant temperature-activated conductance at high temperatures and the long edge channels, equation (5.18) implies that this limit is crossed at high enough temperatures or in smaller devices. However, this would mean that the temperature-activated edge state conductance cannot be carried by a single pair of helical modes, and other channels of edge conductance have to exist. Probing the presence or absence of a high-temperature limit of edge state conductance on more appropriate (i.e. smaller) samples is one of the upcoming tasks. In the context of non-topological conductance, it is worth noting that the temperature-dependence of conductance in the regime of localization-driven MIT has been studied extensively. Figure 5.27 shows the conductivity σ of an n-type GaAs 2DEG for three different carrier densities in the vicinity of the MIT. Data was extracted from [169], and plotted on a log-log scale as function of T^{-1} to simplify the comparison with our data (see insets of figure 5.22). Since the mobility of GaAs 2DEGs is typically one order of magnitude higher than of HgTe 2DEGs, the critical density is much lower (for comparison, see Δn in table 5.2). Strikingly, below the critical carrier density, $\sigma(T)$ can be modelled by a power-law fit [equation (5.15)] with $\alpha = 1$ (black and blue traces), similar to the high-bandgap samples (figure 5.23). Despite this analogy, the power-law increase of conductance, $G_1(T)$, can still be safely characterized as edge localized due to the scaling argument (see figure 5.19 and 5.22). As a possible explanation of this phenomenology, one can think of either an edge which was rendered conducting by edge-localized mechanisms such as etching-damage or inhomo-

geneous gating, or an interaction of topological edge states with the nearby bulk states. Again, a definitive answer cannot be given at this stage.

5.4 Hysteresis effects and edge state conductance

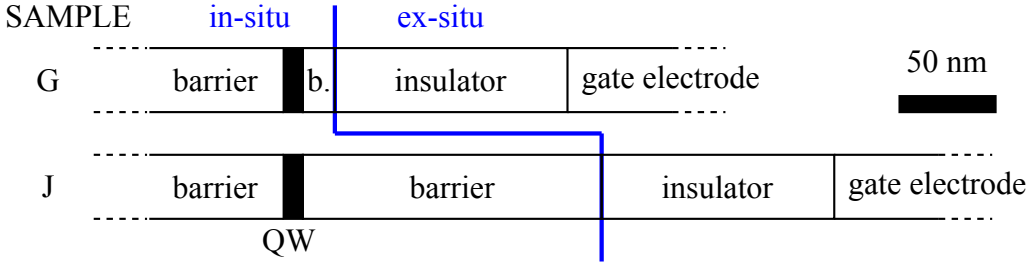

Figure 5.28: True-to-scale sketch of layer stacks of samples G and J. Blue line represents first interface which is exposed to air.

Based on the conclusions from the previous section 5.3.6, a different approach to optimize edge state conductance is presented in the following. In HgTe-based metal-insulator-semiconductor structures, the range of the gate-induced shift of carrier density n in the QW is limited by hysteretic effects [155]. This limitation is explained by trapped states which reside at either the interface of the CdHgTe top barrier and the $Si0_2 - Si_3N_4$ dielectric, or in the whole volume of the insulator [170]. If U_G exceeds a certain threshold, charging of these states sets in, and the gate efficiency dn/dU_G is lowered. This charging effect is hysteretic in the sense that one can no longer assign a distinct value of n to a value of U_G, but instead, the carrier density also depends on the gating history of the sample. Therefore, in a typical magnetotransport experiment, the hysteretic regime is avoided if possible. Since the magnitude of the hysteresis-free shift of carrier density decreases with increasing top barrier thickness, and we have chosen thin barriers ($d_{barr} \approx 15 - 18$ nm) in samples A to H, all experiments discussed until now were far from the hysteretic regime. This is changed in the following set of experiments.

5.4.1 Hysteretic training of edge state conductance

Since we suspect backscattering caused by the irregular electrostatics of the sample to be the cause of the non-quantized edge state conductance (see section 5.3.6), we have investigated a heterostructure where the electrostatics can be changed by hysteretic charging of the interface states. Sample J is a compressively strained QW with an exceptionally large barrier thickness of $d_{barr} = 141$ nm. Therefore, a pronounced hysteretic gating behaviour is expected. The HRXRD scan and the parameters of all layers are illustrated in

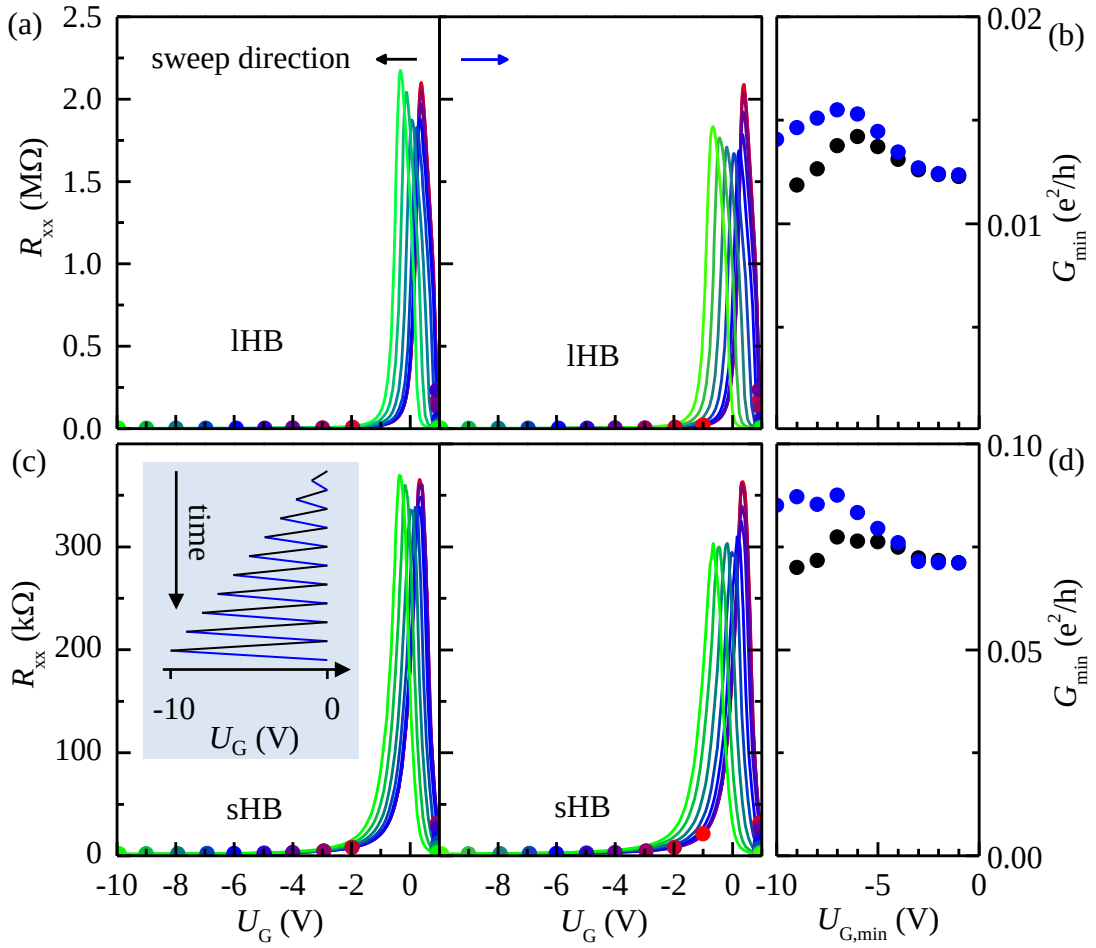

Figure 5.29: (a) and (c) Longitudinal resistance of sample G as function of gate voltage, of large and small Hall bar. Colored dots highlight limits of scans. Inset in (c) illustrates measurement sequence. Colors black and blue indicate scan direction. (b) and (d) Minimum conductance as function of largest negative gate voltage applied to the Hall bar.

figure 2.30. The energy gap $E_G = 33\,\text{meV}$ is confirmed in temperature-activated conductance measurements. To illustrate the influence of the top barrier thickness, comparison measurements have been carried out on sample G (which has a similar $E_G = 33\,\text{meV}$, see table 5.1). The difference in the layer stacks of the two samples is illustrated in figure 5.28. Trapped charges are assumed to exist at the top barrier-insulator interface (blue line) and in the insulator itself. The top barrier of sample J is almost by a factor of ten larger compared to sample G.

In order to probe the effect of hysteretic changes of the electrostatics of the device on the QSH edge state conductance, a fixed sequence of gate sweeps has been carried out at $T \approx 2\,\text{K}$. The procedure is illustrated in the inset of figure 5.29 (c). The sweep limits have

been adjusted for each sweep of the sequence. The maximum positive gate voltage is kept constant, and the maximum negative gate voltage $U_{\mathrm{G,min}}$ is increased by 1 V in negative direction each time. The measured R_{xx} for sample G are shown in figure 5.29 [(a) - large Hall bar, (c) - small Hall bar]. For every gate sweep, the minimum conductances G_{min} have been extracted from the maximum of R_{xx}. Results are shown in (b) and (d) for the large and small Hall bar respectively. The qualitative findings of the measurement are summarized as follows:

- For each gate sweep, a maximum of R_{xx} is present, indicating that the Fermi energy was shifted from the conduction- to the valence band or vice versa.
- For low $|U_{\mathrm{G,min}}| < 3\,\mathrm{V}$, no hysteresis is observed. The traces are almost duplicates.
- At $|U_{\mathrm{G,min}}| \gtrsim 3\,\mathrm{V}$ hysteresis sets in, and the maximum of $R_{\mathrm{xx}}(U_{\mathrm{G}})$ is shifted to lower gate voltages.
- At the same time, the value of the minimum conductance G_{min} changes slightly [figure 5.29 (b) and (d)]. This is another indication that the dominant backscattering mechanism of the QSH edge states is caused by charge puddles. As the interface charge is changed, so is the induced potential landscape in the QW, and finally the puddle density. An optimum negative $U_{\mathrm{G,min}}$ exists above which G_{min} decreases again.
- With increasing $|U_{\mathrm{G,min}}|$, the traces begin to deviate for the different sweep directions [black and blue dots in figure 5.29 (b) and (d)], indicating that some of the charging effects are lifted again as the gate voltage is swept back to zero.

The same set of experiments has been carried out on the highly hysteretic sample J, see figure 5.30. Whereas the behaviour is qualitatively comparable to sample G, the hysteresis-induced changes to the sample are substantially more pronounced. Most strikingly, with hysteretic training, the minimal conductance is significantly enhanced for the large and small Hall bar [blue dots in figure 5.30 (b) and (d)]. Note that the measured conductances are reproduced in a second measurement set at higher resolution (small empty dots). This data has been measured after resetting the sample to its initial condition by warming it up to room temperature. The maximum values ($G_{\mathrm{min,lHB}} = 0.4\ e^2h^{-1}$, $G_{\mathrm{min,sHB}} = 1.6\ e^2h^{-1}$ represent the highest conductances of edge states with the path lengths investigated in this work (620 and 58 µm, see figure 5.1). Both values are below the ideal $2e^2h^{-1}$, and it is remarkable that the relative enhancement of G_{min} significantly differs for the large and small Hall bar (the trained G_{min} exceed the untrained G_{min} by a

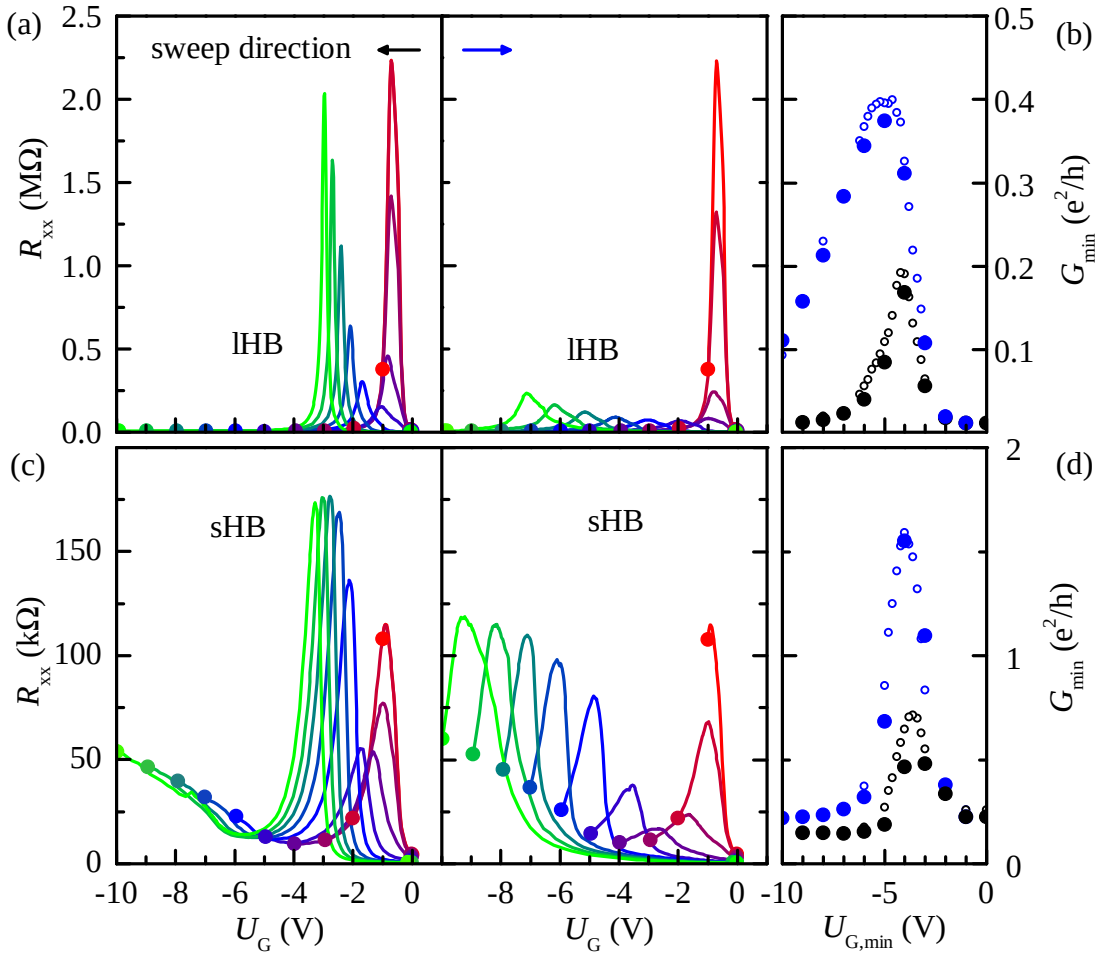

Figure 5.30: (a) and (c) Longitudinal resistance of sample J as function of gate voltage, of large and small Hall bar. Colored dots highlight limits of scans. (b) and (d) Minimum conductance as function of largest negative gate voltage applied to the Hall bar. Measurements with smaller step size (empty dots) have been measured at a different cooldown.

factor of $\times 35$ and $\times 7.7$ for the large and small Hall bar, respectively). This reflects the fact that for low puddle densities n_p, the relationship $G_{min} \sim n_p^{-1}$ no longer holds, since, as the inelastic mean free path between scattering events exceeds the length of the edge in the QSH regime, G_{min} approaches the ideal $2e^2h^{-1}$ asymptotically [8].

The aforementioned enhancement of G_{min} of the large Hall bar by a factor of $\times 35$ shows the effectiveness of the hysteretic training of QSH edge state conductance. In the following paragraphs, further insight into the mechanisms which cause the change in G_{min} are presented. Given the early stage of research on this subject (samples G and J are by now the only two which have been analyzed with the focus on hysteresis), the picture is far from comprehensive, and several open questions will be emphasized.

5.4.2 Studies of the charging mechanism

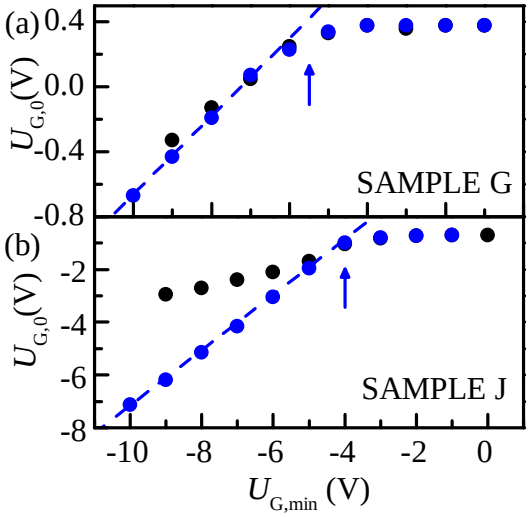

Figure 5.31: The gate voltage where R_{xx} is maximized as function of the largest negative gate voltage, the sample was exposed to. Data from large Hall bar of (a) sample G and (b) sample J. Colors indicate sweep direction. Dashed lines are linear fits. Arrows indicate approximate position where charging sets in.

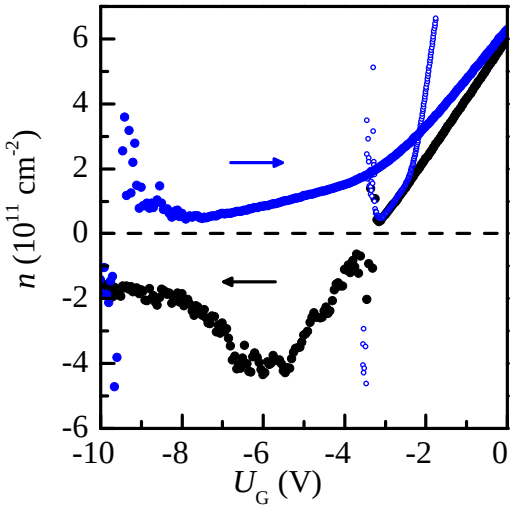

Figure 5.32: Carrier density of small Hall bar of sample J as function of gate voltage for both sweep directions (arrows). Measured after the sample was exposed to $U_G = -10\,V$. Small empty dots denote density from sweep in positive direction, on rescaled and offset x-axis.

As it was demonstrated in the previous section, the overall hysteretic change of transport properties is much more pronounced in sample J compared to sample G. Surprisingly, however, the gate voltage where the charging effects set in is comparable. Figure 5.31 displays $U_{G,0}$, the position of the maximum of R_{xx} as function of the largest $|U_{G,min}|$ to which the sample was exposed to. Colors denote the sweep direction [see inset of figure 5.29 (c)]. Large Hall bar data is shown, small is similar. Charging sets in at approximately $-5\,V$ and $-4\,V$, respectively (blue arrows). This is unexpected if one assumes that charging occurs by tunneling of carriers from the QW to trap states located only at the interface [155]. The onset of hysteresis should scale with the voltage drop across the top barrier. From equation (5.16) one can deduce the ratio of this voltage drop for samples G and J to be rougly 10/1, in contradiction to the almost similar measured values. We speculate that this is an indication that the trap states are not pinned to the top barrier-insulator-interface, but spread in the whole thickness of the $SiO_2 - Si_3N_4$ superlattice. These traps may be present, because the chemical-vapor deposition of the dielectric is done at temperatures significantly lower than the ideal processing parameters in order to avoid thermal

damaging of the Hg-based layers. As a consequence, charged defects may form in the insulator.

Despite the similar onset of the hysteresis, the slope of the shift of $U_{G,0}$ is different for samples G and J. We find $dU_{G,0}/dU_{G,min} = 0.24$ and 1.05, respectively (dashed lines in figure 5.31). With being approximately unity, the latter value implies that above the hysteretic threshold, the entire influence of the gate on the Fermi energy of the QW is compensated by opposite charges in the trap states. This is in agreement with the measured carrier density n, which has been calculated from the gate-dependence of R_{xy} at $B = 300\,\mathrm{mT}$ [equation (5.4)] and is displayed in figure 5.32. Note that, since these measurements were performed after the sample was exposed to the full $U_{G,min} = -10\,\mathrm{V}$, the applied voltage U_G cannot be mapped one-to-one to $U_{G,min}$ of the hysteresis measurements [figure 5.31, figure 5.30 (b) and (d)]. Furthermore, we stress that the high longitudinal resistance in the p-regime complicates the accurate measurement of the pure Hall resistance. Therefore, the accuracy of the calculated carrier density n is limited for $n < 0$. The raw data of the measurements is presented in section C.0.1 of the appendix to illustrate the limitations of the analysis. Nonetheless, the full compensation of the gate influence is reflected in the constant p-type carrier density at large negative gate voltages (black dots). Interestingly, we find two different plateaus of $n = -4 \times 10^{11}\,\mathrm{cm}^{-2}$ and $-2 \times 10^{11}\,\mathrm{cm}^{-2}$ at different gate voltage regimes. Two possible scenarios may be the cause of the two plateaus. Firstly, this may reflect the energy distribution of the trapped states. Tsau et al. [167] report on a density of trap states which is high at the edges of the conduction- and valence band, and low in between. Depending on the applied gate voltage, charging of only one or both regimes may occur. This could be the cause of the two levels of minimum density n. Alternatively, a closer look at the calculation of n (see section C.0.1 of the appendix) shows that the decrease in carrier density with increasing negative voltage at $U_G < -6\,\mathrm{V}$ is exclusively caused by an increase in device resistance, whereas the Hall voltage U_{xy} is constant (see section C.0.1 of the appendix). This can also be seen by comparing the trace of n with R_{xx} at high negative voltages [green trace in left panel of figure 5.30 (c)]. Therefore, as the second explanation, the decrease in n may be an artifact caused by the increase of the resistance of the edge states. Given the still very high total resistance, edge states carry a notable fraction of the total current I and, as shown in figure 5.30 (d), become less conducting in this gate voltage regime. This will alter the Hall resistance, which is calculated as $R_{xy} = U_{xy}/I$, and with this, the carrier density n.

As the gate is swept back to $U_G = 0\,\mathrm{V}$ (blue filled dots in figure 5.32), the majority carriers change rapidly from p-type to n-type, before a regime with a low slope of dn/dU_G is reached. The latter is an indication that discharging of trapped states lowers the gating

efficiency. By rescaling the voltage axis by a factor of 0.18 (small blue empty dots), one can match the gating efficiency with the hysteresis-free regime of the black trace. From this observation, one can show that the broadening of the peaks of R_{xx} in the up-sweep direction [right panels of figure 5.30 (a) and (c)] is caused by the lower gating efficiency, as the widths of the down-sweep maxima [left panels of figure 5.30 (a) and (c)] coincide with the corresponding up-sweep maxima if their gate voltage axis is rescaled by the same prefactor of 0.18. A feature which is somewhat irritating is the presence of a gap in the hysteresis loop at the very beginning of the sweep to $U_G = 0\,V$ (blue dots in figure 5.32, at $U_G \approx -9.5\,V$). Given their high scatter and unphysical evolution with decreasing negative gate voltage, the positive electron densities at $-9.5\,V \lesssim U_G \lesssim -8.3\,V$ are measurement artifacts due to the high sample resistance. Still, in order to close the hysteretic loop, the p-type carrier density has to be removed with a high gating efficiency. We do not have a satisfying explanation for this mechanism, but note that a comparable discontinuity is seen in the transition from p- to n-conductance in the sweep in negative gate voltage direction (black dots in figure 5.32, at $U_G \approx -3\,V$).

5.4.3 Studies of the time dependence

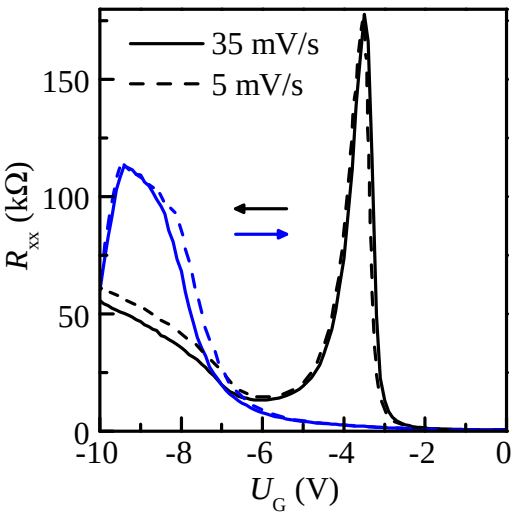

Figure 5.33: Longitudinal resistance of small Hall bar of sample J as function of gate voltage. Two sweep directions and scan speeds are shown. Sample has seen $-10\,V$ before.

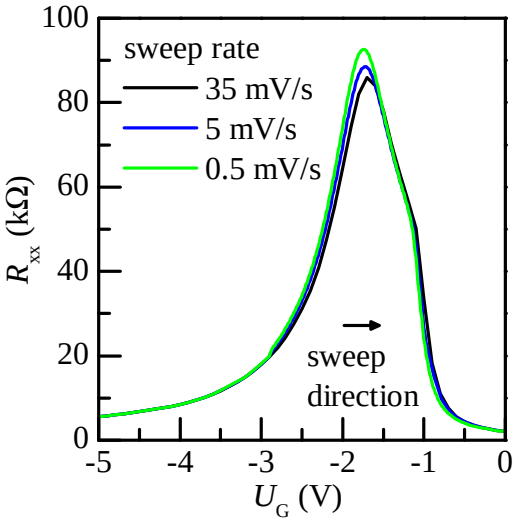

Figure 5.34: Longitudinal resistance of large Hall bar of sample J at close-to-optimal hysteresis level. Color-coding of sweep rate holds from $-3\,V$ to $-1\,V$ and is $35\,mV\,s^{-1}$ in neighboring regimes.

Just as in other material systems [170], the charging hysteresis effects in HgTe based

metal-insulator-semiconductor devices are not fully stable with time [171]. Capacitance-voltage measurements show that if such a system is driven into the hysteretic regime by an abrupt change in gate voltage, the amount of trapped charges changes with time. Both the time scale and the magnitude of this effect depend on various device properties, such as band gap, Fermi energy, insulator type and sample temperature. To address this issue, we have investigated the influence of the sweep rate of the gate voltage on the edge state resistance. The first measurement illustrates the global behavior of the system: figure 5.33 shows a set of bidirectional sweeps over the full range of $0\,\mathrm{V} \rightarrow -10\,\mathrm{V}$ for two different sweep rates. Both the position and magnitude of the maxima in resistance are independent of the sweep rate, but depend on the sweep direction. This indicates that the time at which the trapped states change their charge configuration is short enough to follow the change in gate voltage at both sweep rates, and thus, it is qualitatively justified to map G_{min} to $U_{\mathrm{G,min}}$ as it was done in figure 5.30 (b) and (d). However, the full traces are no perfect copies of each other (consider the regimes $U_{\mathrm{G}} = -7$ to $-10\,\mathrm{V}$ and -8 to $-6\,\mathrm{V}$ for down- and up sweeps), and a more detailed measurement shows that a weak time dependence exists on long timescales. For the data shown in figure 5.34 the large Hall bar was adjusted close to its optimum hysteretic condition ($U_{\mathrm{G,min}} = -5\,\mathrm{V}$). Since the sample was exposed to other voltages before, G_{min} is lowered compared to figure 5.30 (b). Three gate sweeps were performed at different sweep rates in the regime from $-3\,\mathrm{V}$ to $-1\,\mathrm{V}$ [for the fastest scan (black), the rate was kept similar in the full scan range]. An increase in the maximum R_{xx} is seen. The combination of the observations shown in figure 5.33 and figure 5.34 is interpreted as follows: regarding its charge configuration, the dominant response of the device on changes in U_{G} takes place faster than the scan rate in the experiments, and shows the hysteretic memory behavior discussed in the previous paragraphs. However, details change on a very long timescale. Further measurements are required to discriminate between these two types of responses, and to specify their influence on G_{min}.

5.4.4 Hysteresis in the positive gate voltage regime

In the previous discussion, the hysteretic effects have been triggered by sweeping the gate to increasingly negative voltages. This was done because the sample is slightly n-type, i.e., to first measure G_{min}, beginning from $U_{\mathrm{G}} = 0\,\mathrm{V}$, the gate has to be swept to negative voltages. However, hysteresis effects are expected to set in at positive gate voltages as well [155]. Still using sample J, we have probed the positive regime by means of a slightly modified version of the gating sequence shown in the inset of figure 5.29 (c). After cooling down the sample, U_{G} was swept to negative voltages until G_{min} was clearly observed

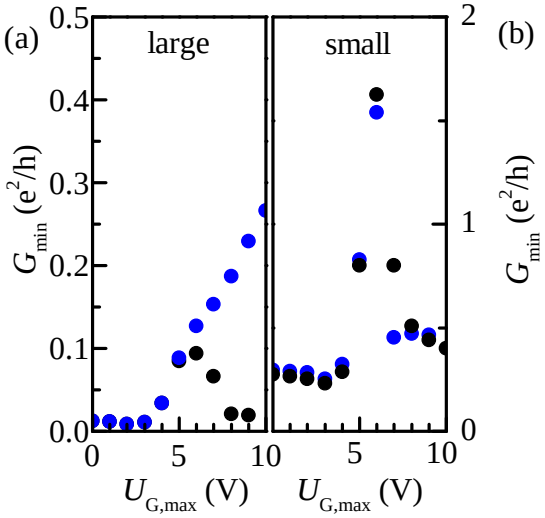

Figure 5.35: Minimum conductance as function of largest positive gate voltage the sample J was exposed to. Gate voltage sequence similar to inset of figure 5.29 (c), with signs inverted. Blue dots: sweep direction from positive to negative U_G, Black dots: reversed.

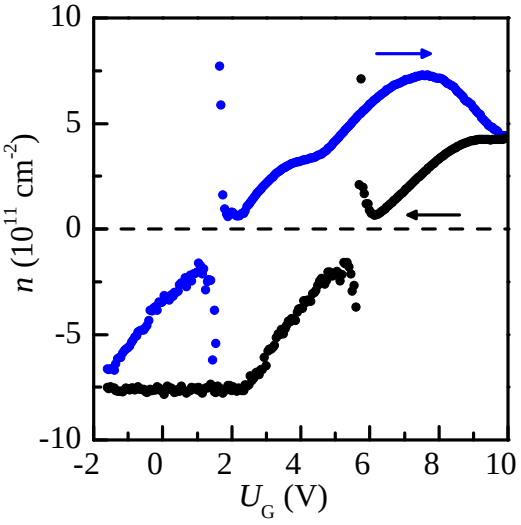

Figure 5.36: Carrier density of small Hall bar of sample J as function of gate voltage for both sweep directions (arrows). Measured after the sample has seen $U_G = +10\,V$.

($U_{G,min} = -1.6\,V$ and $-1.0\,V$ for small and large Hall bar). Sweep sequences were then done with increasing maximum gate voltages, $U_{G,max}$, while $U_{G,min}$ was kept fixed. The extracted G_{min} are shown in figure 5.35 on scales similar to figure 5.29 (b) and (d). It is clearly seen that hysteretic enhancement of G_{min} takes place as well in the positive regime. Even though the data shows some similarities to the results in the negative regime [note, in particular, the comparable maximum values of G_{min} of the small Hall bar in figure 5.35 (b) and figure 5.29 (d)], the overall picture is different, and more irregular. Most striking is the difference between large and small Hall bar regarding the dependency of G_{min} on the sweep direction. Whereas, for the large Hall bar [figure 5.35 (a)], this dependency is even more pronounced compared to figure 5.29 (b), $G_{min}(U_{G,max})$ of the small Hall bar is almost independent of the sweep direction [figure 5.35 (b)]. We do not have a conclusive explanation for this discrepancy, but suggest that, regarding the small Hall bar, the symmetry of $G_{min}(U_{G,max})$ is reflected in the symmetry of the hysteresis loop of the carrier density. Figure 5.36 shows the carrier density n in the positive gate voltage regime, measured in a similar way as the traces in figure 5.32. In contrast to figure 5.32, the sample is clearly in the hysteretic regime for both limits of the gate voltage. This may point to a similar charging condition of the hole-like trap states in the one limit and the electron-

like states in the other, and thus cause the similar G_{min}. For the sake of completeness, we note that the local maximum of n in the positive sweep direction (at around $+7\,\mathrm{V}$) is a true hysteretic overcompensation of carriers, in contrast to the local minimum of n in the sweep to the maximum negative voltage, seen in figure 5.32 (see discussion in section 5.4.2). This can be inferred from the raw Hall voltages, shown in section C.0.1 of the appendix. Even though, a possible relationship between the symmetry of the G_{min} and the carrier density hysteresis loop is found in the small Hall bar data, the pronounced difference to the large Hall bar remains irritating. Unfortunately, the hysteresis loop of the large Hall bar does not contribute helpful information, as it is highly irregular in the p-type regime (it is shown in section C.0.2 of the appendix for completeness).

The previous section 5.4 has demonstrated both the apparent effectiveness of the hysteretic training of QSH devices (figure 5.30), as well as the lack of a comprehensive understanding of the underlying charging mechanisms (sections 5.4.2, 5.4.3 and 5.4.4). Changing this situation is one of the tasks to follow up on this thesis. Similar studies on a set of samples with varying top barrier thickness as well as on samples with different substrate types are presumably most insightful. Ultimately, combining hysteretic training of edge states with maximized energy gaps (section 5.3.4) is a promising route towards stable, highly transparent edge state conductance, even at elevated temperatures.

5.5 The chiral anomaly in compressively strained bulk layers

Initially, in this work, the research on strain-engineering of HgTe layers was motivated by the expected enlargement of the band gap of QWs, i.e. two-dimensional systems. This motivation was expanded towards the end of this work, when new theoretical works drew attention to compressed HgTe bulk layers. Whereas Ruan et al. [11] predict a Weyl semi-metal phase in these systems, Rauch et al. [12] expect a Dirac semi-metal phase to emerge (section 3.2). As already shown in section 2.6, the proposed devices have been successfully fabricated, based on the standard approach for compressively strained QWs. An insight into the first steps to identify the Weyl semi-metal phase in transport experiments is given in the following.

The layout of the sample under investigation ("sample W") is comparable to the one discussed in section 2.6. A 66 nm layer of HgTe is sandwiched in between $Cd_{0.7}Hg_{0.3}Te$ barriers of 10 nm thickness. The structure is grown on a SLS, which applies a compressive strain of $\varepsilon_{||} = +0.3\,\%$ on the HgTe. Hall bar devices with the geometry presented

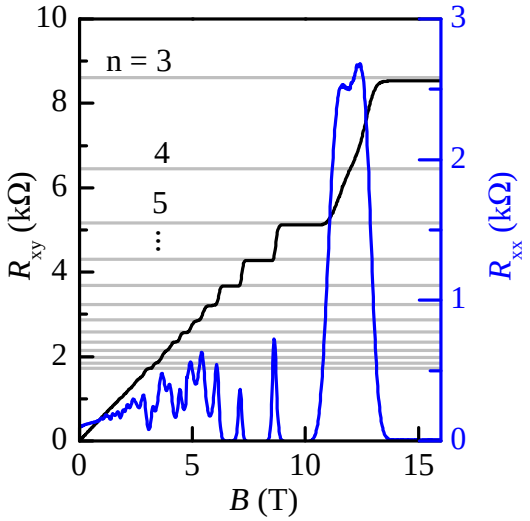

Figure 5.37: Hall- and longitudinal resistance as function of magnetic field of sample W at $U_G = 0\,V$.

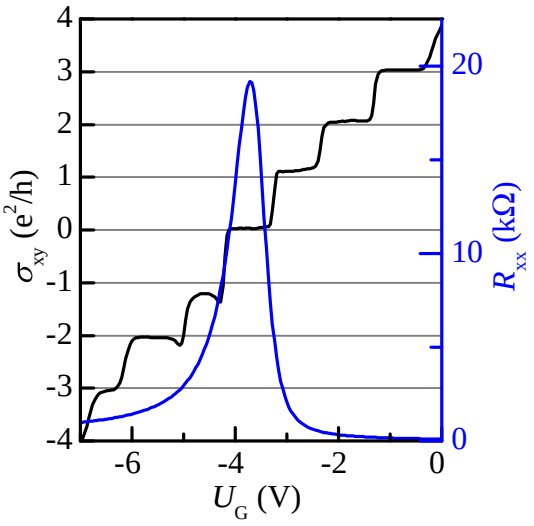

Figure 5.38: Black: Hall conductance σ_{xy} at $B = 12\,T$ of sample W. Blue: longitudinal resistance R_{xx} at $B = 0\,T$. Both as function of gate voltage.

in figure 5.1 have been fabricated. Following the standard approach to study HgTe bulk layers [109], measurements of the Hall- and longitudinal resistance have been carried out in a dilution refrigerator using ac-excitation (in contrast to measurements on QWs, discussed in the previous paragraphs). The data for 0 V gate voltage is shown in figure 5.37. A pronounced QH-quantization of R_{xy} is observed, with plateaus closely matching the expected values [equation (4.1)], and vanishing longitudinal resistance R_{xx} at low-index plateaus ($n \lesssim 7$). This is a strong indication that the current in the device is carried by surface states, just as demonstrated previously in tensile strained bulk HgTe, which is a three dimensional topological insulator [108, 109]. From the Hall- and longitudinal resistance, the Hall conductance can be calculated as $\sigma_{xy} = R_{xy}\,(R_{xy}^2 + \rho_{xx}^2)^{-1}$, with the longitudinal resistivity being related to the resistance by the geometry of the device: $\rho_{xx} = 1/3\ R_{xx}$. For $B = 12\,T$, σ_{xy} is plotted as function of gate voltage in figure 5.38 (black trace). Clear plateaus at $\sigma_{xy} = n\ e^2/h$ are observed for $n \in \mathbb{Z}$, and the $n = 0$ plateau coincides with the maximum of the longitudinal resistance (blue trace). At the surface of Weyl semimetals, a gapless connection is predicted to exist between two Weyl points of opposite chirality (so-called "Fermi arcs" [110]), and one is tempted to assign the surface conductance of the sample to these surface states. However, since the inversion of the Γ_8 and Γ_6 bands (section 3.1), which gives rise to the topological surface states in tensile strained HgTe [10, 108, 109] is present in the compressively strained samples as well, the surface

conductance is no clear sign of the Weyl semi-metal phase. Therefore, we additionally investigated the bulk magnetoconductance signatures of the Weyl nodes.

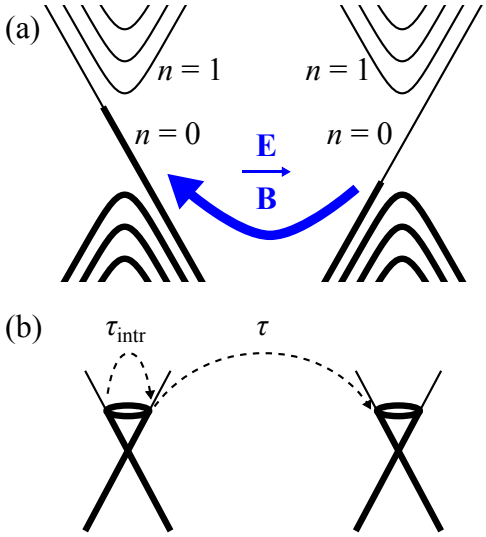

Figure 5.39: (a) Sketch of the chiral imbalance in a two-node Weyl-semimetal in the limit of large magnetic field. Thick lines denote occupied states. Blue arrow signals particle pumping. (b) Intra- and inter-node scattering mechanisms in the classical limit. Adapted from [172, 173].

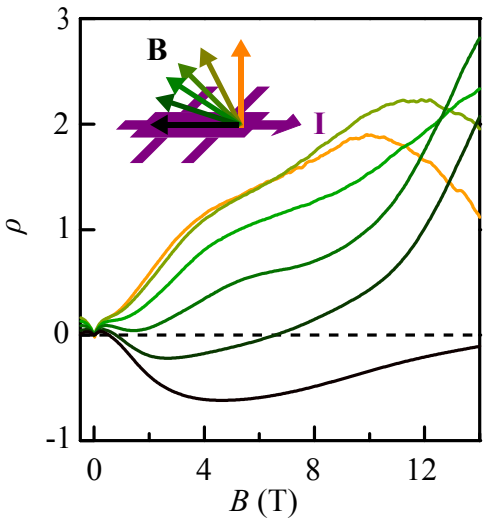

Figure 5.40: Magnetoresistance [equation (5.19)] of sample W as function of magnetic field. Color-coding denotes different orientations of magnetic field. Gate voltage was set to maximum zero-field resistance R_{xx}.

The magnetotransport signature that is commonly used [174–177] to identify a Weyl semi-metal state is the chiral anomaly, or Adler-Bell-Jackiw anomaly. It shows as a negative magnetoresistance if a magnetic field is applied in parallel to the electric field which drives the current in the device. The anomaly has been first adopted to solid state physics by Nielsen et al. for the limit of high magnetic fields [172]. The energy dispersion of the Landau levels of a pair of Weyl nodes is sketched in figure 5.39 (a). At both nodes, a zero-order ($n = 0$) Landau level exists, and is the highest occupied level at charge-neutrality. Due to their mirror energy dispersion, the group velocity of carriers on opposite nodes has opposite signs. If the system is exposed to an electric field $\mathbf{E}$ parallel to $\mathbf{B}$, an imbalance arises in the number of particles in the left and right zero LL [blue arrow and thick lines in figure 5.39 (a)], however, with the total number of particles conserved. This imbalance, proportional to $\mathbf{E} \cdot \mathbf{B}$, is the Adler-Bell-Jackiw anomaly. Son et al. [173] studied the implication of this mechanism in the limit of a low magnetic field, i.e. in the absence of LL quantization. They found a similar anomaly, and predicted an increase in conductance σ proportional to B^2, based on the assumption that the inter-node scattering time τ is much

larger than the intra-node counterpart τ_{intr} [figure 5.39 (b)]. This anomalous contribution to the total conductance causes the magnetoresistance

$$\rho(B) = \frac{R_{\mathrm{xx}}(B) - R_{\mathrm{xx}}(0)}{R_{\mathrm{xx}}(0)} \tag{5.19}$$

to decrease with increasing magnetic field. This is in contrast to almost all metals, where $\rho(B) \geq 0$ [160] (other exceptions exist, e.g. ferromagnetic metals [160]). To probe this anomaly, we have tuned the Fermi level to the charge-neutrality point, i.e. maximized the longitudinal resistance by means of the gate (figure 5.38) and measured the longitudinal resistance as function of magnetic field for different angles θ between **B** and **I** (inset of figure 5.40, the electric field **E** is parallel to the direction of current flow **I** in the device). The resulting $\rho(B)$ [equation (5.19)] is shown in figure 5.40. Indeed, we find a transition from positive to negative magnetoresistance as θ approaches zero, i.e. $\mathbf{B}||\mathbf{E}$. The overall trace closely resembles data from the Weyl semi-metal TaAs [177]. In particular, we also find a kink at very low fields, and an increase in R_{xx} at $B > 5\,\mathrm{T}$. The former is attributed to weak antilocalization in Ref. [177], and the latter may be caused by conventional orbital magnetoresistance, since the alignment of $\mathbf{B}||\mathbf{E}$ is only accurate to $\pm 2^{\circ}$ in our experimental setup. An expression for the conductance is derived in [177] as

$$\sigma(B) = \left(1 + C_{\mathrm{W}}\, B^2\right) \left(\sigma_0 + a\sqrt{B}\right) + \sigma_n, \tag{5.20}$$

which combines the effect of anomaly-driven increased conductance (first bracket) and weak antilocalization (second bracket). The σ_n-term is relevant at higher temperatures only. The conductance $\sigma = R_{\mathrm{xx}}^{-1}$ is shown in figure 5.41 for $\mathbf{B}||\mathbf{E}$. In the low field regime, a good fit to equation (5.20) is obtained with the fitting parameters $C_{\mathrm{W}} = 0.23\,\mathrm{T}^{-2}$, $\sigma_0 = 1.4\ e^2h^{-1}$, $a = 0.15\ e^2h^{-1}\mathrm{T}^{-0.5}$ and $\sigma_n = 0$. At higher fields, the fit fails, similar to Ref. [177].

Since the strength of the anomaly is expected to depend on $\mathbf{B}\cdot\mathbf{E}$, the anomalous signal should be invariant with respect to the direction of the component of **B** that is perpendicular to **I**. However, compared to other experiments on Weyl semi-metals, there is a conceptual difference in the samples we investigate. Instead of using "true" bulk crystals in the sense that the sample has a comparable extent in all directions [174–177], our device has highly uneven dimensions in the symmetry plane of the anomaly (green ellipse in figure 5.42: 66 nm HgTe layer thickness vs. 200 µm Hall bar width). Thus, any magnetoresistance feature caused by orbital effects should exhibit a pronounced angular dependence in this plane. Figure 5.42 shows $\rho(B)$ for three different directions of the magnetic field. The black and orange traces have already been shown in figure 5.40. In contradiction to a

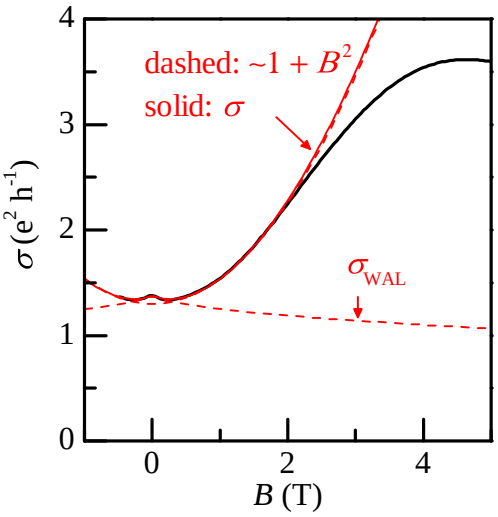

Figure 5.41: Conductance of sample W at low fields and **B**||**E**, and fit to equation (5.20). Gate voltage was set to maximum zero-field resistance R_{xx}.

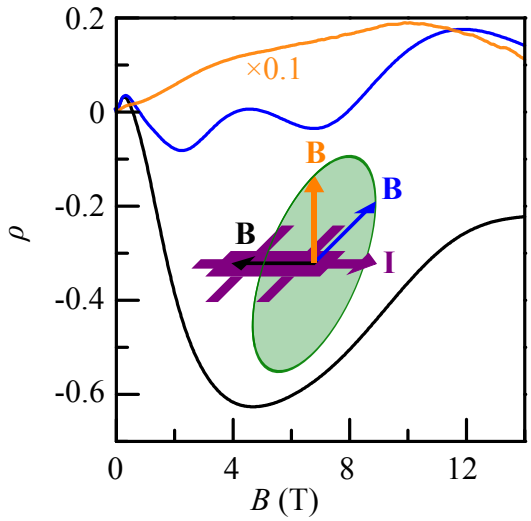

Figure 5.42: Magnetoresistance of sample W for different directions of magnetic field: **B**||**E** (black) and **B** $\perp$ **E** (orange and blue). Orange trace is rescaled ($\times 0.1$) from figure 5.40. Gate voltage was set to maximum zero-field resistance R_{xx}.

simple $\mathbf{B} \cdot \mathbf{E}$ dependency, the magnitude of the magnetoresistance strongly depends on the angle between **B** and the sample plane for **B** $\perp$ **E** (blue and orange trace, note the $\times 0.1$ scaling of the latter). Even though the two traces do not match exactly and the scaling factor is fairly large to be caused by simple misalignment of the field [$\sin^{-1}(0.1) = 6°$], this angle dependency is still an indication of orbital magnetoresistance, and one can map this to the increase of the **E**||**B** - trace (black), where the increase at high fields resembles the blue **E** $\perp$ **B**-trace.

To summarize the first results on the research on Weyl semi-metals in HgTe bulk layers, we note that in particular the negative $\rho(B)$ caused by the chiral anomaly is similar to previous reports in the literature [174, 176, 177] and, at low fields, agrees with the B^2-dependency predicted by theory [173]. What sets the results apart from other works is the well-pronounced QH effect, which is observed away from the charge-neutrality point (figure 5.37). The question whether this is due to surface states caused by the Weyl Fermi arcs or the topological band inversion has to remain unanswered at this point. Apart from more detailed analysis on the angular dependence of the magnetoresistance, possibly in a vector-magnet setup, and studies of the temperature dependence [176, 177], direct imaging of the surface state dispersion in ARPES is most promising to help to understand the system.

Summary

The subject of this thesis is the control of strain in HgTe thin-film crystals. Such systems are members of the new class of topological insulator materials and therefore of special research interest. A major task was the experimental control of the strain in the HgTe films. This was achieved by a new epitaxial approach and confirmed by cristallographic analysis and magneto-transport measurements.

In this work, strain was induced in thin films by means of coherent epitaxy on substrate crystals. This means that the film adopts the lattice constant of the substrate in the plane of the substrate-epilayer interface. The level of strain is determined by the difference between the strain-free lattice constants of the substrate and epilayer material (the so-called lattice mismatch). The film responds to an in-plane strain with a change of its lattice constant perpendicular to the interface. This relationship is crucial for both the correct interpretation of high resolution X-ray diffraction (HRXRD) measurements, and the precise determination of the band dispersion. The lattice constant of HgTe is smaller than the lattice constant of CdTe. Therefore, strain in HgTe is tensile if it is grown on a CdTe substrate. In principle, compressive strain can be achieved by using an appropriate $Cd_{1-x}Zn_xTe$ substrate. This concept was modified and applied in this work.

Epilayers have been fabricated by molecular-beam epitaxy (MBE). The growth of thick buffer layers of CdTe on GaAs:Si was established as an alternative to commercial CdTe and $Cd_{0.96}Zn_{0.04}Te$ substrates. The growth conditions have been optimized by an analysis of atomic force microscopy and HRXRD studies. HRXRD measurements reveal a power-law increase of the crystal quality with increasing thickness. Residual strain was found in the buffer layers, and was attributed to a combination of finite layer thickness and mismatch of the thermal expansion coefficients of CdTe and GaAs. In order to control the strain in HgTe epilayers, we have developed a new type of substrate with freely adjustable lattice constant. CdTe-$Cd_{0.5}Zn_{0.5}Te$ strained-layer-superlattices have been grown by a combination of MBE and atomic-layer epitaxy (ALE), and have been analyzed by HRXRD. ALE of the $Cd_{0.5}Zn_{0.5}Te$ layer is self-limiting to one monolayer, and the effective lattice constant can be controlled reproducibly and straightforward by adjusting

the CdTe layer thickness. The crystal quality has been found to degrade with increasing Zn-fraction. However, the effect is less drastic compared to single layer $Cd_{1-x}Zn_xTe$ solid solutions. HgTe quantum wells (QWs) sandwiched in between CdHgTe barriers have been fabricated in a similar fashion on superlattices and conventional CdTe and $Cd_{0.96}Zn_{0.04}Te$ substrates. The lower critical thickness of the CdHgTe barrier material grown on superlattice substrates had to be considered regarding the sample design. The electronic properties of the QWs depend on the strain and thickness of the QW. We have determined the QW thickness with an accuracy of ± 0.5 nm by an analysis of the beating patterns in the thickness fringes of HRXRD measurements and X-ray reflectometry measurements. We have, for the first time, induced compressive strain in HgTe QWs by an epitaxial technique (i.e. the effective lattice constant of the superlattice is lower compared to the lattice constant of HgTe). The problem of the lattice mismatch between superlattice and barriers has been circumvented by using CdHgTe-ZnHgTe superlattices instead of CdHgTe as a barrier material. Furthermore, the growth of compressively strained HgTe bulk layers (with a thickness of at least 50 nm) was demonstrated as well.

The control of the state of strain adds a new degree of freedom to the design of HgTe epilayers, which has a major influence on the band structure of QWs and bulk layers. Strain in bulk layers lifts the degeneracy of the Γ_8 bands at $\mathbf{k} = 0$. Tensile strain opens an energy gap, compressive strain shifts the touching points of the valence- and conduction band to positions in the Brillouin zone with finite $\mathbf{k}$. Such a situation has been realized for the first time in the course of this work. For QWs in the inverted regime, it is demonstrated that compressive strain can be used to significantly enhance the thermal energy gap of the two-dimensional electron gas (2DEG). In addition, semi-metallic and semiconducting behavior is expected in wide QWs, depending on the state of strain. An examination of the temperature dependence of the subband ordering in QWs revealed that the band gap is only temperature-stable for appropriate sample parameters and temperature regimes. The band inversion is always lifted for sufficiently high temperatures.

A large number of models investigate the influence of the band gap on the stability of the quantum-spin-Hall (QSH) effect. An enhancement of the stability of QSH edge state conductance is expected for enlarged band gaps. Furthermore, experimental studies on the temperature dependence of the QSH conductance are in contradiction to theoretical predictions. Systematic studies of these aspects have become feasible based on the new flexibility of the sample design.

Detailed low-temperature magnetotransport studies have been carried out on QWs and bulk layers. For this purpose, devices have been fabricated lithographically, which consist of two Hall-bar geometries with different dimensions. This allows to discriminate

between conductance at the plane of the 2DEG and the edge of the sample. The Fermi energy in the 2DEG has been adjusted by means of a top gate electrode. The strain-induced transition from semi-metallic to semiconducting characteristics in wide QWs was shown. The magnitude of the semi-metallic overlap of valence- and conduction band was determined by an analysis of the two-carrier conductance and is in agreement with band structure calculations. The band gap of the semiconducting sample was determined by measurements of the temperature dependence of the conductance at the charge-neutrality point. Agreement with the value expected from theory has been achieved for the first time in this work. The influence of the band gap on the stability of QSH edge state conductance has been investigated on a set of six samples. The band gap of the set spans a range of 10 to 55 meV. The latter value has been achieved in a highly compressively strained QW, has been confirmed by temperature-dependent conductance measurements, and is the highest ever reported in the inverted regime. Studies of the carrier mobility reveal a degradation of the sample quality with increasing Zn-fraction in the superlattice, in agreement with HRXRD observations. The enhanced band gap does not suppress scattering mechanisms in QSH edge channels, but lowers the conductance in the plane of the 2DEG. Hence, edge state conductance is the dominant conducting process even at elevated temperatures. An increase in conductance with increasing temperature has been found, in agreement with reports from other groups. The increase follows a power-law dependency, the underlying physical mechanism remains open. A cause for the lack of an increase of the QSH edge state conductance with increasing energy gap has been discussed. Possibly, the sample remains insulating even at finite carrier densities, due to localization effects. The measurement does not probe the QSH edge state conductance at the situation where the Fermi energy is located in the center of the energy gap, but in the regime of maximized puddle-driven scattering. In a first set of measurements, it has been shown that the QSH edge state conductance can be influenced by hysteretic charging effects of trapped states in the insulating dielectric. A maximized conductance of 1.6 e^2/h was obtained in a 58 µm edge channel. Finally, measurements on three dimensional samples have been discussed. Recent theoretical works assign compressively strained HgTe bulk layers to the Weyl semi-metal class of materials. Such layers have been synthesized and studied in magnetotransport experiments for the first time. Pronounced quantum-Hall- and Shubnikov-de-Haas features in the Hall- and longitudinal resistance indicate two-dimensional conductance on the sample surface. However, this conductance cannot be assigned definitely to Weyl surface states, due to the inversion of Γ_6 and Γ_8 bands. If a magnetic field is aligned parallel to the current in the device, a decrease in the longitudinal resistance is observed with increasing magnetic field. This is a signature of the chiral

anomaly, which is expected in Weyl semi-metals.

Finally, the major result of this work is highlighted again. The state of strain in HgTe has been established as an experimental degree of freedom. This leads to a drastic increase in the diversity of the electronic properties of the topological material HgTe. Based on these results, the fabrication of systems with tailor-made band sequences is possible. In the medium term, this should help to gain a deeper understanding of various aspects of topological condensed matter physics.

Zusammenfassung

Die vorliegende Dissertation befasst sich mit der Verspannung in kristallinen HgTe Dünnschichtsystemen. Solche Systeme sind aufgrund ihrer Zugehörigkeit zur Materialklasse der topologischen Isolatoren von besonderem Interesse. Eine wesentliche Aufgabe bestand in der experimentellen Kontrolle der Verspannung der HgTe Schichten. Dies wurde durch ein neues Epitaxieverfahren erreicht. Der Erfolg des Verfahrens konnte durch kristallografische Analysemethoden und Magnetotransportmessungen bestätigt werden.

Im Rahmen dieser Arbeit wurde Verspannung in dünnen Schichten durch kohärentes Wachstum auf kristallinen Substraten induziert. Kohärentes Wachstum bedeutet hierbei, dass die Schicht unter Beibehaltung der Substratgitterkonstante in der Ebene parallel zu der Substrat-Epischicht-Grenzfläche auf ein Substrat aufgewachsen wird. Die Abweichung der Gitterkonstanten von Substrat und unverspannter Epischicht (sog. Gitterfehlpassung) bestimmt den Grad der Verspannung. Die Schicht antwortet auf die Verspannung in der Ebene mit einer Änderung der Gitterkonstante senkrecht zur Grenzfläche. Dieser Zusammenhang ist entscheidend sowohl für die korrekte Interpretation von Messungen durch hochauflösende Röntgendiffraktometrie (engl. high resolution X-ray diffraction, HRXRD), als auch für die exakte Bestimmung der Banddispersion. Die Gitterkonstante von HgTe ist kleiner als die von CdTe. Daher ist HgTe tensil verspannt wenn es auf ein CdTe Substrat aufgewachsen wird, es kann aber durch die Verwendung von geeigneten $Cd_{1-x}Zn_xTe$ Substraten prinzipiell auch kompressiv verspannt gewachsen werden. Dieses Konzept wurde in dieser Arbeit modifiziert und angewandt.

Epischichten wurden mittels Molekularstrahlepitaxie (engl. molecular-beam epitaxy, MBE) hergestellt. Als Alternative zu kommerziellen CdTe und $Cd_{0.96}Zn_{0.04}Te$ Substraten wurde zunächst das epitaktische Wachstum dicker Schichten (sog. Buffer) CdTe auf GaAs:Si Substraten etabliert. Der Parameterraum für optimales Wachstum wurde anhand von Rasterkraftmikroskopie- und HRXRD Studien eingegrenzt. HRXRD Messungen zeigen eine Zunahme der Qualität mit zunehmender Dicke, die einem Potenzgesetz folgt. Im Vergleich zu reinen CdTe Substraten wurde eine Restverspannung im Buffer beobachtet, wobei eine Kombination aus endlicher Schichtdicke und unterschiedlichen

thermischen Ausdehnungskoeffizienten von CdTe und GaAs als Ursache ausgemacht wurde. Um die Verspannung in HgTe Epischichten kontrollieren zu können, wurde ein neuer Substrattyp mit frei einstellbarer Gitterkonstante entwickelt. Durch eine Kombination aus MBE und Atomlagenepitaxie (ALE) wurden spezielle CdTe $-$ $Cd_{0.5}Zn_{0.5}Te$ Übergitter auf GaAs:Si gewachsen, und wiederum mittels HRXRD analysiert. Die ALE der $Cd_{0.5}Zn_{0.5}Te$ Schicht ist selbstbegrenzend auf eine Monolage, und die effektive Gitterkonstante des Übergitters konnte durch die Variation der Dicke der CdTe Schicht einfach und reproduzierbar kontrolliert werden. Eine Abnahme der Schichtqualität wurde mit zunehmendem Zinkgehalt beobachtet, der Effekt ist allerdings weniger stark ausgeprägt als in vergleichbaren ternären $Cd_{1-x}Zn_xTe$ Einfachschichten. HgTe Quantentröge (engl. quantum wells, QWs) zwischen CdHgTe Barrieren wurden auf vergleichbare Weise auf Übergittern und konventionellen CdTe bzw. $Cd_{0.96}Zn_{0.04}Te$ Substraten hergestellt. Dabei ist eine geringere kritische Schichtdicke des CdHgTe Barrierenmaterials auf Übergittersubstraten zu beachten. Neben der Verspannung ist die Trogdicke der zweite entscheidende Parameter für die elektronischen Eigenschaften der Schicht. Sie wurde anhand von Schwebungen in den Schichtdickenoszillationen der HRXRD Messung oder durch Röntgenreflektometrie auf etwa $\pm 0.5\,\mathrm{nm}$ genau bestimmt. Es konnte erstmalig mit epitaktischen Mitteln kompressive Verspannung in HgTe QWs induziert werden (d.h. die effektive Gitterkonstante des Übergitters ist kleiner als die des HgTe). Es wurde gezeigt, dass das Problem der Gitterfehlpassung von Übergitter und Barriere durch die Verwendung von CdHgTe-ZnHgTe Übergittern anstelle von CdHgTe als Barrierenmaterial umgangen werden kann, und dass das kompressiv verspannte Wachstum von dickeren Schichten HgTe (sog. Bulk Material, Dicke mindestens 50 nm) ebenfalls möglich ist.

Mit dem Verspannungszustand steht ein neuer Freiheitsgrad in der Fertigung von HgTe Epischichten zur Verfügung. Dieser beeinflusst die elektronische Bandstruktur von QWs und Bulk Schichten entscheidend. Verspannung in Bulk-Material hebt die Energieentartung der Γ_8 Bänder bei $\mathbf{k} = 0$ auf. Tensile Verspannung öffnet dabei eine Energielücke, kompressive Verspannung schiebt die Berührpunkte von Valenz- und Leitungsband an Stellen in der Brillouinzone mit $\mathbf{k} \neq 0$. Eine derartige Situation wurde im Rahmen dieser Arbeit erstmals experimentell realisiert. Es wurde weiterhin demonstriert, dass in QWs mit topologisch invertierter Bandreihenfolge die thermische Bandlücke des zweidimensionalen Elektronengases (2DEG) durch kompressive Verspannung signifikant erhöht werden kann. Außerdem wird, je nach Verspannungszustand, halbmetallisches bzw. halbleitendes Verhalten in QWs mit hoher Trogdicke erwartet. Anhand einer Betrachtung der Temperaturabhängigkeit der Subbänder in QWs wurde gezeigt, dass eine temperaturstabile Bandlücke nur bei geeignet gewählten Probenparametern und Temperaturintervallen

gegeben ist, und dass die Bandinversion für ausreichend hohe Temperaturen immer aufgehoben wird.

Es existieren zahlreiche Modelle die die Stabilität des Quanten-Spin-Hall (QSH) Randzustandes in Verbindung mit der Bandlücke betrachten. Es wird insbesondere eine Zunahme der Stabilität des QSH Zustandes mit zunehmender Bandlücke erwartet. Außerdem besteht eine Diskrepanz zwischen theoretischen Modellen und experimentellen Daten bezüglich der Temperaturabhängigkeit der QSH-Leitfähigkeit. Diese Zusammenhänge konnten mit der neuen Flexibilität im Probendesign gezielt untersucht werden.

QWs und Bulk Schichten wurden in Tieftemperatur- Magnetotransportmessungen eingehend untersucht. Dazu wurden Proben lithographisch hergestellt, deren Layout aus zwei Hallbar-Strukturen mit verschiedenen Abmessungen besteht. Dies ermöglicht die Unterscheidung zwischen Ladungstransport in der Fläche des 2DEGs, und dem Probenrand. Das Ferminiveau im 2DEG ist über eine Topgate-Elektrode einstellbar. Es wurde der verspannungsinduzierte Übergang von halbmetallischer zu halbleitender Charakteristik in breiten Quantentrögen gezeigt. Eine Analyse des zwei-Ladungsträger-Verhaltens bestätigt die Größe des halbmetallischen Überlapps von Valenz- und Leitungsband aus Bandstrukturberechnungen. Die Bandlücke der halbleitenden Probe wurde anhand der Temperaturabhängigkeit des Leitwertes am ladungsneutralen Punkt bestimmt. Die Übereinstimmung mit dem theoretisch erwarteten Wert wurde in dieser Arbeit zum ersten Mal erzielt. Der Einfluss der Bandlücke auf die Stabilität des QSH Randkanaltransports wurde anhand einer Serie von sechs Proben untersucht. Die Bandlücke wurde dabei von 10 auf 55 meV erhöht. Der letztgenannte Wert wurde in einem hochkompressiv verspannten QW erreicht, in temperaturabhängigen Leitwertsmessungen bestätigt, und stellt den Bestwert im invertierten Regime dar. Untersuchungen der Beweglichkeit der Ladungsträger zeigen, in Übereinstimmung mit HRXRD Messungen, dass die Probenqualität mit zunehmendem Zinkgehalt im Übergitter abnimmt. Die erhöhte Bandlücke verursacht keine effektive Unterdrückung der Rückstreuung der QSH Randkänale, verringert allerdings die Flächenleitung im 2DEG, sodass der Randkanaltransport auch bei höheren Temperaturen den dominanten Transportmechanismus darstellt. In Übereinstimmung mit Arbeiten anderer Gruppen wurde ein Anstieg des Leitwertes mit der Temperatur gefunden. Dieser lässt sich mit einem Potenzgesetz modellieren, seine Ursache blieb aber ungeklärt. Als Ursache für den ausbleibenden Anstieg des QSH Leitwertes mit zunehmender Bandlücke wurde diskutiert, dass die Probe aufgrund von Lokalisationseffekten auch bei endlicher Ladungsträgerdichte noch isolierend ist. Die Messung des QSH Leitwertes erfolgt möglicherweise nicht bei in der Bandlücke zentrierter Fermienergie, sondern im Regime maximaler Inselrückstreuung. In einer ersten Messreihe

wurde weiterhin gezeigt, dass der QSH Leitwert durch hysteretische Umladungseffekte von Störstellen im Isolatormaterial beeinflusst werden kann. Dadurch wurde ein maximaler Leitwert von 1.6 e^2/h in einem 58 µm Randkanal erreicht. Abschließend wurden noch Messungen an dreidimensionalen Systemen diskutiert. Neue theoretische Studien ordnen kompressiv verspannte Bulk HgTe Schichten der Materialklasse der Weyl-Halbmetalle zu. Im Rahmen dieser Arbeit wurden zum ersten Mal derartige Schichten gewachsen und in Magnetotransportmessungen studiert. Ausgeprägte Quanten-Hall- und Shubnikov-de-Haas Signaturen im Hall- und Längswiderstand sind ein klares Indiz für zweidimensionalen Transport an der Probenoberfläche. Dieser lässt sich aufgrund der Γ_6-Γ_8 Bandinversion in HgTe allerdings nicht eindeutig den Weyl-Oberflächenzuständen zuordnen. Orientiert man ein Magnetfeld parallel zum Probenstrom, so wird eine Abnahme des Längswiderstandes mit zunehmendem Magnetfeld beobachtet. Dies ist eine Signatur der chiralen Anomalie, die in Weyl Halbmetallen erwartet wird.

Abschließend sei als wesentlichstes Ergebnis dieser Arbeit hier noch einmal die Etablierung des Verspannungszustandes von HgTe als experimentell zugänglicher Freiheitsgrad hervorgehoben. Dadurch wird die Vielfalt der elektronischen Eigenschaften topologischer Materialen basierend auf HgTe drastisch erhöht. Aufbauend auf diesen Ergebnissen können Systeme mit maßgeschneiderter Bandabfolge hergestellt werden, welche mittelfristig zu einem tieferen Verständnis von topologischen Festkörperphänomenen beitragen sollten.

Appendix A

Material parameters

Material parameters are collected in this section.

mat.	$a_{300\,\mathrm{K}}$ (Å)	Ref.	c_{11}	c_{12} (GPa)	c_{44}	Ref.
GaAs	5.6533	[64]	118	54	59	[178]
HgTe	6.4615	[65]	54	37	21	[28]
ZnTe	6.104	[179]	71	41	31	[28]
CdTe	6.4815	[65]	54	37	20	[28]
$Cd_{0.5}Zn_{0.5}Te$	6.2928	mean value	63	39	26	mean value

Table A.1: Lattice parameter a and elastic constants for crystals fabricated in this thesis. Most publications list more than two valid digits for the c_{ij}. However, deviations from publication to publication may be as high as some percent (see for example [180] and [28]).

A	B	C
	($\mathrm{meV\,nm^2}$)	
611	745	571

Table A.2: Band parameters of bulk HgTe. From [105].

Appendix B

Fits of temperature dependent minimum conductance

In the following, the minimum conductance G_{min} of samples C, D, F, G and H is shown, together with a fit of equation (5.14) to the data, assuming a power-law dependency of the low-temperature part of G_{min} [equation (5.15)]. The power-law fit is shown in the inset on a log-log scale. The green dots indicate the change in G_1 caused by changing $G_0 + G_{\mathrm{th}}$ by $\pm 10\,\%$. The fit of sample E is shown in the main text [figure 5.22]. As already noted in the main text, the fit does not reproduce the data for all samples in all temperature regimes. In particular, it breaks down in the high-temperature regime of small Hall bars with small energy gaps (figure B.2, figure B.4). A feature worth noting is the increase of G_{min} with decreasing temperature in the large Hall bar data of sample F (see inset of figure B.5). This is the only time we have seen, at low temperatures, a temperature dependence in qualitative agreement with the common predictions made by theory (that is a decrease in G_{min} due to temperature-activated backscattering mechanisms, see section 4.3.2). However, we did not observe this dependency in the small Hall bar of the same wafer (figure B.5), or in any other sample, and were therefore not able to study this feature in greater detail.

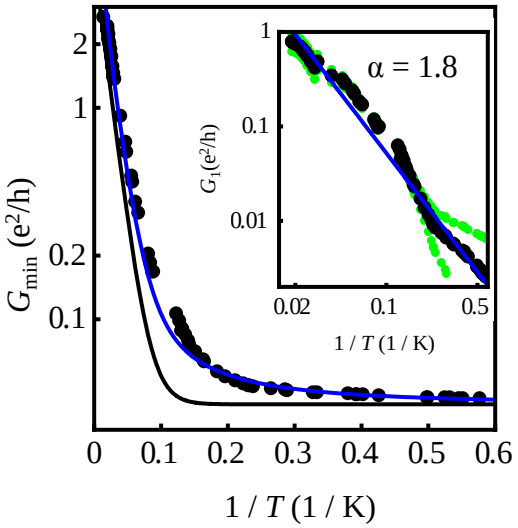

Figure B.1: Sample C ($E_G = 10\,meV$), large Hall bar.

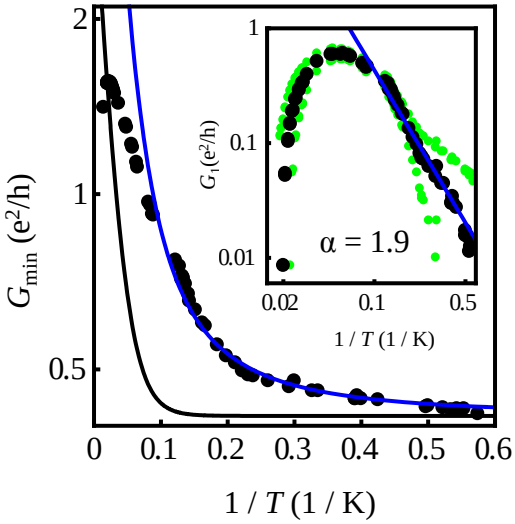

Figure B.2: Sample C ($E_G = 10\,meV$), small Hall bar.

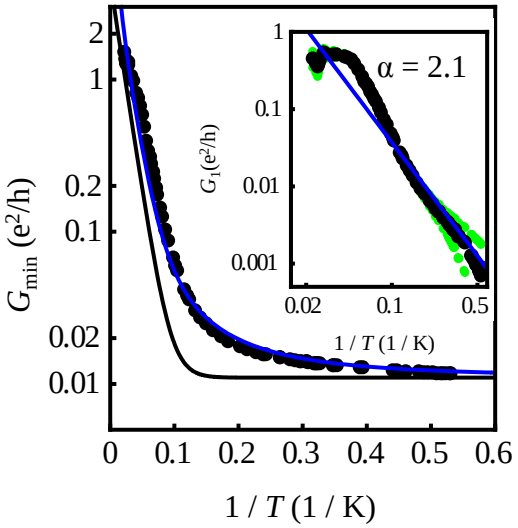

Figure B.3: Sample D ($E_G = 14\,meV$), large Hall bar.

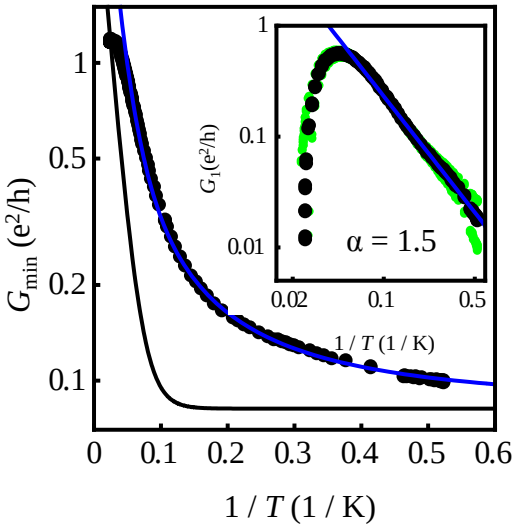

Figure B.4: Sample D ($E_G = 14\,meV$), small Hall bar.

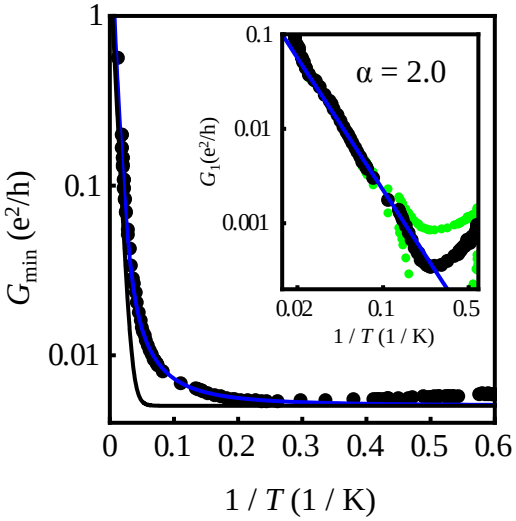

Figure B.5: Sample F ($E_G = 31\,meV$), large Hall bar.

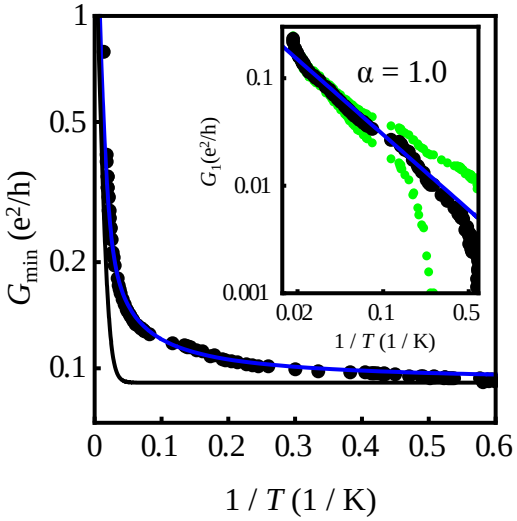

Figure B.6: Sample F ($E_G = 31\,meV$), small Hall bar.

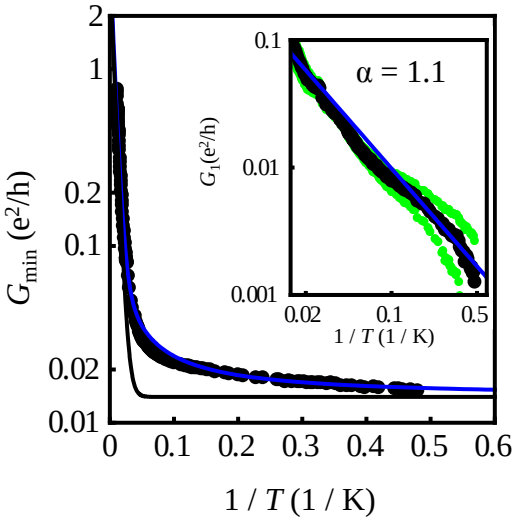

Figure B.7: Sample G ($E_G = 33\,meV$), large Hall bar.

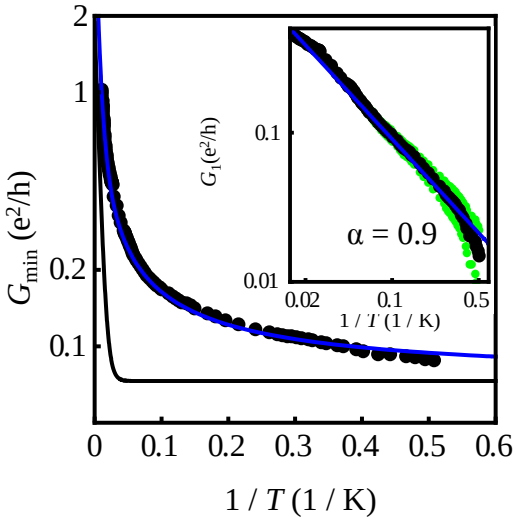

Figure B.8: Sample G ($E_G = 33\,meV$), small Hall bar.

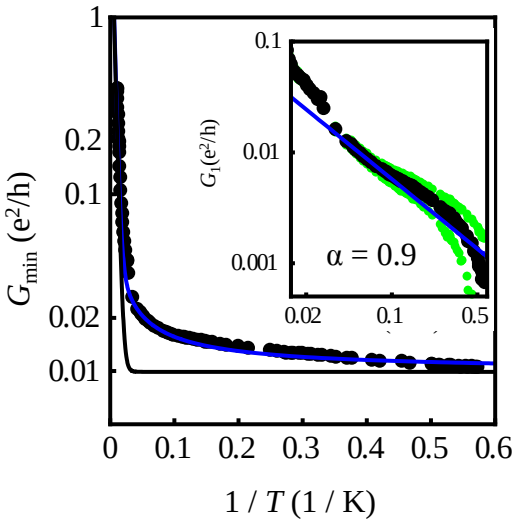

Figure B.9: Sample H ($E_G = 55\,meV$), large Hall bar.

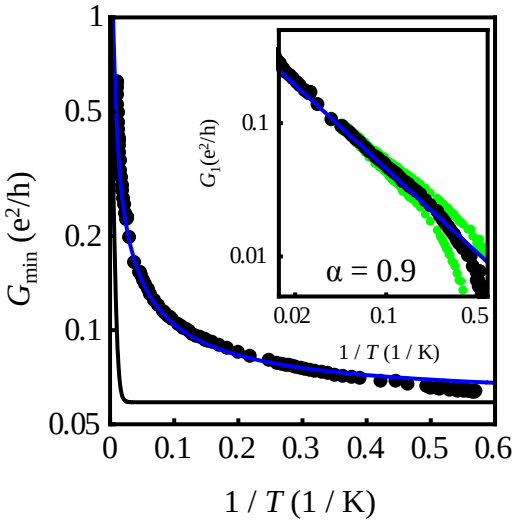

Figure B.10: Sample H ($E_G = 55\,meV$), small Hall bar.

Appendix C

Additional data of hysteresis measurements of sample J

This paragraph provides additional measurements on the hysteresis effect observed in sample J - see section 5.4.

C.0.1 Raw data of Hall resistance measurements

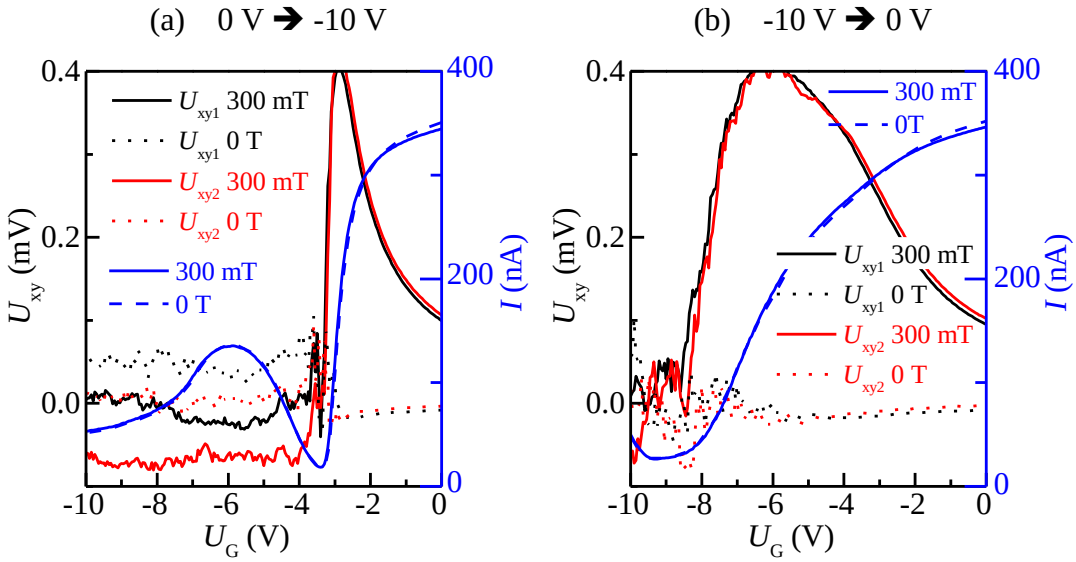

Figure C.1: Hall voltages and sample current of small Hall bar of sample J as function of gate voltage. (a) and (b) show measurements of different sweep directions - see labels on top.

Figure C.1 shows the raw Hall voltages and sample current, which were used to calculate the hysteretic carrier density of sample J, as shown in figure 5.32. Hall voltages

were measured at $B = 0\,\mathrm{T}$ and 300 mT on both contact pairs. Resistances were determined from the difference of the 0 T and 300 mT data, and the respective sample current. The carrier density n was calculated from the mean value of the Hall resistances. Note that the change in carrier density at approximately $-7\,\mathrm{V}$ (black trace figure 5.32) is only reflected in a (gradual) change in sample current. The Hall voltage is noisy, but approximately constant in the full p-type regime. Also note the offset between the data pairs, which is in the same order of magnitude as the signal itself, indicating a pronounced longitudinal resistance pickup.

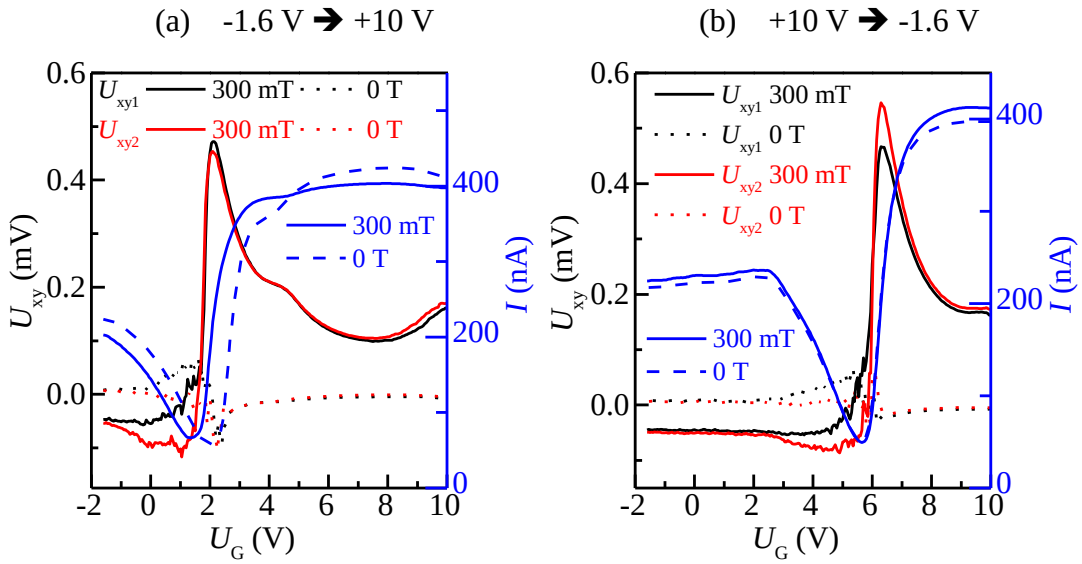

Figure C.2: Hall voltages and sample current of small Hall bar of sample J as function of gate voltage. (a) and (b) show measurements of different sweep directions- see labels on top.

Figure C.2 shows the raw Hall voltages and sample current, which were used to calculate the hysteretic carrier density of sample J in the positive gate voltage regime, as shown in figure 5.36. The carrier density was calculated with the same approach as discussed above. The hysteretic overcompensation of carrier density at $U_\mathrm{G} \approx 7 - 10\,\mathrm{V}$ is reflected in an increase in U_xy, as well as in a slight decrease in current in figure C.2(a). Between the measurements of the Hall voltages and the reference at $B = 0\,\mathrm{T}$, an abrupt shift of the CNP took place. This can be seen in the horizontal offset of the current traces, and is probably the cause of the slight difference observed in n at $U_\mathrm{G} = -1.6\,\mathrm{V}$ for the two sweep directions. The pronounced plateau in n at $U_\mathrm{G} = +2.5\,\mathrm{V}$ to $-1.6\,\mathrm{V}$ (black trace in figure 5.36) is reflected in the constant U_xy and I in this regime [figure C.2(b)].

C.0.2 Carrier density of the large Hall bar

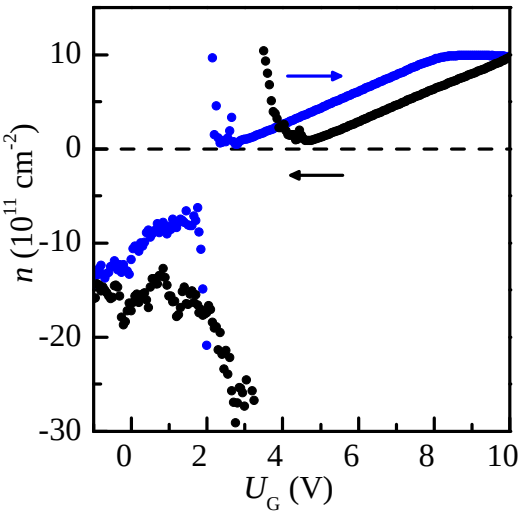

Figure C.3: Carrier density of large Hall bar of sample J as function of gate voltage for both sweep directions (arrows). Measured after the sample has seen $U_G = +10\,V$.

Figure C.3 shows the carrier density n of the large Hall bar of sample J in the positive gate voltage regime. Measurement and evaluation have been performed in the same manner as discussed in section C.0.1. Hysteresis is seen for high positive voltages. In the p-type regime, the data is highly irregular. However, a weak indication of hysteresis can be seen as well.

Abbreviations

2DEG	two-dimensional electron gas
2DTI	two-dimensional topological insulator
AFM	atomic force microscopy
ALE	atomic-layer epitaxy
CMT	CdHgTe (only in figures and indexes)
CNP	charge-neutrality point
CT	CdTe (only in figures and indexes)
CZT	$Cd_{0.5}Zn_{0.5}Te$ (only in figures and indexes)
FWHM	full-width-at-half-maximum
HRXRD	high-resolution X-ray diffraction
lHB	large Hall bar (only in indexes)
MBE	molecular-beam epitaxy
MIT	metal-insulator transition
ML	monolayer
MOVPE	metalorganic vapor phase epitaxy
MT	HgTe (only in figures and indexes)
QH	quantum Hall
QSH	quantum spin Hall
QW	quantum well
RHEED	reflection high-energy electron diffraction
SEM	scanning-electron microscope
sHB	small Hall bar (only in indexes)
SLS	strained-layer superlattice
SQUID	superconducting quantum interference device
UCF	universal conductance fluctuations
UHV	ultra-high vacuum
XRR	X-ray reflectometry
ZT	ZnTe (only in figures and indexes)

Bibliography

[1] B. Abbott, R. Abbott, T. Abbott, M. Abernathy, F. Acernese, K. Ackley, C. Adams, T. Adams, P. Addesso, R. Adhikari, et al., Physical Review Letters **116**, 061102 (2016).

[2] K. v. Klitzing, G. Dorda, and M. Pepper, Physical Review Letters **45**, 494 (1980).

[3] R. N. Hall, G. Fenner, J. Kingsley, T. Soltys, and R. Carlson, Physical Review Letters **9**, 366 (1962).

[4] C. L. Kane and E. J. Mele, Physical Review Letters **95**, 146802 (2005).

[5] B. A. Bernevig and S.-C. Zhang, Physical Review Letters **96**, 106802 (2006).

[6] M. König, S. Wiedmann, C. Brüne, A. Roth, H. Buhmann, L. W. Molenkamp, X.-L. Qi, and S.-C. Zhang, Science **318**, 766 (2007).

[7] J. I. Väyrynen, M. Goldstein, and L. I. Glazman, Physical Review Letters **110**, 216402 (2013).

[8] J. I. Väyrynen, M. Goldstein, Y. Gefen, and L. I. Glazman, Physical Review B **90**, 115309 (2014).

[9] E. Kane, in *Narrow Gap Semiconductors Physics and Applications* (Springer, 1980), pp. 13–31.

[10] C. Brüne, C. Liu, E. Novik, E. Hankiewicz, H. Buhmann, Y. Chen, X. Qi, Z. Shen, S. Zhang, and L. Molenkamp, Physical Review Letters **106**, 126803 (2011).

[11] J. Ruan, S.-K. Jian, H. Yao, H. Zhang, S.-C. Zhang, and D. Xing, Nature Communications **7**, 11136 (2016).

[12] T. Rauch, S. Achilles, J. Henk, and I. Mertig, Physical Review Letters **114**, 236805 (2015).

[13] J. F. Nye, *Physical properties of crystals: their representation by tensors and matrices* (Oxford university press, 1985).

[14] D. Dunstan, Journal of Materials Science: Materials in Electronics **8**, 337 (1997).

[15] R. Beanland, D. Dunstan, and P. Goodhew, Advances in Physics **45**, 87 (1996).

[16] E. Fitzgerald, Materials Science Reports **7**, 87 (1991).

[17] D. Dunstan, S. Young, and R. Dixon, Journal of Applied Physics **70**, 3038 (1991).

[18] G. Cohen-Solal, F. Bailly, and M. Barbé, Journal of Crystal Growth **138**, 68 (1994).

[19] R. People and J. Bean, Applied Physics Letters **47**, 322 (1985).

[20] C. Fontaine, J. Gailliard, S. Magli, A. Million, and J. Piaguet, Applied Physics Letters **50**, 903 (1987).

[21] A. Drigo, A. Aydinli, A. Carnera, F. Genova, C. Rigo, C. Ferrari, P. Franzosi, and G. Salviati, Journal of Applied Physics **66**, 1975 (1989).

[22] L. Sugiura, K. Shigenaka, F. Nakata, and K. Hirahara, Journal of Crystal Growth **145**, 547 (1994).

[23] J. Tersoff and F. LeGoues, Physical Review Letters **72**, 3570 (1994).

[24] T. Colin, T. Skauli, and S. Løvold, Journal of Crystal Growth **175**, 670 (1997).

[25] T. Skauli, T. Colin, R. Sjølie, and S. Løvold, Journal of Electronic Materials **29**, 687 (2000).

[26] P. Ballet, C. Thomas, X. Baudry, C. Bouvier, O. Crauste, T. Meunier, G. Badano, M. Veillerot, J. Barnes, P. Jouneau, et al., Journal of Electronic Materials **43**, 2955 (2014).

[27] J. Basson and H. Booyens, Physica Status Solidi (a) **80**, 663 (1983).

[28] M. Berding, W. Nix, D. Rhiger, S. Sen, and A. Sher, Journal of Electronic Materials **29**, 676 (2000).

[29] T. Skauli, R. Haakenaasen, and T. Colin, Journal of Crystal Growth **241**, 39 (2002).

[30] K. Pinardi, U. Jain, S. Jain, H. Maes, R. Van Overstraeten, and M. Willander, Journal of Applied Physics **83**, 4724 (1998).

[31] C. Ames, Ph.D. thesis, Universität Würzburg (2015).

[32] E. H. Parker, *The technology and physics of molecular beam epitaxy* (Plenum Press New York, 1985).

[33] M. A. Herman and H. Sitter, *Molecular beam epitaxy: fundamentals and current status*, vol. 7 (Springer Science & Business Media, 2012).

[34] A. Cho, Journal of Applied Physics **41**, 2780 (1970).

[35] L. Chang, L. Esaki, W. Howard, and R. Ludeke, Journal of Vacuum Science & Technology **10**, 11 (1973).

[36] A. Y. Cho, Journal of Crystal Growth **201**, 1 (1999).

[37] J. Faurie, A. Million, R. Boch, and J. Tissot, Journal of Vacuum Science & Technology A **1**, 1593 (1983).

[38] J. Faurie and A. Million, Journal of Crystal Growth **54**, 582 (1981).

[39] O. K. Wu, R. Rajavel, and J. Jensen, Materials Chemistry and Physics **43**, 103 (1996).

[40] T. De Lyon, J. Jensen, M. Gorwitz, C. Cockrum, S. Johnson, and G. Venzor, Journal of Electronic Materials **28**, 705 (1999).

[41] R. Haakenaasen, E. Selvig, C. Tonheim, K. Kongshaug, T. Lorentzen, L. Trosdahl-Iversen, J. Andersen, and P. Gundersen, Journal of Electronic Materials **39**, 893 (2010).

[42] L. He, C. R. Becker, R. Bicknell-Tassius, S. Scholl, and G. Landwehr, Journal of Applied Physics **73**, 3305 (1993).

[43] S. Oehling, M. Ehinger, W. Spahn, A. Waag, C. Becker, and G. Landwehr, Journal of Applied Physics **79**, 748 (1996).

[44] F. Goschenhofer, J. Gerschütz, A. Pfeuffer-Jeschke, R. Hellmig, C. Becker, and G. Landwehr, Journal of Electronic Materials **27**, 532 (1998).

[45] G. Landwehr, J. Gerschütz, S. Oehling, A. Pfeuffer-Jeschke, V. Latussek, and C. Becker, Physica E: Low-dimensional Systems and Nanostructures **6**, 713 (2000).

[46] H. R. Reß, Ph.D. thesis, Julius-Maximilians Universität Würzburg (1998).

[47] L. Spieß, G. Teichert, R. Schwarzer, H. Behnken, and C. Genzel, *Moderne Röntgenbeugung* (Vieweg+Teubner, 2009), 2 ed.

[48] W. Braun, *Applied RHEED* (Springer-Verlag Berlin Heidelberg, 1999).

[49] A. Ichimiya and P. L. Cohen, *Reflection High-Energy Electron Diffraction* (Cambridge University Press, 2004).

[50] J. L. McCall and P. M. French, *Interpretive techniques for microstructural analysis* (Springer, 1977).

[51] Y. Asaoka, Journal of Crystal Growth **251**, 40 (2003).

[52] Z. Wasilewski, J.-M. Baribeau, M. Beaulieu, X. Wu, and G. Sproule, Journal of Vacuum Science & Technology B **22**, 1534 (2004).

[53] A. Ballestad, B. Ruck, M. Adamcyk, T. Pinnington, and T. Tiedje, Physical Review Letters **86**, 2377 (2001).

[54] H. Shtrikman, M. Oron, A. Raizman, and G. Cinader, Journal of Electronic Materials **17**, 105 (1988).

[55] J. Ayers, Journal of Crystal Growth **135**, 71 (1994).

[56] G. Lentz, A. Ponchet, N. Magnea, and H. Mariette, Applied Physics Letters **55**, 2733 (1989).

[57] H. Sitter and W. Faschinger, Thin Solid Films **225**, 250 (1993).

[58] H. Tatsuoka, H. Kuwabara, H. Fujiyasu, and Y. Nakanishi, Journal of Applied Physics **65**, 2073 (1989).

[59] L. S. Dang, J. Cibert, Y. Gobil, K. Saminadayar, S. Tatarenko, et al., Applied Physics Letters **55**, 235 (1989).

[60] R. Jacobs, J. Markunas, J. Pellegrino, L. Almeida, M. Groenert, M. Jaime-Vasquez, N. Mahadik, C. Andrews, and S. Qadri, Journal of Crystal Growth **310**, 2960 (2008).

[61] A. Jordan, Journal of Crystal Growth **49**, 631 (1980).

[62] P. Capper and J. Garland, *Mercury Cadmium Telluride: Growth, Properties and Applications* (John Wiley & Sons, Chichester, 2011).

[63] A. Rogalski, Reports on Progress in Physics **68**, 2267 (2005).

[64] S. Adachi, *Properties of Semiconductor Alloys: group-IV, III-V and II-VI semiconductors* (John Wiley & Sons, Ltd, Chichester, 2009).

[65] T. Skauli and T. Colin, Journal of Crystal Growth **222**, 719 (2001).

[66] P. Capper, *Narrow gap II-VI compounds for optoelectronic and electromagnetic applications*, vol. 3 (Springer Science & Business Media, 1997).

[67] O. Karavilovski, Nippon mining, private communication.

[68] G. Gouws, R. Muller, and R. Bowden, Journal of Crystal Growth **130**, 209 (1993).

[69] S. Johnson, J. Vigil, J. James, C. Cockrum, W. Konkel, M. Kalisher, R. Risser, T. Tung, W. Hamilton, W. Ahlgren, et al., Journal of Electronic Materials **22**, 835 (1993).

[70] G. Devyatykh, A. Moiseev, A. Kotkov, V. Dorofeev, N. Grishnova, V. Krasil'nikov, and A. Suchkov, Inorganic Materials **38**, 99 (2002).

[71] R. Feldman, R. Austin, A. Dayem, and E. Westerwick, Applied Physics Letters **49**, 797 (1986).

[72] T. De Lyon, J. Roth, O. Wu, S. Johnson, and C. Cockrum, Applied Physics Letters **63**, 818 (1993).

[73] S. Johnson, T. De Lyon, C. Cockrum, W. Hamilton, T. Tung, F. Gesswein, B. Baumgratz, L. Ruzicka, O. Wu, and J. Roth, Journal of Electronic Materials **24**, 467 (1995).

[74] R. Feldman, R. Austin, P. Fuoss, A. Dayem, E. Westerwick, S. Nakahara, T. Boone, J. Menendez, A. Pinczuk, J. Valladares, et al., Journal of Vacuum Science & Technology B **5**, 690 (1987).

[75] S. B. Qadri, M. Fatemi, and J. Dinan, Applied Physics Letters **48**, 239 (1986).

[76] T. Skauli, T. Colin, and S. Løvold, Journal of Crystal Growth **172**, 97 (1997).

[77] G. Monfroy, S. Sivananthan, X. Chu, J. Faurie, R. Knox, and J. Staudenmann, Applied Physics Letters **49**, 152 (1986).

[78] R. Miles, G. Wu, M. Johnson, T. McGill, J. Faurie, and S. Sivananthan, Applied Physics Letters **48**, 1383 (1986).

[79] T. Golding, S. Qadri, and J. Dinan, Journal of Vacuum Science & Technology A **7**, 616 (1989).

[80] W. Faschinger, F. Hauzenberger, P. Juza, A. Pesek, and H. Sitter, Journal of Electronic Materials **22**, 497 (1993).

[81] A. Ponchet, G. Lentz, H. Tuffigo, N. Magnea, H. Mariette, and P. Gentile, Journal of Applied Physics **68**, 6229 (1990).

[82] D. Dunstan, A. Prins, B. Gil, and J. Faurie, Physical Review B **44**, 4017 (1991).

[83] G. Osbourn, Journal of Applied Physics **53**, 1586 (1982).

[84] C. Mailhiot and D. L. Smith, Critical Reviews in Solid State and Material Sciences **16**, 131 (1990).

[85] J. Cibert, Y. Gobil, L. S. Dang, S. Tatarenko, G. Feuillet, P. Jouneau, K. Saminadayar, et al., Applied Physics Letters **56**, 292 (1990).

[86] L. Besombes, L. Marsal, K. Kheng, T. Charvolin, L. S. Dang, A. Wasiela, and H. Mariette, Journal of Crystal Growth **214**, 742 (2000).

[87] J. Eymery, S. Tatarenko, N. Bouchet, and K. Saminadayar, Applied Physics Letters **64**, 3631 (1994).

[88] Y. Takemura, M. Konagai, H. Nakanishi, and K. Takahashi, Journal of Crystal Growth **117**, 144 (1992).

[89] B. Daudin, S. Tatarenko, and D. Brun-Le Cunff, Physical Review B **52**, 7822 (1995).

[90] J. Benson, B. Wagner, A. Torabi, and C. Summers, Applied Physics Letters **49**, 1034 (1986).

[91] A. Waag, Y. Wu, R. Bicknell-Tassius, and G. Landwehr, Applied Physics Letters **54**, 2662 (1989).

[92] S. Tatarenko, B. Daudin, and D. Brun-Le Cunff, Applied Physics Letters **66**, 1773 (1995).

[93] F. Birch, Physical Review **71**, 809 (1947).

[94] A. Jankowski and T. Tsakalakos, Journal of Physics F: Metal Physics **15**, 1279 (1985).

[95] R. Cammarata and K. Sieradzki, Physical Review Letters **62**, 2005 (1989).

[96] E. Selvig, C. Tonheim, K. Kongshaug, T. Skauli, T. Lorentzen, and R. Haakenaasen, Journal of Vacuum Science & Technology B **25**, 1776 (2007).

[97] J. Arias and J. Singh, Applied Physics Letters **55**, 1561 (1989).

[98] L. He, C. R. Becker, R. Bicknell-Tassius, S. Scholl, and G. Landwehr, Semiconductor Science and Technology **8**, 216 (1993).

[99] L. Tapfer and K. Ploog, Physical Review B **40**, 9802 (1989).

[100] J. Chu and A. Sher, *Physics and properties of narrow gap semiconductors* (Springer, 2008).

[101] G. Hansen, J. Schmit, and T. Casselman, Journal of Applied Physics **53**, 7099 (1982).

[102] T. Harman, W. Kleiner, A. Strauss, G. Wright, J. Mavroides, J. Honig, and D. Dickey, Solid State Communications **2**, 305 (1964).

[103] A. Moritani, K. Taniguchi, C. Hamaguchi, and J. Nakai, Journal of the Physical Society of Japan **34**, 79 (1973).

[104] A. Chen, Y. Lai-Hsu, S. Krishnamurthy, and M. Berding, Semiconductor Science and Technology **5**, 100 (1990).

[105] L. Liu and W. Leung, Physical Review B **12**, 2336 (1975).

[106] A. Germanenko and G. Minkov, Physica Status Solidi (b) **184**, 9 (1994).

[107] X. Dai, T. L. Hughes, X.-L. Qi, Z. Fang, and S.-C. Zhang, Physical Review B **77**, 125319 (2008).

[108] C. Brüne, C. Thienel, M. Stuiber, J. Böttcher, H. Buhmann, E. G. Novik, C.-X. Liu, E. M. Hankiewicz, and L. W. Molenkamp, Physical Review X **4**, 041045 (2014).

[109] C. Thienel, Ph.D. thesis, Universität Würzburg (2014).

[110] X. Wan, A. M. Turner, A. Vishwanath, and S. Y. Savrasov, Physical Review B **83**, 205101 (2011).

[111] H. Weyl, Zeitschrift für Physik A Hadrons and Nuclei **56**, 330 (1929).

[112] A. Pfeuffer-Jeschke, Ph.D. thesis, Universität Würzburg (2000).

[113] V. Latussek, Ph.D. thesis, Universität Würzburg (2004).

[114] X. Zhang, A. Pfeuffer-Jeschke, K. Ortner, V. Hock, H. Buhmann, C. Becker, and G. Landwehr, Physical Review B **63**, 245305 (2001).

[115] G. Bir and G. Pikus, *Symmetry and Strain-induced Effects in Semiconductors* (John Wiley & Sons, Ltd, Chichester, 1974).

[116] V. Latussek, C. Becker, G. Landwehr, R. Bini, and L. Ulivi, Physical Review B **71**, 125305 (2005).

[117] K. Takita, K. Onabe, and S. Tanaka, Physica Status Solidi (b) **92**, 297 (1979).

[118] G. Minkov, A. Germanenko, O. Rut, A. Sherstobitov, S. Dvoretski, and N. Mikhailov, Physical Review B **88**, 155306 (2013).

[119] E. Olshanetsky, Z. Kvon, N. Mikhailov, E. Novik, I. Parm, and S. Dvoretsky, Solid State Communications **152**, 265 (2012).

[120] Z. Kvon, E. Olshanetsky, E. Novik, D. Kozlov, N. Mikhailov, I. Parm, and S. Dvoretsky, Physical Review B **83**, 193304 (2011).

[121] E. Olshanetsky, Z. Kvon, M. Entin, L. Magarill, N. Mikhailov, I. Parm, and S. Dvoretsky, JETP Letters **89**, 290 (2009).

[122] Z. D. Kvon, E. Olshanetsky, D. A. Kozlov, N. N. Mikhailov, and S. A. Dvoretskii, JETP Letters **87**, 502 (2008).

[123] C. Becker, V. Latussek, A. Pfeuffer-Jeschke, G. Landwehr, and L. W. Molenkamp, Physical Review B **62**, 10353 (2000).

[124] C. Becker, V. Latussek, G. Landwehr, and L. W. Molenkamp, Physical Review B **68**, 035202 (2003).

[125] S. Wiedmann, A. Jost, C. Thienel, C. Brüne, P. Leubner, H. Buhmann, L. W. Molenkamp, J. Maan, and U. Zeitler, Physical Review B **91**, 205311 (2015).

[126] X.-L. Qi and S.-C. Zhang, Physics Today **63**, 33 (2010).

[127] H. L. Stormer, D. C. Tsui, and A. C. Gossard, Reviews of Modern Physics **71**, 298 (1999).

[128] B. A. Bernevig, T. L. Hughes, and S.-C. Zhang, Science **314**, 1757 (2006).

[129] M. König, H. Buhmann, L. W. Molenkamp, T. Hughes, C.-X. Liu, X.-L. Qi, and S.-C. Zhang, Journal of the Physical Society of Japan **77**, 031007 (2008).

[130] A. Ström, H. Johannesson, and G. Japaridze, Physical Review Letters **104**, 256804 (2010).

[131] M. Büttiker, Physical Review Letters **57**, 1761 (1986).

[132] M. Büttiker, Science **325**, 278 (2009).

[133] A. Roth, C. Brüne, H. Buhmann, L. W. Molenkamp, J. Maciejko, X.-L. Qi, and S.-C. Zhang, Science **325**, 294 (2009).

[134] C. Brüne, A. Roth, H. Buhmann, E. M. Hankiewicz, L. W. Molenkamp, J. Maciejko, X.-L. Qi, and S.-C. Zhang, Nature Physics **8**, 485 (2012).

[135] C. Brüne, A. Roth, E. Novik, M. König, H. Buhmann, E. Hankiewicz, W. Hanke, J. Sinova, and L. W. Molenkamp, Nature Physics **6**, 448 (2010).

[136] G. Grabecki, J. Wróbel, M. Czapkiewicz, S. Gierałtowska, E. Guziewicz, M. Zholudev, V. Gavrilenko, N. Mikhailov, S. Dvoretski, F. Teppe, et al., Physical Review B **88**, 165309 (2013).

[137] E. Olshanetsky, Z. Kvon, G. Gusev, A. Levin, O. Raichev, N. Mikhailov, and S. Dvoretsky, Physical Review Letters **114**, 126802 (2015).

[138] G. Gusev, Z. Kvon, O. Shegai, N. Mikhailov, S. Dvoretsky, and J. Portal, Physical Review B **84**, 121302 (2011).

[139] G. Gusev, Z. Kvon, E. Olshanetsky, A. Levin, Y. Krupko, J. Portal, N. Mikhailov, and S. Dvoretsky, Physical Review B **89**, 125305 (2014).

[140] K. C. Nowack, E. M. Spanton, M. Baenninger, M. König, J. R. Kirtley, B. Kalisky, C. Ames, P. Leubner, C. Brüne, H. Buhmann, et al., Nature materials **12**, 787 (2013).

[141] M. König, M. Baenninger, A. G. Garcia, N. Harjee, B. L. Pruitt, C. Ames, P. Leubner, C. Brüne, H. Buhmann, L. W. Molenkamp, et al., Physical Review X **3**, 021003 (2013).

[142] C. L. Kane and E. J. Mele, Physical Review Letters **95**, 226801 (2005).

[143] C. Wu, B. A. Bernevig, and S.-C. Zhang, Physical Review Letters **96**, 106401 (2006).

[144] J. Luttinger, Journal of Mathematical Physics **4**, 1154 (1963).

[145] N. Lezmy, Y. Oreg, and M. Berkooz, Physical Review B **85**, 235304 (2012).

[146] G. Dolcetto, M. Sassetti, and T. L. Schmidt, ArXiv e-prints (2015), 1511.06141.

[147] J. Maciejko, C. Liu, Y. Oreg, X.-L. Qi, C. Wu, and S.-C. Zhang, Physical Review Letters **102**, 256803 (2009).

[148] J. C. Teo and C. Kane, Physical Review B **79**, 235321 (2009).

[149] A. Ström and H. Johannesson, Physical Review Letters **102**, 096806 (2009).

[150] J. C. Budich, F. Dolcini, P. Recher, and B. Trauzettel, Physical Review Letters **108**, 086602 (2012).

[151] Y. Tanaka, A. Furusaki, and K. Matveev, Physical Review Letters **106**, 236402 (2011).

[152] F. Crépin, J. C. Budich, F. Dolcini, P. Recher, and B. Trauzettel, Physical Review B **86**, 121106 (2012).

[153] F. Geissler, F. Crépin, and B. Trauzettel, Physical Review B **89**, 235136 (2014).

[154] T. L. Schmidt, S. Rachel, F. von Oppen, and L. I. Glazman, Physical Review Letters **108**, 156402 (2012).

[155] J. Hinz, H. Buhmann, M. Schäfer, V. Hock, C. Becker, and L. W. Molenkamp, Semiconductor Science and Technology **21**, 501 (2006).

[156] S. Essert, V. Krueckl, and K. Richter, Physical Review B **92**, 205306 (2015).

[157] M. Bendias, Master's thesis, Universität Würzburg (2012).

[158] N. Ashcroft and N. Mermin, *Solid State Physics*, HRW international editions (Holt, Rinehart and Winston, 1976), ISBN 9780030839931.

[159] G. Tkachov, C. Thienel, V. Pinneker, B. Büttner, C. Brüne, H. Buhmann, L. W. Molenkamp, and E. Hankiewicz, Physical Review Letters **106**, 076802 (2011).

[160] A. B. Pippard, *Magnetoresistance in Metals* (Cambridge University Press, 1989).

[161] M. Knap, J. D. Sau, B. I. Halperin, and E. Demler, Physical Review Letters **113**, 186801 (2014).

[162] T. Ihn, *Semiconductor nanostructures* (Oxford University Press New York, 2010).

[163] T. Ando, A. B. Fowler, and F. Stern, Reviews of Modern Physics **54**, 437 (1982).

[164] S. Khondaker, I. Shlimak, J. Nicholls, M. Pepper, and D. Ritchie, Physical Review B **59**, 4580 (1999).

[165] Y. Nemirovsky and G. Bahir, Journal of Vacuum Science & Technology A **7**, 450 (1989).

[166] S. Pollitt, M. Pepper, and C. Adkins, Surface Science **58**, 79 (1976).

[167] G.-H. Tsau, A. Sher, M. Madou, J. Wilson, V. Cotton, and C. Jones, Journal of Vacuum Science & Technology A **4**, 1983 (1986).

[168] J. Wilson and V. Cotton, Journal of applied physics **57**, 2030 (1985).

[169] S. D. Sarma and E. Hwang, Solid state communications **135**, 579 (2005).

[170] J. Buxo, D. Esteve, J. Farre, G. Sarrabayrouse, and J. Simonne, Applied Physics Letters **33**, 969 (1978).

[171] M. Daugherty and B. Janousek, Applied Physics Letters **42**, 290 (1983).

[172] H. B. Nielsen and M. Ninomiya, Physics Letters B **130**, 389 (1983).

[173] D. Son and B. Spivak, Physical Review B **88**, 104412 (2013).

[174] H.-J. Kim, K.-S. Kim, J.-F. Wang, M. Sasaki, N. Satoh, A. Ohnishi, M. Kitaura, M. Yang, and L. Li, Physical Review Letters **111**, 246603 (2013).

[175] J. Du, H. Wang, Q. Mao, R. Khan, B. Xu, Y. Zhou, Y. Zhang, J. Yang, B. Chen, C. Feng, et al., arXiv preprint arXiv:1507.05246 (2015).

[176] C. Shekhar, F. Arnold, S.-C. Wu, Y. Sun, M. Schmidt, N. Kumar, A. G. Grushin, J. H. Bardarson, R. D. d. Reis, M. Naumann, et al., arXiv preprint arXiv:1506.06577 (2015).

[177] X. Huang, L. Zhao, Y. Long, P. Wang, D. Chen, Z. Yang, H. Liang, M. Xue, H. Weng, Z. Fang, et al., Physical Review X **5**, 031023 (2015).

[178] R. Cottam and G. Saunders, Journal of Physics C: Solid State Physics **6**, 2105 (1973).

[179] U. Rössler, in *New Data and Updates for several Semiconductors with Chalcopyrite Structure, for several II-VI Compounds and diluted magnetic IV-VI Compounds*, edited by U. Rössler (Springer Berlin Heidelberg, 2013), Landolt-Börnstein - Group III Condensed Matter.

[180] J. Mavroides and D. Kolesar, Solid State Communications **2**, 363 (1964).

List of publications

Full papers - published

- M. Baenninger, M. König, A. G. F. Garcia, M. Mühlbauer, C. Ames, **P. L.**, C. Brüne, H. Buhmann, L. W. Molenkamp and D. Goldhaber-Gordon, *Fabrication of samples for scanning probe experiments on quantum spin Hall effect in HgTe quantum wells*, J. Appl. Phys. **112**, 103713 (2012)

- M. König, M. Baenninger, A. G. F. Garcia, N. Harjee, B. L. Pruit, C. Ames, **P. L.**, C. Brüne, H. Buhmann, L. W. Molenkamp and D. Goldhaber-Gordon, *Spatially Resolved Study of Backscattering in the Quantum Spin Hall State*, Phys. Rev. X **3**, 021003 (2013)

- K. Nowack, E. Spanton, M. Baenninger, M. König, J. Kirtley, B. Kalinsky, C. Ames, **P. L.**, C. Brüne, H. Buhmann, L. W. Molenkamp, D. Goldhaber-Gordon and K. Moler, *Imaging currents in HgTe quantum wells in the quantum spin Hall regime*, Nat. Mat. **12**, 787 (2013)

- S. Hart, H. Ren, T. Wagner, **P. L.**, M. Mühlbauer, C. Brüne, H. Buhmann, L. W. Molenkamp and A. Yacoby, *Induced superconductivity in the quantum spin Hall edge*, Nat. Phys. **10**, 638 (2014)

- E. Y. Ma, M. Reyes Calvo, J. Wang, B. Lian, M. Mühlbauer, C. Brüne, Y-T. Cui, K. Lai, W. Kundhikanjana, Y. Yang, M. Baenninger, M. König, C. Ames, H. Buhmann, **P. L.**, L. W. Molenkamp, S-Z. Zhang, D. Goldhaber-Gordon, M. A. Kelly, and Z-X. Shen, *Unexpected edge conduction in mercury telluride quantum wells under broken time-reversal symmetry*, Nat. Comm. **6**, 7252 (2015)

- S. Wiedmann, A. Jost, C. Thienel, C. Brüne, **P. L.**, H. Buhmann, L. W. Molenkamp, J. C. Maan and U. Zeitler, *Temperature-driven transition from a semiconductor to a topological insulator*, Phys. Rev. B **91**, 205311 (2015)

- T. Khouri, M. Bendias, **P. L.**, C. Brüne, H. Buhmann, L. W. Molenkamp, U. Zeitler, N. E. Hussey and S. Wiedmann, *High-temperature quantum Hall effect in finite gapped HgTe quantum wells*, Phys. Rev. B **93**, 125308 (2016)

- **P. L.**, L. Lunczer, C. Brüne, H. Buhmann and L. W. Molenkamp, *Strain Engineering of the Band Gap of HgTe Quantum Wells using Superlattice Virtual Substrates*, Phys. Rev. Lett. **117**, 086403 (2016)

- S. Hart, H. Ren, M. Kosowsky, G. Ben-Shach, **P. L.**, C. Brüne, H. Buhmann, L. W. Molenkamp, B. I. Halperin and A. Yacoby, *Controlled Finite Momentum Pairing and Spatially Varying Order Parameter in Proximitized HgTe Quantum Wells*, Nat. Phys. **13**, 87 (2017)

- E. Bocquillon, R. S. Deacon, J. Wiedenmann, **P. L.**, T. M. Klapwijk, C. Brüne, K. Ishibashi, H. Buhmann and L. W. Molenkamp, *Gapless Andreev bound states in the quantum spin Hall insulator HgTe*, Nat. Nanotech. **12**, 137 (2017)

- R. S. Deacon, J. Wiedenmann, E. Bocquillon, T. M. Klapwijk, **P. L.**, C. Brüne, S. Tarucha, K. Ishibashi, H. Buhmann and L. W. Molenkamp, *Josephson radiation from gapless Andreev bound states in HgTe-based topological junctions*, Phys. Rev. X **7**, 021011 (2017)

Full papers - submitted

- M. R. Calvo, F. de Juan, R. Ilan, E. J. Fox, A. J. Bestwick, M. Mühlbauer, J. Wang, C. Ames, **P. L.**, C. Brüne, S. C. Zhang, H. Buhmann, L. W. Molenkamp and D. Goldhaber-Gordon, *Interplay of chiral and helical states in a Quantum Spin Hall Insulator lateral junction*, ArXiv:1702.08561, submitted to Phys. Rev. Lett. (Feb. 2017)

- A. Budewitz, M. Bendias, **P. L.**, C. Brüne, H. Buhmann and L. W. Molenkamp, *Quantum anomalous Hall effect in Mn-doped HgTe quantum wells*, ArXiv:1706.05789, submitted to Phys. Rev. Lett. (June 2017)

Manuscripts in preparation

- D. Mahler, J. Wiedenmann, C. Thienel, C. Ames, **P. L.**, C. Brüne, H. Buhmann, D. Di Sante, C. Gould, G. Sangiovanni and L. W. Molenkamp, *Observation of 1/B oscillations from an insulating topological state of matter*, in preparation

- D. Mahler, **P. L.**, F. Schmitt, C. Brüne, H. Buhmann and L. W. Molenkamp, *Coexistence of Weyl-Bulk and Dirac-Surface states in strained HgTe*, in preparation
- K. Bendias, A. Budewitz, S. Shamim, **P. L**., J. Kleinlein, E. Bocquillon, H. Buhmann and L. W. Molenkamp, *Wet etching of HgTe Quantum Spin Hall microstructures*, in preparation

Acknowledgements

It is my great pleasure to acknowledge all the people who helped in the progress of this work. In particular, I want to thank

- Prof. Laurens W. Molenkamp for giving me the opportunity to work as a PhD student at the chair of Experimental Physics III, and for his support.
- Prof. Hartmut Buhmann for the excellent supervision of my work, which involved not only scientific guidance, but also a considerable deal of independence and a never-ending encouragement.
- Christoph Brüne for the excellent co-supervision of my work. In particular, for always standing in for the MBE team and its needs.
- The MBE team for the outstanding team spirit, the unmatched level of know-how and the coffee: Christopher Ames, Carmen Bundschuh, Felicitas Gerhard, Volkmar Hock, Prof. Gregorz Karczewski, Rebekka Pfeuffer, Christoph Pohl, Raimund Schlereth, Steffen Schreyeck, Claus Schumacher, Mirko Trabel, Petra Wolf-Müller and Martin Zipf.
- My two long-term office fellows Rebekka Pfeuffer and Holger Thierschmann for the great atmosphere and the constant supply of distractions.
- My master students Maximilian Kessel and Lukas Lunczer, for their numerous contributions to this work, provided in the form of hard experimental data, creative input and entertainment.
- My bachelor students, who did the same in a condensed fashion: Michael Bathon, Benedikt Halbig, Florian Hau and Dennis Hein.
- All my colleagues and former colleagues at the EPIII, who made the past years so very joyful and special. I will miss you guys! Utz Bass, Martin Baußenwein, Kalle Bendias, Erwann Bocquillon, Andreas Budewitz, Amandeep Singh Buppal, Petra

Fries, Simon Hartinger, Oliver Herrmann, Thomas Khouri, Johannes Knorr, Bruno Krefft, David Mahler, Luis Maier, Mathias Mühlbauer, Graciely Santos, Rainer Schaller, Fabian Schmitt, Michael Stuiber, Cornelius Thienel, Timo Wagner, Jonas Wiedenmann and many others.

Finally, I want to express my very special gratitude to my family Christa, Franz, Simon and Christian for the support. Thanks for everything!